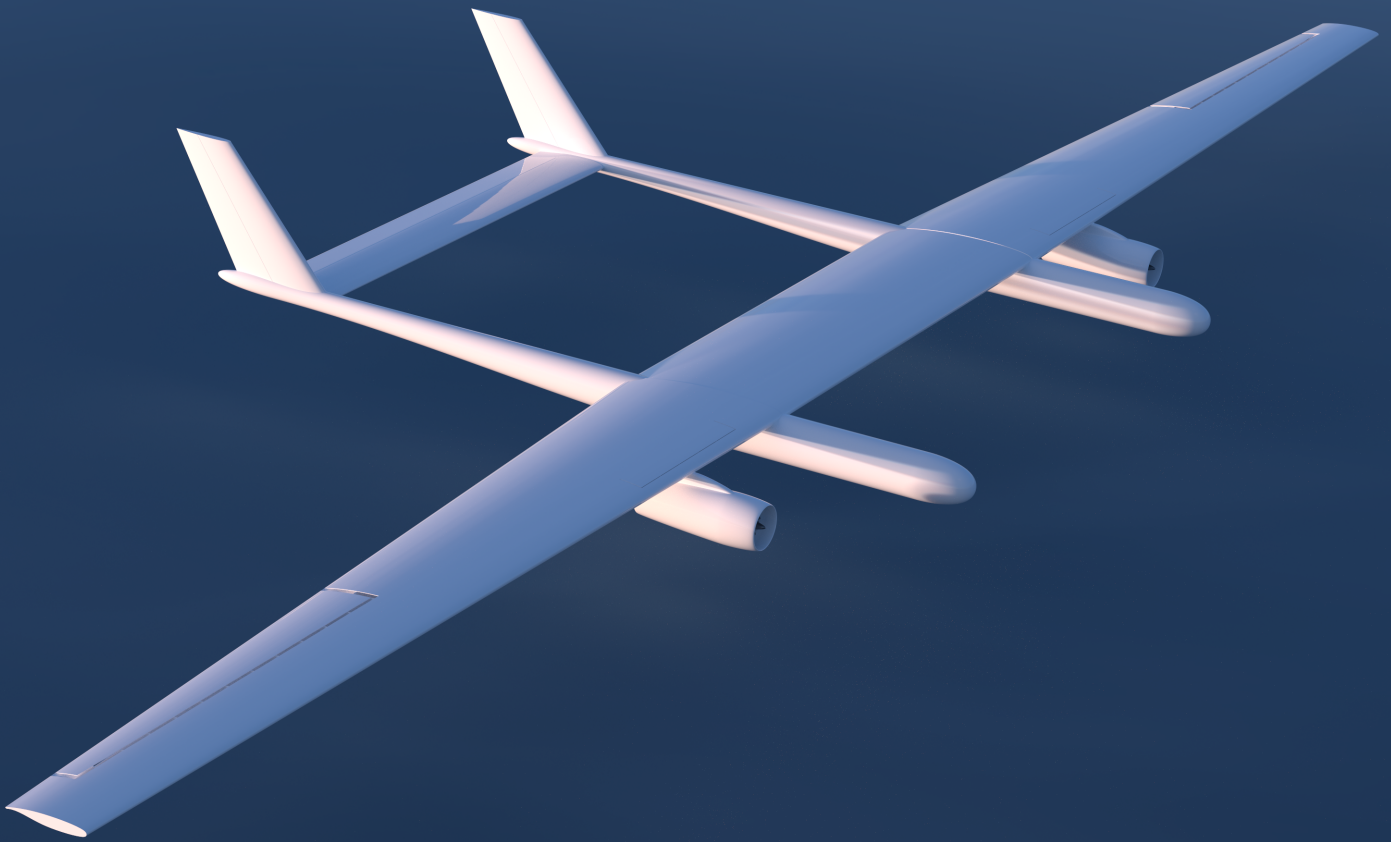


Final Report

Stratospheric Aerosol Injection of CaCO_3

AE3200: Design Synthesis



Delft University of Technology

Final Report

Stratospheric Aerosol Injection of CaCO_3

by

Konstantinos Barmounis	5749840
Inés Blanco Fuentes	5725860
Pavel de Bode	5764645
Máté Cser	5688299
Blanca Gomez-Guillamon Jurado	5682177
Maxine Van Houtven	5480140
Barnabás Kardos	5785707
Carmen Marzal Sanchez-Vegazo	5824230
Bas Oudejans	5779421
Moritz Rokitta	4845501



SCAI
STRATOSPHERIC
 CaCO_3 AEROSOL
INJECTION

Tutor: S. Hulshoff
Coaches: A. Tassanbi and T. Zhang
Project Duration: April, 2025 - June, 2025
Faculty: Faculty of Aerospace Engineering, Delft

Cover: 3D model of the SCAI aircraft at cruise
Generated Using CATIA 3D Experience

Preface

This document represents the final report of the *Design Synthesis Exercise*. It is the concluding part of the undergraduate degree in Aerospace Engineering at Delft University of Technology. In this project, students apply all their knowledge in this discipline and work together as a team to engineer a solution for a challenging task. Over a period of ten weeks, ten aerospace engineering students at the Delft University of Technology worked together to design a fleet of aircraft capable of delivering 6Mt of aerosols into the stratosphere in a sustainable and low-cost manner. Following this initiative from Dr. Steven Hulshoff, the group made a preliminary design of the aircraft and a detailed operational plan. Chapter 2 provides more insight into the background of the project while Chapter 15 delivers an overview of its cost. Readers interested in the final design of the aircraft are referred to Chapter 16.

Acknowledgments

We would like to thank our supervisor, Dr. Steven Hulshoff, and our two coaches, Aidana Tassanabi and Tingyu Zhang, for their guidance and advice during this project. Furthermore, we would like to show our gratitude to the faculty of Aerospace Engineering at Delft University of Technology for providing us with the opportunity to partake in this project and with the necessary facilities and tools. Finally, the team would like to acknowledge George Kelesidis for his expertise and guidance on aerosols, which proved to be a major design component.

Konstantinos Barmounis

Inés Blanco Fuentes

Pavel de Bode

Máté Cser

Blanca Gomez-Guillamon Jurado

Maxine Van Houtven

Barnabás Kardos

Carmen Marzal Sanchez-Vegazo

Bas Oudejans

Moritz Rokitta

Nomenclature

Abbreviations

Abbreviation	Definition
APU	Auxiliary Power Unit
AR	Aspect Ratio
ATR	Average Temperature Response
CCS	Carbon Capture and Storage
CG	Centre of Gravity
CONOPS	Concept of Operations
CS	Control Surface
DOT	Design Option Tree
DS	Design Synthesis
EAS	Equivalent Airspeed
ECB	European Central Bank
E&H	Electrical and Hydraulic Subsystems
EoL	End of Life
FF	Fuel Fraction
FM	Fuel mass
Fus	Fuselage
G	Geometry definition in BCS
GHG	Greenhouse gass
HBPR	High-Bypass Ratio
HLD	High Lift Device(s)
IATA	International Air Transport Association
ICAO	International Civil Aviation Organization
ISA	International Standard Atmosphere

Abbreviation	Definition
Land	Landing
LBPR	Low-Bypass Ratio
LCA	Life Cycle Assessment
LCI	Life Cycle Inventory
LG	Landing Gear
MAC	Mean Aerodynamic Chord
MF	Mass Fraction
MLG	Main Landing Gear
MTOM	Maximum Take-Off Mass
NLG	Nose Landing Gear
OEM	Operative Empty Mass
PI	Payload
PIS	Payload Subsystem
Prop	Propulsion
ROC	Rate Of Climb
SAI	Stratospheric Aerosol Injection
SFC	Specific Fuel Consumption
Stab	Stabilizer
TO	Take-Off
TOP	Take-off Parameter
TRL	Technology Readiness Level
RAMS	Reliability, Availability, Maintainability and Safety
RDT&E	Research, Development, Testing and Evaluation
w	Wing
V&V	Verification and Validation

Symbols

Symbol	Definition	Unit
b	Wing span	[m]
\bar{c}	Mean Aerodynamic Chord	[m]
S	Surface Area	[m ²]
C_D	Drag Coefficient	[-]
C_L	Lift Coefficient	[-]
C_f	Skin Friction Coefficient	[-]
e	Oswald Factor	[-]
F	Form Factor	[-]
D	Drag	[N]
d	Diameter	[m]
h	Height	[m]
L	Lift	[N]
l	Length	[m]
M	Mach number	[-]
A	Aspect Ratio	[-]
\dot{m}	Mass Flow	[kg/s]
G	Shear Modulus	[Pa]
E	Young's Modulus	[Pa]
I	Moment of Inertia	[m ⁴]
t	Thickness	[m]
q	Shear Flow	[N/m]
A_m	Enclosed Area	[m ²]
ν	Poisson Ratio	[-]
T	Torque	[Nm]

Symbol	Definition	Unit
M	Moment	[Nm]
n	Load Factor	[-]
g	Gravitational Acceleration	[m/s ²]
P	Power	[W]
S	Wing Surface	[m ²]
T	Thrust	[N]
t	Time	[s]
V	Velocity	[m/s]
W	Weight	[N]
x	Longitudinal Coordinate	[m]
y	Spanwise Coordinate	[m]
z	Height Coordinate	[m]
α	Angle of Attack	[°]
β	Compressibility Correction Factor	[-]
γ	Climb Angle	[°]
Γ	Dihedral	[°]
δ	Deflection	[°]
λ	Taper Ratio	[-]
Λ	Sweep	[°]
ρ	Density	[kg/m ³]
σ	Stress	[Pa]

Executive Overview

Contributors: Inés, Maxine

In recent years, the effects of climate change has become strikingly clear, with record-breaking summer temperatures and a growing number of extreme weather events, including hurricanes, floods and droughts ¹. These increasingly frequent and unpredictable phenomena pose a threat to humanity, potentially having devastating effects on agriculture, ecosystems and biodiversity.

To address these challenges, the Paris Agreement was established on 12 December 2015. As the Secretary General of the UN, Ban Ki-moon, said: “The Paris Agreement provides a viable blueprint to mitigate the serious threats to our planet. It sets clear targets to restrict rising temperatures, limit greenhouse gas emissions, and facilitate climate-resilient development and green growth. ²”

One of the primary targets of the Paris Agreement is to limit the temperature increase to 1.5°C above pre-industrial levels, and that is where the geoengineering technologies come into play. Geoengineering involves the deliberate manipulation of the Earth’s atmosphere to influence the climate in a manner that mitigates or counteracts certain impacts of global warming, such as rising global temperatures, melting polar ice caps, sea level rise, and the increasing frequency and intensity of extreme weather events³.

Although it is now clear that addressing climate change requires reducing the emission of greenhouse gases [1], progress has been slow and future global warming remains uncertain. To mitigate potential delays in the development of reduction and capture technologies, researchers have started exploring geoengineering techniques that could temporarily prevent excessive global warming.

These technologies primarily focus on solar radiation management strategies (SRM), which are capable of lowering the planet’s temperature by reflecting incoming sunlight to prevent excessive warming. The main strategy of SRM is Stratospheric Aerosol Injection (SAI), which aims to mimic the cooling effect of volcanic eruptions by reflecting sunlight through the injection of aerosols in the stratosphere.

This technique appears to be the most affordable and effective option for the prevention of excessive global warming, where previous studies have shown the possibility of decreasing the temperature of the planet by 1°C with continuous yearly injection into the stratosphere [2]. Therefore, the current need is the following:

Need: “Decrease Earth’s temperature by 1°C during the time it takes for the reduction and capture strategies of greenhouse gases to become effective.”

In the past, liquid sulfate aerosols were considered for the design of this mission, based on the composition of natural volcanic eruptions. However, recent results show solid aerosols such as Al₂O₃ or CaCO₃ could be superior options. Even though they require more mass to be injected, they absorb less terrestrial infrared (less stratospheric heating) and produce less diffuse radiation, leading to smaller changes in circulation, precipitation, and vegetation of the planet. This results in a great advantage since it diminishes the severity of possible unknown side effects in the world’s ecosystem [3].

To allow for solid aerosol injection to the stratosphere, this team has the goal of designing an optimised and cost-effective aircraft-based fleet, defined in the following mission need and project objective statements:

Mission Need Statement: “Demonstrate the economic and technological feasibility of injecting solid aerosols into the stratosphere to decrease Earth’s temperature by 1°C”

Project Objective Statement: “Design a fleet of aircraft for the sustainable and low-cost delivery of 6 Mt of solid aerosols annually to the stratosphere, with a team of 10 students in 10 weeks.”

In order to achieve this mission and project objective in such a short time frame, a clear organisation is required. For that reason, the project is divided into four different phases: the Project Plan, Baseline Report, Midterm Report and Final Report.

This is the Final Report, where the outcome of the last 10 weeks of work is thoroughly explained and divided into departments. A summary can be found below for the reader’s convenience, providing an overview of the

¹URL:<https://science.nasa.gov/climate-change/extreme-weather> cited 2 May 2025

²URL:<https://unfccc.int/process-and-meetings/the-paris-agreement> cited 1 May 2025

³URL:<https://www.maximizemarketresearch.com/market-report/geoengineering-market/214149/> cited 29 April

project objectives, technical design and operations.

Market Analysis

The project is positioned in the sector of Stratospheric Aerosol Injection (SAI), a form of Solar Radiation Management (SRM), which is one of the principal technological segments within the geoengineering market. To understand the market potential of solid aerosol injection through an aircraft-based fleet, a market analysis was performed. For this, all the current technology concepts in the market were explained, and their share in the market is shown in Figure 2.1, where SMR has the highest share. The market value was USD 28.0 billion in 2024, and is estimated to be 73.9 billion by 2030. North America is the geographical leader of the market.

The main users of SRM (the most relevant for this team's mission) would most likely be a coalition of countries or an international organisation, while private companies might also be contracted by this coalition for manufacturing, operational or funding purposes.

Since this mission is a temporary solution, alternative uses for the future use of the aircraft fleet were defined. Hypersonic testing, satellite launch at high altitude and stratospheric sampling to prove the efficiency of the possible future carbon capture and storage (CCS) technologies were proposed. This specific mission will reach its maturity level in 15 years after its first deployment, with an approximate market value of USD 40.65 billion. A SWOT analysis, shown in Figure 2.4, was performed, with an emphasis on the incorporation of solid aerosols. A stakeholder analysis can be found in this section, which serves as a starting point for the definition of the stakeholder requirements table shown in Table 3.1

Configuration Selection

In order to decide on the configuration of the aircraft, a process consisting of two trade-offs was followed. In the first trade-off, the aircraft design concepts that originated from the Design Option Tree underwent an extensive literature study to find information on certain established criteria: high altitude performance, stability and control, operational costs, technology readiness, payload storage and sustainability. Once information was gathered from the four concepts, the trade-off was performed, and the scores were determined, clearly indicating that the flying wing subsonic aircraft and the supersonic conventional aircraft should be discarded. This was due to their unacceptable scores in certain criteria and low final score.

On the other hand, the conventional subsonic and twin-body subsonic aircraft obtained the same final score. For that reason, a second trade-off was performed to decide on a final concept. This trade-off was based on the preliminary design of both concepts. The following trade-off parameters were established for this second trade-off: wing bending stress, parasitic drag, lift-to-drag ratio, payload capability per unit thrust and operational costs per unit payload. Based on the trade-off scores, the subsonic twin body aircraft was clearly the winner, outperforming the conventional aircraft in all criteria except for the zero-lift drag and operational costs, as expected due to its double fuselage and operations being optimised for conventional aircraft.

For both the first and second trade-offs, a sensitivity analysis was performed to make sure the best configurations were chosen despite the uncertainties in the criteria weights and scores. Both sensitivity analyses proved that the decisions made were indeed the correct ones.

Aerodynamic Analysis

In this analysis, the sizing of the aircraft's aerodynamic surfaces was carried out. The study begins by identifying the key aerodynamic parameters, including the critical Mach number (M_{crit}) and the maximum lift-to-drag ratio (L/D_{max}), among others, that drive the design. Relevant environmental conditions at cruise altitude were examined and obtained, and the primary aerodynamic requirements were subsequently summarised.

An airfoil trade-off took place, ensuring that the optimal geometry was selected for the mission profile specified. Trade criteria were identified and discussed, weights were assigned and calculations were performed, leading to the selection of SC(2)-0612 as the airfoil of the wing. The attention was subsequently shifted to a 3D analysis, where the wing planform was designed. This was an iterative process, directly depended on the aerodynamic parameters obtained using DATCOM equations. As a result, the values found in Section 8.3 and Section 8.4 were iterated till convergence. These include geometric values such as the wingspan and taper, and aerodynamic parameters such as the lift and drag coefficient, in particular for the take-off, cruise and landing flight phases. A summary of these values can be found in Table 3.

Table 3: Aerodynamic parameters summary

$C_{L_{max}}$ [-]	$C_{L\alpha}$ [1/rad]	$C_{L_{des}}$ [-]	α_{stall} [deg]	$C_{D_{des}}$ [-]	A [-]	b [m]	S [m ²]	λ [-]
1.292	5.33	0.87	11.94	0.0332	21.7	77	272.96	0.45

The analysis continued with a fuselage sizing, where a diameter of 1.344 m was determined to minimise wave drag. This led to the final fuselage length of 22.76 m. Finally study of the near wake characteristics was performed, such as the spanwise circulation distribution and the engine plume characteristics. The study concluded with a sensitivity analysis to assess the volatile nature of the aerodynamic parameters obtained and a verification and validation to ensure correct design tools implementation and reasonable data acquisition.

Payload Analysis

In order to decide between CaCO_3 and Al_2O_3 for this mission's application, an analysis was performed where both were compared for their environmental effects, amount of aerosol needed, costs, technology readiness and abundance. Calcite outperformed alumina in every criterion except for the technology readiness level, mainly due to the agglomeration complications calcite experiences.

Calcite was therefore chosen as the aerosol material, and an aerosol dispersal strategy to avoid agglomeration was proposed. A fluidisation technology with mechanical (steel balls) and acoustic (subwoofer) agitation was considered. The nozzles chosen for dispersal have an air inlet to help further de-agglomerate the aerosol particles.

After the delivery system was defined, a range of realistic injection rates was proposed, the lower boundary representing Neukermans' [4] experimental results, and an upper boundary based on a recalculation of McNeill's experimental results [5] for stratospheric conditions. The upper boundary value was selected to design this mission. This is supported by the fact that the obtained values are derived from experimental results reported by the McNeill group, which have been recalculated to reflect the specific conditions of our stratospheric flight regime.

Furthermore, a sensitivity study on the injection rate of the aircraft was performed to analyse how a slight change would change the optimal design of the aircraft, which clearly shows how injection rates lead to a more efficient mission. Finally, verification and validation were performed to ensure the injection rate calculations were correct and realistic.

Weight Estimation and Iterations

This chapter gives an overview of the design process and the weight estimations done. The N2 chart showing interfaces between the different subsystems was reworked. The class I weight estimation is explained, which was used to determine the maximum take-off mass of the design. Then, the process of obtaining the thrust and wing loading diagram is explained. This diagram results in the design point. Then, the process of performing the class II weight estimations is given, which was used to create better estimates of the subsystem weights. Finally, the iterative process between class I and class II estimations is explained, which was used to obtain the final values for the masses of the aircraft, the wing area and the thrust required, shown in Table 4.

Table 4: Main Required Design Parameters After Global Iterations

Parameter	Payload [kg]	MTOM [kg]	OEM [kg]	FM [kg]	S [m ²]	T_{cruise} [N]
Value	17000	61191	34381	9810	273	30510

Flight Performance

In the flight performance chapter, all flight phases were analysed in detail to obtain an optimal flight profile. Take-off, landing, climb and descent were analysed, leading to the following payload-range diagram:

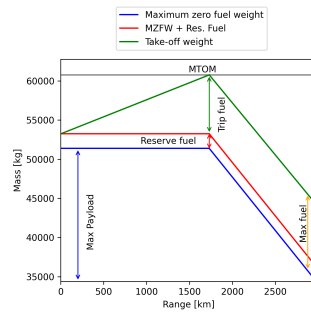


Figure 1: Payload range diagram showing aircraft mass composition for increasing range

The flight profile of the cruise phase was divided into two phases. Given that the aerosol will be injected during cruise, the weight of the aircraft becomes significantly lower; therefore, half of the range of the aircraft was defined to be flown at 20 km altitude, while the other half at 21.7 km. A powered descent phase was calculated for a descent slope of -4.5° , followed by a worst-case loiter phase at a height of 3 km and for a time of 45 minutes, as described by CS-25 regulations. Finally, the descent phase to the airbase was calculated for a glide slope of -3.2° . Verification was carried out by ensuring compliance with CS-25 regulations. Additionally, validation was performed by applying the designed tool to existing aircraft with known flight performance data, and comparing the results to those reference values. The final main parameters determined are given in Table 5.

Table 5: Flight Performance Parameters

Parameter	Take-off Distance [m]	Landing Distance [m]	Climb [min]	Cruise [min]	Descent and Loiter [min]
Value	527.7	1522	26.2	101.2	61.4

Propulsion

An analysis of the different kinds of propulsion systems for aircraft was performed to determine the most suitable option for carrying the heavy payload to stratospheric altitudes. From analysing existing propulsion systems, it turned out that existing jet engines were either too heavy to fly at the desired cruise conditions, too inefficient to be reasonably used or too small and requiring a larger number of engines. To combine the power density of low-bypass turbofans and turbojets and the efficiency of modern turbofans, a new engine was sized to better suit this mission.

By analysing the engine performance for a number of key design parameters, such as the bypass ratio, overall compression ratio and turbine inlet temperature, a more efficient yet still power-dense engine was sized. The engine, a large turbojet with an overall compression ratio of 26 and a turbine inlet temperature of 1550 K, was found to be able to deliver the required thrust at cruise of 30.5 kN, needing only 2 engines on the aircraft. These engines are more power-dense than modern high-bypass turbofans and despite their higher specific fuel consumption, these engines are still notably lighter than the more fuel efficient engine types. This lower engine mass allows for a higher payload-to-fuel ratio. The engine was sized using a 1-D analysis of the flow, as per *Gas Turbine Theory* [6], through the engine, followed by a sizing of the turbomachinery to determine whether the upscaled size would be problematic. This concluded in a sized engine with desirable performance figures.

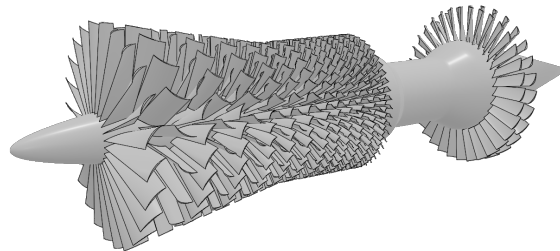


Figure 2: A representation of the SCAI engine turbomachinery

Stability and Control

A stability and control analysis was performed to determine the aircraft's balance and size the tail and control surfaces of the aircraft. Firstly, a loading diagram to determine the most forward and aft centre of gravity was

plotted, where only the fuel and the aerosol mass were considered, since all the other equipment was considered part of the operational empty weight. For simplification, the aerosol was assumed to be loaded from front to back. From the scissor plot, the ratio of the surface area of the horizontal tail to the main wing was obtained, and the surface area of the horizontal tail was defined to be 39 m^2 . A conventional tail with a joint horizontal tail was decided to avoid deep stall and allow for more structural efficiency. The vertical stabiliser was sized to maintain directional control, obtaining a 20.4 m^2 surface area.

The control surfaces were designed, consisting of one aileron and rudder per wing, and an elevator in the horizontal stabiliser. The rudder was sized for asymmetric thrust at sea-level, near stall speed, since it was found to be the most critical scenario. On the other hand, the elevator design was based on take-off rotation rate requirements, and longitudinal trim was also proven to be obtained during cruise. Finally, the aileron was sized for the required roll rate to comply with the 30-degree bank angle in 2.5 seconds requirement.

The landing gears were positioned longitudinally to comply with the requirement that the nose landing gear must at least carry 8% of the MTOM of the aircraft. For load-bearing and storage space reasons, two nose landing gears and two main landing gears were placed in each fuselage. They are positioned such that there is no risk of tip-over or tip-back during take-off.

Structural Analysis

The structure of the wingbox was designed to determine the structural rigidity of the wing and estimate the mass. Firstly, the complete geometry of the wing was determined. The geometry of the wing was simplified by idealising it as a structure with boom areas. Moreover, the wing was split into three sections. The middle wing is one section, while the outer wings are split into 2 parts. Afterward, the loading on the wing was determined by all the forces acting on it. Moreover, limiting load cases were determined by implementing a manoeuvre-gust diagram based on government regulations. After load calculations, a design selection was performed, which consisted of the selection of the materials and stringers. In the end, two types of aluminium alloys were used, the 7075-T6 and 2024-T86 alloys. Furthermore, the Z-stringer was chosen as a stiffener, and the spars are modelled as I-beams. The analysis of the wingbox started off with the section properties, including the moments of inertia and the centre of gravity. Then the forces on the wing were calculated; previously, the bending and shear were determined and by implementing them the stresses, shear flow, and torque were calculated. The failure modes of the wing can now be checked to determine whether the configuration is feasible. The failure modes used for analysis were crippling, shear buckling, Euler column buckling and yielding. After the failure modes, the deflection and twist of the wingbox were plotted to see whether the design would fail by the requirements set for them.

Finally, a dynamic analysis of the wingbox was performed. Static aeroelastic phenomena, namely divergence and control reversal, were assessed to ensure that the aircraft is suitable for high-speed operations in the planned atmospheric conditions. After the static analysis, flutter characteristics were also calculated for the given elastic properties. The coupled motion was found to be damped for the planned cruise velocity and to ensure rigid calculations, a sensitivity analysis was performed on the damping. The failure modes and aeroelasticity lead to the final design of the wingbox

Internal Layout and Aircraft Systems

The aircraft's internal layout integrates injection, fuel, hydraulic, and electrical systems as well as communication, hardware/software, and data handling systems. The design chosen ensures operational efficiency and redundancy.

Firstly, the injection system employs 62 generators in the wings and horizontal stabilisers to feed calcite into nozzles near the airfoil trailing edge. These nozzles are aligned close together, increasing collisions and breaking up agglomerates. Fluidised calcite is transported from the two storage tanks located inside the fuselage to the generator using feeding lines, and outside air is supplied via an air inlet for further fluidisation. Then, the fuel system consists of seven symmetrically placed tanks: one central main tank, two inner tanks, two outer tanks and two surge tanks at the wingtips. Further, two independent hydraulic systems, one in each fuselage, are powered through engine-driven and electric motor-driven pumps, with a Ram Air Turbine for redundancy. Next, the electrical system consists of two symmetric power networks, with two main buses connected through the middle wing. The Auxiliary Power Unit (APU) provides power on the ground and during engine failures.

Lastly, communication, hardware, and software systems enable interaction between aircraft operations and

ground control. Three flight controllers oversee monitoring, control, and external communication for navigation and mission instructions. For unmanned flight, these controllers rely on large amounts of aircraft data to manage autopilot functions. The flight computer processes sensor data for decision-making, while code systems monitor, control, and navigate, using each other's outputs..

Resource Allocation

Resource allocation was performed for costs, mass and power of the system. Firstly, A Cost Breakdown Structure (CBS) was plotted to identify costs involved in system development, production, and operation. The CBS includes three top-level categories: Research, Development, Testing, and Evaluation (RDT&E), Production, and Operational Costs. The total cost was determined to be USD 58.07 billion. By 2030, the market value of the system was estimated to be USD 40.65 billion, and the total profit was estimated to be 31.91 billion euros.

Next, the mass budget was determined for system components and can be seen in Table 15.3 and Table 15.4.

Lastly, a power budget was created by estimating the maximum power consumption of each subsystem. Two engines, each producing 50 kVA, will provide 100 kVA of power. The APU will provide start-up and emergency power, and two 28VDC batteries, each with a 28Ah capacity, will provide emergency power for half an hour.

Operations and Logistics

The operations and logistics focused on payload handling, airport ground operations, and flight operations, which were summarised in a CONOPS diagram as seen in Figure 19.1. 3000 t of payload will be delivered to each of the 8 airports per day by 100 trucks, each performing 10 deliveries. Ground operations such as pre- and post-flight operations and maintenance will be carried out at the same airport to minimise reliance on multiple locations. Departures and arrivals will be staggered throughout the day to improve operational efficiency. The unmanned aircraft will release payload along meridian tracks at altitudes of 20 km and 21.7 km to minimise plume interactions. Ground operators will monitor and control the 24-hour flights. Additionally, the initial fleet sizes was determined to be 33 aircraft operating from 4 airports. These airports are located in South Africa, Brazil, Thailand, and the USA. The fleet size increases to 385 aircraft in the final phase, operating from an additional 4 airports, located in Australia, the Dominican Republic and Egypt. All aircraft will perform 5 flights per day. In case the calcite injection technology is not ready, a fallback mission using alumina was proposed, using a fleet size of initially 43 to later 506 aircraft.

Reliability, Availability, Maintainability and Safety

In this chapter, analyses were performed on the Reliability, Availability, Maintainability and Safety of the system. To analyse the reliability, the failure rate of components of the payload injection system was analysed to estimate the reliability of the characteristic subsystem of the designed aircraft. The availability was found to be closely related to the reliability (Mean Time Between Failure) and maintainability (Mean Time To Repair) of the system. It was found that the fleet availability is proportional to the number of aircraft, and that using a fleet increases the availability exponentially. For maintainability, a maintenance scheme of A, C, and D checks was determined. This scheme was found to ground a single aircraft on average about 66 days per year, which is necessary downtime to prevent far more drastic repairs or even decommissioning of the aircraft. Finally, the safety of the design was analysed by identifying possible health and system hazards. For each hazard, possible mitigation strategies have been identified.

Sustainable Development Strategy

The sustainable design is a criterion heavily constrained by the top-level requirements. Therefore, a thorough analysis that spans 3 levels was performed. Firstly, during the conceptual design phase, the design was optimised for minimum fuel consumption, which indirectly reduces the environmental impact of the design as well. Concerning the engine decision, designing a more efficient engine with a fuel type with a lower environmental impact was found to be beneficial. Additionally, during the trade-off selection, the sustainability criterion was weighted highly to ensure that the environmentally non-feasible options were quickly discarded.

Secondly, a detailed plan was established to assess the sustainability of the final design. The Average Temperature Response (ATR) developed measured the aircraft's lifetime climate impact, while the Life Cycle Assessment (LCA) evaluated the environmental effects from material sourcing to manufacturing and assembling. Thirdly, the End-of-Life (EoL) phase was also considered to ensure responsible decommissioning. All in all, all three levels ensure full coverage of the system's lifetime. Lastly, social sustainability was addressed through ethical material sourcing, fair production practices, and ensuring workers' rights and fair wages across all project phases.

Sensitivity Analysis

In addition to all the previously explained sensitivity analyses per department, this chapter shows the overall sensitivity of the aircraft to the most important parameters, giving an overview of the design sensitivity.

Verification and Validation

The verification and validation (V&V) strategy was also developed to ensure that the design is well implemented and fulfils the intended purpose. To begin with, the design tools used to develop each subsystem were verified in each chapter. Then, the results obtained were validated against papers from the literature or other design tools. Then, the requirements themselves were verified, to ensure that they were properly formulated, using the “SMART” method.

A mission V&V was strategised to make certain that the final design and its mission comply with the requirements. For each requirement, an appropriate verification method was identified, accompanied by a rationale. Verification was carried out using one or more of the following methods: inspection, analysis, demonstration, or testing. Additionally, a cost estimate was generated to inform stakeholders of the resources required for the V&V process. The final step was determined to be the acceptance phase, during which the design will be validated to confirm it meets its intended purpose. This includes certification and documentation review, pre- and post-flight inspections and tests, and a flight test conducted using a flight model from the operational fleet. Last but not least, a compliance table can be found in Table 18.2 and Table 18.3, indicating which requirements have already been validated and which ones are to be checked when the model is manufactured.

Production Plan

A production plan was established focusing on the manufacturing, assembly and integration plan of the aircraft. Firstly, subassembly manufacturing will be done in a batch process, reducing costs per part while still allowing for quality testing and customisation. Next, the aircraft will be assembled in a final assembly line (FAL). The location of the subassembly production processes and FAL will depend on the international governmental coalition funding and controlling the process. Lastly, the integration of the aircraft systems will be performed. The production rate of the fleet was estimated to be about 3 months per aircraft. This results in 1 year of production for the initial fleet size and 10 years for the final.

Calcium carbonate powder will be prepared through precipitation and will be produced at a large scale in industrial installations and transported to the airports of operation.

Future Planning

A future planning was developed in the form of a project design and development logic as well as a project Gantt chart. The planning starts after the end of DSE and starts with a detailed design phase, focusing on the reduction of assumptions and uncertainties using extended analysis. Next, the testing and certification phase will commence, focusing on the testing of necessary systems and the collection of data for certification. After the certification has been received, the production phase will start. This phase will continue while the operation commences once the initial fleet is ready. Lastly, the end-of-life was planned out.

Contents

Preface	i
Nomenclature	ii
Executive Overview	iii
1 Introduction	1
I. Project overview	1
2 Market analysis	2
2.1 Market Definition	2
2.2 Current Technology Concepts	2
2.3 Market Size	3
2.4 Market Segmentation	3
2.5 Stakeholder Analysis	4
2.6 SWOT Analysis	7
2.7 Costs Budget of the System	8
2.8 Market Analysis Requirements	8
3 Requirements	9
3.1 Stakeholders' Requirements	9
4 Technical Risks	11
4.1 Risk Identification	11
4.2 Risk Map and Mitigation Plan	11
4.3 Risk Management	13
5 Functional Analysis	14
5.1 Top Level Functions	14
5.2 Functional Analysis Diagrams	14
II. Technical Design	17
6 Configuration Selection	17
6.1 Initial Concept Trade-Off	17
6.2 Second Trade-off	18
6.3 Trade-off Analysis	19
6.4 Sensitivity Analysis	20
7 Weight Estimation and Iterations	21
7.1 Design Process and Iteration Loops	21
7.2 Class I Weight Estimation	22
7.3 Thrust Loading and Wing Loading	23
7.4 Class II Weight Estimation	24
8 Aerodynamic Analysis	25
8.1 Stratospheric Aerodynamic Considerations	25
8.2 Airfoil Analysis	26
8.3 Planform Design	28
8.4 Wing Analysis	30
8.5 Fuselage design	33
8.6 Study on Basic Near Wake Characteristics	34
8.7 Verification and Validation	36

8.8	Sensitivity study	37
9	Payload Analysis	38
9.1	Aerosol Material	38
9.2	Aerosol Dispersal	38
9.3	Verification and Validation	41
9.4	Sensitivity Study on Injection Rate	41
9.5	Discussion of Assumptions and Uncertainties	42
10	Flight Performance	43
10.1	Take-off and Landing Performance	43
10.2	Climb and Descent Performance	43
10.3	Payload Range	45
10.4	Flight Profile	45
10.5	Verification & Validation	46
10.6	Sensitivity Study	48
11	Propulsion	50
11.1	Preliminary Analysis	50
11.2	Jet Engine Modelling	52
11.3	Design Point Selection	54
11.4	Final Design	58
11.5	Propulsion Sensitivity Analysis	58
11.6	Results Validation	60
12	Stability and Control	61
12.1	Aircraft Balance	61
12.2	Horizontal Stabiliser	61
12.3	Vertical Stabiliser	63
12.4	Control Surfaces	64
12.5	Landing Gear Design	68
12.6	Dynamic Stability	69
12.7	Verification and Validation	70
12.8	Sensitivity Study	71
13	Structural Analysis	72
13.1	Design Methodology	72
13.2	Loading	72
13.3	Design Selection	73
13.4	Wingbox Analysis	75
13.5	Dynamic analysis - Aeroelasticity	80
13.6	Wingbox Design	83
13.7	Verification and Validation	84
14	Internal Layout and Aircraft Systems	85
14.1	Injection system layout	85
14.2	Fuel System Layout	86
14.3	Hydraulic System Layout	86
14.4	Electrical System Layout	87
14.5	Communication Flow Diagram	88
14.6	Hardware / Software Diagram	89
14.7	Data Handling Diagram	90
15	Resource Allocation	92
15.1	Cost Breakdown	92
15.2	Mass Breakdown	95
15.3	Power Breakdown	96

16 3D Model	97
16.1 3D Model	97
16.2 Engineering Drawing	97
17 Sensitivity Analysis	99
17.1 Aircraft Size Sensitivity	99
17.2 Efficiency Sensitivity	100
18 Verification and Validation	102
18.1 Design Tools Verification and Validation	102
18.2 Requirement Validation	102
18.3 Design Requirements Compliance	106
 III. Operations	 114
19 Operations and Logistics	115
19.1 Concepts of Operations and Logistics Diagram	115
19.2 Fleet size	116
19.3 Selected Airports	117
19.4 Fallback Mission: Calcite Injection Technology not Ready	118
20 Reliability, Availability, Maintainability and Safety	119
20.1 Reliability	119
20.2 Availability	120
20.3 Maintainability	121
20.4 Safety	121
21 Sustainable Development Strategy	123
21.1 Sustainable Conceptual Design Choices	123
21.2 Methods of Assessment of Sustainable Design	124
21.3 End of Life	126
21.4 Social Sustainability	127
21.5 Verification and Validation	128
22 Production Plan	129
23 Future Planning	131
23.1 Project Design and Development Logic	131
23.2 Project Gantt Chart	132
24 Conclusion	134
24.1 Recommendations	134
Bibliography	137

Introduction

Contributors: Máté, Inés

Climate change is one of the primary challenges humanity is facing at this moment. Due to the greenhouse effect, the average temperature of the Earth is rising, causing extreme weather events and posing a significant threat to humanity in the near future. Besides aiming to reduce greenhouse gas emissions, it is widely agreed upon that carbon dioxide will need to be captured from the atmosphere to keep global warming below 1.5 °C. However, carbon capture techniques and powerful sustainable energy sources to operate them are proving costly and difficult to develop. Therefore, the need arises to temporarily decrease the Earth's temperature by 1 K until the reduction and capture strategies of greenhouse gases become effective. One way to achieve this is Stratospheric Aerosol Injection (SAI). This involves dispersing an aerosol in the stratosphere that reflects sunlight more than Earth's thermal radiation.

Several Aerosols have been investigated for SAI. However, most of them have negative side effects, namely stratospheric heating and depletion of the ozone layer. Solid aerosols, particularly calcite, seem to minimise these effects and therefore are a promising solution. This report aims to start the preliminary design of a fleet of aircraft capable of delivering 6 Mt of CaCO_3 into the stratosphere annually, based on the functions the requirements and concepts established in the Baseline Report.

The final design is thoroughly described throughout this report. Firstly, an overview of the project is given, consisting of a market analysis in Chapter 2, a stakeholder requirement description in Chapter 3, the technical risks of the mission in Chapter 4 and a detailed functional analysis in Chapter 5. Secondly, the technical design of the fleet of aircraft is divided into departments, where the configuration selection can be found in Chapter 6, and the weight estimations and iteration in Chapter 7. Furthermore, the aerodynamic analysis, payload analysis, flight performance, propulsion, stability and control and structural analysis can be found in the subsequent chapters, respectively. Finally, the internal layout of the aircraft systems in Chapter 14, resource allocation of costs, mass and power in Chapter 15 and final 3D drawing in Chapter 16 conclude the technical design of the aircraft. To ensure the parameters calculated are correct, and determine their sensitivity, the Chapter 17, Chapter 18 are included. Finally, an operations analysis of the mission is performed, where the operations and logistics in Chapter 19, Reliability, Availability, Maintainability and Safety in Chapter 20, sustainable plan in Chapter 21, production plan in Chapter 22 and future planning in Chapter 23 are included.

Market analysis

Market analysis is an essential tool in the design of novel concepts, allowing for insight into unmet needs, project viability, and improving stakeholder understanding. This section details the process of this analysis for Stratospheric Aerosol Injection, including the market definition, current technology, and market size and segmentation.

2.1. Market Definition

Contributors: Inés

By designing a fleet of aircraft for the sustainable and cost-effective delivery of solid aerosols to the stratosphere, the team aims to enter the emerging geoengineering market. The project is positioned in the sector of Stratospheric Aerosol Injection (SAI), a form of Solar Radiation Management (SRM), which is one of the principal technological segments within the geoengineering market.

This mission design represents a technological innovation, not only by developing an aircraft fleet specifically optimised for SAI, but also by enabling the injection of solid aerosols rather than the extensively researched sulfate-based aerosols, which show evidence of possible serious side effects in our ecosystem.

In order to define the market potential of this project, a market analysis of the geoengineering market was performed. Geoengineering is defined as follows:

”Geoengineering involves the deliberate manipulation of the Earth’s atmosphere with the objective of influencing the climate in a manner that mitigates or counteracts certain impacts of global warming. This terminology also frequently encompasses a range of technologies under development for such objectives, normally referred to as negative emission technologies“¹

2.2. Current Technology Concepts

Contributors: Inés

The geoengineering market can be divided into Solar Radiation Management and Carbon Dioxide Removal. These two segments are composed of different types of technologies.

2.2.1. Solar Radiation Management

The Solar Radiation Management segment is the leading climate mitigation strategy. In order to mitigate global warming while other capture and reduction strategies for greenhouse gases are developed, solar radiation management (SRM) is the most researched geoengineering practice².

Current existing technologies under development include:

- Stratospheric aerosol injection (SAI), consisting of the addition of small aerosol particles to the stratosphere to increase the reflection of incoming sunlight to prevent excessive global warming. Our strategy would form part of SAI technologies.
- Marine cloud brightening (MCB) is a strategy for adding aerosol to the lower atmosphere over ocean regions to increase the reflectivity of low-lying marine clouds.
- Space-based methods, consisting primarily of concepts such as large mirrors to reflect sunlight
- Cirrus cloud thinning (CCT): The idea behind CCT is to modify the microphysical properties of cirrus clouds to reduce their thickness or coverage. Thinner cirrus clouds would allow more long-wave (terrestrial) radiation to escape into space, which could slightly cool the planet.
- Surface albedo enhancement involves increasing the Earth’s reflectivity through the use of the high albedo properties of light-coloured surfaces, such as white roofs or reflective land coverings

¹URL: <https://www.maximizemarketresearch.com/market-report/geoengineering-market/214149/> cited 29 April 2024

²URL: <https://www.climate.gov/news-features/understanding-climate/solar-radiation-modification-noaa-state-science-factsheet> cited 30 April 2024

There are significant concerns surrounding solar radiation management (SRM), including geopolitical risks and ethical considerations, as well as long-term environmental consequences.

2.2.2. Carbon Dioxide Removal

Carbon Dioxide Removal (CDR) focuses on extracting CO₂ from the atmosphere and storing it in long-term reservoirs. Unlike Solar Radiation Management (SRM), which addresses the symptoms of climate change, CDR tackles its root cause by directly removing greenhouse gases like CO₂. The primary approaches in this category include²:

2.2.2.1. Land Based Approaches

Land-Based Approaches include changes to agriculture, forests and other activities as well as Direct Air Capture of CO₂. Some technologies include:

- Direct Air Capture (DAC), which describes a number of processes that remove CO₂ from the air with a liquid or solid adsorbent and then store the carbon in underground reservoirs.
- Agricultural Sequestration, which consists of methods for increasing solid carbon uptake in agricultural systems.
- Other methods include the transformation of biomass, which is crop residues, into a more stable form of carbon, known as biochar, which can be stored long-term in soils or underground. As well as reforestation or afforestation efforts.

2.2.2.2. Ocean Based Approaches

Marine CDR approaches strengthen the ocean's natural ability to pull carbon from the atmosphere and transport it into the deep ocean. Ocean alkalinity enhancement, which increases the ocean's drawdown of CO₂ by lowering surface water acidity, has the potential added benefit of mitigating ocean acidification. Alternatively, engineered approaches can strip CO₂ from seawater in a process known as direct ocean removal (DOR).

2.3. Market Size

Contributors: Inés

Statistics Market Research Consulting (MRC) reports that the market was valued at USD 28.0 billion in 2024 and is expected to reach USD 73.9 billion by 2030, growing at a compound annual growth rate (CAGR) of 17.5% during the forecast period. [7]. Taking into account all the aforementioned geoengineering technologies, a pie chart of the size of each segment in the geoengineering market can be seen in Figure 2.1

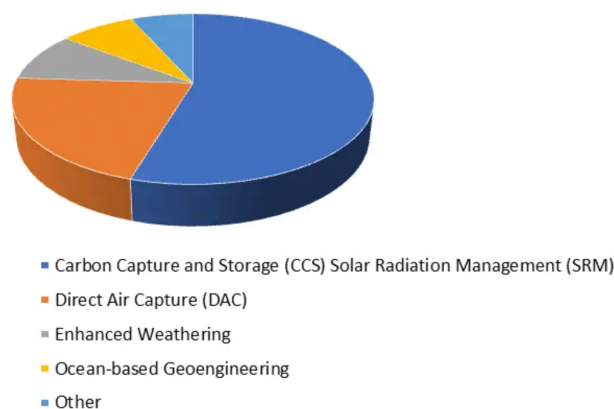


Figure 2.1: Technological Segment's Size in the Market [7]

2.4. Market Segmentation

Contributors: Inés

To gain a deeper understanding of market behaviour, a segmentation analysis was conducted. This allowed for an analysis of the geographical and technological trends, identification of key competitors, as well as the definition of the mission's target audience.

2.4.1. Geographical Trends

North America is the current leader of the market, given their strong governmental support and funding, as well as institutional research efforts. Various carbon capture and climate modification technologies are currently under development.

Europe is next in line, with its emission targets encouraging the development of carbon capture and storage (CCS) initiatives. Germany, the UK, and France have made financial commitments to emerging geoengineering approaches, ranging from bioenergy with carbon capture and storage (BECCS) to efforts aimed at restoring degraded landscapes.

Finally, China, India and Japan are currently concentrating in nature-based geoengineering strategies, focusing intensely on large-scale forestation campaigns which, they hope, will draw down their total carbon emissions as well as recover wildlife.³

2.4.2. Dynamic Analysis

The geoengineering sector is a relatively new market; thus, no great historical development of the market has been recorded. However, two major trends seem to be developing. Firstly, the rise of nature-based solutions like reforestation or afforestation. Secondly, major advancements in carbon capture and solar radiation management technologies, including SAI, which offer the potential for fast, large-scale climate intervention. The increasing frequency and severity of extreme weather phenomena have increased concern among governments and increased interest in technologies capable of modifying weather patterns or diminishing the impact of these events.

As for the last years, there have been unclear regulations and ethical debates on large-scale interventions, and a big reliance on academic research and pilot projects, as well as government or private funding¹.

2.4.3. Competitors

Furthermore, analysis of the existing geoengineering companies was performed to analyse the competitor's share in the market, as can be seen in the pie chart shown in Figure 2.2.

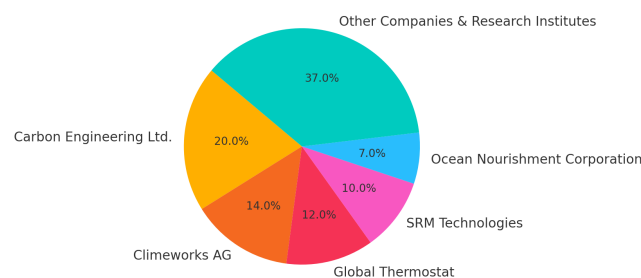


Figure 2.2: Market Share of Key Market Players

2.4.4. Target Audience

The main users of SRM, the most relevant for this team's mission, would most likely be a coalition of countries or an international organisation. The reason for this is that SRM consists of procedures that will affect the entire globe. Therefore, international agreements similar to the Paris Agreement would need to support or authorise the use. Deployment by a single government could cause tension or conflict. This coalition will likely be the main funder and will be responsible for commissioning operations. On the other hand, CDR technologies and strategies will probably be handled by regional governments.

International alliances and governments might contract private companies for the manufacturing or operation of these geoengineering strategies. Private companies might also co-found and operate missions as part of corporate social responsibility.

2.5. Stakeholder Analysis

Contributors: Konstantinos

Early on, it was important to identify all parties that affect or can be affected by the system being developed.

³ URL: <https://www.futuremarketinsights.com/reports/geoengineering-market> cited 29 April 2024

These were the stakeholders of the mission and were defined as "internal" and "external" stakeholders below. The stakeholders' needs and wants have a direct influence on the design process. Identifying and characterising the stakeholders was essential for any project in order to have a clear overview of the involved parties and to define the system boundaries. An "internal" stakeholder is one that is directly related to the system. "External" stakeholders refer to parties that have a less direct link, are affected by the system and have less decision-making power and interest in it:

Internal Stakeholders

1. The Designing Team: They are responsible for translating the stakeholder needs into requirements. These requirements are then mapped to hardware choices and design solutions, effectively bridging the gap between the "how" and the "what" needed to make the mission feasible.
2. The Manufacturing Team: They are responsible for implementing the production plan, put together by the designing team, and manufacturing all necessary components of the mission. Throughout the process, the design and manufacturing teams maintain continuous communication, developing their strategies in parallel to ensure mutual support and that their efforts remain aligned and feasible.
3. The Climate Modellers: The scientific community is the primary stakeholder responsible for the payload. A successful stratospheric aerosol injection is essential for them to gather data, evaluate its environmental impact and assess it as a viable solution to slow down the rate of climate crisis. If the mission succeeds, it simplifies their work by reducing the number of mitigation strategies and scenario outcomes that must be considered.
4. The System Operators: They are the ones responsible for operating the fleet during its lifetime, that is, from the moment it is manufactured until it gets decommissioned, during the mission execution phase. They are in continuous communication with the Climate Modellers to jointly layout the payload strategy and mission profile per flight.
5. The Air Traffic Control: They ensure a safe, organised, and efficient fleet operation in the sky and on the ground. They are responsible for ensuring the aircraft-based mission is uninterrupted by external factors such as other aircraft and weather. They are essential in the mission execution phase, keeping in contact with the operations team.
6. The Airport Operators: They are responsible for the airports where the mission is based. They provide clearance for aircraft and chemical storage.
7. Aviation Authorities: They affect the mission, certifying the aircraft and passing legislations that allow chemical injection into the stratosphere. They are also the regulators for aviation-related rules that the mission must follow.
8. International coalition of governments: This will be the main customer of the entire final system, who will be in charge of setting the goals for operations of the mission, which will be directed and carried out by the aforementioned internal stakeholders. Funding will most likely be provided by this coalition, making this customer the most important stakeholder of the final system.

External Stakeholders

1. Public Policy Planning Authorities: They focus on the societal and political side of the mission. They, influenced by the mission's outcome, use the results to inform and shape long-term and government policies related to climate. By conducting cost-benefit analyses and evaluating socio-economic impacts, they determine the viability and the effectiveness of the mission. They also often play a key role in securing funding for climate-related missions.
2. The engineering community: They are influenced by the innovative and cutting-edge technologies investigated throughout this project. The development of aerosol injection mechanisms and aircraft-based systems capable of reaching the stratosphere involves complicated design initiatives that offer valuable insights and advances to the broader engineering community.
3. The general public: Reducing the rate of global warming works in favour of humanity as a whole. The climate crisis is a leading challenge of the 21st century, creating irreversible problems to nature, human and animal health and the economy. It has a far-reaching impact on every living thing on Earth, and working on projects that aim to deal with it is in their favour.

There is another important distinction that was made between the aforementioned stakeholders. This is between "Key Stakeholders" and those of secondary importance. "Key Stakeholders" were given priority, and the requirements that originate from them are "key", meaning they impact the design more than usual, being of high priority.

The main key stakeholder of this mission is the international coalition of governments, for the reasons stated above. Other key stakeholders include: the engineering teams (design and manufacturing), the scientific community, political authorities, and the system operators. These are the ones that affect and get affected by the mission more than average, meaning that they have high decision-making power and interest in it. The scientific community, mainly responsible for the payload, determine which aerosol is to be injected into the atmosphere and under what conditions, thus greatly affecting the final design. The system operators, on the other hand, are primarily responsible for the mission execution side of the mission, determining all possible flight scenarios that need to be satisfied. The political authorities inform and shape the policies that directly influence the design and procedures to follow. Last but not least, the engineering teams are tasked with "translating" the needs and wants of the aforementioned key stakeholders into technical terms and making a feasible system. The remaining stakeholders are classified as "secondary" and their requirements as "top-level" but not "key". They are the ones who, although they are either affected by or have an impact on the system, do so at a lower level, limiting their ability to influence it.

These important distinctions can be visualised with an "Interest-Influence Graph", shown in Figure 2.3. Notice that "key stakeholders" were grouped in the "Manage Closely" segment, as they have a high interest and influence on the project. External Stakeholders were grouped in the "Keep Informed" box, backing up the aforementioned definition given as parties with high interest but little decision-making power. Lastly, the airworthiness authorities, classified as internal stakeholders, exert significant influence on the design but show limited interest in the project. Contrarily, ATC and airport operators, though still stakeholders, showcase low levels of both interest and influence and should therefore be simply monitored

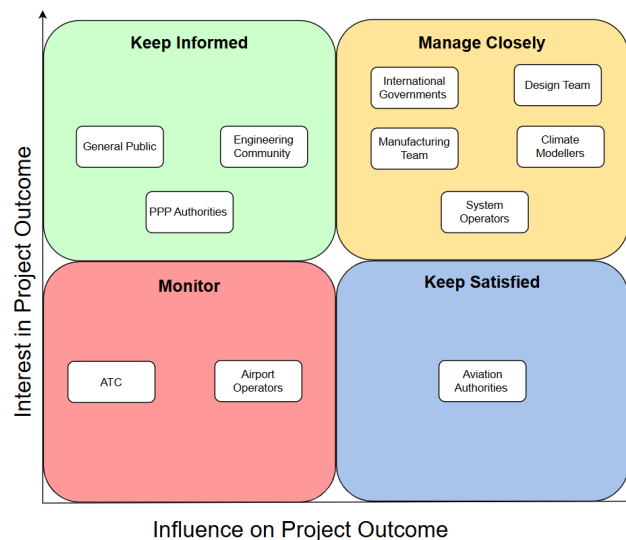


Figure 2.3: Interest-Influence Graph of the Stakeholders

2.5.1. Added Value and Prediction of Future Market

The system under analysis is the fleet of aircraft for stratospheric solid aerosol injection. The main function of this aircraft fleet is to inject solid aerosols into the stratosphere to prevent excessive global warming during the time it takes for reduction and capture strategies for greenhouse gases to be developed.

Other research teams have primarily focused in the past on gaseous (SO_2) or liquid ($\text{AM} - \text{H}_2\text{SO}_4$) sulphur-based aerosols. However, there is evidence that sulphur-based SAI could come along with a number of serious side effects. For that reason, this team is considering solid aerosols, specifically calcite (CaCO_3), instead of sulphurous species, for which some adverse SAI effects could potentially be alleviated [3].

With the introduction of this new technology, a new market segment is established in the already existing geoengineering market, specifically inside the Stratospheric Aerosol Injection strategies. An aircraft-based

system that delivers solid aerosols to the stratosphere is a niche that has not been explored before. Since SAI is a measure that would be performed in the case of Carbon Capture and Storage strategies that would still be under development, the team assumed a scenario in which SRM technologies will take over the whole blue segment in the market shown in Figure 2.1.

Given the optimal characteristics of solid aerosols and the potential scalability of aircraft operations, this strategy appears well-positioned to capture a significant share of the market. If this technology is proven effective, the aircraft-based solid aerosol injection system will dominate approximately the entire SRM market share, which corresponds to a 55% of the geoengineering market, corresponding to the blue segment shown in Figure 2.1. Based on this share, an estimated market value for this strategy will be at least USD 40.65 billion, based on market value estimations explained in Section 2.3.

However, this market share analysis was based on the assumption that carbon capture and storage (CCS) technologies have not yet been proven feasible. If a carbon capture solution becomes both effective and widely scalable, or if an alternative method for mitigating greenhouse gas emissions is developed, this mission would become redundant. This would result in a null future market share for this mission in the geoengineering market. Although such developments are expected to take a long time, it is of utmost importance to define the alternative uses this aircraft could have after this mission is no longer needed.

Using as a guide the current uses of the Stratolaunch⁴, this aircraft fleet could be used for hypersonic flight testing, enabling tests at high speeds without the need of a rocket launcher. Similarly to the original purpose of the Stratolaunch, it could also be used to launch satellites into orbit from high altitude, which enables a bigger flexibility in trajectory and launch compared to ground systems. Furthermore, this mission could also be repurposed for stratospheric sampling to prove the efficiency of the technologies in place for CCS.

The product is expected to go through the stages of the product lifecycle. These include the introduction phase, growth phase, maturity and decline phases. Assuming at least 15 years will be needed to achieve full operation of this mission, launch will consist of an initial fleet payload of 0.5 Mt of calcite. In the year 15, when the maturity level would be reached, an amount of 6-7.9 Mt of calcite should be injected annually into the stratosphere. Maturity and Decline phases durations are still to be determined, depending on the time needed for CCS technologies to be developed and implemented on a large scale.

2.6. SWOT Analysis

Contributors: Inés

A SWOT Analysis in the market was performed and is presented in Figure 2.4.

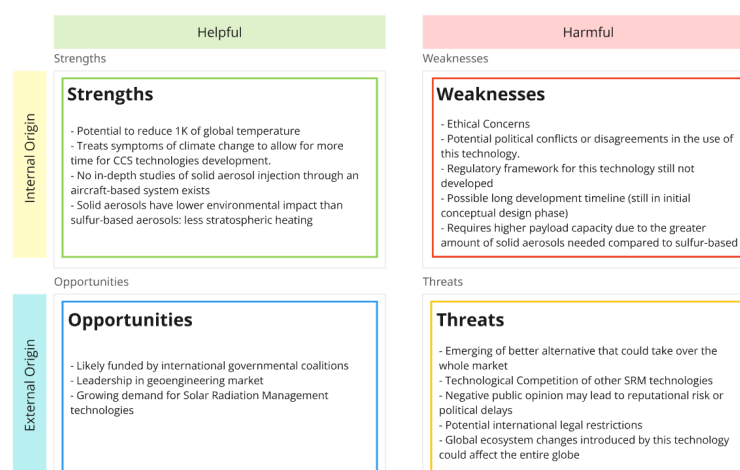


Figure 2.4: SWOT Analysis

⁴<https://arstechnica.com/space/2025/05/stratolaunch-successfully-flies-a-modern-replacement-for-the-x-15-rocket-plane/> Cited 17 June 2025

2.7. Costs Budget of the System

Contributors: Inés

This mission is not intended to generate profit. Its primary objective is to provide a cost-effective solution for governmental use. Consequently, the following cost thresholds, already provided by stakeholders, must not be exceeded to ensure economic viability:

- **Development cost** must remain below € 5 billion if existing engines can be adapted, and below € 9 billion if new engine development is required.
- **Manufacturing cost** per aircraft must not exceed € 150 million.
- **Annual direct operating cost** per aircraft must stay below € 60 million, including aerosol material, fuel, crew, maintenance, depreciation, airport fees, and insurance.

2.8. Market Analysis Requirements

Contributors: Inés

Based on this market analysis, several key constraints on the mission have been identified. These will be further refined into formal mission requirements in Chapter 3:

- The mission must reduce the global average temperature by 1 K.
- The system must support an initial payload injection of 0.5 Mt of calcite per year.
- The aircraft fleet must be capable of delivering 6 Mt/year of calcite into the stratosphere by year 15
- The mission must enable sustained operations and scalability over a minimum of 15 years (time to reach maturity level).
- Development cost must not exceed: €5 billion if adapting existing engines, €9 billion if new engine development is required.
- Per aircraft manufacturing cost must be smaller than €150 million.
- Annual direct operating cost per aircraft must be smaller than €60 million.
- System maturity should be achievable in less than 15 years from first deployment.
- Aircraft must operate at stratospheric altitudes for reliable aerosol dispersion.
- Solid aerosols must minimise stratospheric heating and ozone depletion.

Requirements

Requirements are a central part of the design process, with stakeholder requirements quantifying the main stakeholder needs the project must adhere to. Therefore, this section shows these requirements.

3.1. Stakeholders' Requirements

Contributors: Konstantinos

All stakeholder requirements are presented in Table 3.1. These are top-level requirements expressed in the “language” of the stakeholders and form the basis of system (high-level) and subsystem (low-level) requirements. All stakeholder requirements are identified by the code initials “REQ-STK”¹:

Table 3.1: Top-Level Stakeholder Requirements for Stratospheric Aerosol Injection (SAI) Aircraft-Based System, including Characterisation

ID	Requirement Category	Description
REQ-STK-1	System Capability	The initial fleet payload shall be solid aerosol with a radiative forcing equivalent to 0.5 Mt of CaCO ₃ per year.
REQ-STK-2	System Capability	The fleet payload shall be expanded to solid aerosol with a radiative forcing equivalent to 6 Mt of CaCO ₃ per year within 15 years from the start of operation.
REQ-STK-3	System Capability	The fleet shall be active for 250 operational days per year.
REQ-STK-4	System Capability	The system shall deliver the payload at the stratosphere, to altitudes of at least 20 km.
REQ-STK-5	Deployment Base	The system shall operate from a minimum of 4 airports.
REQ-STK-6	Deployment Base	It shall operate from existing airports near latitudes 30N, 15N, 15S, and 30S.
REQ-STK-7	Deployment Base	The system shall operate from airports with runways of at least 2500 m.
REQ-STK-8	Approach Conditions	It shall operate in crosswinds of at least 20 knots.
REQ-STK-9	Approach Conditions	The system shall be certified for CAT II landings.
REQ-STK-12	Sustainability	Environmentally conscious materials shall be used, to reduce environmental impact.
REQ-STK-14	Sustainability	The system shall have a detailed end-of-life plan.
REQ-STK-15	Development Cost	The development costs shall remain under €5 billion if using existing engines, or €9 billion if new engine development is required.
REQ-STK-16	Manufacturing Cost	The cost per aircraft shall be less than €150 million.
REQ-STK-17	Operating Cost	The annual direct operating cost per aircraft shall remain below €60 million, all expenses included.
REQ-STK-18	Climate effect	The fleet’s operation shall result in a net decrease in average global temperature over its operational lifetime.
REQ-STK-20	Safety and Reliability	The system shall comply with all applicable airworthiness regulations.
REQ-STK-21	Schedule	The initial fleet shall be operational within 5 calendar years after the start of manufacturing.
REQ-STK-23	Schedule	The conceptual design of the system shall be completed by the end of the 2025 spring DSE.
REQ-STK-24	Deployment Base	The system shall operate from a maximum of 8 airports.

As mentioned, all stakeholder requirements are “top-level requirements”. However, some are more important, driving the design. As a result, a further distinction takes place in the last column of Table 3.1, following the colour code introduced below in Table 3.2. The distinction is based on communicating with the customer and discussing the significance of each requirement further:

¹ID codes are not reassigned when a requirement is removed to improve traceability and bookkeeping.

Table 3.2: Requirement Characterization Legend

Type of Requirement	Explanation	Colour Code
Driving	A requirement which drives the design more than average.	Blue
Key	A requirement which is of primary importance for the customer	Green
Killer	A requirement which drives the design to an unacceptable extent.	Red
Top-Level	Stakeholder requirements are top-level requirements expressed in the “language” of the stakeholder. All indicate the “starting point” of the requirement analysis process.	Yellow

Note that “REQ-STK-24” has been excluded as it was identified as a Killer Requirement and subsequently negotiated with the customer. Considering that “REQ-STK-2” specifies an annual injection of 6 megatonnes of CaCO_3 , and “REQ-STK-3” restricts operations to 250 days per year, this implies a required daily injection rate of 24,000 tonnes. After some preliminary operational planning, the team is confident that more than 8 airports will be needed to accommodate the increased fleet number, something that the customer has agreed on, leading to this requirement being discarded.

Technical Risks

Several unknown factors in the design and operation of the system could endanger the successful completion of the project. If left unaccounted for, these risks can negatively impact the product or even cause the project to completely fail. In this chapter, Section 4.1 and Section 4.2 explain how the technical risks were identified and what mitigation strategies were followed before the start of the design of the system. Section 4.3 details how the risks will be managed as the project continues.

4.1. Risk Identification

Contributors: Máté

As the project is very complex, there can be many different risks connected to its design and operation. To make sure that all major risks are discovered, certain risk categories were identified. These main categories are as follows:

1. **Requirements:** covers risks associated with changes to the top-level requirements from the client. The design team has no power to prevent this, but contingency measures have been identified to reduce the effects.
2. **(Financial) Budget:** risks stemming from running over the budget.
3. **Logistics/operation:** risks associated with operating a large aircraft fleet in a real (unpredictable) environment.
4. **Science and Engineering Unknowns:** risks stemming from limited understanding of cutting-edge science and engineering concepts. This covers risks directly related to aerospace and climate engineering.

Risks were kept as general as possible to keep them applicable irrespective of the design concept. This also results in similar risks being grouped, leading to fewer risks overall, to ease risk management.

4.2. Risk Map and Mitigation Plan

Contributors: Inés, Máté

The risks identified according to the strategy in Section 4.1 are listed in Table 4.2 along with their category and unique ID, including the TR (Technical Risk) identifier. The table also shows the mitigation plans and the severity and probability before and after the mitigation. Table 4.1 places these risks on the risk map (the TR identifier is omitted). Here, it is shown side by side how the mitigation helps to make the risks less dangerous. The red area means that the risk is unacceptable, yellow means that it needs special attention, while green stands for less dangerous risks. The probability of occurrence (PR) is quantified as follows:

- Almost certain (5); $PR \geq 90\%$
- Probably occurs (4); $50\% \leq PR < 80\%$
- Possibly occurs (3); $30\% \leq PR < 50\%$
- Remotely possible (2); $1\% \leq PR < 30\%$
- Extremely unlikely (1); $PR < 1\%$

Table 4.1: Risk Map Before and After Mitigation

		Before Mitigation				After Mitigation			
		Might negatively influence project	Some negative influence, affecting stakeholders	Significant issue affecting main stakeholders	Critical threat to project success	Might negatively influence project	Some negative influence, affecting stakeholders	Significant issue affecting main stakeholders	Critical threat to project success
		1	2	3	4	1	2	3	4
Almost certain	5		3.1, 6.2	1.2, 3.2		3.2, 6.2	1.2		
Probably occurs	4			1.1, 3.3, 3.6, 5.2		3.1	3.3		
Possibly occurs	3			2.1, 2.2, 3.4, 5.1	2.3, 3.5, 4.1, 6.1	1.1	3.6, 5.2		
Remotely possible	2				1.3, 4.2, 4.3, 4.4, 4.5		1.3, 2.1, 2.2, 3.5, 5.1	2.3, 3.4, 4.1, 6.1	
Extremely unlikely	1							4.2, 4.4, 4.5	4.3

Table 4.2: List Of Operational Risks and Their Mitigations

ID	Category	Description	Category	Mitigation	Before	After	
TR-1.1	Requirements	Required aerosol type changes	Probability	Our analysis demonstrates that using calcite for SAI is feasible for the aircraft design perspective	4	3	
			Severity	Re-use most of the design for the old aerosol, ensure payload density is an adjustable parameter	3	1	
TR-1.2		Required aerosol amount changes	Probability	-	5	5	
			Severity	Re-use aircraft design, modify fleet size to match new demand	3	2	
TR-1.3		A killer requirement is found	Probability	-	2	2	
			Severity	Update and check compliance matrix on every design and requirement change	4	2	
TR-2.1	Budget	Development budget is exceeded	Probability	Ensure timeline is kept, leave more margin for more uncertain parts of the design	3	2	
			Severity	If possible, scale back on project goals to reduce complexity; scale down initial operation to re-allocate budget to finish development.	3	2	
TR-2.2		Production budget is exceeded	Probability	Take cost into account for trade-offs, use reliable contractors and well-developed technologies	3	2	
			Severity	Scale down initial operation to re-allocate budget to finish production	3	2	
TR-2.3		Operational budget is exceeded	Probability	Trade-offs should prioritise modular, maintainable, safe designs.	3	2	
			Severity	Scale down operation	4	3	
TR-3.1	Logistics/ operation	High temperature on ground bases	Probability	Make sure parts used in the design can withstand high temperatures or store fleet in enclosed hangars	5	4	
			Severity	Determine a cut-off temperature based on the design, do not fly above this temperature	2	1	
TR-3.2		High winds on ground	Probability	Make sure plane can take-off and land in high winds	5	5	
			Severity	Determine a cut-off wind on the design and regulations, do not fly in these winds	3	1	
TR-3.3		Intense storm, rainfall	Probability	-	4	4	
			Severity	Stop operations	3	2	
TR-3.4		Airspace closure preventing operation	Probability	Have a lot of alternate airport options	3	2	
			Severity	-	3	3	
TR-3.5		Logistics/ operation	Malfunction leads to accident	Probability	Make and certify aircraft according to FAA, EASA regulations. Maintain an honest workplace culture	3	2
				Severity	Make unmanned aircraft; fly aircraft far from populated areas	4	2
TR-3.6	Supplier fails to deliver parts on time		Probability	Make use of standard parts that have more than one supplier	4	3	
			Severity	Stockpile spare parts to keep up operation in case of shortage	3	2	

TR-4.1	Unknowns	Aerosol ineffective or has negative effect	Probability	Use aerosol with the most research behind it. Test aerosol at a smaller scale first.	3	2
			Severity	See TR-1.1	4	3
TR-4.2		Key innovative subsystem does not work	Probability	Consider TRL in trade-offs	2	1
			Severity	Parametrise design, document design decisions to make redesign easier	4	3
TR-4.3		Project releases so much CO ₂ it cancels out the positive climate effect	Probability	Optimise flight profile, aerodynamics and payload for minimum fuel consumption	2	1
			Severity	Consider alternative fuel	4	4
TR-4.4		Degradation of aircraft components is quicker than expected	Probability	Take tropical conditions into consideration for material trade-offs	2	1
			Severity	Make modular design with inspectable and replaceable components	4	3
TR-4.5		Major change of design needed	Probability	Develop design options to a sufficient extent before discarding them. Take possible future customer needs into consideration at trade-offs	2	1
			Severity	Parametrise design, document design decisions to make redesign easier	4	3
TR-5.1	End of Life and Decommissioning	Limited recyclability of materials	Probability	Use Life Cycle Assessment (LCA) during design to choose materials with high recyclability; prioritise modular design.	3	2
			Severity	If some parts are still unrecyclable, have fallback waste handling plans with certified partners to contain the impact.	3	2
TR-5.2		Lack of Disassembly Infrastructure	Probability	Plan for training, tools, and staffing in advance; distribute decommissioning capability across bases.	4	3
			Severity	If bottlenecks arise, outsource to certified aerospace maintenance organisations to avoid delays.	3	2
TR-6.1	Maintenance	Unexpected component degradation due to high altitude	Probability	Choose validated high-altitude components and apply design margins	3	2
			Severity	Maintain on-site replacement capability	4	3
TR-6.2		Inspection delays	Probability	-	5	5
			Severity	Apply schedule buffers to absorb unexpected downtimes.	2	1

After mitigation, the identified risks in the red area have been successfully moved to either the yellow or green areas. However, the seven risks belonging to the yellow cells will require special attention and monitoring. This is not optimal but reflects the real uncertainty of the success of the project, especially related to scaling up the operation and the huge uncertainties in the actual effects of stratospheric aerosol injection. However, since there are no risks in the red area, the project is still worth pursuing.

4.3. Risk Management

Contributors: Inés, Máté

As the risks will evolve during the project, they will be continuously managed. The areas of responsibility for managing different risks are divided based on risk category.

- Requirement risks (3 risks) are managed by the systems engineer.
- Budget risks (3 risks) are managed by the finance manager.
- Logistics and operation risks (6 risks) are managed by the chief of operations.
- Risks related to technical unknowns (5 risks) are managed by the chief engineer.
- End of Life and Decommissioning (2 risks) will also be managed by the chief of operations
- Maintenance risks (2 risks) will be managed by the Safety and Reliability manager

This leaves every person with fewer than 10 technical risks to manage.

Functional Analysis

In this chapter, functional analysis is introduced. The system is designed to perform a set of functions that need to be identified. These were grouped into 10 top-level functions spanning from “Manufacture” to “End of Life”. These were collected and can be found in a Functional Breakdown Diagram, showcased in Figure 5.1. The flow of these functions in a chronological order was taken into account in a Functional Flow Diagram, indicated in Figure 5.2. Both figures were essential for the system’s design, as they provide a clear and, most importantly, structured overview of what the system should do before proceeding with designing how to do it. Notice that for both diagrams, verbs were used to describe the functions according to the convention.

5.1. Top Level Functions

Contributors: Konstantinos

In this section, the 10 top-level functions are introduced, and a brief explanation is provided. To begin with, the aircraft system was designed. This has already been done, and is the subject of this report. The design process involved a preliminary sizing and determination of the engineering parameters necessary. It also involved the project management aspect of the mission and the derivation of the operation process and logistics.

To move on, the next top-level function involves the “Manufacturing” of the system. This includes management aspects, such as setting up the production operations, hardware and software, and engineering aspects such as subsystem production and system assembly. Once the system is produced, the focus shifts to fleet operations. The mission profile is made, and the payload injection strategy is determined. An important part of every project is its financial management, the topic of function n.3 in Figure 5.2. This includes acquiring the necessary funds, managing them and allocating them as needed.

Another important function that shall be performed is the physical preparation of the system to ensure that the mission is successful. This includes preparing the aircraft (fuel, payload, etc.) and its documentation (airworthiness certifications, flight manifest, etc.) and performing inspections, repairs and maintenance.

The next step, function 5 in Figure 5.2, involves the first part of the flight profile. This is taxing and take off, climb to altitude and cruise to the mission location. When arriving there, the attention shifts to function 6, which is configuring the aircraft as necessary to take measurements and perform the aerosol injection. This happens in two different altitudes, as described in Chapter 10 and Chapter 19. When completed, the “Return to base” function is initiated, essentially repeating function 5 in reverse.

Having performed the flight, a mission debrief shall take place to ensure that the mission was successful. This primarily includes collecting the flight data from aircraft’s onboard computers, processing it and communicating it with the responsible team. The procedure is then performed again in iteration from block 4 to 8, as shown in Figure 5.2. Last but not least, when the aircraft is ready to be decommissioned, function 9 is performed, which includes the End of Life procedure. This is explained in detail in Section 21.3 and includes documentation, disassembly and recycling.

5.2. Functional Analysis Diagrams

Contributors: Konstantinos, Bas

In this section, the two diagrams of the functional analysis are presented. The Functional Breakdown Diagram, describing all the functions the system shall perform, is presented in Figure 5.1. Similarly, the Functional Flow Diagram, showcasing the order these functions shall be conducted, can be found in Figure 5.2.

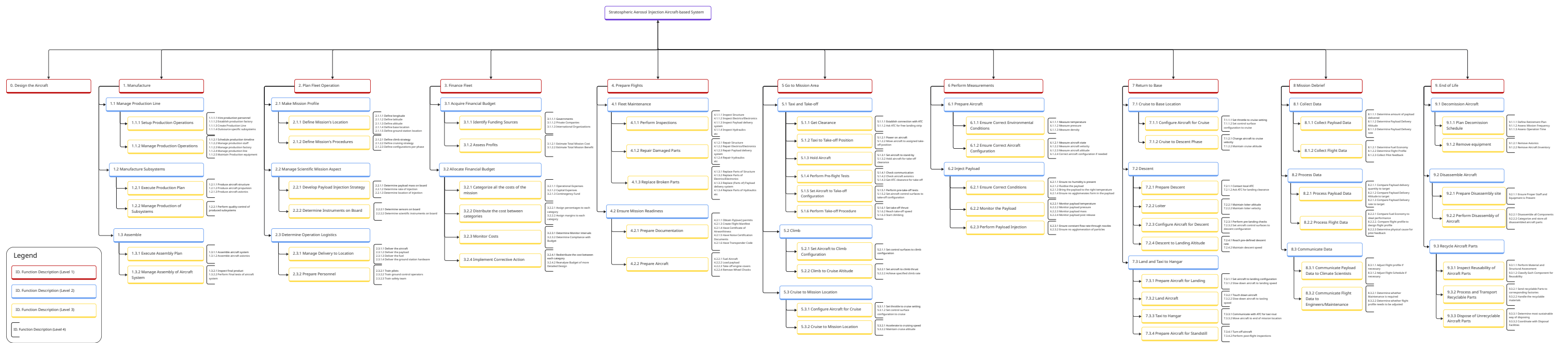
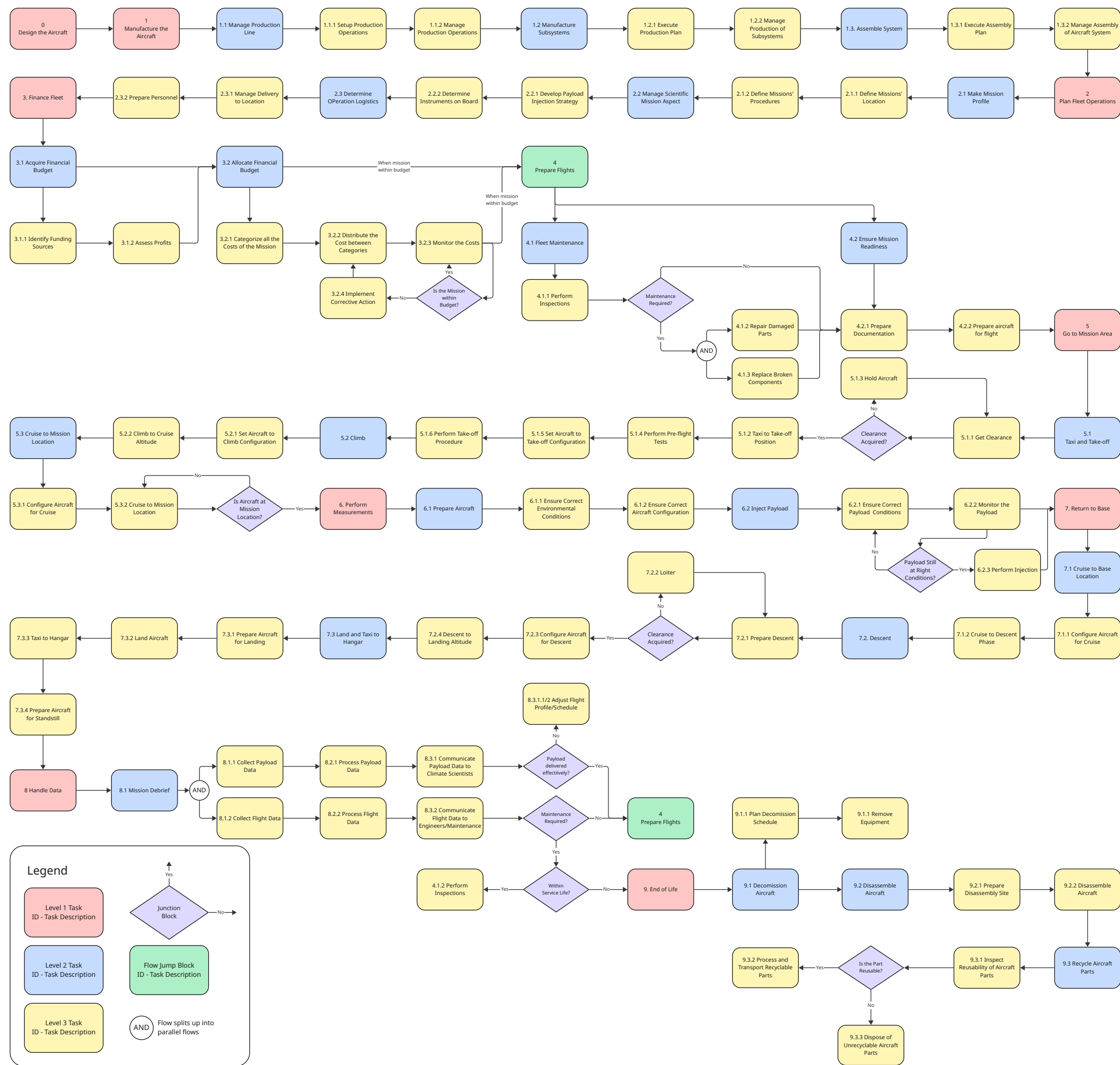


Figure 5.1: Functional Breakdown Structure



Configuration Selection

A trade-off between the possible system concepts was performed in two stages. Initially, a first qualitative trade-off based on the literature review was performed, where the design options were reduced to two concepts. To decide on the final concept, a quantitative trade-off based on the preliminary design was used.

6.1. Initial Concept Trade-Off

Contributors: Blanca, Carmen, Inés, Maxine, Barnabás

The following four different system concepts were considered and analysed in an initial concept trade-off:

Subsonic conventional aircraft: This design option was selected due to the easy access to the technology and proven viability. Flying in the subsonic regime results in better overall aerodynamic performance, which is of utmost importance for stratospheric flights.

Subsonic twin-body aircraft: As opposed to the conventional aircraft option, the vehicle has two identical fuselages that balance weight distribution along the wing and reduce the weight required for the aimed structural stability. In addition to in-flight loads, the dynamic loads of ground operations are also reduced as the landing gears are typically placed on the fuselage.

Subsonic flying wing: Concerning flying wings, various examples demonstrate their feasibility and efficiency, especially with high-altitude operations. The absence of a fuselage eliminates part of the drag, leading to better aerodynamic efficiency. Stability in this aircraft, however, is a concern.

Supersonic conventional aircraft: Limiting operations to the subsonic velocity range constrains the maximum achievable payload, potentially reducing overall efficiency. Operating in the subsonic regime with a subsonic aircraft fleet avoids the main current challenge, the coffin corner.

6.1.1. Trade Criteria and Weights

Several criteria were considered for the trade-off. These were based on the key requirements identified in the initial requirement analysis and on system-level requirements in which the concepts differ significantly. The chosen criteria, together with their weight out of 1 are; High Altitude Performance [0.25], Stability and Control [0.1], Operational Costs [0.1], Technology Readiness Level [0.15], Payload Storage Capability [0.2], and Sustainability [0.2].

High Altitude Performance The main challenge of Stratospheric Aerosol Injection is flying at altitudes of 20 km and above. Due to altered atmospheric conditions, the range of acceptable speeds narrows with increasing altitude as a result of the thin atmosphere. A high performance in the stratosphere determines the ability to perform the mission. Hence, this trade criterion is considered one of the most important and is given a weight of 0.25.

Stability and Control

This criterion was mainly chosen due to the consideration of the flying wing as a possible design concept, since it poses a challenge in comparison to conventional aircraft. However, even though stability and controllability can be complex for the flying wing, it was not considered as a key or driving requirement. Hence, it was given a weight of 0.1, as it was thought not to determine the feasibility of the mission, but still has to be considered, as given in requirements REQ-SYS-ARD-4 to REQ-SYS-ARD-6.1.

Operational Costs

Operational costs refer to the final system costs of operations if a decision is made for deployment. This is given as a stakeholder requirement, REQ-STK-17 and is therefore considered as a criterion. However, this is not a top-level or driving requirement, as these costs would be taken up by a coalition of governments, and the budget could be flexible. This criterion is thus given a score of 0.1.

Technology Readiness Level

Technology Readiness Level (TRL) is a scale used to assess the maturity of a technology, from basic research

(low TRL) to proven systems in operational use (high TRL). This criterion is weighted 0.15 out of 1, selecting a concept with a low TRL would involve higher technical risk and significantly increase research and development time and cost. To score the different concepts in this aspect, the ESA TRL handbook was used, which defines the TRL from 1, meaning “Basic principles observed and reported”, to 9, meaning “Actual system flight proven through successful mission operations” [8]. These scores were then converted to a 1–6 scale for the trade-off analysis.

Payload Storage Capability

The chosen aircraft must carry and disperse a large volume of aerosol to comply with the driving requirement of injecting solid aerosol with radiative forcing equivalent to 6Mt of CaCO_3 , REQ-STK-2. Therefore, payload storage capability is a key factor in the effectiveness of stratospheric aerosol injection. A greater capacity reduces the number of required flights, and thus the fleet size. This could improve operational efficiency.

Although essential, it is considered slightly less critical than the ability to reach the target altitude or the overall environmental impact, which is why it is given a high, but not maximum, weight of 0.2.

Sustainability: Noise and greenhouse gas emissions

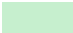

Since Stratospheric Aerosol Injection is proposed as a climate intervention to decrease the average global temperature, as given by REQ-STK-18, it is important that the method used to deliver the aerosol does not cause significant environmental harm. A climate solution should not create new environmental problems, and thus, the sustainability criteria are given a weight of 0.2, especially due to the greenhouse gas emissions category.



6.1.2. Trade-off Summary Table

The initial concept trade-off summary table is given in Table 6.1. Based on the results, supersonic conventional aircraft and flying wing were discarded, not only because they present unacceptable scores in different criteria, but also because their final score is significantly lower than the other two concepts under consideration. Subsonic conventional aircraft and TBA configurations score the same, which is the reason why a more detailed trade-off is performed as shown in Section 6.2, to be able to choose one final concept. A summary of the reasons for the given scores is given inside each cell. For further details on this, the reader should refer to the Midterm Report.

Table 6.1: Trade-off of SAI Delivery Concepts

Criterion Parameters	High Altitude Performance [0.25]	Stability & Control [0.1]	Oper. Cost [0.1]	Technology Readiness [0.15]	Payload Storage [0.2]	Sustainability [0.2]	Score
Conventional Subsonic	5 Successful stratospheric missions	5 Horizontal stabilizer	4 Good	6 Excellent	4 M_{pt}/OEM ≈ 0.3626	3 Lower fuel eff. than other	4.45
Supersonic Con- ventional	6 Avoid Coffin Corner	4 Mach tuck	2 Higher than subs.	4 Sonic boom	3 M_{pt}/OEM ≈ 0.1753	1 Sonic Boom CO_2 emissions	3.6
Flying Wing Subsonic	6 Higher L/D than conventional	1 No tailplane	5 Low DOC	2 Stability unreadiness	3 M_{pt}/OEM ≈ 0.250	5 40% less fuel & noise reduction	4
Twin-Body Sub- sonic	5 High AR	4 Shorter fuselage	4 High efficiency	4 Lower service ceiling	5 M_{pt}/OEM ≈ 1.381	4 9.4% fuel reduction & 28% less MTOM	4.45

 Excellent: 6
 Poor, Correctable Deficiencies: 2,3

 Fair, Good: 4,5
 Unacceptable: 1

6.2. Second Trade-off

Contributors: Konstantinos, Bas

Having established two concepts to shift the team’s attention to, a second trade-off based on preliminary calculations took place. This involved the preliminary calculation of five parameters for both concepts and comparing the two. These calculations are summarised in Table 6.2, achieving full coverage of the criteria that obtained similar scoring between the single and twin body, as shown in Table 6.3.

Table 6.2: Preliminary Calculations for Conventional and Twin Body Aircraft Configurations

Parameter	Single Body	Twin Body
Maximum Bending Stress (MPa)	157.26	83.75
CD ₀ (Zero-lift Drag Coefficient)	0.0200	0.0241
Lift-to-Drag ratio	15	20
Payload Capability per Unit Thrust	0.0639	0.0851
Operational Cost (Billion Euros)	25.64	23.52

To understand how these parameters affect the selection of the most optimal configuration of the mission, the following explanation is provided:

Maximum Wing Bending Stress (σ_{max})

The maximum wing bending stress along the wingspan serves as a valuable metric for comparing the two concepts, as bending loads are the dominant structural forces acting on the wing and largely dictate the required reinforcement.

Parasitic Drag (C_{D0})

C_{D0} is an important metric for stratospheric aircraft, as the parasitic drag has an influence on different performance aspects of the aircraft. For example, the higher the zero drag parameter, the lower the high altitude performance, reducing the ceiling altitude. In a similar way, the drag parameter can be used to assess operational costs. The parasitic drag results in a constant force opposing the thrust and, thus, a higher value requires a higher thrust. Considering the simple jet thrust equation $T = \dot{m} \cdot (V_j - V_0)$ [9, Eq. 13.1], this will automatically result in more mass flow needed and, thus, higher fuel consumption, increasing the operational costs. For the same reason, a lower fuel consumption causes fewer emissions, thus improving the sustainability of the design.

Lift-to-Drag Ratio

The Lift-to-Drag ratio can assist the trade-off analysis, offering a meaningful metric to evaluate and compare their aerodynamic efficiency. Given the mission's high-altitude and payload requirements, it is crucial to aim for drag polars that deliver high lift with minimal drag.

Payload Capability per Unit Thrust ($W_p/l/T$)

The payload capability per unit of thrust is an important parameter and affects multiple criteria. First of all, the payload capability per unit of thrust parameter affects the operational costs of the design, as this ratio describes the amount of fuel that will be consumed for a given payload mass. The amount of fuel used is indirectly related to the emissions and thus the sustainability of the aircraft concepts.

Operational Costs per Year (OC/year)

This metric provides an important way to compare the operational cost of the mission since it takes into account the whole fleet, which changes depending on the concept.

Table 6.3: Parameters used for quantitative analysis and criteria satisfied.

Parameters \ Criterion	High Altitude Performance	Operational Costs	Payload Storage Capability	Sustainability
Structures				
Wing Bending Stress	✓		✓	
Aerodynamics				
Parasitic Drag	✓	✓		✓
Lift to Drag Ratio	✓	✓		✓
Flight Performance				
Payload Capability per Unit Thrust		✓	✓	✓
Operational Costs per year		✓		

6.3. Trade-off Analysis

Contributors: Konstantinos, Bas

After the trade-off parameters were defined and calculated for the different configurations, the trade-off itself was performed. As the configurations were compared relative to each other, the parameters were expressed as ratios between the two. For an easy comparison, the subsonic conventional configuration was treated as the baseline by setting all parameters equal to 1. The values of the trade-off parameters for the subsonic twin-body then show the relative change compared to the baseline configuration. The results of this process are shown in Table 8.1. For parameters that are favourable when smaller,

specifically the C_{D_0} , maximum wing bending stress and operational costs per year, the reciprocal was taken to ensure a fair trade-off where a higher score is preferred. Each parameter is provided with a weight, showcasing the extent of its effect on the trade-off. This is already considered in Table 8.1. The weights were determined from Table 6.3, based on the number of “checks” each parameter satisfies. That is, parameters that are found to affect more criteria are naturally weighted more, resulting in, for instance, the “Parasitic Drag” and the “Lift to Drag Ratio” scoring a 3/12, affecting the trade-off more than the “Operational Costs per Unit payload” (1/12). Just like the first trade-off analysis, these are normalised, resulting in the weights shown in Table 8.1.

Table 6.4: Parameters used for quantitative analysis and criteria satisfied (lower is better).

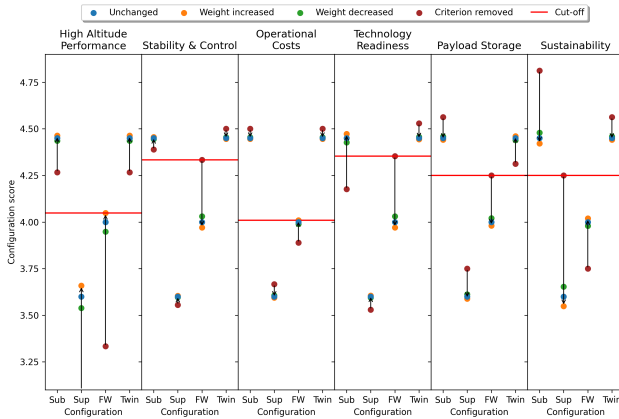
Parameter Configuration	$1 / \sigma_{max}$ [0.15]	$1/C_{D_0}$ [0.25]	$\frac{L}{D}$ [0.25]	W_{pl}/T [0.25]	$1/(OC/year)$ [0.1]	Score
Subsonic Conventional	[red] 1	[green] 1	[red] 1	[red] 1	[red] 1	1
Subsonic Twin-body	[green] 1.878	[red] 0.830	[green] 1.187	[green] 1.333	[green] 1.1	1.23

Where [green] indicates a favourable configuration and [red] a configuration that is less favourable compared to the other concept. As can be seen from Table 8.1, the subsonic twin-body configuration received a higher score and is, thus, the chosen design option.

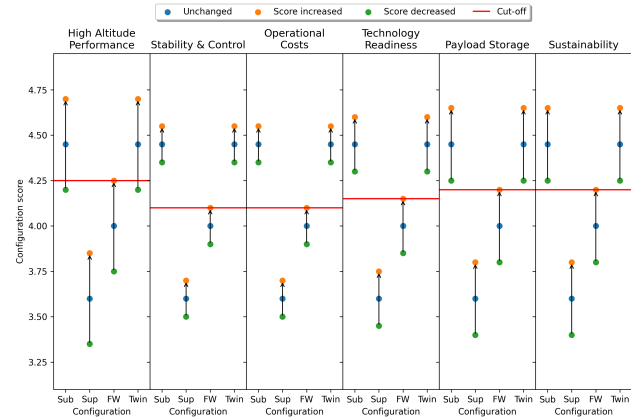
6.4. Sensitivity Analysis

Contributors: Konstantinos, Bas

A sensitivity analysis was performed for both the weights and scores in the final and second trade-off. The outcomes of both Figure 6.1a and Figure 6.1b increase the robustness of the first trade-off, proving that the reduction of the design space to two concepts was indeed the correct decision.

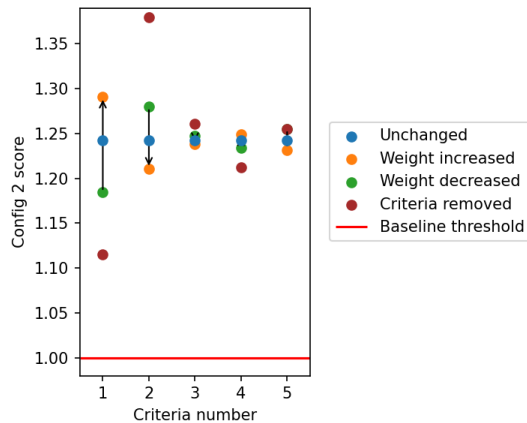


(a) Effect on criteria scores when the weights are varied for all 4 configurations.

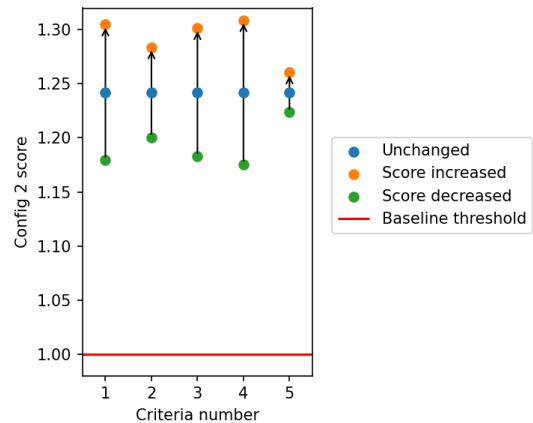


(b) Effect on criteria scores when the criteria are varied for all 4 configurations.

For the second trade-off, Figure 6.2a and Figure 6.2b indicate that the twin-body configuration consistently outperforms the conventional subsonic aircraft, regardless of moderate errors in weighting or scoring definition.



(a) Twin-body score sensitivity to changing weights



(b) Twin-body score sensitivity to changing scores

Weight Estimation and Iterations

This chapter gives an overview of the entire design process and starts the design with the weight estimation. It will be shown that the weight calculations are interdependent with the results of the following chapters, so it will also be discussed how the iteration procedure is performed to get to a design solution.

7.1. Design Process and Iteration Loops

Contributors: Máté

In the midterm report [10], Class I methods were used to size the aircraft, along with a lot of assumed values based on past data. This report expands on this by increasing the fidelity of the analysis. This also means that different parts of the design become more interconnected, which is illustrated by Table 7.1.

Table 7.1: N2 Chart of Subsystems

Fleet	W _{Pl}	W _{Pl}		W _{Pl}							N _{Fleet}
t _{Flight} , W _{Fuel}	Flight profile	n	n, M, EAS, h				M, h				W _{Fuel}
	D _{Fus}	Fus		G _{Fus}	I _{Fus}					I _{Fus}	W _{Fus} , G _{Fus}
	L _w , D _w	Wing place- ment	Wing	G _w	G _w	G _w			Wing place- ment	G _w	W _w , G _w
				PIS				P _{Pl}			W _{PIS} , G _{Pl}
	injec- tion rate				CS			P _{CS}			W _{CS} , G _{CS}
						HLD		P _{HLD}			W _{HLD} , G _{HLD} , CL _{Land} , CL _{TO}
	SFC	Engine place- ment	Engine place- ment	P _{Pl}			Prop	P _{Prop}	Engine Place- ment		W _{Prop} , G _{Prop}
							P _{Excess}	E&H			W _{E&H} , G _{E&H}
								P _{LG}	LG		W _{LG} , G _{LG}
		D _{stab}			G _{stab}					Stab	W _{Stab} , G _{Stab}
MTOM	MTOM, T	MTOM, W _{Fuel}	CG, S, W _{Fuel}		CG		T		MTOM, CG	CG	DS

The N2 chart was reworked from the baseline report to reflect the actual dependencies used in the design. The most important change is that the aerosol injection rate of the payload system depends on the wingspan. This has a significant effect on the overall design as shown in Chapter 9. Contrary to what was assumed in the baseline report, the thrust requirement on the propulsion system does not affect the SFC significantly as explained in Chapter 11. Due to the lack of time and resources, the stabiliser and the wing structure design were not iterated to get a new take-off weight, but the mass budgets outlined in Chapter 15 are satisfied.

To handle all the dependencies, an iteration management system was implemented in Python. All the relevant design values (all inputs and outputs for all design calculations) are stored in a centralised toml file that represents the current state of the aircraft. The toml values can be updated based on the output of the design calculations until the stored and computed version of every value is within the specified margin (1% was used for this report).

For this reason, most of the calculations given below may have outputs derived in later sections. The final numerical results are obtained after the global iterations are performed.

7.2. Class I Weight Estimation

Contributors: Máté

Class I weight estimation was used to get the initial maximum take-off weight. It is briefly repeated here from the midterm report because the method was slightly changed and a modified version of these calculations was used for subsection 7.4.1.

Firstly, the MTOM was related to the OEM with Equation 7.1 based on past aircraft data. The regression is plotted in Figure 7.1.

$$\text{OEM} = a \cdot \text{MTOM} + b \quad [\text{kg}] \quad (7.1)$$

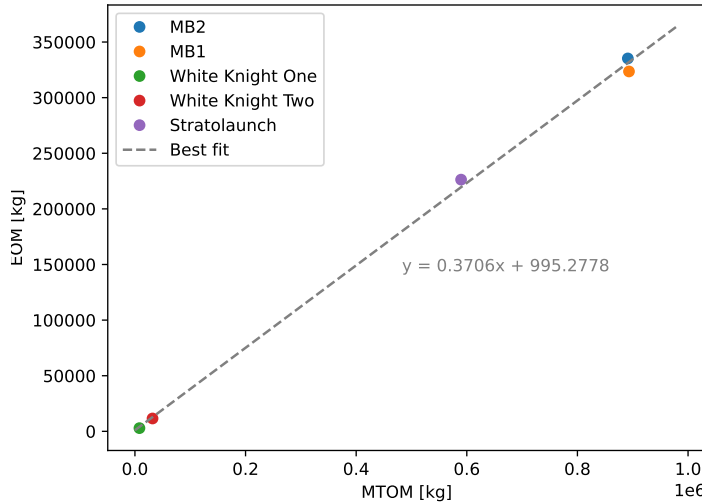


Figure 7.1: OEM vs MTOM reference Twin-body aircraft [10]

Then to estimate the fuel weight, the method of fuel fractions is used, namely Equation 7.2, where the index i corresponds to different mission phases. For the given mission this equation gives a conservative estimate, since it assumes no payload is dropped.

$$FF = \frac{W_f}{W_i} = \prod_{i=1}^n \frac{W_i}{W_{i-1}} \quad (7.2)$$

For the startup, taxi, take-off and climb, descent and landing, taxi and shut-down phases, standard values for transport jets were used. For the cruise phase Equation 10.17 [9] was used with a time just enough to drop the payload. An additional loiter phase of 45 minutes is added for contingency as recommended by Raymer [9]. As opposed to the midterm report, the SFC and L/D values are taken from Chapter 11 and Chapter 8, respectively. Atmospheric properties at different altitudes are determined using the ISA function of AeroSandbox [11].

$$\frac{W_i}{W_{i-1}} = e^{\frac{-t \cdot \text{SFC} \cdot g}{L/D}} \quad (7.3)$$

$$(7.4)$$

Assuming that the maximum take-off weight is composed of the empty operating weight, payload weight and fuel weight, and that the payload is not dropped (to get a conservative mass estimate), the MTOM can be determined using Equation 7.5. Here M_{tfo} is the mass fraction of trapped fuel and oils, and it is assumed to be 0.003, based on Roskam. [12]. If the OEM is given, Equation 7.6 is used instead. This will be used for the weight iterations.

$$\text{MTOM} = \frac{b + W_{\text{pl}}}{FF - M_{\text{tfo}} - a} \quad (7.5)$$

$$\text{MTOM} = \frac{\text{OEM} + W_{\text{pl}}}{FF - M_{\text{tfo}}} \quad (7.6)$$

7.3. Thrust Loading and Wing Loading

Contributors: Máté, Barnabás

Once the take-off weight is determined, the thrust and the wing area can be calculated. The same method was used here as in the midterm report [10], but with updated aerodynamic properties, including compressibility. In the formulas below, the aerodynamic coefficients are for cruise conditions by default. For take-off and landing, they are converted to the incompressible values using the Prandtl–Glauert correction. The equations for the curves are taken from Roskam [12] and modified as needed.

The landing constraint was computed using Equation 7.8. As shown by Equation 7.7, landing with half fuel and full payload was assumed as recommended by Raymer [9].

$$MF_{land} = \frac{OEM + 0.5 \cdot FM + W_{Pl}}{MTOM} \quad (7.7)$$

$$\frac{W}{S} = \frac{C_{L_{max}} \cdot \rho \cdot (l_{land}/0.5847)}{2 \cdot MF_{land}} \quad (7.8)$$

For stall, the limiting condition is cruise, because the air density is very low. The wing loading was computed using Equation 7.9, asserting that the stall speed must not be higher than 95 % of the cruise speed.

$$\frac{W}{S} = 0.5 \cdot \rho \cdot (V \cdot 0.95)^2 \cdot C_{L_{max}} \quad (7.9)$$

The take-off limitation was computed using Equation 7.10. The TOP of 11000 was calculated based on the minimum required 2500m runway length for a twin-engine jet aircraft.

$$\frac{T}{W} = \frac{\frac{W}{S}}{TOP \cdot \left(\frac{C_{L_{max}} \cdot \sqrt{1-M_{cruise}}}{1.21} \right)} \quad (7.10)$$

The cruise requirement is to be able to sustain a cruise speed of $M=0.7$ at the target altitude. This speed was chosen based on airfoil analysis in the midterm report [10]. Equation 7.11 defines the T/W constraint for the cruise. Equation 7.12 and Equation 7.13 are used to correct the cruise weight and thrust to MTOM and sea-level thrust.

$$\frac{T}{W} = \frac{(C_{D,0} + C_{D,W}) \cdot q}{\frac{W}{S} \cdot MF_{cruise}} + \frac{\frac{W}{S} \cdot MF_{cruise}}{\pi \cdot AR \cdot e \cdot q} \quad (7.11)$$

$$T_{sealevel} = T \left(\frac{\rho_0}{\rho} \right)^{0.75} \quad (7.12)$$

$$W_{TO} = \prod_{i=1}^3 \frac{W_i}{W_{i-1}} \cdot W \quad (7.13)$$

Finally, the rate of climb thrust requirement was calculated using Equation 7.15. The lift coefficient for maximum instantaneous ROC was assumed as given by Equation 7.14. The ROC requirement is 15 m/s as given by regulations [13].

$$C_{L_{climb}} = \sqrt{3\pi \cdot e \cdot C_{D,0} \cdot AR} \quad (7.14)$$

$$\frac{T}{W} = ROC \sqrt{\frac{\rho \cdot C_{L_{climb}}}{2 \cdot \frac{W}{S}}} \quad (7.15)$$

The constraints for all conditions are shown in Figure 7.2. The design point is always the lowest thrust loading among the points with the highest wing loading. Multiplying by the MTOM, the thrust and wing area are obtained.

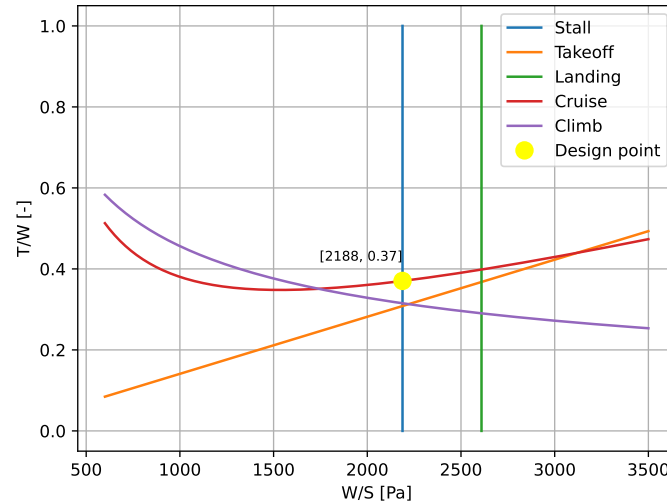


Figure 7.2: Loading Diagram With Final Parameters

7.4. Class II Weight Estimation

Contributors: Máté, Bas, Barnabás

Class II weight estimations were performed based on the work of Raymer [9]. It uses more accurate empirical relations compared to Class I to get a component-wise weight estimation for the aircraft, based on data for each of the components. Relations were used to determine the masses of all structural components, including the wing, horizontal and vertical tails and fuselages. Additionally, the weights of the main and nose landing gear, engine nacelles and fuel system were determined.

The empirical relations depend on a large set of parameters. Some parameters are constant as they describe, for example, a specific configuration, and the value of these follows from lists created by Raymer [9]. However, most of the parameters used in the empirical relations describe the geometry and size of the different components. The subsystem sizes often depend on the total mass of the aircraft, and can therefore not yet be determined precisely. Therefore, a first Class II weight estimation was made using the maximum take-off mass and the operating empty mass from the Class I estimation, as well as a large number of assumptions and values found in literature for reference aircraft. Most often, data on the Lockheed U-2 was used for this purpose. This resulted in an initial mass estimation for the different subsystems, which can be found in the mass breakdown in Table 15.3 of Section 15.2. An iterative process is however, needed to replace the assumptions made during the Class II weight estimation with actual subsystem data.

7.4.1. Iterations for Weight Estimation

Once the Class II estimation was performed, a new OEM was obtained. This OEM can be used as an input of Equation 7.6 to get an updated MTOM estimate from the Class I iteration. Then the thrust and wing area are updated as described in Section 7.3 and the input of the Class II estimation is updated. This process is repeated until the change in both OEM and MTOM compared to the previous iteration is less than 0.1 %. Then, for the final time, the thrust and wing area are computed. The final values for the computed MTOM, OEM, fuel mass, thrust and wing area (after the global iterations) are shown in Table 7.2. These serve as a basis and determine the budgets for the design of all other subsystems.

Table 7.2: Main Design Parameters After Global Iterations

Payload [kg]	17000
MTOM [kg]	61191
OEM [kg]	34381
FM [kg]	9810
S [m ²]	273
T _{cruise} [N]	30510

Aerodynamic Analysis

This chapter presents the analysis conducted to size the aerodynamic surfaces of the configuration and to determine their aerodynamic parameters. It commences, in Section 8.1, by outlining the unique cruising environment of a stratospheric flight and identifying the key parameters driving the aerodynamic design. The analysis then proceeds with a trade-off between potential airfoils, in Section 8.2. The criteria were established, weighted, and applied to evaluate 4 different supercritical candidates. The aerodynamic performance of the selected airfoils was assessed using XFOIL to identify the most suitable profile.

Following the 2D airfoil selection, the focus shifted to a 3D planform analysis, in Section 8.3. This involves determining the geometric dimensions of the platform and the wing's vertical placement relative to the fuselage. The process was carried out iteratively, in parallel with the evaluation of the wing's aerodynamic figures across multiple flight conditions, including cruise, takeoff, and landing, as described in Section 8.4. Parameters such as lift, drag, and overall aerodynamic efficiency were assessed. Initial fuselage sizing was also addressed in Section 8.5, including the estimations for the fuselage length and nose geometry.

Following that, the analysis switched to the basic near-wake characteristics, in Section 8.6, determining the induced velocity and angle of attack in the 3D flow. The engine plume characteristics were also visualised and described in detail. The chapter concludes with a verification and validation of the aerodynamic data in Section 8.7, followed by a sensitivity analysis to evaluate their volatility in Section 8.8.

8.1. Stratospheric Aerodynamic Considerations

Contributors: Konstantinos

Before the calculations and the sizing of the aerodynamic surfaces took place, the design drivers were outlined. These are key parameters around which the design process revolved in order to optimise their values. Given the distinct conditions of stratospheric flight, the operational environment at cruise was also analysed, as it was necessary for the calculations to come. Similarly, values obtained throughout the report and used for the aerodynamic design are also summarised.

8.1.1. Aerodynamic Design Drivers

The aerodynamic design for stratospheric flight should account for the unique atmospheric conditions encountered at high altitudes. One of the primary challenges addressed is the significant reduction in air density. For instance, at an altitude of 20 km, the air density decreases to approximately 7.3% of its sea-level value¹, which substantially reduces the aerodynamic forces produced and required to sustain steady flight. As a result, and as discussed in Chapter 11, the engine performance deteriorates with altitude, making the propulsion system less effective. Consequently, minimising aerodynamic drag became critically important in this thrust-limited environment.

Three primary components of drag were considered in this analysis [14, p. 514–515]. According to John D. Anderson, Jr. [14], parasitic (or zero-lift) drag arises from the form and skin friction of the body as it moves through the air. On the other hand, induced drag originates from the generation of aerodynamic forces, caused by the pressure differentials around the body. Finally, wave drag, which becomes significant at higher Mach numbers, is associated with the compressibility of the airflow with the formation of shock waves in the vicinity of the body.

Considering the substantial amount of payload that needs to be carried on board (Chapter 9) and the MTOM value of about 60 tons obtained at subsection 7.4.1, lift was maximised. As a result, maximising the Lift over Drag ratio for cruise became of critical importance. It ensured that sufficient lift is generated with minimal drag, optimising performance while reducing the thrust requirements for the engine.

Another important parameter taken into account is the critical Mach number. At higher altitudes, where the speed of sound decreases, aircraft fly closer to the sonic regime, where shock-induced separation and drag divergence occur. To avoid that, the aerodynamic design was optimised for values below this threshold value. Last but not least, to account for this velocity limitation, the desired lift coefficient and surface area of the wing were optimised to achieve the necessary lift requirements. All these while ensuring that the mass of the aerodynamic subsystem was minimised.

8.1.2. Aerodynamic Mission Requirements and Operational Environment

A Mach critical value was calculated, making use of Figure 8.1, where the critical pressure coefficient over a range of Mach numbers and the approximate minimum pressure coefficient for supercritical airfoils and adjusted for compressibility,

¹URL: <https://aerospacweb.org/design/scripts/atmosphere/> Accessed: 27/05/2025

are plotted. As seen in Figure 8.1 two equations ([14, Eq.11.55] and [14, Eq.11.60]) from John D. Anderson, Jr, were used and the intersection point of the curves was identified providing a value for M_{cr} equal to 0.7350. Since the flight envelope is constrained by the critical Mach number, the cruise speed was adjusted to be as close as possible to this value, while leaving some room for conservatism. As a result, M_{cruise} was constrained to 0.7. By flying below the M_{cr} value, weak shocks are avoided at any point over the airflow, as a result keeping the wave drag at low levels and aeroelasticity significantly simplified, as described in Section 13.5.

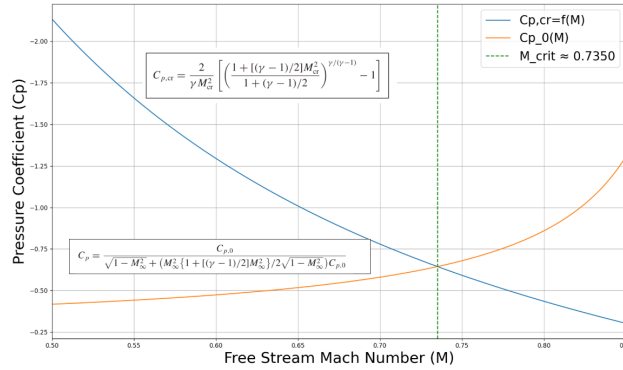


Figure 8.1: Estimation of critical Mach number.

Having determined the M_{cruise} and knowing that the desired altitude is at 20 km, V_{cruise} and the operational Reynolds Number were calculated using Equation 8.1 and Equation 8.2 respectively,

$$V_{cruise} = M_{cruise} \cdot \sqrt{\gamma \cdot R \cdot T} \quad (8.1)$$

$$Re_c = \frac{\rho \cdot V_{cruise} \cdot c}{\mu} \quad (8.2)$$

with all atmospheric variables found using the ISA calculator ² and c being the chord of the airfoil, found in a later point during the analysis in Section 8.3. As a result, Re expressed in terms of c was then calculated to be $1.28 \cdot 10^6 \cdot c$. The limited range of permissible velocities, limited due to the effect fact that flight occurs at the coffin corner is shown in Figure 8.2. In Figure 8.2, V_{cruise} of 206.5 m/s, V_{stall} of 192.0 m/s and the speeds corresponding to M_{crit} and M_{dd} , 216.9 and 228.7 m/s respectively, can be seen.

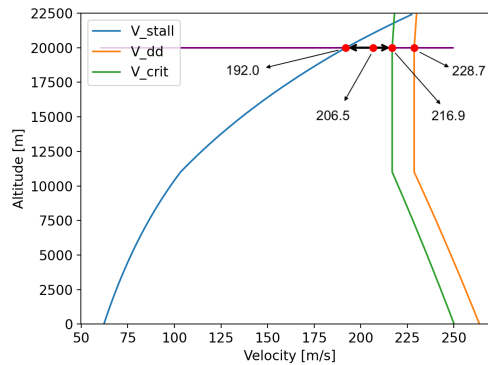


Figure 8.2: The coffin corner at 20 km altitude and V_{cruise} , V_{stall} , V_{crit} , V_{dd}

8.2. Airfoil Analysis

Contributors: Konstantinos

Given the mission profile and the subsonic nature of the design, the flight will occur within the coffin corner to reach the highest altitudes possible, likely in the transonic regime. For that reason, the use of supercritical airfoils (NASA SC[2] series) was considered optimal. Supercritical airfoils are designed to delay shock-induced separation by increasing M_{crit} and reduce wave drag [14, p. 775-777].

8.2.1. Initial Selection

To select the most suitable airfoil from the NASA SC(2) supercritical series, the options were narrowed down based on thickness-to-chord ratio (t/c), the target design lift coefficient ($C_{l_{des}}$) and intended Reynolds Number, as suggested by Daniel P. Raymer [9, p. 46-54].

²URL: <https://aerospacweb.org/design/scripts/atmosphere/> Accessed: 27/05/2025

Concerning the t/c ratio, given that the wings should not only store fuel, but also accommodate the hydraulics and injection nozzles for the SAI operations, airfoils with higher t/c ratios to provide increased internal volume were preferred, while ensuring that there is not a significant increase in drag and structural weight. Having said that, Equation 8.3 [15, p. 246] was used to determine the t/c for the given Mach region:

$$\frac{t}{c} = 0.24 \left\{ \left[1 - \left(\frac{5 + M_{cr}^2}{5 + (M^*)^2} \right)^{3.5} \right] \left(\frac{\sqrt{1 - M_{cr}^2}}{M_{cr}^2} \right) \right\}^{2/3} \quad (8.3)$$

with M^* a constant equal to 1.12 for the SC(2) series [15, p. 246]. A value of 0.1376 was achieved, which is further backed up by historical trends [9, Fig.4.14]. For a design Mach number of 0.7, and allowing for an uncertainty of 0.2 (being the accuracy of the historical trends graph at both the x and y axes), a range between 0.12 and 0.16 was selected.

For the operational Reynolds Number, the value of $1.28 \cdot 10^6$ was used. As determined at subsection 8.1.2, this corresponds to the product of the Reynolds Number and the chord length “c” for an altitude of 20 km. Considering that for the airfoil analysis, XFOIL was used, the chord length was normalised to 1 to ensure consistency with the software.

Last but not least, the $C_{l_{des}}$ is the lift coefficient for which the L/D ratio of the wing is maximised. According to Daniel P. Raymer [9, Eq. 4.4, 4.5], a preliminary design coefficient can be obtained using $C_{l_{des}} = \frac{1}{q} \cdot \frac{W}{S}$, with q the dynamic pressure at desired speed and altitude and $\frac{W}{S}$ the wing loading determined during the Class I Estimation (subsection 7.4.1). A value of 0.6246 was obtained.

Having said that, with the selection restricted to airfoils designed for an Re of $1.28 \cdot 10^6$, ranging from 0.12 to 0.16 t/c and with a $C_{l_{des}}$ of about 0.6, the following were obtained: the SC(2)-0612, SC(2)-0614, SC(2)-0712 and SC(2)-0714.

8.2.2. Trade-off Criteria

In order to select a suitable airfoil out of the four, the following criteria and their corresponding weights were considered; Zero-Lift Drag Coefficient (C_{d_0}) [0.35], Zero-Lift Moment Coefficient (C_{m_0}) [0.1], Lift to Drag Ratio (L/D) at design point [0.2], and Drag Divergence Mach Number (M_{DD}) [0.35].

Zero-Lift Drag Coefficient (C_{d_0})

The zero-lift drag coefficient, C_{d_0} , is a major contributor to total drag and becomes increasingly dominant at high flight speeds. At transonic Mach numbers in stratospheric cruise, induced drag diminishes while parasite drag, which is primarily governed by C_{d_0} , dominates [14, fig. 1.60]. Choosing an airfoil with minimal C_{d_0} is therefore critical for enhancing aerodynamic efficiency and reducing fuel consumption during cruise. For this, it was given the highest weight of 0.35.

Zero-Lift Moment Coefficient (C_{m_0})

The zero lift moment coefficient is the moment about the aerodynamic centre that is independent of the angle of attack [14, p. 365] and indicates the required tail size, as a larger moment will require a larger tail to trim the aircraft. This results in more drag and weight, which is undesired. Therefore, a small negative (pitch down) C_{m_0} is wanted. This criterion is not considered driving, however, so a weight of 0.1 was awarded.

Maximum Lift to Drag Ratio (L/D)

The lift-to-drag ratio, L/D , is a key indicator of aerodynamic efficiency. A higher L/D implies that more lift is produced per unit of drag, leading to reduced fuel consumption and increased range or endurance. In stratospheric flight, maximising L/D at the reference design flight phase ($C_{l_{des}}$) is essential for sustaining altitude with minimal energy consumption, and, thus, a weight of 0.2 was given.

Drag Divergence Mach Number (M_{DD})

The drag-divergence Mach number is the Mach number after which there is a sudden increase in drag [14, p. 765–772]. Beyond the drag-divergence Mach number, the drag coefficient can become very large, typically increasing by a factor of 10 or more [14, p. 766]. This large increase in drag is associated with an extensive region of supersonic flow over the airfoil, terminating in a shock wave.

In the mission context, the aircraft will fly at the coffin corner, where large Mach number values will be reached. Thus, delaying drag divergence, which reduces wave drag, is key. The drag divergence Mach number is found in Equation 8.4.

$$M_{dd} + \frac{C_{l_{des}}}{10} + \left(\frac{t}{c} \right) = \kappa_A \quad (8.4)$$

where κ_A is an airfoil technology factor, having a value of 0.95 for a supercritical airfoil. Given the high importance of the criterion, a high weight of 0.35 was awarded.

8.2.3. Trade-off

Having identified the trade-off criteria, a trade-off analysis took place to determine the most suitable airfoil for the wing. The airfoils were compared using XFOIL data analysed in a Python script under similar conditions. The Reynolds Number was set to $1.28 \cdot 10^6$, as aforementioned, while it is important to note that in XFOIL the Mach Number was set to 0, given that the software is incapable of correcting for compressibility effects. For that reason, the values in Table 8.1 were used for comparison and are not representative of the actual flight conditions of the cruise flight.

The values obtained from XFOIL were treated as scores for the trade-off analysis. Since lower values of C_{m_0} and C_{D_0} are preferable, while higher values of M_{dd} and $[L/D]_{des}$ are desired, the scoring system was designed accordingly: the scores for C_{m_0} (in absolute) and C_{D_0} were inverted and then multiplied with the weights, whereas the scores for M_{dd} and $[L/D]_{des}$ were directly weighted. The overall score is the sum of these weighted components, with the highest total score indicating the most favourable airfoil. Based on this analysis, SC(2)-0612 was chosen as the optimal choice for the wing.

Table 8.1: Trade-off Analysis for Airfoil Selection using the XFOIL results for Re of $1.28 \cdot 10^6$ and $M=0$.

Parameter Airfoil	C_{m_0} [0.1]	C_{D_0} [0.35]	M_{dd} [0.35]	$[L/D]_{max}$ [0.2]	Score
SC(2)-0614	[Good] -0.1150	[Excellent] 0.00611	[Fair] 0.75	[Poor] 77.6	73.94
SC(2)-0612	[Excellent] -0.1090	[Good] 0.00615	[Excellent] 0.77	[Fair] 79.3	74.14
SC(2)-0714	[Poor] -0.1329	[Poor] 0.00768	[Poor] 0.74	[Good] 81.2	62.82
SC(2)-0712	[Fair] -0.1241	[Fair] 0.00686	[Good] 0.76	[Excellent] 85.3	69.15

Poor Fair Good Excellent

Legend: Shading represents performance from "Poor" to "Excellent"

8.2.4. Airfoil Characteristics

Having identified the airfoil, some of its characteristics were obtained that were necessary for the Wing Analysis to come at Section 8.4. To begin with, the $C_l - \alpha$ curve was plotted, to obtain $C_{l_{max}}$, C_{l_α} and α_{0L} , the airfoil zero-lift angle. This is shown in Figure 8.3. Through the analysis, it was obtained that $C_{l_{max}}$ is equal to 1.658 at an α of 14.50 degrees. Likewise, a slope C_{l_α} of 0.1 [1/deg] or 5.7296 [1/rad] was obtained, with the α_{0L} being -3.94 degrees. All values were incompressible for $M=0$ and $Re=1.28e6$.

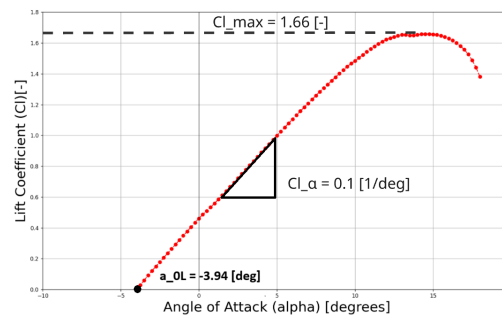


Figure 8.3: The $C_l - \alpha$ curve of the airfoil visualising the $C_{l_{max}}$, C_{l_α} and α_{0L} for Re of $1.28 \cdot 10^6$ and $M=0$.

8.3. Planform Design

Contributors: Konstantinos, Blanca, Carmen

An iterative process to perform a planform geometry sizing took place. This depends on values found in both Section 8.2 and Section 8.4, where the airfoil and wing were analysed respectively, and as a result, the values of the aerodynamic analysis were iterated constantly until convergence.

To begin with, the wing surface area was estimated to be about 273 m² during the Class I estimation, in subsection 7.4.1. During the iterative design process, the wingspan was found to increase uncontrollably to unfeasibly large values. To address this, the span was capped at 77 m, leaving a margin below the regulatory maximum allowable span of 80 m [16]. Having determined this, the aspect ratio was easily found using Equation 8.5. A sweep angle was considered, as it is mainly applied to increase the critical Mach number, a driving criterion of the analysis, as discussed in Section 8.1. Introducing sweep for the same wing area, however, decreases the aspect ratio by increasing the chord for the same wing structure.

Higher aspect ratio improves aerodynamic efficiency, which is crucial in high-altitude flights; hence, the design features an unswept wing.

Additionally, given the low transonic regime of the aircraft at cruise, it is highly unlikely that any portion of the airflow will accelerate to sonic speeds. This was estimated considering the expansion of the flow, using $(M_{\text{airflow}} - M_{\text{aircraft}}) \cdot a = V_{\text{airflow}} - V_{\text{aircraft}}$. This provides an estimate of the velocity increase required relative to the free stream for a local airflow to reach Mach 1. Investigating the extreme scenario of the aircraft cruising at its critical Mach number, $M_{\text{aircraft}} = M_{\text{crit}} = 0.735$, by definition $M_{\text{airflow}} = M^* = 1$ and a speed of sound of $a = 295$ m/s (ISA calculation at 20 km altitude), the resulting velocity difference is $V_{\text{airflow}} - V_{\text{aircraft}} = 80$ m/s. Given the calculated cruise speed of $V_{\text{aircraft}} = 206.55$ m/s, this implies that the local flow would need to accelerate by approximately 40% to reach sonic conditions. Such a large margin makes the formation of local supersonic regions highly unlikely under cruise conditions.

Other important geometric parameters were determined using Equation 8.6 to Equation 8.9, as suggested by Torenbeek [15]. These include the root and tip chords, the chord length of the MAC (Mean Aerodynamic Chord) and its lateral position y_{mac} :

$$A = \frac{b^2}{S_{\text{wing}}} \quad (8.5) \quad c_r = \frac{2 \cdot S}{[b_{\text{middle}} + (b - b_{\text{middle}})] \cdot (1 + \lambda)} \quad (8.6) \quad c_t = \lambda \cdot c_r \quad (8.7)$$

$$\bar{c} = \frac{2}{3} \cdot c_r \cdot \left(\frac{1 + \lambda + \lambda^2}{1 + \lambda} \right) \quad (8.8) \quad y_{\text{mac}} = \frac{b}{6} \cdot \left(\frac{1 + 2 \cdot \lambda}{1 + \lambda} \right) \quad (8.9)$$

Last but not least, the use of twist was considered. During the iteration process (at subsection 8.4.3), it was found that a_{cruise} is considerably high, resulting in possible airflow separation issues. According to Anderson [14, p.359–363], in wing design it is desirable to stall the wing first at the root rather than at the tip. The reason is to retain aileron control during the initial stages of a stall. In addition to that, stall near the fuselage is more stable and easier to recover. To induce this behaviour, a geometric twist was considered so that the tip has a lower incidence angle than the root. That is to apply a positive geometric twist at the root, decreasing linearly to zero at the mean aerodynamic chord (MAC), and becoming negative at the tip [9, p.159]. Given that a detailed aerodynamic design of the twist distribution was not conducted at this stage, as it requires advanced computational fluid dynamics (CFD) tools beyond the scope of this study, twist was not included and is therefore recommended as a subject for future work. The assigned geometric values are summarised in Table 8.2. Notice that b_{middle} refers to the part of the wing connecting the two fuselages and that y_{mac} is taken from a fuselage's longitudinal centreline.

Table 8.2: Wing parameters for planform sizing

$\Lambda_{c/4}$ [°]	S [m ²]	A [-]	b [m]	b_{middle} [m]	λ [-]	c_r [m]	c_t [m]	MAC [m]	y_{mac} [m]	twist [-]
0	272.96	21.7	77	16	0.45	4.67	2.10	3.55	16.01	no

A detailed 3D model and sketch of the wing can be found at Figure 12.3 and Chapter 16.

8.3.1. Wing Vertical Position

The wing's vertical location with respect to the fuselage was determined by the real-world environment in which the aircraft will operate. To select the best placement, a small trade-off was performed, in Table 8.3, with aerodynamic criteria receiving a slightly higher score than the rest. All scoring justification provided below are found in *Aircraft Design: A Conceptual Approach* by Raymer [9, p.68–72].

High wing configurations are widely used for carrier aircraft as they allow placement of the fuselage closer to the ground while providing the necessary engine ground clearance, eliminating the need for any dihedral. They are, however, more difficult to maintain and refuel due to the increased height of the wing. Thus, they receive a moderate score for ground handling. They score lower than the competitors, however, for aerodynamics because the fairing used in the wing-fuselage intersection creates more drag. Structurally, they provide a solid choice as they can be directly attached to the top of the fuselage, increasing payload capacity, while they are considered the most laterally stable.

A mid-wing configuration offers excellent aerodynamics due to the minimal interference at the wing-fuselage intersection, giving it a good score. Its vertically balanced placement leads to optimised lateral and longitudinal characteristics, yet lacks the natural pendulum stability of a high-wing, leading to a good but not excellent stability score. Ground handling is also good, as the wing does not interfere with any fuselage-mounted equipment. However, its structural complexity is a challenge given that the wing spar must pass through the body, complicating the design and increasing weight. Overall, it provides a balanced trade-off across all criteria.

A low-wing configuration provides the most favourable aerodynamic characteristics of the three, originating from the natural downward force due to the wing's position that increases stability and lift. It also simplifies landing gear integration. Ground handling is rated poorly due to lower ground clearance and more difficult access to load/unload. Structurally, the configuration allows the wing to pass under the fuselage, making it easier to integrate.

It can be seen that the high wing configuration received the higher value and, thus, was the one selected, mainly for providing effective ground clearance for the engines.

Table 8.3: Trade-off Analysis for Vertical Wing Placement

Parameter Configuration	Aerodynamics[0.3]	Stability[0.3]	Ground Handling [0.2]	Structural Complexity [0.2]	Score
High Wing	2.Fair	4.Excellent	3.Good	3.Good	3
Middle Wing	3.Good	3.Good	3.Good	2.Fair	2.8
Low Wing	4.Excellent	2.Fair	1.Poor	3.Good	2.6

1.Poor 2.Fair 3.Good 4.Excellent

Legend: Shading represents performance from “Poor” to “Excellent”

8.4. Wing Analysis

Having analysed the 2D airfoil and determined the planform geometry, a 3D analysis was performed. This included determining the lift and drag profiles of a clean configuration. That is, no flaps were considered, for the reasons explained in Section 10.1, and the spoilers' angle was set to 0°, having virtually no effect.

8.4.1. Lift Estimation

Contributors: Konstantinos

In order to determine the maximum wing coefficient, the gradient of the lift curve and the stall angle, DATCOM and Daniel P.Raymer [9, p. 322–333] were used. The analysis commenced with using Equation 8.10 [9, Eq. 12.6-8] to determine a lift slope for the aircraft:

$$C_{L\alpha} = \frac{2\pi AR}{2 + \sqrt{4 + \frac{AR^2 \cdot \beta^2}{(\eta)^2}}} \cdot \left(\frac{S_{wet}}{S} \right) \cdot F \quad (8.10)$$

where β , η , and F are correction factors depending on geometry, compressibility and data obtained from the 2D airfoil analysis:

$$\beta^2 = 1 - M^2 \quad (8.11) \quad \eta = \frac{C_{l_a} \cdot \beta}{2\pi} \quad (8.12) \quad F = 1.07 \cdot \left(1 + \frac{D_{fus}}{b} \right)^2 \quad (8.13)$$

Having determined $C_{L\alpha}$, the next step was to find $C_{L_{max}}$. To do so, Equation 8.14 alongside semi-empirical figures from Daniel P.Raymer [9, Fig. 12.8-12.9] were used. An arbitrary leading edge sharpness parameter was used to obtain the values from these graphs. Raymer [9, p.329] defines this as Δy , and a value of 0.2 was used for the SC(2) series.

$$C_{L_{max}} = C_{l_{max}} \cdot \left(\frac{C_{L_{max}}}{C_{l_{max}}} \right) + \Delta C_{L_{max}} \quad (8.14)$$

From the aforementioned figures from literature, a $\frac{C_{L_{max}}}{C_{l_{max}}}$ value of 0.9 and $\Delta C_{L_{max}}$ of 0.2 were determined. $\Delta C_{L_{max}}$ is a compressibility correction factor so the $C_{L_{max}}$ determined is compressed. Last but not least, the stall angle was determined using Equation 8.15, where α_{0L} was found at subsection 8.2.4, $\frac{C_{L_{max}}}{C_{L\alpha}}$ in subsection 8.4.1 and $\Delta \alpha_{C_{L_{max}}}$ from literature [9, Fig. 12.10]. For Δy of 0.2, $\Delta \alpha_{C_{L_{max}}}$ is 2 degrees:

$$\alpha_{stall} = \alpha_{0L} + \frac{C_{L_{max}}}{C_{L\alpha}} + \Delta \alpha_{C_{L_{max}}} \quad (8.15)$$

All in all, the values found in this section, accounting for compressibility, are summarised in Table 8.4.

8.4.2. Drag Estimation

Contributors: Konstantinos, Bas, Blanca, Carmen

Next up is the Drag Estimation. This was split into 3 main components. First, the parasitic drag was considered using empirical formulas taking into account skin friction and interference. Then, a formula for lift-induced drag was derived, and its value for the design lift coefficient, derived in subsection 8.4.3, was calculated. Lastly, wave drag, a prominent form of drag in the transonic region of cruise, was considered, taking into account both the fuselage and the wing contribution.

Parasitic Drag

The Parasitic Drag accounts for the zero-lift drag due to skin friction, form, interference, and additional miscellaneous drag sources. The parasitic drag coefficient was determined using the component build-up method [9], which is shown in Equation 8.16.

$$C_{D_p} = \frac{1}{S_{ref}} \sum_c C_{f_c} \cdot FF_c \cdot IF_c \cdot S_{wet_c} + C_{D_{misc}} \quad (8.16)$$

For each aircraft component, specifically the wing, horizontal and vertical stabilisers, the fuselage, and the engine nacelles, the various drag contributions were calculated together with their wetted areas. First of all, the skin friction coefficient was determined for each component based on empirical relations, dependent on the Reynolds' and Mach numbers. The skin friction was calculated for both the laminar and turbulent portions of the flow over a component. The relations are given in Equation 8.17 and Equation 8.18. The Reynolds number Re was calculated for the characteristic length (c) of each individual component at V_{cruise} , as given by Equation 8.2.

$$C_{f,lam} = \frac{1.328}{\sqrt{Re}} \quad (8.17) \quad C_{f,turb} = \frac{0.455}{(\log_{10} R)^{2.58} \cdot (1 + 0.144M^2)^{0.65}} \quad (8.18)$$

The total component skin friction coefficient is the combination of the two, weighted by the transition point of the flow, $\left(\frac{x}{c}\right)_{cr}$.

$$C_f = \left(\frac{x}{c}\right)_{cr} C_{f,lam} + \left(1 - \left(\frac{x}{c}\right)_{cr}\right) C_{f,turb} \quad (8.19)$$

Next, the form drag was determined by calculating the form factor FF for each component using empirical relations, specifically equations 12.30 to 12.32 in [9, P. 344]. These include the interference factor determined for each component based on its placement and type. Raymer [9, p. 346] provides a range of these values, with the highest bound used for conservatism. The wetted surface areas were calculated using simple geometric relations based on the sizing of the different components that take place throughout the report, from the Class II weight estimation and aerodynamics, to propulsion and fuselage analyses. The sum of these is the reference area, S_{ref} .

Next to these three contributions, the miscellaneous drag was estimated, specifically the leakage and protuberance drag. This contribution to the parasitic drag was caused by air moving in and out of the fuselage due to pressure differences, as well as extrusions from the aircraft perturbing the flow. This drag was estimated to be 5 % of the parasitic drag. [9, p. 350].

Lift Induced Drag

The Induced Drag is defined as follows in Equation 8.20:

$$C_{D_i} = \frac{C_L^2}{\pi A e} \quad (8.20)$$

where C_L is the wing lift coefficient, A is the aspect ratio, and e is the Oswald efficiency factor, which was the only parameter still to be determined. A method proposed by Dr-Ing. Mihaela Nita [17] was used for a top-level estimation of the Oswald efficiency factor using simple wing parameters, given by Equation 8.21:

$$e = e_{theo} \cdot k_{e,F} \cdot k_{e,D_0} \cdot k_{e,M} \quad (8.21)$$

The theoretical Oswald factor, e_{theo} was corrected to account for the losses due to the fuselage, $k_{e,F}$, the viscous drag due to lift, k_{e,D_0} and the compressibility effects on induced drag, $k_{e,M}$. The value of k_{e,D_0} can be taken from statistics on reference aircraft, and is equal to 0.873 for jet aircraft [17]. The rest of the correction factors are given by Equation 8.22 to 8.24 respectively:

$$e_{theo} = \frac{1}{1 + f(\lambda) \cdot A} \quad (8.22) \quad k_{e,F} = 1 - 2 \left(\frac{d_F}{b}\right)^2 \quad (8.23) \quad k_{e,M} = -0.00152 \left(\frac{M}{0.3} - 1\right)^{10.82} + 1 \quad (8.24)$$

In Equation 8.22, $f(\lambda)$ is an approximation of Horner's function, given in Equation 8.25, with λ being the taper ratio determined to be 0.45 in Section 8.3:

$$f(\lambda) = 0.0524\lambda^4 - 0.15\lambda^3 + -0.0706\lambda + 0.0119 \quad (8.25)$$

In Equation 8.23, d_F is the fuselage diameter, found in Section 8.5. It should be noted that $k_{e,F}$ was squared to account for both fuselages of the twin body. In subsection 8.4.3, the design lift coefficient was determined, which was used to calculate the induced drag provided in Table 8.4.

Wave Drag

Unlike in low Mach Numbers, the wave drag should be taken into account. To do that, equations found in the Stanford Aircraft Design, Synthesis, and Analysis tool codenamed SUAVE were used³, which takes into account both volume (subscript v) and lift (subscript l) dependent wave drag. For the wing, Equation 8.26 and Equation 8.27 were used:

$$C_{D_{wvw}} = \frac{4(t/c)^2(\beta^2 + 2x^2)}{(\beta^2 + x^2)^{1.5}} \quad (8.26)$$

$$C_{D_{wl}} = \frac{C_L^2 x (\sqrt{1 + \beta^2/x^2} - 1)}{4} \quad (8.27)$$

with x , AR , and β found in Equation 8.28 to 8.30:

$$x = \frac{\pi AR}{4} \quad (8.28)$$

$$AR = \frac{b^2}{S_{wing}} \quad (8.29)$$

$$\beta = \sqrt{1 - M^2} \quad (8.30)$$

The wave drag for the fuselage was then calculated using Equation 8.31, with R_{max} representing the maximum radius of the fuselage, L_{fus} representing its length and S_{fus} its surface area.

$$C_{D_{wvf}} = \frac{9\pi^3 R_{max}^4}{2L_{fus}^2 S_{fus}} \quad (8.31)$$

$C_{D_{wvw}}$ and $C_{D_{wvf}}$ were then added together to obtain the C_{D_w} shown in Table 8.4, while $C_{D_{wl}}$ was used in subsection 8.4.3 to get the drag polar.

Table 8.4: Aerodynamic parameters obtained during the 3D Wing Analysis in Section 8.4, accounting for compressibility

$C_{L_{max}}$ [-]	$C_{L\alpha}$ [1/rad]	α_{stall} [deg]	C_{D_0} [-]	C_{D_w} [-]	$C_{D_{ides}}$ [-]	$C_{D_{wlides}}$
1.292	5.33	11.94	0.0039	0.011	0.012	0.0063

Notice that $C_{D_0} + C_{D_w}$ make the lift-independent part, while $C_{D_{ides}} + C_{D_{wlides}}$ the lift dependent, as visible in Figure 8.4a.

8.4.3. Cruise Conditions

With all the parameters determined, the maximum lift over drag ratio was determined. This was done by plotting the drag polar with Equation 8.32, using dependent and independent lift parameters:

$$C_D(C_L) = C_{D_0} + C_{D_w} + C_{D_i}(C_L) + C_{D_{wl}}(C_L) \quad (8.32)$$

with all the parameters determined in Section 8.4. The $C_{L_{des}}$ is defined as the lift coefficient that maximizes the lift over drag ratio, an aerodynamic design driver (subsection 8.1.1), and is found at the point at which a line from the origin is tangent to the drag polar curve [9, P. 321]. This is shown in Figure 8.4a where values of $C_{L_{des}} = 0.87$ and $\frac{L}{D_{max}} = 29.2$ are found. This $C_{L_{des}}$, corrected for compressibility, is used to fly in the second half of the cruise, as discussed in Chapter 10.

Lastly, an approximate lift curve was obtained to estimate the cruise angle of attack, α_{cruise} . From Section 8.4, values for $C_{L_{des}}$, $C_{L_{max}}$, $C_{L\alpha}$, and α_{stall} were determined. Additionally, the zero-lift angle of attack for the airfoil, α_{0L} , was calculated in Section 8.2.

Given that there is no empirical formula to directly determine the wing's α_{0L} , a range of possible α_{cruise} values was estimated, giving two extreme cases. The lower angle bound was found by obtaining a straight line between the points $(\alpha_{0L}, 0)$ and $(\alpha_{cruise}, C_{L_{des}})$. At this point, it is important to note that, because the wing has no twist, the geometric angle of the wing and the airfoil are the same. Furthermore, at zero lift, there is no significant induced angle of attack due to the absence of downwash; no net pressure difference exists between the upper and lower wing surfaces, and thus no vortices

³URL: <https://suave.stanford.edu/> Accessed: 28 May 2025

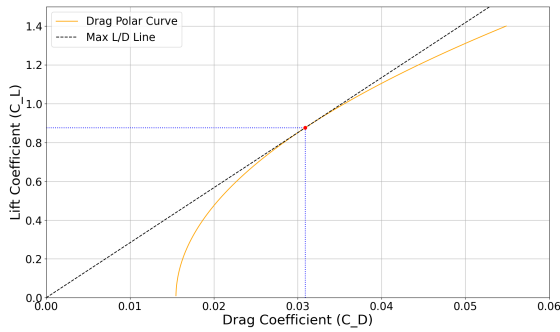
are generated. As a result, the assumption that the α_{0L} of the airfoil is similar to that of the wing was reasoned. This line, calculated using Equation 8.33, is shown in grey in Figure 8.4b.

For the lower limit of the lift curve, points $(\alpha_{cruise}, C_{L_{des}})$ and $(\alpha_{stall}, C_{L_{max}})$ were used. This is an underestimation of the lift curve, leading to a higher α_{cruise} being calculated for the same $C_{L_{des}}$, due to the non-linearity of the curve not being taken into account. This line, calculated using Equation 8.34, is shown in brown in Figure 8.4b.

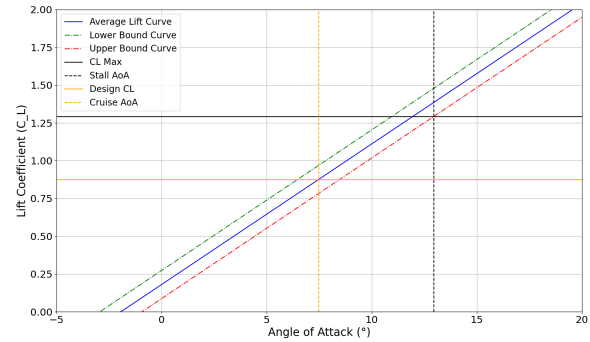
$$\alpha_{cruise_{lower}} = \alpha_{0L} - \frac{0 - C_{L_{des}}}{C_{L_{\alpha}}} \quad (8.33)$$

$$\alpha_{cruise_{upper}} = \alpha_{stall} - \frac{C_{L_{max}} - C_{L_{des}}}{C_{L_{\alpha}}} \quad (8.34)$$

Last but not least, the average between the two was taken to determine a lift curve between the aforementioned bounds. As a result, an average for α_{cruise} of 7.47° is determined. These values represent the geometric angle of attack, with the effective value determined subtracting the induced angle ($a_{eff} = a - a_i$), found at subsection 8.6.1. Lastly, a C_{L_0} of 0.181 was obtained using the blue line (average of the two “extreme cases”) in Figure 8.4b.



(a) The Drag Polar and the tangent from the origin to determine $C_{L_{des}}$ and $\frac{L}{D}_{max}$.



(b) The Lift Curve to obtain α_{cruise} .

Figure 8.4: Cruise Conditions for the aircraft.

8.5. Fuselage design

Contributors: Inés

Given that the fleet of this mission consists of unmanned aircraft, the fuselage design is not constrained by the need for a cabin or passenger seating. This allows for a cylindrical fuselage section dedicated to the aerosol storage tanks, while ensuring the most efficient shape in the rest of the fuselage. For this reason, a tail boom configuration was chosen, given that it allows for a longer tail length, and therefore smaller control surface area, which is required for longitudinal stability considerations, as explained in Section 12.2

The first step in the fuselage design is to determine the total length, which in this case was estimated by simplifying the geometry into three main components: a nearly cylindrical section for aerosol storage, a nose cone at the front, and a tail boom at the rear. The length of the tail boom was determined as the optimum length for longitudinal stability, as explained in Section 12.3. On the other hand, the nose cone length was found through the graph shown in Figure 8.5 [18]. The slenderness of the nose has a large impact on the value of Drag Divergence. The necessary length-to-diameter ratio is 1.15 for a $M_{Div} = 0.77$ corresponding to the NASA SC(2)-0612 airfoil of this mission.

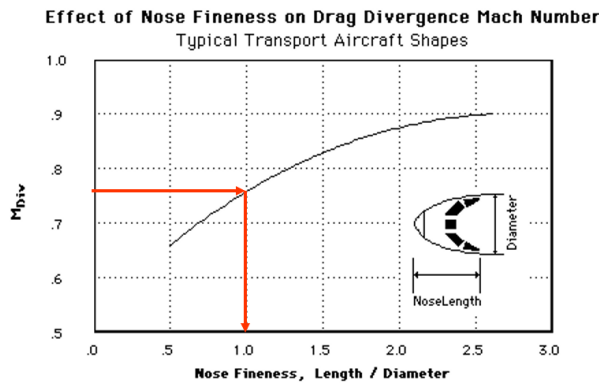


Figure 8.5: Effect of Nose Fitness on Drag Divergence Mach Number [18]

Knowing this ratio, the total length of the fuselage can be computed using Equation 8.35.

$$l_f = l_{cyl} + l_{tb} + l_{nc} = \frac{V_{tank}}{\pi \cdot \left(\frac{D_{max} \cdot \beta}{2}\right)^2} + l_{tb} + 1.15 \cdot D_{max} \quad (8.35)$$

Where V_{tank} is the volume of one of the two tanks that the aircraft will carry in each fuselage, as explained in Section 14.1. Furthermore, l_{tb} is the tail boom length, and l_{nc} the nose cone length determined by the ratio of Figure 8.5. Finally, D_{max} is the diameter of the cylindrical section of the fuselage, which is at the same time the maximum diameter of the fuselage. The constant β is an assumed coefficient that accounts for the difference in the diameter of the aerosol tanks and the total diameter of the fuselage (D_{max}), which was chosen to be 0.9 for crashworthiness reasons.

As mentioned above, there are no constraints regarding passenger seating requirements, and the aerosol tanks can be shaped freely, so D_{max} remains a design variable to be defined. For this reason, the fuselage diameter can be optimised for aerodynamic performance. To achieve this, the *Sears-Haack body* was considered, as it provides the lowest theoretical wave drag in supersonic flow⁴. Since our aircraft operates in the transonic regime, where wave drag is already a concern, minimising it remains a priority, making the Sears-Haack profile a suitable baseline for fuselage shaping.

The following Sears-Haack equation, which defines the optimal fuselage shape for minimum wave drag at a given length and volume, was therefore used to guide the design of D_{max} :

$$V = \frac{3\pi^2}{16} \left(\frac{D_{max}}{2}\right)^2 l_f \quad (8.36)$$

Inserting Equation 8.35 into this equation leads to a cubic polynomial as a function of D_{max} , as shown in Equation 8.37.

$$V = \frac{3\pi^2}{16} \left(\frac{D_{max}}{2}\right)^2 \left(\frac{V_{tank}}{\pi \cdot \left(\frac{D_{max} \cdot \beta}{2}\right)^2} + l_{tb} + 1.15 \cdot D_{max} \right) \quad (8.37)$$

In this case, a buffer of 30% was considered for the difference between the total volume (V) and the volume of the aerosol tanks (V_{tank}), since the rest of the available volume is solely the rest on the volume in the cylindrical section, the nose cone and the tail boom.

$$0.3 \cdot V_{tank} = \frac{3\pi^2}{16} \left(\frac{D_{max}}{2}\right)^2 \left(\frac{V_{tank}}{\pi \cdot \left(\frac{D_{max} \cdot \beta}{2}\right)^2} + l_{tb} + 1.15 \cdot D_{max} \right) \quad (8.38)$$

Solving this equation for the lowest positive solution led to a diameter of 1.35 m, and a fuselage length of 22.76 m was determined.

8.6. Study on Basic Near Wake Characteristics

Contributors: Inés

In order to get an idea of how the aerosol will be distributed after injection, an initial basic near-wake analysis was performed. For this, both the vortex strength of the wing as well as the engine plume characteristics were analytically calculated.

8.6.1. Vortex Strength

Given that a wing with a taper ratio of 0.45 and no geometric twist was selected for the design, as specified in Section 8.3, the wing can be analysed under the assumption of an elliptical lift distribution. Based on this assumption, Prandtl's classical lifting line theory [14, p.442–447] was used to evaluate the vortex strength along the wing planform, as shown in Equation 8.39:

$$\Gamma(y) = \Gamma_0 \sqrt{1 - \left(\frac{2y}{b}\right)^2} \quad (8.39)$$

where y is the spanwise position along the wing, b the wingspan and Γ_0 the circulation at the wing centre, defined for an elliptical distribution using Equation 8.40:

⁴URL: https://en.wikipedia.org/wiki/Sears%E2%80%93Haack_body cited 5 April 2025

$$\Gamma_0 = \frac{4L}{\rho_\infty V_\infty b\pi} = \frac{2V_\infty C_L S}{b\pi} \quad (8.40)$$

Following this, the total velocity induced by the trailing edge vortex sheet was determined using Equation 8.41, where a change of variables from the spanwise coordinate y to the angular variable θ takes place to simplify the calculation to a standard integral:

$$w(y_0) = -\frac{1}{4\pi} \int_{-b/2}^{b/2} \frac{(d\Gamma/dy)dy}{y_0 - y} = -\frac{\Gamma_0}{2\pi b} \int_0^\pi \frac{\cos \theta}{\cos \theta - \cos \theta_0} d\theta = -\frac{\Gamma_0}{2b} \quad (8.41)$$

Similar vortex circulation distributions can be obtained for all different flight profiles, as shown in Figure 8.6

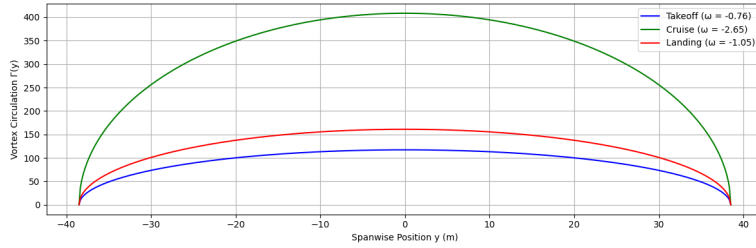


Figure 8.6: Circulation distribution along the wing planform for different flight phases

This proves that the downwash is constant along the lifting line. Having determined this the induced angle of attack (a_i), which decreases the geometric angle of attack to the effective angle of attack ($a_{eff} = a - a_i$) can be determined using $a_i = \arctan(\frac{w}{V_{cruise}})$ [14, Eq. 5.16]. This was determined to be 0.74° , a significant value that should be taken into account in performance calculations, as it directly affects the lift generation and contributes to induced drag.

Furthermore, the freestream turbulent kinetic energy, as well as the free-stream dissipation rate of the airfoil, can also be analytically calculated using empirical relations based on [19]. The specific dissipation rate characterises the rate at which turbulent energy decays. These expressions in Equation 8.42 and Equation 8.43 are useful for initialising turbulence models in CFD simulations:

$$k_\infty = 0.1 \frac{\mu_\infty U_\infty}{\rho_\infty L} \quad (8.42) \quad u_\infty = 10 \frac{U_\infty}{L} \quad (8.43)$$

where μ_∞ is the free-stream dynamic viscosity [Pa·s], U_∞ is the free-stream velocity [m/s], ρ_∞ is the free-stream density [kg/m³], L is the reference domain length [m], k_∞ is the turbulent kinetic energy [m²/s²], and u_∞ is the specific dissipation rate [1/s].

In the case of our aircraft for cruise conditions, the turbulent kinetic energy and the specific dissipation rate are found to be $1.85e-05 \text{ m}^2/\text{s}^2$ and 11.472 s^{-1} respectively.

8.6.2. Initial Engine Plume Characteristics

In order to have an initial estimate of the engine plume characteristics, the centreline velocity decay of the propulsion system was calculated. The centreline velocity decay refers to how the axial velocity at the centre of a jet (along the plume axis) decreases with distance downstream from the engine nozzle.

For this, the engine maximum velocity decay model proposed by Witze [20] was used. This model is applicable over a wide range of both sub- and supersonic jets. The expression for the jet centreline velocity is given as:

$$\bar{u}_c(\bar{x}) = 1 - \exp\left(\frac{-1}{\kappa \bar{x} (\bar{\rho}_e)^{0.5} - X_c}\right) \quad (8.44)$$

where \bar{u}_c is the ratio between the centerline velocity and jet exhaust velocity as a function of downstream coordinate \bar{x} , which is the ratio of axial distance to the radial coordinate at the jet exit. κ is a proportionality constant, $\bar{\rho}_e$ is the density ratio between the external and jet exit flow, and X_c is a non-dimensional correlation parameter for core length. The centerline velocity is normalised by the peak core velocity. The core length parameter X_c was determined by Kleinstein [21] to have a universal value of 0.70. The value of the proportionality constant was determined by the relationship

$$\kappa = 0.08(1 - 0.16M_j)(\bar{\rho}_e)^{-0.22} \quad (8.45)$$

where M_j is the jet exhaust Mach number. It is important to mention that this model assumes it is a single jet (representative of turbojet engines), not the coaxial jets that arise from the high bypass turbofan engines installed on commercial transport

aircraft [20]. Given that the engine selected for the aircraft is a low-bypass turbofan, as explained in Section 11.4, this model was considered appropriate.

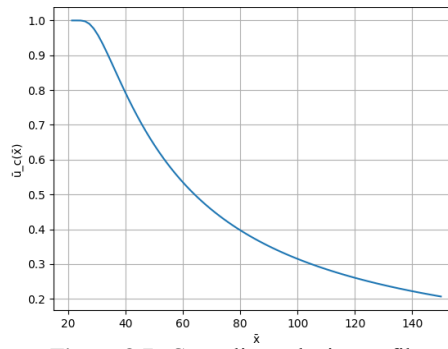


Figure 8.7: Centreline velocity profile

This graph serves as a starting point for an engine plume analysis and particle dispersion model. For this mission’s application, the centreline velocity profile shown in Figure 8.7 illustrates how the injected aerosol that interacts with the engine plume will be pushed further from the wing and slowly decay until mixing with ambient air, which will improve the spreading efficiency of the aerosol.

8.7. Verification and Validation

Contributors: Konstantinos

Just like all design tools used for the design process, unit and system checks were performed for the aerodynamic analysis to assess the function’s implementation into code and the flow of information between them. The coverage of tested functions was high at 91% and 96%, with only the run statements not included, as shown in Figure 18.1.

Requirements verification was also performed; aerodynamics is an important design part for a challenging environment such as the stratosphere, so there are multiple requirements restricting the design. A stakeholder requirement, “REQ-STK-4”, specifies the minimum cruise altitude of twenty kilometres. All cruise performance parameters were derived accordingly to ensure that the twin-body configuration can reach this altitude at MTOM, adjusted by the appropriate fuel fraction. This capability is demonstrated in Chapter 10, where the flight path analysis confirmed compliance with the altitude requirement. Similarly, as shown in Section 18.3, “REQ-SYS-ARD-1.1” is met with the configuration providing enough lift to sustain steady flight. “REQ-SYS-ARD-2”, which constrains drag, is met through an optimised aerodynamic configuration, and “REQ-SYS-ARD-7” with C_L being 0.7. Last but not least, it was proven in Chapter 10 that the stall speed exceeds the limit imposed by “REQ-SYS-ARD-8”. A detailed analysis of all aerodynamic requirements met is found at Section 18.3.

Lastly, validation of the parameters obtained is performed. To achieve that, two measures were taken. Given the unique mission profile and the non-conventional configuration used, it was increasingly difficult to reproduce or obtain from the literature data to validate the aerodynamic parameters against. As a result, reference values from the 2016 DSE project *Stratospheric Aerosol Geoengineering Aircraft (SAGA)* [22] and 2023 DSE project *European Stratospheric Research Aircraft (ESRA)* [23] are included in Table 8.5. All values are compressible at cruise conditions and serve as a validation tool, yet it should be noted that some of the underlying design characteristics differ significantly between the concepts, explaining the discrepancies. Lastly, a validation strategy is also outlined for future work. This refers to the methods and tools that shall be used to validate the data acquired, that include the Stanford University’s SUAVE design tool (discussed in subsection 8.4.2) and the Athena Vortex Lattice (AVL) tool developed by MIT ⁵:

Table 8.5: Validation of Aerodynamic Parameters obtained from DATCOM with reference data

Parameter	Baseline	SAGA [22]	ESRA [23]	[Max. % Discrepancy]	Future Validation Method
$C_{L_{max}}$ [-]	1.292	1.13	1.479	14.5%	SUAVE
$C_{L_{des}}$ [-]	0.87	0.77	0.93	11.5%	SUAVE, AVL
C_{L_0} [-]	0.181	—	0.177	2.2%	AVL
$C_{L\alpha}$ [1/rad]	5.33	6.87	6.1744	28.9%	AVL
α_{stall} [deg]	11.94	8.00	11.30	33.0%	SUAVE
C_{D_0} [-]	0.0039	0.0090	0.0060	130.8%	SUAVE
C_{D_i} [-]	0.018	0.020	—	11.1%	SUAVE

The majority of the results show good agreement between the values obtained in Chapter 8 and those reported in similar

⁵URL: <https://web.mit.edu/drela/Public/web/avl/Accessed: June 15th 2025>

studies from the literature [22, 23]. Notable exceptions include the coefficients C_{L_α} and C_{D_0} . The discrepancy in C_{L_α} can be attributed to differences in the aspect ratio (AR), amount and sizing of fuselage(s) and airfoil selection between the current design and those in previous studies, as indicated by Equation 8.10. Furthermore, according to Dr.J.Roskam [12, Eq.4.32], the lift slope of the wing is lower than that of the selected airfoil. Given that, in subsection 8.2.4, a slope of 5.73 [1/rad] was determined for the 2D scenario, the value of the 3D case indicated in Table 8.5 seems to fall within a reasonable range. The difference in α_{stall} is, then, a direct outcome of the discrepancy in C_{L_α} : lower slope in the lift curve results in higher stall angles achieved. This trend is evident, for instance, in the results from *ESRA*, where the reported α_{stall} closely matches that obtained in Table 8.5, consistent with its relatively low C_{L_α} . Regarding C_{D_0} , it is highly configuration dependent and strongly influenced by the geometry of the aircraft. The lower fuselage diameter (d_f) and higher AR of the baseline design explain the obtained lower C_{D_0} compared to the literature values.

8.8. Sensitivity study

Contributors: Konstantinos

Given the preliminary nature of the analysis, a sensitivity study was performed to establish the extent of the volatile nature of the design. Three variables were varied. To begin with, the t/c of the airfoil section was varied, and the change in wing weight was quantified. The range was taken from 0.12 to 0.16, as determined in Section 8.2 to be feasible for the cruise conditions. The results are shown in Figure 8.8, where it is evident that for increased t/c the weight decreases, as more area is moved away from the neutral axis and the bending criteria are met with lower mass. Similarly, the taper ratio was varied from 0.25 to 0.6, a suitable range suggested for conventional planforms by Raymer [9]. In this case, the weight of the wing increases unboundedly with an increase in λ . Notice, however, that for both cases the change is not significant, accounting for a bit more than 10% of the total wing weight, indicating that these parameters are not primary drivers in the design process.

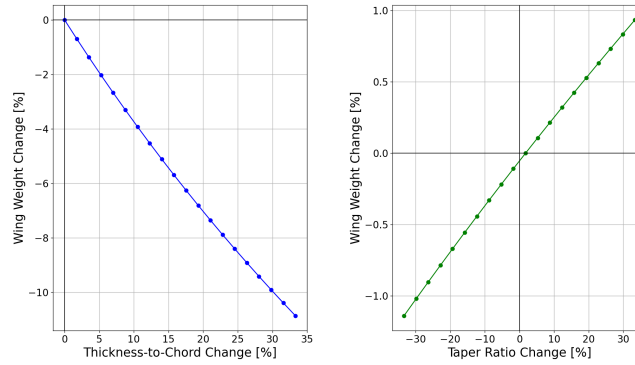


Figure 8.8: Sensitivity analysis of the wing weight in response to variations in thickness-to-chord ratio (t/c) and taper ratio (λ).

Similarly, M_{cruise} was varied and its effect on various aerodynamic parameters quantified. In Section 8.1, it was determined that M_{crit} is 0.735, so it was decided that cruise will happen slightly below, at 0.7. To quantify the effect of this choice, the aforementioned value was varied by ± 0.1 , resulting in a M_{cruise} between [0.6, 0.8]. The effect of varying the M_{cruise} on various parameters is plotted at Figure 8.9:

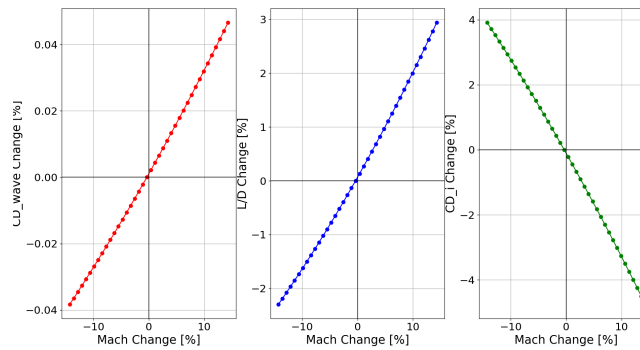


Figure 8.9: Sensitivity analysis of aerodynamic parameters in response to variations in M_{cruise} .

Again, it is evident that varying the cruise Mach number has little effect to most of the aerodynamic parameters, with the maximum % change recorded being about 5% for the lift dependent drag (specifically, $C_{D_{ides}} + C_{D_{wl_{des}}}$). Interestingly, this value tends to decrease as the Mach number increases, primarily due to the reduction in $\beta = \sqrt{1 - M^2}$, the compressibility correction factor.

Payload Analysis

Stratospheric aerosol is the main mission goal of the aircraft. Thus, the aerosol injection system must be designed to maximise the positive climate effects while minimising the uncertainties and risks. This chapter describes the design of the injection system, starting from the choice of aerosol in Section 9.1. Then the system design is explained in Section 9.2. Lastly, verification and validation of the analysis and the design is performed in Section 9.3, followed by a sensitivity analysis that determines the effects of varying injection rates in Section 9.4.

9.1. Aerosol Material

Contributors: Inés

The selection of a suitable solid aerosol is critical to achieve the desired results with a minimal negative environmental impact and optimal injection characteristics. Alumina (Al_2O_3) and calcite (CaCO_3) exhibit the most promising properties, particularly due to the more efficient scattering of solar radiation and a reduction in terrestrial infrared radiation absorption [3]. Additionally, a lower stratospheric burden is needed to achieve the same radiative forcing for these aerosols. There is evidence that shows that these solid aerosols might have a very small effect on ozone depletion. However, large uncertainties exist due to heterogeneous chemistry on solid particles [4].

Calcite has been selected as the payload for this mission, rather than alumina, due to its more favourable characteristics. Calcite shows lower stratospheric temperature increases, around 0.6 K per W/m^2 compared to alumina's 1.1 K per W/m^2 , and has a slightly lower atmospheric burden [3]. Additionally, although there are significant uncertainties regarding ozone depletion, calcite is more likely to lead to positive ozone change, whereas alumina carries a greater risk of ozone depletion.

Furthermore, a big difference was determined in the required amount to be injected annually, which would increase the fleet size and therefore the costs of the mission. For a -1.0 W/m^2 , 5.7 Mt/yr are needed for calcite, while 7.5 are needed for alumina [3]. Based on the cost values for different aerosols, alumina has a cost of \$ 400 per ton [24], while calcite has a cost of \$ 350 per ton [24]. This seems like a small difference, but on the megaton scale, this would lead to a difference of 50 million dollars.

Concerning the abundance of aerosols, calcite also presents a significant advantage. According to Neukermans *et al.* [4], calcium carbonate is mined at a rate of about 15 billion metric tons. The necessary amount of 6Mt aerosol is thus less than 0.04 % of the annual mined quantity. In comparison, alumina production in 2024 was 142 Mt globally [25]. Thus, a significant amount of about 5% of the current annual global production would be used for the SAI mission, assuming 7.8 Mt of alumina to achieve the desired radiative forcing.

On the downside, choosing calcite as the aerosol for this mission also introduced a significant challenge. The production and dispersion of calcite nanoparticles of the desired diameter of around 240 nm faces a number of difficulties. These are mostly related to calcite's sticky property, which causes particles to agglomerate, thus exceeding the desired particle size. So far, the production of the desired particle size distribution has not been successful. For that reason, this mission depends entirely on the possibility of developing and scaling this technology on time.

Consequently, a fallback plan was established to address the scenario in which the fluidisation technology aiming to avoid agglomeration of these particles is not developed on time or ultimately proven to be unfeasible. It was decided that in case the ideal particle size for calcites cannot be achieved, alumina would be the substitute payload. This would entail some changes in the operations that were taken into account in Section 19.4.

9.2. Aerosol Dispersal

Contributors: Inés, Maxine

Based on the fluidisation criteria defined by Geldart (1973), CaCO_3 falls under Group C, characterised by particles that are extremely difficult to fluidise [4]. For this reason, a specialised fluidisation method for calcite was selected to achieve successful dispersion, consisting of a fluidised bed incorporating mechanical vibration and acoustic agitation. The acoustic waves impact the base of the generator, causing a rubber dam to oscillate and lift particles into suspension [5], as visualised in Figure 9.1. Additionally, as proposed by the group led by V. Fay McNeill at Columbia University, carbon steel balls (OnlineMetals, 0.1875" diameter, alloy 1018) are added to assist in breaking down particle agglomerates [5].

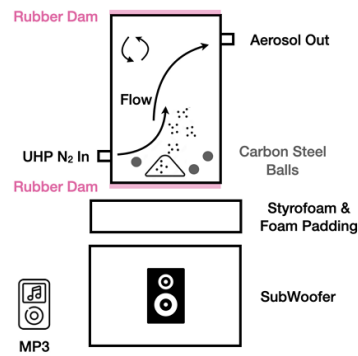


Figure 9.1: Generator for fluidisation of calcite[5]

Contrary to the approach proposed by the McNeill group, this mission will use ambient stratospheric air to fluidise the aerosol instead of nitrogen. This avoids the need to carry large quantities of pressurised nitrogen onboard, which would significantly increase the weight of the injection system.

Experimental trials demonstrated the generator's stability during repeated daily operation for six hours, without significant changes in aerosol output concentration or particle size distribution. This indicated good system reliability and potential for scale-up within this time frame [5]. Additionally, performance peaks were observed in the 70–80 Hz frequency range.

Once fluidised, the aerosol is routed through nozzles placed along the aircraft wing and horizontal stabiliser. The position of the nozzles was chosen to avoid injecting the SA in the wake of the aircraft. The nozzle selected for this application is a two-fluid atomising nozzle proposed by Neukermans *et al.*, specifically the Schlick Model 940 Form 6, shown in Figure 9.2 [4]. The additional air inlet helps further de-agglomerate particles at the nozzle exit by inducing swirl and promoting particle collisions. To minimise clogging and particle adhesion, stainless steel was the material chosen for these nozzles, which offers low surface adhesion to the calcium carbonate particles.

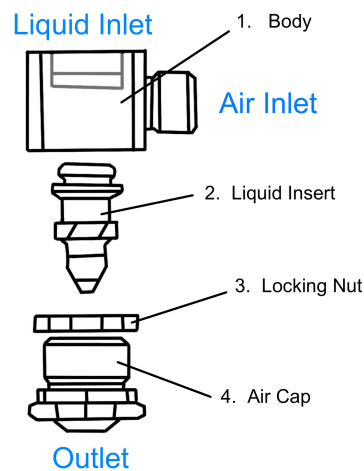


Figure 9.2: Schlick Model 940 Form 6 two-fluid nozzle, where the liquid inlet is the fluidised aerosol [4]

A pulsed spray system was initially considered, in which a valve opens for 0.2 seconds at 1-second intervals. While this method reduces clogging risk, it decreases the injection rate by a factor of five, reducing the total injection rate of the aircraft to an unacceptable extent. Discarding the pulsed spray mechanism, at a pressure of 40 psig, the mass delivery rate of calcite can reach at least 0.4 g/s per nozzle, as reported by Neukermans *et al.*[4]. This value was decided to represent the lower boundary of the injection rate for this mission, since this experimental value is obtained with a simpler fluidisation technology than the one proposed above.

Based on this lower boundary, the parameters shown in Table 9.1 were calculated. To estimate the total injection rate the aircraft can achieve, the maximum number of nozzles was first determined. This estimate was obtained by dividing the total span of the wing and horizontal stabiliser by the nozzle width, since injection through both the wing and the horizontal stabiliser was decided to maximise the injection rate of the aircraft. The total injection rate is then the product of the maximum number of nozzles and the nozzle mass flow rate.

The maximum number of nozzles per generator was estimated based on a liquid (fluidised) aerosol flow rate of 25 L/min for this lower boundary scenario [4]. The generator proposed by the McNeill group has a volume of 15 L. Assuming this generator volume can be replenished every second, the number of nozzles per generator was calculated as:

$$n_{\text{nozzles/generator}} = \frac{V}{\dot{m}} \quad (9.1)$$

where V is the generator volume and \dot{m} is the flow rate of the liquid (fluidised) aerosol. The total number of generators is then the total number of nozzles divided by the number of nozzles per generator.

An estimated generator mass of 30 kg was calculated based on the parts specifications found in Neukermans *et al.* [4]. The nozzle mass was conservatively estimated by assuming it has a cubic shape with dimensions 40x40x47 mm, as specified by the manufacturer ¹, with a density of 7.93 g/cm³, corresponding to stainless steel. This resulted in a mass of approximately 0.6 kg per unit. The total mass was therefore calculated using a generator mass of 30 kg and an approximate nozzle mass of 0.6 kg, which is a conservative estimate.

The total power was estimated taking into account the power needed for the aerosol to be pumped to the generators, as well as the power needed to operate the subwoofer. The subwoofer power is specified to be 150 W [5], which was then multiplied by the total number of generators to obtain the final value. A buffer of 10 % was added.

It was decided that the fleet size will have a buffer of 10% to leave spare aircraft in case an operating aircraft is grounded for maintenance and needs to be replaced, or if additional aircraft are needed due to delays. For the initial delivery of 0.5 Mt of CaCO₃ per year, with 250 operational days, and for a 17,000 kg payload per aircraft, 3 flights per day per aircraft would be needed. A fleet of 54 aircraft would be required for the initial stage of the mission for this injection rate. Later on, for the delivery of 6 Mt of CaCO₃ per year, a fleet of 641 aircraft was required.

Table 9.1: Lower boundary injection rate scenario

Parameter	Value
Maximum Number of Nozzles	2232
Injection Rate (per aircraft)	0.93 kg/s
Number of Nozzles per Generator	36
Number of Generators	65
Total Injection System Mass	3198.6 kg
Total Power of Injection System	13.12 kW
Cruise Time	4.11 hours

The upper boundary of the injection rate was determined for the same technology, assuming a higher injection efficiency may be achieved by increasing the calcite to carrier ratio. To determine a larger, but achievable ratio, the inter-particle interactions were first considered. Since the calcite particles were assumed not to be charged, there will be no electrostatic repulsive force working on the particles. Thus, only the Van der Waals forces are considered in this estimation. Here, Equation 9.2 represents the van der Waals energy W between two spherical particles of radius R_1 and R_2 in air when $R \gg h$ is not valid [26].

$$W(h) = -\frac{A}{6} \left\{ \frac{2R_1R_2}{(2R_1 + 2R_2 + h)h} + \frac{2R_1R_2}{(2R_1 + h)(2R_2 + h)} + \ln \frac{(2R_1 + 2R_2 + h)h}{(2R_1 + h)(2R_2 + h)} \right\} \quad (9.2)$$

Here h is the distance from the surface to the surface of the spheres and A is Hamaker's constant, which is equal to $10.1 \cdot 10^{-20}$ J for calcium carbonate [27].

To determine the minimum distance between the particles, the distance at which the random motion due to thermal effects "wins out" over the attractive energy was determined as suggested by Israelchvili [26]. This is described by Equation 9.3

$$W(h) < kT \quad (9.3)$$

Here, k is the Boltzmann constant and T is the temperature at the operational altitude of 20 km, which is equal to 216.7 K. Solving Equation 9.3 for h results in $h > 64.02$ nm.

Due to the presence of Brownian motion in the mixture, particles will not remain in their respective location. To estimate the displacement caused by this motion, the diffusion coefficient D was calculated using Equation 9.4 [28].

$$D = \frac{kT}{6\pi R\eta_L} \quad (9.4)$$

Where η_L is the viscosity of the liquid, which is equal to $1.42 \cdot 10^{-5}$ Pa·s for air. The diffusion coefficient is thus equal to $8.94 \cdot 10^{-11}$ m²/s. Then, the displacement of the particle was estimated using the root mean square in function of time as described in Equation 9.5 [28].

¹URL: <https://myschlick.com/produkte/modelle/zweistoff/940> Cited 12 June 2025

$$\bar{x} = \sqrt{6Dt} \quad (9.5)$$

The average displacement \bar{x} over a time frame of 1s is then 23163 nm. As this is much larger than the minimum distance between particles as calculated based on the Van der Waals energy, a suitable distance between particles was determined based on experimental results as described by the McNeill group [5]. Using an equivalent ratio of distance between particles to average displacement due to Brownian motion resulted in a distance between particles of 1817 nm at an altitude of 20 km with a temperature of 216.7 K. This deduction in temperature allowed for a slightly denser packing of the aerosol mixture, as particles move more slowly. Assuming an average particle diameter of 250 nm, this resulted in a density for the mixture of 0.0025 g/cm³ of calcite. Using the chosen nozzle, this resulted in a total flow rate of 1.05 g/s of calcite per nozzle. The corresponding values were then calculated for this upper boundary scenario using the same methods described above, and the results are shown in Table 9.2. In this case, the cruise time is significantly reduced given the increase in injection rate, allowing the operations to increase to 5 flights per day, which translates into a smaller fleet size consisting initially of 33 aircraft, and 385 for the final phase .

Table 9.2: Upper boundary injection rate scenario

Parameter	Value
Maximum Number of Nozzles	2232
Injection Rate (per aircraft)	2.33 kg/s
Number of Nozzles per Generator	36
Number of Generators	65
Total Injection System Mass	3198.6 kg
Total Power of Injection System	13.3 kW
Cruise Time	1.64 hours

Given that the lower boundary of the injection rate was based on experimental data using low-tech setups, the upper boundary was still considered an achievable injection rate. This decision was supported by the fact that the obtained values are derived from experimental results reported by the McNeill group, which have been recalculated to reflect the specific conditions of our stratospheric flight regime. As previously discussed, the lower temperatures in the stratosphere enabled slightly denser packing of the aerosol mixture.

9.3. Verification and Validation

Contributors: Maxine

Most calculations related to the analysis are grounded in physical principles. Therefore, the verification procedure of the model focused on ensuring the correct implementation of these physical relationships and equations in the code. This was primarily achieved through unit tests, where the individual functions were systematically checked. These tests included checking the outputs through hand calculations for both unit and random input values. Additionally, the correct implementation of tasks within the code and integration within the model was checked through integration tests to ensure data flows through the code as expected.

As the injection system is fully based on novel technology, the validation of the simulated results, such as injection rates, system mass and power usage, was limited. Comparing values of similar components from experiments performed by the McNeill group [5] and Neukermans et al. [4] to the simulated results provided a sanity check, which aided in ensuring values are within the expected range. Here, Neukermans et al. [4] achieved an injection rate of 0.4 g/s per nozzle using a low-tech system; thus, the simulated injection rate of 1.05 g/s per nozzle was determined to be within a reasonable range. Additionally, the sensitivity analysis as described in Section 9.4 aided in quantifying the effects of uncertainties on crucial parts of the design, thus allowing for a higher confidence in the theoretical results obtained. However, as similar systems have not been established, testing must be performed to validate performance, such as the real achieved injection rates and power usage.

9.4. Sensitivity Study on Injection Rate

Contributors: Inés, Barnabás

Given that the injection rate was based on theoretical estimations, a slight change in the final injection rate might occur. A modification to the injection rate directly impacts a number of critical design parameters in the aircraft, most importantly, the optimal payload-to-fuel fractions and cruise time. For this reason, the plot for payload-to-fuel fraction against payload mass for different injection rates is shown in Figure 9.3, to visualise the loss in efficiency of the design in the case that the injection rate changes.

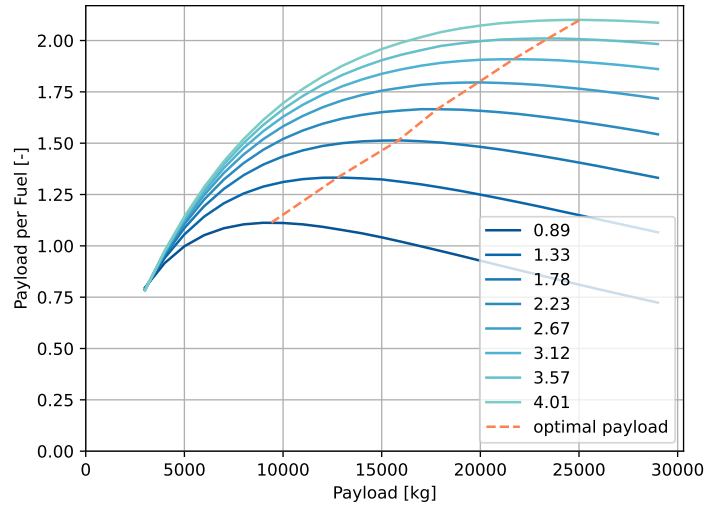


Figure 9.3: Payload-to-fuel fraction against payload mass for different injection rates

In this case, a fixed value for the weight of the injection system is assumed. Since the injection rates considered are relatively low, the maximum number of nozzles and generators will always be the most optimal decision, so this will be fixed.

As shown in Figure 9.3, a higher injection rate enables the aircraft to carry a higher payload while still maintaining the optimal payload-to-fuel ratio. This is easily visualised by the graph's peak shifting toward the top right corner as the injection rate increases. At the same time, a higher injection rate leads to a change in the cruise time, which directly translates to more flights per day, significantly diminishing the fleet size as well as the costs of the aircraft fleet. The sensitivity of the injection rate to the costs of the aircraft can be visualised in Figure 9.4.

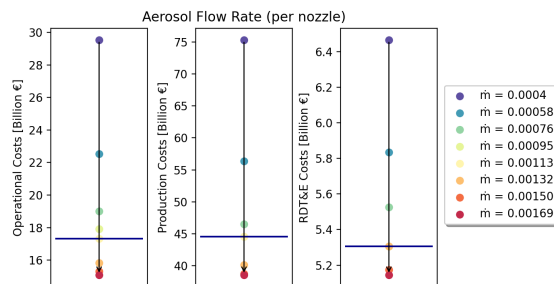


Figure 9.4: Sensitivity Injection Rate

This sensitivity study showed the importance of the investment in the development and scalability of CaCO_3 fluidisation technology to achieve higher injection rates. Increasing efforts in this technology development would make this mission's implementation much more affordable for governmental organisations. Furthermore, it would enhance the overall efficiency of the operations and logistics.

9.5. Discussion of Assumptions and Uncertainties

The design of the injection system was based on a series of assumptions and uncertainties. First of all, it was assumed that the right particle size range can be achieved. Currently, no experiments using these technologies are able to produce the desired particle sizes, however, as technologies are still in the early stages, it was assumed that this would be achievable as technology matures. Additionally, it was assumed that, even in continuous operation, the aerosol would not clog without the use of the pulsed spray system. However, if clogging does occur, this assumption could lead to a significant reduction in the injection rate, as the pulsed spray system would then need to be implemented. Lastly, the assumption that 36 nozzles may be connected to one generator was determined based on the assumption that the required mass for fluidisation could be replenished every second. In the case that this would be an overestimation, more generators could be added the aircraft given the large available volume inside the wing. The number of generators could be increased to 320, for which in this case 7 nozzles would be connected to each generator. However, this would increase the payload system mass by 7650 kg, and would thus reduce the amount of calcium carbonate powder carried per flight, so more flights per day would be required, increasing the fleet size. In conclusion, this preliminary design contains some assumptions that may be significantly improved with further analysis and as technology matures, as well as some changes to the current design.

Flight Performance

A typical mission of the design consists of multiple different phases, which will all be analysed separately throughout the sections following in this chapter. This includes take-off and landing procedures in Section 10.1 as well as climb and descent in Section 10.2. Based on the calculations done, a payload-range diagram was made in Section 10.3, and an optimal flight profile was determined in Section 10.4. Then, the design tools are validated, and compliance with the different system, stakeholder and airworthiness authorities requirements is verified in Section 10.5. At the end of this chapter in Section 10.6, a sensitivity study is done.

10.1. Take-off and Landing Performance

Contributors: Bas

The take-off distance of the design is made up of three parts: the ground run, transition and climb-out phases distances. These distances were calculated with Equation 10.1 to Equation 10.3 respectively.

$$s_g = \frac{V_{lof}^2}{2\bar{a}} \quad (10.1) \quad s_t = \frac{V_{lof}^2}{(n-1)g} \sin \gamma_{cl} \quad (10.2) \quad s_{cl} = \frac{h_{scr} - \frac{V_{lof}^2}{(n-1)g} (1 - \cos \gamma_{cl})}{\tan \gamma_{cl}} \quad (10.3)$$

As shown in Equation 10.1, the ground run distance s_g depends on the average acceleration, \bar{a} . This average acceleration follows from a balance of forces and was calculated using Equation 10.4. As shown by the equation, the average acceleration was calculated using the average thrust, drag and lift, which in turn were calculated using the average velocity; $\bar{V}_a = V_{lof} \sqrt{2}$. The friction coefficient μ depends on the tires and contact surface, and was assumed to be 0.04 following from [29].

$$\bar{a} = \frac{g}{W} (\bar{T} - \bar{D} - \mu (W - \bar{L})) \quad (10.4)$$

The computed value of \bar{a} , which was based on the current $C_{L_{TO}}$ without flaps, and with the high thrust of the engine determined in Chapter 11, showed that the aircraft could still accelerate rapidly enough to reach take-off speed within the required runway distance, even without flaps. So, no flaps were required and were thus omitted to reduce weight, drag and complexity.

The total take-off distance is then the sum of the three distances calculated in Equation 10.1 to Equation 10.3, which resulted in a final distance for s_{to} of 527.7 meters. This distance is relatively short, and can be explained by the fact that the thrust-to-weight ratio for the design is significantly higher than commercial aircraft caused by the high sea-level thrust required due to the 20 km high cruise phase. This allowed for a higher acceleration and climb angle, which shortened the total horizontal take-off distance required. The computed take-off distance is lower than the limit set by stakeholder requirement 'REQ-STK-7'; this requirement is thus complied with for the take-off phase.

A similar analysis was done for the total landing distance, which consists of four different phases: approach, flare, de-rotation and deceleration. These distances were calculated with Equation 10.5 to Equation 10.8 respectively.

$$s_{app} = \frac{h_{scr} - h_{fl}}{\tan \gamma_{gs}} \quad (10.5) \quad s_{fl} = R \sin \gamma_{gs} \quad (10.6) \quad s_{rot} = V_{app} \Delta t_{rot} \quad (10.7) \quad s_{dec} = \frac{V_{app}^2}{2\bar{a}} \quad (10.8)$$

In these equations, h_{scr} followed from CS-25[13] and was set to 15.2 meters (50 feet), as well as the glide slope γ_{gs} , which was set to -3 degrees. The total landing distance was again the sum of these four distances, which resulted in a final distance for s_{ld} of 1,522 meters. This is lower than the constraint set by 'REQ-STK-7', thus showing compliance with the requirement.

10.2. Climb and Descent Performance

Contributors: Bas

The climb phase of the mission is a fuel-intensive stage, while the aerosol is not yet disposed. The length of this part of the mission, therefore, must be minimised, which will be done by climbing at the maximum Rate-of-Climb (ROC). This means that the aircraft will climb at its maximum vertical rate, which happens at the maximum vertical speed V_y . The ROC was determined by the difference in available power and required power, as shown by Equation 10.9.

$$ROC = V \sin \gamma = \frac{P_a - P_r}{W} = \frac{TV - DV}{W} \quad (10.9)$$

To maximise the ROC, the power required needs to be minimised, where P_r is equal to the drag multiplied by the aircraft velocity. To do so, $C_L^{3/2}/C_D$ had to be maximized. From this, the relations in Equation 10.10 and Equation 10.11 were found.[12]

$$C_{L_{ROC,max}} = \sqrt{3C_{D_0}\pi Ae} \quad (10.10)$$

$$C_{D_{ROC,max}} = 4C_{D_0} \quad (10.11)$$

As altitude increases, the excess power decreases, therefore lowering the ROC. At a specific altitude, the ceiling altitude, the ROC reaches zero, and the aircraft is unable to climb any more.

The time the climb phase lasts before the aircraft reaches the cruise altitude was found by calculating the ROC at small intervals along the climb, and then integrating these ROC values over the climb height, as shown in Equation 10.12.

$$t_{climb} = \int_0^h \frac{1}{ROC} dh \quad (10.12)$$

It was found that the climb phase to the initial cruise altitude of 20 km takes 26.3 minutes. A significant part of this time is spent in the last 5 km of the climb, where the optimal speed increases above the maximum cruise speed of Mach 0.7. At this point, the ROC decreases significantly, as the speed has to be kept around this cruise speed to prevent a huge increase in drag due to shock waves forming (which would further reduce the ROC).

In addition to the rate of climb and time to climb, the angle of the climb, the climb gradient also had to be calculated. Instead of the rate of climb, which maximises the vertical speed, the climb gradient is maximum for covering the largest vertical distance in the shortest horizontal distance. This climb gradient is important for clearing obstacles such as buildings or mountains, and was calculated using Equation 10.13, with G being the climb gradient.

$$G = \sin \gamma = \frac{T - D}{W} \quad (10.13)$$

Using this equation, the climb angle just after take-off at maximum take-off mass was found to be 19.2 degrees. This is a rather steep climb angle, which can again be explained by the relatively large thrust-to-weight ratio of the design.

A similar procedure was followed for the approach phase. The glide angle is strictly regulated by airworthiness authorities [30, Regulation 2-6-2], with a standard value of 3° , which may be increased by up to 0.2° without requiring special approval. A steeper descent angle of $\gamma_{app} = 3.2^\circ$ is considered optimal, as it enables noise reduction by keeping the aircraft at a higher altitude for a longer portion of the descent. In this analysis, the glide path descent was treated as the limiting case where the thrust (T) was assumed to be zero in Equation 10.13.

Without the use of spoilers, the aircraft was found to achieve a descent angle of -1.1° at approach speed, at the required C_L and thus C_D , which does not reach the allowed regulatory limit of -3.2° . To meet this, Equation 10.13 was simplified to $\sin(-3.2^\circ) = \frac{-D}{W}$, which was used to size the spoilers. A drag force of 6 kN was determined, and the excess drag found (i.e. the difference between this value and the drag in the spoiler-free configuration) was attributed to the spoilers. This spoiler drag was then normalised to obtain the drag coefficient C_{D_s} , and the spoiler surface area S_s was calculated using Equation 10.14 [31]. From the same source, a typical deflection for a spoiler was considered between 30° to 90° , with the lower limit used as the limiting case, which will be the setting used during descending. The 90° setting will only be used during landing after touchdown to reduce lift and increase drag as much as possible. Lastly, V_{app} was taken as $1.3 \cdot V_{stall}$ [32, p.748]:

$$\frac{D_{difference}}{0.5 \cdot \rho \cdot V_{app} \cdot S_w} = C_{D_s} = 1.9 \sin(\delta_s) \frac{S_s}{S_w} \quad (10.14)$$

Having determined the required surface area, sizing could take place using $S_s = b_s \cdot c_s$. Dieter Scholz suggests in “Aircraft Design” [32] that the chord of the spoiler can be estimated to be 20% of the c_{root} , which resulted in a c_s of 0.72 meters and a spoiler span b_s of 8.9 meters. Last but not least, the deployment of spoilers resulted in a 12% decrease in the $C_{L_{Land}}$ as was found using Equation 10.15:

$$\Delta C_{L_s} = -C_{L_{Land}} \cdot \frac{b_s}{b_{wing}} \quad (10.15)$$

This decrease in lift was used in Section 10.1, as this decrease in lift means the aircraft pushes harder into the ground, decelerating the aircraft slightly quicker as shown in Equation 10.4, which decreases the total landing distance.

10.3. Payload Range

Contributors: Bas

The range of the design was analysed using the Breguet formula, shown in Equation 10.16, where c_j is the jet thrust coefficient which followed from the propulsion analysis in Section 11.4 and $\frac{W_4}{W_5}$ is the cruise phase fuel fraction. This fuel fraction was analysed for different aircraft weight compositions, by varying the fuel and payload masses. This then resulted in the payload-range diagram shown in Figure 10.1.

$$R = \left(\frac{V}{g \cdot c_j} \right)_c \left(\frac{L}{D} \right)_c \ln \left(\frac{W_4}{W_5} \right) \quad (10.16)$$

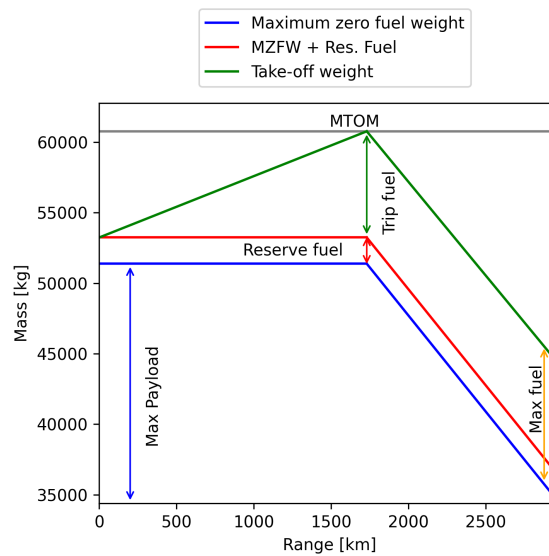


Figure 10.1: Payload range diagram showing aircraft mass composition for increasing range

The plot shows the increasing range for increasing fuel mass, up until the point where the maximum take-off mass is reached. After this point, the range is increased further by decreasing the amount of payload mass brought on board. Payload is thus traded in for additional range beyond the design range. Usually, a third section is present in between the two regions in Figure 10.1, where payload mass is traded in for additional fuel mass. However, for this design, the fuel mass required for a complete mission where the maximum amount of payload is distributed was taken as the maximum fuel mass the fuel tanks should be able to carry. No additional fuel can therefore be loaded into the aircraft once the maximum take-off mass has been reached, even if payload mass is removed.

The final range with no payload present is also called the ferry range, which is the range the aircraft can reach in case it needs to be relocated to a different airbase, and was found to equal 2,978 km. The point at which the aircraft will operate during a standard mission is the point of maximum payload mass and maximum take-off mass. This is the design point, or the point of maximum productivity[33]. At this point, the most aerosol can be brought up into the stratosphere while having enough fuel mass on board to inject all of the payload into the air. This point gives a design range of almost 1,800 km.

10.4. Flight Profile

Contributors: Bas

The flight profile shows the mission altitude that will be flown during the mission. The flight profile is shown in Figure 10.2. The flight profile is created based on the design point in Figure 10.1, meaning that the aircraft will be loaded to maximum take-off mass, as well as maximum payload mass.

As fuel is burned and solid aerosol is injected into the stratosphere, the total mass of the aircraft decreases. When the weight of the aircraft decreases, it requires less lift to fly, allowing the aircraft to fly higher at lower densities. This is both more efficient for the fuel consumption (as determined in Chapter 11), as well as for the payload, as the injected aerosol will stay in the stratosphere longer if injected at heights higher than 20 km. As the aircraft can not continuously slowly climb upwards due to other possible SCAI aircraft traffic nearby and ATC orders assigning specific flight levels, the cruise phase is instead divided into two sections, where for the second section, the aircraft will be lighter, and thus fly at a new, higher altitude for this section. This step-climb has the added benefit that the aerosol spread during the second cruise leg on the way back to the airbase is spread significantly above the aerosol spread during the first cruise leg, reducing agglomeration between the aerosol particles. For each section, the achievable height for the current mass at the start of the section was

calculated, which will be the height the section will be flown at. The start of the cruise section is flown at a lift coefficient C_L close to $C_{L_{max}}$. As fuel is used and payload is distributed, the aircraft's weight decreases. The C_L required to sustain flight thus decreases, until the point where the aircraft has flown the first leg of the mission and the returning flight leg back to the airbase starts. A climb phase and corresponding fuel fraction to the height of the returning cruise section were calculated. The mass lost during the climb phase increases the possible height of the second cruise phase until the change is insignificant. This determined the height of the second cruise phase, which was found to be 21.7 kilometres. A powered descent phase was calculated for a descent slope of -4.5° , followed by a worst-case loiter phase at a height of 3 km and for a time of 45 minutes, as described by CS-25 regulations [13]. Finally, the descent phase to the airbase was calculated for a glide slope of -3.2° , as explained in Section 10.2. The final flight profile is shown in Figure 10.2. The data for each flight phase is also given in Table 10.1. This flight profile shows the worst-case scenario where a maximum loiter phase of 45 minutes is required. In the case that the aircraft can land almost directly without a loiter or diversion phase, only one descent phase from cruise stage 2 to the airport is required.

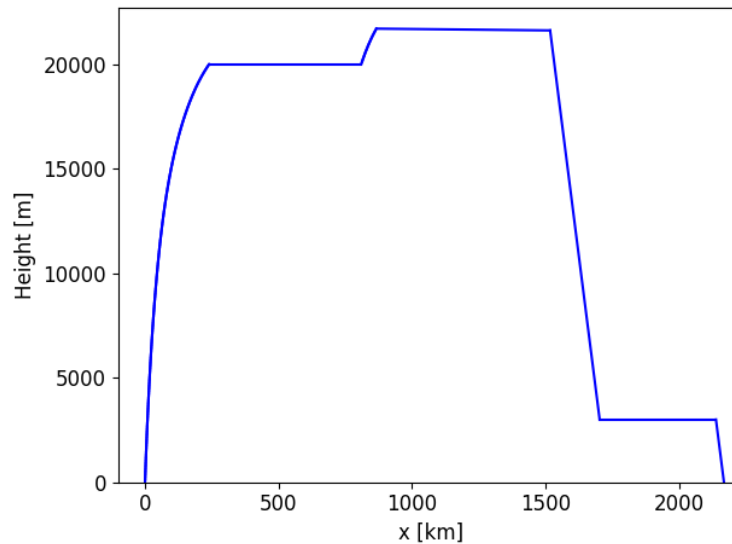


Figure 10.2: Full payload and fuel flight profile including a loiter phase

Table 10.1: Flight profile phases data

Phase	Height [km]	Length [km]	Total distance [km]	Time since take-off [min]
Initial climb	0 → 20	240.2	240.2	26.3
Cruise stage 1	20	557.8	798.0	72.3
Climb to stage 2	20 → 21.7	61.8	859.8	74.13
Cruise stage 2	21.7	626.6	1,486.4	127.5
Descent to loiter altitude	21.7 → 3	185.5	1,671.9	141.8
Loiter	3	436.4	2,107.4	186.8
Final descent	3 → 0	29.9	2,137.3	188.9

10.5. Verification & Validation

Contributors: Bas

For the flight performance calculations, the equations used were not difficult to implement in code. However, a challenge arose in keeping track of the many different values for parameters such as the velocities, lift and drag coefficients and masses. The script is therefore thoroughly verified to ensure the model equations are correctly implemented, and the correct values for the mentioned parameters are used.

Verification of the flight performance code was done using unit tests, which were mostly based on hand calculations with simple values. Certain important edge cases were also tested to ensure the program remains functioning correctly. Each test ran successfully, resulting in a final code coverage of 96%. Only the initial run statements were not covered.

Additionally, compliance with all requirements was verified with the results from the flight performance calculations. These requirements partly follow from the mission and constrain the take-off and landing distance as well as the ceiling altitude. Additional requirements follow from regulations related to diversion procedures and one-engine-inoperative performance.

To start off, the take-off and landing distances are constrained by REQ-STK-7 to 2500 meters. As shown in Section 10.1, certain constants such as screen height, rotation time and glide slope angle follow from CS-25 requirements. Additionally,

CS-25 differentiates between dry and wet runways; the take-off and landing distances were therefore calculated for two different friction coefficients μ . For take-off, the ground friction was assumed to be 0.03 for a dry surface and 0.05 for a wet surface. For landing, the brake friction coefficient was assumed to be 0.4 for dry conditions and 0.25 for wet conditions. All values were found in [29]. For take-off, the one-engine-inoperative distances were also calculated. Due to the relatively large thrust-to-weight of the design, even in a one-engine-inoperative scenario, the remaining engine does not need to run at a 100% throttle setting. As flying with one engine out creates a large yawing moment due to the total thrust not being inline with the x-axis any more, the vertical stabilizer needs to account for this yawing moment and is thus one of the sizing conditions in Section 12.3. To reduce this yawing moment as much as possible, the remaining engine will be throttled back to the minimum thrust setting required to meet the take-off and later also gradient of climb requirements. This finally resulted in the values shown in Table 10.2, with a one-engine-inoperative thrust of 0.17 times the maximum thrust (the remaining engine is thus operating at a 34% thrust setting). As shown in the table, all distances are less than 2500 meters, showing compliance with REQ-STK-7.

Table 10.2: Take-off and landing distances for different circumstances

Condition	Distance [m]
Dry take-off with both engines	528
Wet take-off with both engines	531
Dry take-off with one engine (at 34% throttle)	2,219
Wet take-off with one engine (at 34% throttle)	2,394
Dry landing	1,521
Wet landing	2,108

Next, compliance with the ceiling altitude requirement of twenty kilometres following from REQ-STK-4 was checked. The ceiling altitude is defined as the point where the rate of climb reaches zero meters per second. This ROC was calculated using the procedure shown in Section 10.2, for the weight at the start of cruise. For this, a fuel fraction at the start of cruise of 0.87 was used, based on taxiing, take-off and climb fuel fraction calculations. This resulted in plot Figure 10.3, showing the ROC for altitudes up to 20 km. As can be seen in the figure, the rate of climb is higher than zero at the required height of 20 kilometres, showing compliance with REQ-STK-4.

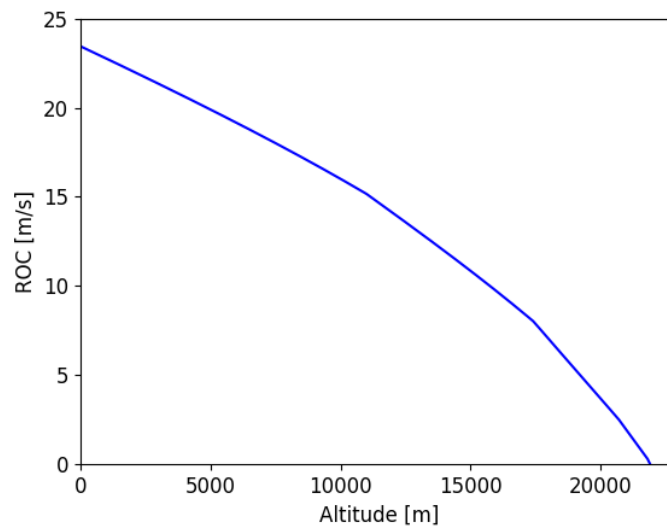


Figure 10.3: Rate of Climb varying with altitude

After checking the compliance with the system requirements, compliance with the CS-25 regulations [13] was checked. One of the CS-25 requirements concerns the climb gradient with only one out of two engines operative. A minimum climb gradient is required for the various phases of the take-off procedure to ensure the aircraft can clear obstacles even in the case of this emergency. As explained in the paragraph checking compliance with the take-off distance requirement, the remaining engine during a one-engine-inoperative scenario is throttled back to the minimum required thrust level to meet the requirements, to reduce the yawing moment created by the single engine as much as possible. It was found that to meet all take-off and climb requirements, a thrust of 0.17 times the maximum thrust is needed, meaning a thrust setting of 34% for the remaining engine. The possible climb gradient was calculated for the take-off phases with landing gear extended, retracted and end of take-off, as well as the en-route climb and approach phases. The climb gradient was calculated using the approach explained in Section 10.2. For the first take-off phase and approach phase, an additional 0.015 was added to the total $C_{D,0}$ due to the extended landing gear[34]. For each phase, a thrust of half the total maximum thrust was used,

which assumes one engine does not produce any thrust while the other engine runs at maximum capacity. Each gradient of climb was calculated for maximum take-off mass, except for the approach phase, for which a landing mass of maximum take-off mass minus the payload and half the fuel mass was used. For the end of the take-off phase, a height of 457 meters is used in accordance with requirement CS-25.111(a)[13]. The resulting gradients of climb together with the required climb gradients from CS-25 [13] are shown in Table 10.3, together with the speeds used for calculating the drag for each phase.

Table 10.3: Required and actual gradients of climb for the one-engine-inoperative scenario with a 34% thrust setting ($T = 0.17T_{max}$)

Phase	Required gradient of climb	Calculated gradient of climb	Velocity
Take-off (Landing gear extended)	0%	7.4 %	$V_{lof} = 1.05 \times V_{stall, LG \text{ extended}}$
Take-off (Landing gear retracted)	2.4%	9.2 %	$1.2 \times V_{lof}$
Final take-off	1.2%	7.1 %	$1.2 \times V_2, h=457m$
En-route climb	1.1%	1.7 %	$V_{maxROC} = V_{(DV)_{min}}$
Approach	2.1%	9.7 %	$V_{app} = 1.3 \times V_{stall, LG \text{ extended, landing mass}}$

As can be seen from Table 10.3, the design easily meets the requirements set by EASA for one-engine-inoperative gradients of climb. This can be explained by the combination of low drag with a relatively high sea-level thrust compared to commercial aircraft due to the high altitude requirement.

Finally, CS-25 requires an amount of reserve fuel on board to allow for a loitering phase lasting at least 45 minutes at a height of 3048 meters (10,000 ft). Compliance with these requirements was checked by determining the endurance of the aircraft at 3048 meters after injecting all of the payload, with only the reserve fuel mass remaining. The endurance is calculated using the Breguet Endurance formula given in Equation 10.17[34]. For the final mass M_f , $OEM + FM_{land}$ was used, which is the empty operative mass plus the fuel required for landing and taxiing, which was determined using a fuel fraction of 0.992 [12]. The initial mass is the same as the final mass, with only the reserve fuel mass FM_{res} added.

$$E = \frac{1}{gc_j} \frac{L}{D} \ln \frac{M_i}{M_f} \quad (10.17)$$

Using Equation 10.17 then results in an endurance of 71.1 minutes, which is larger than the required 45 minutes, which shows compliance with the CS-25 requirement CS25-353(a)[13]. Compliance with all mentioned CS-25 requirements has thereby been verified. Additionally, compliance with system requirement REQ-MIS-MPR-3 following from stakeholder requirement REQ-STK-4 was verified in a similar manner. Using Equation 10.17, a total cruise endurance of 316 minutes was found, showing compliance with REQ-MIS-MPR-3.

Validation of the different flight performance scripts was done by performing calculations on modern existing aircraft with known results. For example, the range calculator was used on A320-200 data, resulting in a range of 6,320 km instead of the actual range of 6,200 km¹, an error of 2%.

The time to climb calculator, which includes the rate of climb calculations, was validated using data from the Lockheed U2 aircraft. An error of 2.7% was found between the calculated time to climb to 60,000 feet of 46.2 minutes, compared to the actual time of 45 minutes².

The take-off distance calculator, which uses the same average acceleration calculations also used by the landing distance calculator, was validated using Airbus A380-841 data. The total take-off distance was computed and compared to the required runway length for operating the A380. The take-off distance was calculated to be 1,887 meters, 6% short of the runway length given by Airbus of 2,000 meters³.

The design tools used showed errors between 2 and 6 % when used with real-world data. The discrepancies can be caused by both inaccuracies in inputs due to limited data available on certain parameters and simplifications in the models used. However, these percentages were deemed acceptable for the conceptual design phase, and the design tools were therefore validated.

10.6. Sensitivity Study

Contributors: Bas

Sensitivity studies were performed on the effect of important aircraft characteristics, such as ceiling altitude and aspect ratio, on the aircraft performance. An example is shown in Figure 10.4. In this plot, the variation in aircraft maximum take-off mass and required fuel mass is shown when increasing the ceiling altitude. As can be seen from the plots, cruising at a higher altitude would significantly increase both masses, and from a height of about 21.5 km would exceed the specification value of the MTOM (shown by the red horizontal line). The blue horizontal line shows the current MTOM and required

¹URL: <https://aircraft.airbus.com/en/aircraft/a320-family/a320ceo>

²URL: <https://www.lockheedmartin.com/en-us/news/features/2015/webt-u2-innovation.html#>

³URL: <https://www.airbus.com/sites/g/files/jlcbta136/files/2021-11/Airbus-Aircraft-AC-A380.pdf>

fuel mass of the final design. The ceiling height was therefore chosen to remain at 20 km for the first cruise phase, as explained in Section 10.4.

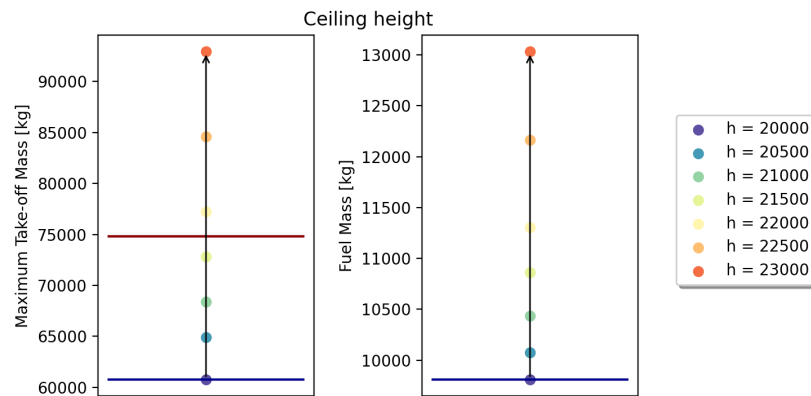


Figure 10.4: Maximum Take-off Mass and Fuel Mass sensitivity to change in ceiling altitude

Additionally, a sensitivity study was performed on the variation in the time-to-climb (TTC) metric for climbing to the ceiling altitude. The result can be found in Figure 10.5. Again, the dark blue horizontal line in the plots shows the value for the time to climb of the final design. As can be seen from the result, the aspect ratio has a minor effect on the TTC, with a lower aspect ratio decreasing the TTC. A higher aspect ratio is, however, desired for aerodynamic efficiency as explained in Chapter 8. The aspect ratio is therefore a compromise between different aircraft performance characteristics, meaning the current wing aspect ratio was not lowered. Logically, increasing the ceiling altitude also increases the TTC to this altitude. From Figure 10.5 it was concluded that the TTC increases exponentially when increasing the ceiling altitude, which happens due to the density and thus climb performance decreasing exponentially as explained in Section 10.2. This helped provide more confidence in the code and the chosen ceiling altitude of 20 km.

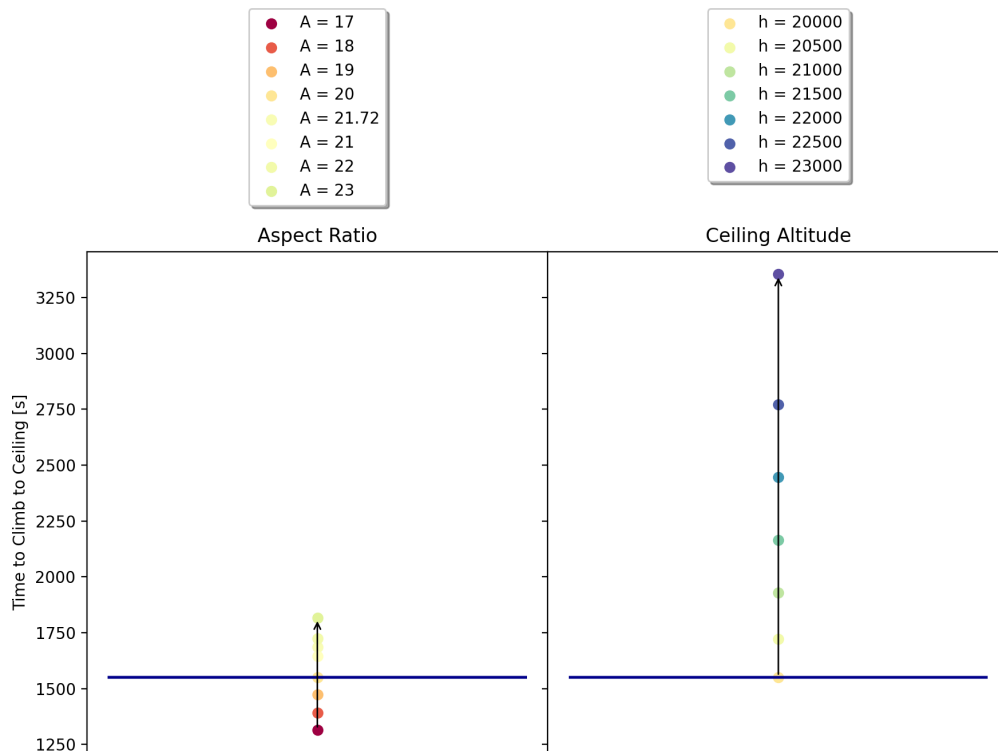


Figure 10.5: Time to climb sensitivity to change in ceiling altitude and wing aspect ratio

Propulsion

With the flight profile determined, there is a thrust requirement that needs to be met. Providing enough thrust at 20 kilometres altitude is challenging as the air density is less than 8% of the air density at sea level. Next to this, the high-subsonic flight speed of Mach 0.7 also does not make the choice for a specific engine type as clear-cut. In this chapter, a preliminary engine design will be made for SCAI. This will also allow the rest of the subsystems to get a more accurate estimate of the engine weight and efficiency.

11.1. Preliminary Analysis

Contributors: Moritz

This section will briefly repeat the analysis of the different engine types and justify some of the design decisions made later in this section.

11.1.1. Difference Between Engine Types

Flying at high altitude and at high subsonic speeds significantly decreases engine performance, in particular for the, in static conditions, more efficient high-bypass turbofan engines. The difference in thrust and TSFC between sea-level and the cruise altitude of 20 kilometres is comparable between turbojets, low-bypass turbofans and high-bypass turbofans. As can be seen in Figure 11.1, the difference in thrust variation with Mach number is very significant. Similarly, the variation of the TSFC with altitude is comparable between engine types, but once again the difference becomes prominent when the variation over the Mach number is observed, as can be seen in the difference between Figure 11.2 and Figure 11.3.

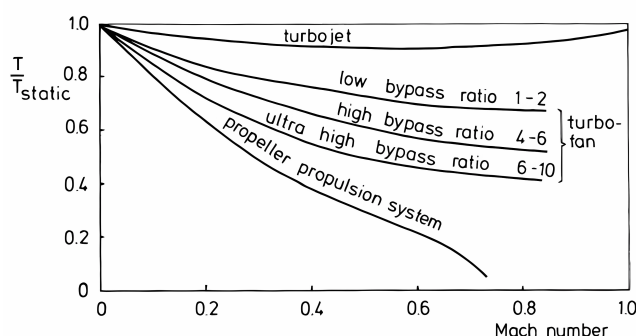


Figure 11.1: Typical variation of thrust with Mach number for a variety of turbine engines.[35]

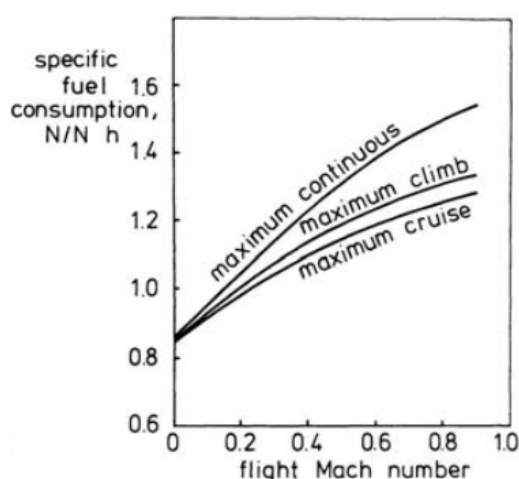


Figure 11.2: TSFC variation with Mach number for a typical turbojet.[35]

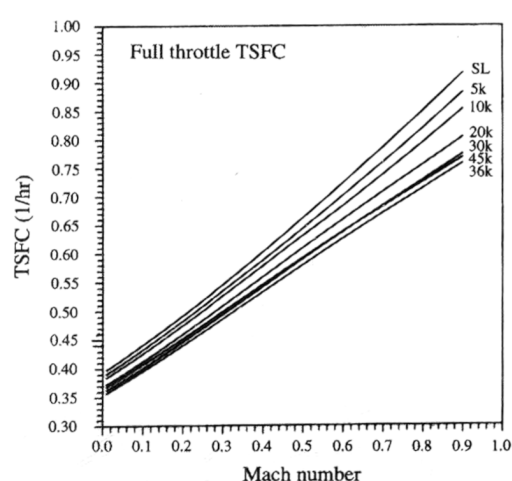


Figure 11.3: TSFC variation with Mach number for a high-bypass turbofan for a variety of altitudes.[9]

It is important to note, however, that high-bypass turbofans typically still have a lower total TSFC than turbojets, even at Mach 0.7; the difference is just smaller. It is possible to compare the weight of the two systems as a combination of the engine plus the weight of the required fuel for a typical flight. By gathering the performance characteristics of a range of jet engines and computing how much fuel each engine would use to fly at a specified thrust for a given time and using

the thrust-to-weight ratio to determine the engine weight at that specified thrust, it is possible to determine what engine would be lightest for a given flight time. As can be seen in Figure 11.4, the EJ200 and Snecma M88 come out as the lightest options of these engines for the estimated total flight time of 3.14 hours. Both of these engines are very low-bypass turbofans. Do note that for flight durations longer than approximately 8 hours, the fuel efficiency of the GE90 would make it the lighter total option, despite being notably heavier due to worse thrust-to-weight at altitude and Mach 0.7. This shows that selecting or designing an engine heavily depends on the mission profile as well.

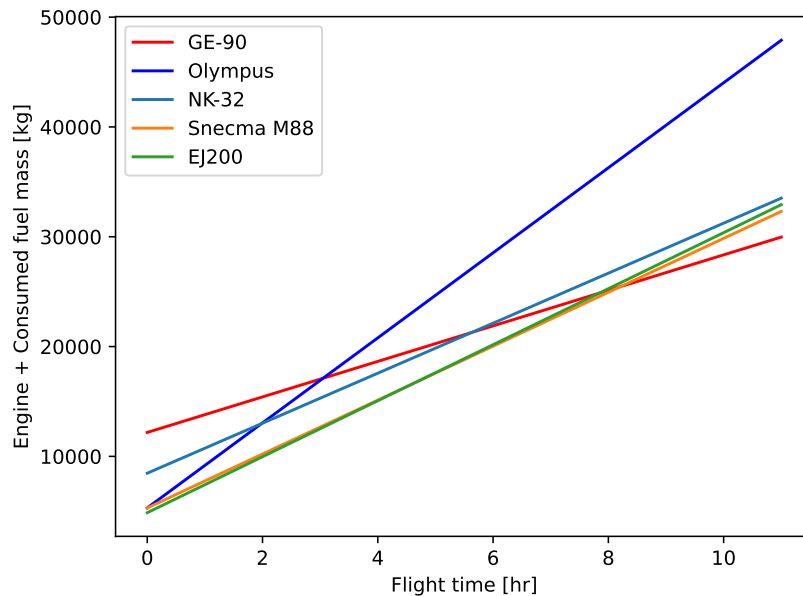


Figure 11.4: The engine plus fuel mass of a variety of turbojets and turbofans to fly for a duration of time.

Concluding the analysis of existing engines, a final trade-off was performed to determine what engine type could be used if an existing design was selected:

Table 11.1: Trade-off for the engine type

Parameter Configuration	Engine+Fuel mass [0.3]	T/W [0.2]	Purchase Costs [0.1]	SFC [0.4]	Score
HBPR Turbofan	[yellow] 1	[red] 1	[red] 1	[yellow] 1	1
LBPR Turbofan	[green] 0.91	[green] 0.44	[yellow] 0.87	[green] 0.88	0.8
Turbojet	[red] 1.31	[green] 0.42	[yellow] -	[red] 1.37	1.14

11.1.2. Existing Engine vs New Design

The question now arises whether an existing engine can be used, or if a new design is necessary. A number of considerations come into play:

- **Technology Age:** Most, if not all of the jet engines analysed for their weight are at least 30 years old. It is not unlikely that engine technology has improved in the past 3 decades, such that a more efficient or power-dense engine can be designed, such as better heat-resistant materials for the turbine, improved bearing technology for lower mechanical losses, etc.
- **Engine Configuration:** The most efficient engines for this particular mission are both *reheated* turbofans. Although there is a power limit in cruise conditions, it does not require reheat, as that would unnecessarily increase the fuel consumption. Removing or omitting this system from the engine saves some weight, which makes the aircraft more efficient as a result.
- **Number of Engines:** This selection is driven by the interfaces between aerodynamics and propulsion. It was determined that having fewer but bigger engines is beneficial for parasite drag, as the number of interference points with the wing decreases. Quantitatively, doubling the number of engines was found to increase the zero-lift drag coefficient, C_{D_0} , by 4.02% compared with fewer yet larger engines producing the same thrust. Fewer engines are also beneficial for weight considerations, substantially decreasing MTOM. Interestingly, an increase in the number of engines can enhance lift performance, a scenario attributed to the increased airflow velocity in front of the engine inlets, which also benefits the aerodynamic conditions incident on the wing.

It was decided to size a new engine, as the best option for existing engines, namely the low-bypass turbofans, would require a larger number of engines than what could be possible, but these engines simply don't exist in this type and size combination. A turbojet with modern technologies could also prove better than the trade-off would suggest.

11.2. Jet Engine Modelling

Contributors: Moritz

For sizing the engine, it was decided to find and optimise a number of key design parameters of the engine, namely the size (inlet diameter, length, nozzle areas etc.), bypass ratio, overall and stage pressure ratios and turbine inlet temperature. With these values as parameters, it is possible to get a range of thrusts and TSFCs and determine an "optimum" within these parameters. The engine performance is calculated by using a 1-D analysis of the flow through the entire engine. The engine performance is calculated as follows, largely based on the method described in *Gas Turbine Theory* (2001) by H. Saravanamuttoo, G. Rogers, and H. Cohen [6] and lecture slides of the Power & Propulsion course of TU Delft's Aerospace BSc:

First, it is given that p_0 is the total pressure at a given altitude at static conditions. At ISA sea-level, this is 101325 Pa, whereas at 20 kilometres altitude, this is roughly 5530 Pa. The performance at cruise conditions, with a Mach number of 0.7, is more interesting, however. In this situation, the fan/compressor inlet pressure $p_{0,1}$ increases due to the ram effect; this ram pressure ratio is given by:

$$p_{0,1} = p_0 \cdot (1 + \eta_i \cdot (\frac{\gamma - 1}{2}) \cdot M_0^2)^{\frac{\gamma}{\gamma - 1}} \quad (11.1)$$

Where η_i is the isentropic efficiency and γ is the constant heat capacity ratio, which is 1.4 for air. The temperature increases accordingly and becomes:

$$T_{0,2} = T_0 \cdot (1 + (\frac{\gamma - 1}{2}) \cdot M_0^2) \quad (11.2)$$

Onto the turbomachinery, the air first encounters the fan or the first low-pressure compressor. As the particular example in *Gas Turbine Theory* describes a turbofan, that will be the case here as well. It is not special compared to a turbojet, with the exception that it is often fewer or even only 1 stage, compared to the multi-stage LP compressors one would see on turbojets. As compressors are often characterised by their pressure ratio, the pressure after the fan simply becomes:

$$p_{0,2} = p_{0,1} \cdot PR_f \quad (11.3)$$

Where PR_f is the fan pressure ratio. This value is typically between 1.5-1.7 for single stage fans. With this increase in pressure, the static temperature also increases with:

$$T_{0,2} = T_{0,1} \cdot PR_f^{\frac{\gamma - 1}{\gamma}} \quad (11.4)$$

Note that this equation describes the isentropic temperature rise. As jet engines are not perfect and suffer from heat loss and friction, one can describe the polytropic temperature rise by:

$$T_{0,2} = T_{0,1} \cdot PR_f^{\frac{1}{\eta_c} \cdot \frac{\gamma - 1}{\gamma}} \quad (11.5)$$

Where η_c is the fan/compressor polytropic efficiency. The same relations hold for the transition for the compression over the high-pressure compressor ($P/T_{0,2}$ to $P/T_{0,3}$), but instead of PR_f one would use PR_{comp} as the compressor pressure ratio here instead. This number depends on the number of stages in the compressor, where each stage has a pressure ratio of roughly 1.2-1.4.

As $T_{0,4}$ is an input parameter, namely the turbine inlet temperature, this value is fixed. The pressure usually drops a bit, which is once again the same formula as Equation 11.3, with the exception that PR_{comb} is lower than 1, meaning the air gets slightly expanded in this section of the engine. With the turbine inlet temperature known, it is possible to calculate the required fuel flow:

$$\dot{m}_f = \frac{(\dot{m}_c \cdot c_{p,g} \cdot (T_{0,4} - T_{0,3}))}{(LHV \cdot \eta_b)} \quad (11.6)$$

Where \dot{m}_c is the air mass flow into the core, η_b is the burner efficiency, and LHV is the fuel caloric value. It is also important to note that from this point onwards, one must take into account that the flow is no longer purely air and as such γ and c_p take on the values for the mixed, hot flow rather than the values for air.

It is possible to calculate the temperature drop over the turbine(s) using the required work to achieve the temperature differences caused by the compression in the fan/compressor stages. For the high-pressure turbine, where the mass flow in the compressor is the same as in the turbine, plus the fuel mass flow.

$$T_{0,4} - T_{0,5} = \frac{\dot{m}_{turb}}{\dot{m}_{comp}} \frac{c_{p,a}}{\eta_m c_{p,g}} \cdot (T_{0,3} - T_{0,2}) \quad (11.7)$$

For the low-pressure turbine (which drives the fan/LP compressor), it is important to remember that the temperature increase is acted upon the total airflow, not just the airflow in the core and as such:

$$T_{0,5} - T_{0,6} = (B + \frac{\dot{m}_{turb}}{\dot{m}_{comp}}) \cdot \frac{c_{p,a}}{\eta_m c_{p,g}} \cdot (T_{0,2} - T_{0,1}) \quad (11.8)$$

As $T_{0,4}$ is known $T_{0,5}$ and $T_{0,6}$ can easily be found. $p_{0,6}$ can then be found using:

$$\frac{p_{0,4}}{p_{0,5}} = \left(\frac{T_{0,4}}{T_{0,5}} \right)^{\frac{1}{\eta_t} \cdot \frac{\gamma}{\gamma-1}} \quad (11.9)$$

$$\frac{p_{0,5}}{p_{0,6}} = \left(\frac{T_{0,5}}{T_{0,6}} \right)^{\frac{1}{\eta_t} \cdot \frac{\gamma}{\gamma-1}} \quad (11.10)$$

$$p_{0,6} = \frac{p_{0,4}}{\frac{p_{0,4}}{p_{0,5}} \frac{p_{0,5}}{p_{0,6}}} \quad (11.11)$$

Here, η_t is the turbine *polytropic* efficiency.

To calculate the thrust, it must first be determined whether or not the nozzle pressure ratio is higher than the critical pressure ratio and thus whether it is choking or not. The critical pressure ratio is described by:

$$\frac{p_{0,6}}{p_c} = \frac{1}{\left(1 - \frac{1}{\eta_j} \frac{\gamma-1}{\gamma+1} \right)^{\frac{\gamma}{\gamma-1}}} \quad (11.12)$$

As can be seen, the pressure ratio depends only on the nozzle efficiency η_n and the heat capacity ratio γ . In the nozzle, $\gamma = 1.33$ due to the increased temperature and the fact that the flow is now a mixture of air and combustion exhaust gases. For a nozzle efficiency of 95%, the critical pressure ratio would be 1.914. If the nozzle pressure ratio $\frac{p_{0,6}}{p_0}$ is smaller than this ratio, then it is the case that $p_7 = p_0$, and as such:

$$F_T = \dot{m}_n \cdot (V_7 - V_0) \quad (11.13)$$

Where V_7 is the exhaust velocity and \dot{m}_n is the nozzle mass flow, which is the intake mass flow plus the fuel mass flow (which is the same as the turbine mass flow), to find the exhaust velocity:

$$T_{0,6} - T_7 = \eta_j \cdot T_{0,6} \cdot \left(1 - \left(\frac{p_0}{p_{0,6}} \right)^{\frac{\gamma-1}{\gamma}} \right) \quad (11.14)$$

$$V_7 = \sqrt{2 \cdot c_p \cdot (T_{0,6} - T_7)} \quad (11.15)$$

And then the thrust can be computed. If the nozzle pressure ratio is bigger than the critical pressure ratio, the thrust is computed as follows:

$$F_T = \dot{m}_n \cdot (V_7 - V_0) + A_7 \cdot (p_7 - p_0) \quad (11.16)$$

As the nozzle is choked and the flow can not fully expand, the pressure now also contributes to the thrust. The inputs for this formula are found as followed:

$$T_7 = \left(\frac{2}{\gamma + 1} \right) \cdot T_{0,6} \quad (11.17)$$

$$p_7 = p_c = p_{0,6} \cdot \left(\frac{p_c}{p_{0,6}} \right) \quad (11.18)$$

$$\rho_7 = \frac{p_7}{R \cdot T_7} \quad (11.19)$$

$$V_7 = \sqrt{\gamma \cdot R \cdot T_7} \quad (11.20)$$

$$A_7 = \frac{\dot{m}_n}{\rho_7 \cdot V_7} \quad (11.21)$$

With these values known, the thrust for a choked nozzle can also be computed. The same procedure for computing the thrust for the bypass section is used, with the difference being that the pressure to which the critical pressure ratio is compared and from which the nozzle exit parameters are computed is $p_{0,2}$.

11.3. Design Point Selection

Contributors: Moritz

To select a set of bypass ratio, turbine inlet temperature, overall pressure ratio and mass flow, it is important to first decide on the order in which these are determined, as the engine performance (both thrust and fuel consumption) depends on most of these. Before looking at these parameters, it is important to define the design space that is available. While these parameters themselves are not necessarily hard-capped, the effects that they have on, for example, the size or weight could. The most important design limitations are listed below.

- **Weight:** Both the engine and fuel can not exceed a certain weight as stated by the system requirements in Section 18.3. The mass budgets define that the engine can not be more than 46% of the operational empty weight. At the same time, the fuel mass has been calculated to be 9810kg. The significant part about this is that for the bypass ratio in particular, these limitations constrain the design in both ways. The engine needs to stay within the mass budget, but mass increases as the bypass ratio increases (higher bypass ratios have a lower specific thrust). On the other hand, the fuel must remain within the maximum, but TSFC and thus total required fuel per flight decreases with increasing bypass ratio (next to this, lower fuel consumption is desirable in general).
- **Size:** As the fuselages are rather small, space for the engine is not a given, even with the high-wing design. The engines must stay above a line that extends laterally at an angle of 5° upwards from the point where the main landing gear touches the ground. This can be seen in Figure 11.5. An important observation is that this means that the engine placement (both lateral and height) could affect the engine size.
- **Turbine Inlet Temperature:** The temperature of the flow going over the turbines must not exceed the point where the materials are weakened and the turbine blades will break. A higher turbine inlet temperature generally means a higher TSFC but also a higher specific thrust. Modern engines have been able to increase this temperature more and more with the introduction of turbine blade cooling, thermal barrier coatings and new materials such as single-crystal cast metals.
- **Technology Readiness:** To ensure the engine design is feasible, it should fall within, or very close to, the design ranges of existing turbine engines.

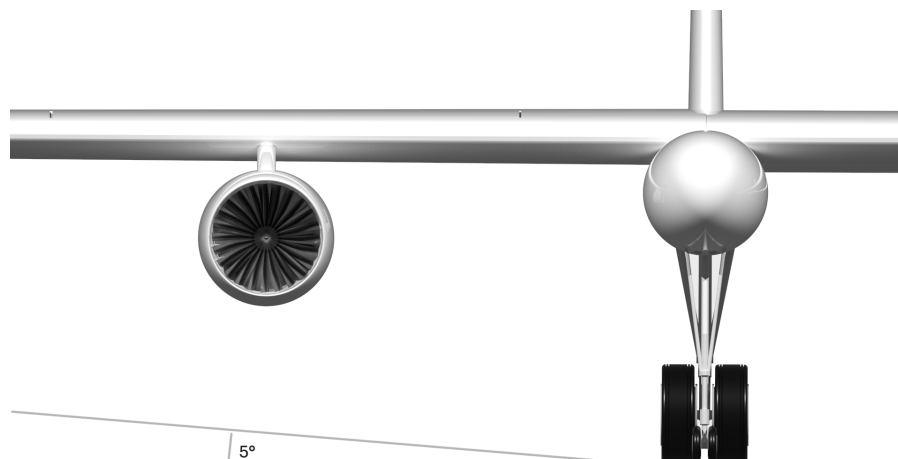


Figure 11.5: Engine size constraint by the landing gear. Made in 3D Experience

11.3.1. Bypass Ratio

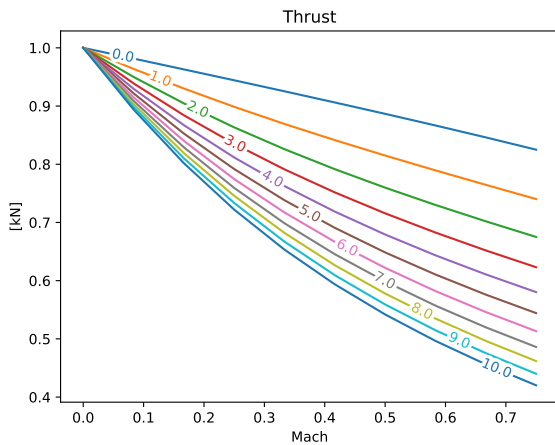
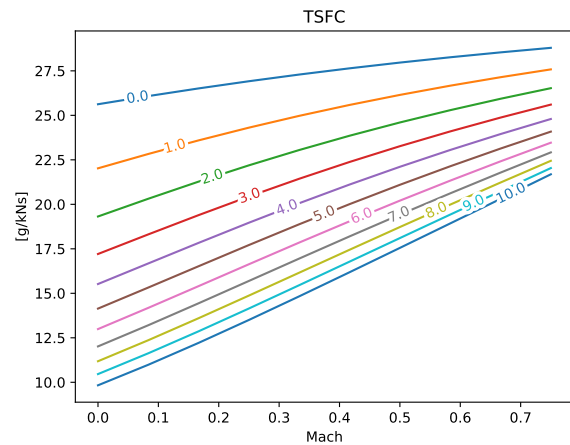
The bypass ratio probably has the biggest impact on the performance of the chosen design parameters. The engine performance of a range of bypass ratios can be seen in Figure 11.6. These and all further plots have been obtained using the characteristics listed in Table 11.2. Furthermore, these plots were created using a turbine inlet temperature of 1550 K, an overall pressure ratio of 26 and a total mass flow of 265 kg/s at sea level, which results in a mass flow of 19.2 kg/s at an altitude of 20 km.

As thrust decreases practically the same over altitude for all bypass ratios, the primary interest point of comparison is how the engine thrust according to the 1-D model changes with Mach number. Plotting the thrust and TSFC as a function of the Mach number for a range of bypass ratios yields the plots in Figure 11.6 and Figure 11.7.

As was expected through the preliminary analysis, the thrust decreases more for higher bypass turbofans compared to lower bypass turbofans and turbojets. This makes sense with Equation 11.13 in mind. As a larger portion of a high-bypass is propelled at a slower speed, the thrust contribution of the bypassed air will decrease faster than the thrust contribution of the core airflow and as such will result in a lower thrust at higher Mach numbers compared to its thrust at standstill. This swifter reduction of thrust will also result in a more rapid increase in TSFC, as can be seen in Figure 11.7. Note that these values are absolute, not ratios. As such, it can be seen that the high-bypass turbofans remain more efficient than the lower-bypass turbofans or turbojets.

Table 11.2: Constants used for engine calculations

γ_{air}	1.4 [-]
$c_{p,a}$	1005 [J/kgK]
γ_{hot}	1.33 [-]
$c_{p,g}$	1150 [J/kgK]
R	287 [kJ/kg]
LHV	42 [MJ/kg]
η_i	0.93 [-]
η_c	0.90 [-]
η_b	0.99 [-]
η_m	0.99 [-]
η_j	0.95 [-]

**Figure 11.6:** Thrust ratio compared to static thrust for a variety of bypass ratios**Figure 11.7:** TSFC variation with Mach number for a variety of bypass ratios

As the cruise and climb time are known and assuming that both phases require to be flown on maximum thrust, it was possible to plot the engine plus fuel mass as a function of the bypass ratio. To estimate the weight of the engine, a thrust-to-weight ratio of 6.1 was used. This corresponds roughly to the most weight-efficient modern jet engines, such as the EJ200, IAE V2500 and Rolls-Royce Trent XWB. As this thrust-to-weight ratio corresponds to sea-level static thrust for these engines, the 1D analysis has calculated the engine weight using the sea level thrust, but to still take the cruise flight into account, it used the cruise ($M = 0.7$ at 20 km) TSFC to compute the fuel weight. Calculating these values for a range of bypasses yields the plot in Figure 11.8. In this plot, the lower horizontal dark red line indicates the engine weight limit from its mass budget of the OEM, the upper horizontal dark blue line indicates that mass plus the calculated fuel mass.

It becomes clear that the fuel mass does not impact the total mass as much as the engine mass does. Using the mass budget as a limit, the maximum allowable bypass ratio is 4.65. However, after global iterations have been performed, it was determined that the overall aircraft mass is lowest using a bypass ratio of 0. This can be attributed to the rather short flight time, meaning it was always worth having a lighter engine over more fuel efficiency, because the fuel savings were comparatively small. Therefore, a bypass ratio of 0, ergo a turbojet engine, was selected.

11.3.2. Overall Compression Ratio and Turbine Inlet Temperature.

The compression ratio and turbine inlet temperature heavily influence the performance of the engine. Finding an optimum for these values is difficult, however. Figure 11.9 shows how the specific thrust (Thrust per kg of mass flow into the engine) varies with the turbine inlet temperature (red lines) and the overall pressure ratio (blue lines).

As the required thrust is known for both sea level and cruise conditions, it is possible to determine the limiting condition. By finding a set of parameters that satisfies the thrust requirement in cruise conditions and setting the flight conditions to static at sea level, it becomes clear that a singular engine can produce all of the required sea level thrust if it is set as such that it produces half of the required thrust in cruise conditions.

As specific thrust is defined as:

$$F_s = \frac{F_T}{\dot{m}} \quad (11.22)$$

As the required thrust F_T is already known, the primary unknown becomes the engine mass flow. Naturally, engine mass

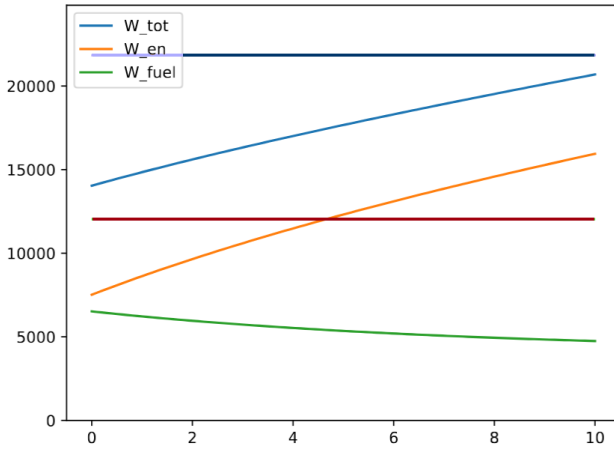


Figure 11.8: Engines, fuel and total weight as a function of bypass ratio for the determined cruise plus climb time.

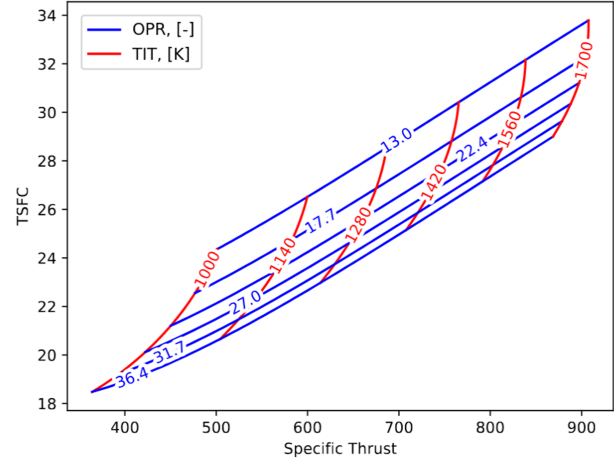


Figure 11.9: Specific thrust [N/kg] and TSFC [g/kNs] variation for a range of Turbine Inlet Temperatures and Overall Pressure Ratios

flow heavily depends on the intake area. The intake area is given by:

$$A_i = \frac{\dot{m}}{\rho_0 \cdot V_i} \quad (11.23)$$

Where V_i is the internal flow velocity, which is in the range of 150 to 200 m/s [6]. ρ_1 is simply the static density. For this engine design, an internal intake flow speed of 180 m/s was chosen.

With these relations known, it was possible to work backwards by selecting a desired specific thrust and TSFC, which yielded a needed turbine inlet temperature and overall pressure ratio. As it is desirable to lower the TSFC, a high overall pressure ratio is preferred. Along the same line, lowering the turbine inlet temperature also lowers the TSFC, with the main difference being that this also decreases the specific thrust more strongly than the overall pressure ratio. Picking a viable design point also depended on the range of realistic values. The values of the overall pressure ratio and turbine inlet temperature as they have increased over the years can be seen in Figure 11.10 and Figure 11.11, respectively¹.

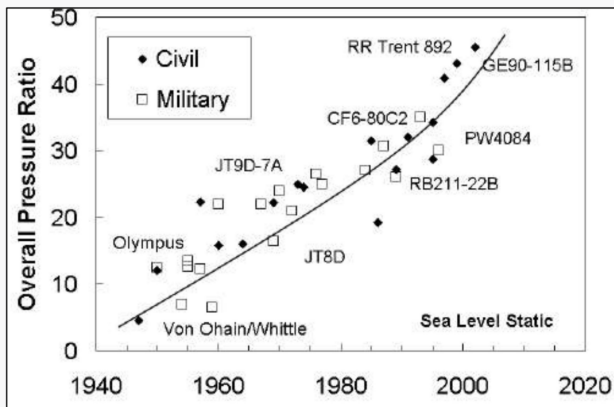


Figure 11.10: Turbofan Overall Pressure ratio growth over time¹

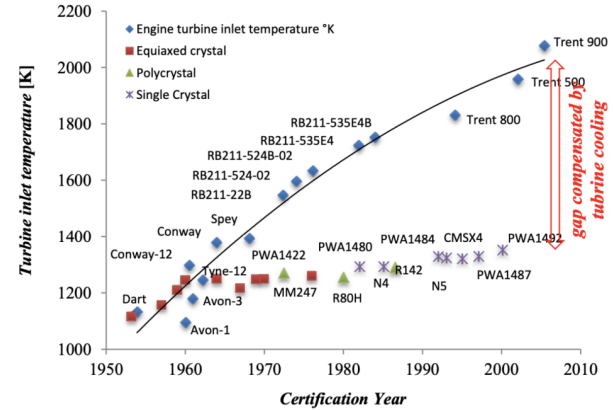


Figure 11.11: Turbine Inlet Temperature increase over time¹

As phenomena of like compressor surging or choking can occur at high compression ratios, it was decided to limit the overall pressure ratio to 26. This is still high for the (older) existing turbojets, but comparatively low when compared to modern high-bypass turbofans. This is roughly in the range for the military jets with the highest pressure ratios in their category. The actual compressor design was determined in subsection 11.3.3.

As for the turbine inlet temperature, it was decided to use a temperature of 1550 K to both limit the TSFC increase and limit the reliance on turbine cooling. Using modern techniques such as the use of thermal barrier coatings, the amount of air needed to cool the turbine blade can be reduced. While the air that is “bypassed” to cool the turbine blades and the resultant drop in temperature of the cold and hot air mixing was not taken into account in the cycle calculations, it has been compensated for by increasing the required thrust a little (which is done regardless as to have a little margin in the available thrust at cruise conditions). It is then found that the resultant specific thrust is 810.7 N/kg. To achieve this specific thrust at cruise conditions, the engine needs a sea level mass flow of 265 kg/s (19.2 kg/s at cruise conditions). This mass flow results in a required engine intake area of 1.2 m², or an intake diameter of 1.24 m.

¹Image source: <https://odayaviation.com/jet-engines-evaluation-overall-pressure-ratio/>, retrieved 18-6-2025.

11.3.3. Compressor Stages

With the overall compression ratio known, a final step in determining the engine layout is defining the compressor stages. As the jet model is designed to be used for a turbofan, it breaks the compression ratio of the spools down into the fan and a compressor, but in reality, a 2- (or more) spool compressor would be used for an engine of these dimensions. The advantage of using multiple spools is that the first, generally larger outer diameter compressor, can be run at a lower speed than the second, generally smaller outer diameter compressor. This allows both compressors to run with blade tip speeds close to the limit, roughly Mach 1.1, without going over and losing efficiency. One disadvantage of using a large number of stages is the reduction of work done per stage due to the increasing thickness of the boundary layer in the engine. This has the effect that the axial flow velocity near the walls becomes lower and that it becomes lower for larger distances away from the wall. This reduces the work efficiency, as less flow is now flowing at the maximum velocity. See Figure 11.12 [6] for a graphical example of the effect of an increasing boundary layer thickness on the axial flow and Figure 11.13 [6] for the effect of increasing the number of stages on the individual stage effectiveness.

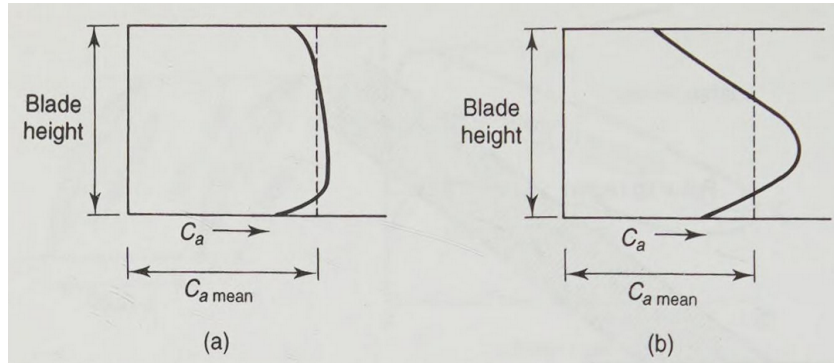


Figure 11.12: The change in axial velocity (C_a) compared to the mean in the (a) 1st stage and (b) 4th stage [6]

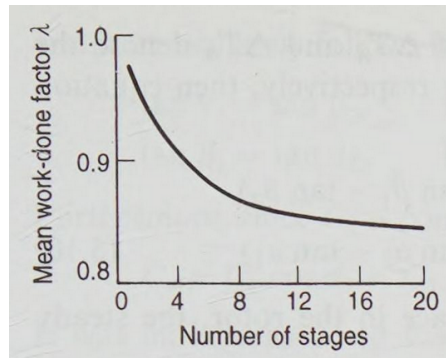


Figure 11.13: Mean work-done factor variation with number of compressor stages [6]

If the maximum compressor blade tip speed is set at Mach 1.1, the maximum allowable blade tip speed for the 1st stage is $\sqrt{1.4 \cdot 287 \cdot 216.7 \cdot 1.1} = 324.6$ m/s. With a diameter of 1.24 m, this results in a rotational speed of almost exactly 5000 rpm for the 1st spool. To compute the number of stages in the compressor, the temperature rise over the compressor was used. As already mentioned, the desired overall pressure ratio is 26 and the temperature rise for the total compressor as a result is computed to be: $T_3 - T_0 = 652.8 - 288.2 = 364.6$ K. First, the total number of stages was computed under the assumption that all stages are on the same spool at 5000 rpm, with a constant mean blade speed for all stages. The temperature rise of all stages combined must add up to 364.6 K to achieve the desired compression ratio. The temperature rise of a single compressor stage is:

$$\Delta T_{0,S} = \frac{\lambda}{c_p} \cdot U \cdot C_a \cdot (\tan \beta_1 - \tan \beta_2) \quad (11.24)$$

Here, λ is the mean work-done factor corresponding to Figure 11.13, U is the mean blade speed, C_a is the axial speed and β_1 and β_2 are the blade inlet and outlet angles, respectively. If the hub in the centre of the first stage is 10% of the total diameter and the tip speed is 325 m/s, the mean blade speed U is roughly $325 \cdot 0.71 \approx 231$ m/s (this is the speed at the length of the blade such that half of the air volume passes on either side of this length). All of the parameters can then be calculated as follows:

$$\tan \beta_1 = \frac{U}{C_a} = \frac{231}{180} \quad (11.25)$$

$$\beta_1 = 52.1^\circ \quad (11.26)$$

$$V_1 = \frac{C_a}{\cos \beta_1} = \frac{180}{\cos 52.1} = 244.2 \text{ m/s} \quad (11.27)$$

The stage outlet angle can be calculated using V_2 , which is related to V_1 using the de Haller criterion², which can not be smaller than 0.72 [6]. Setting this value to 0.8 for this stage to leave some margin to this limit, V_2 then becomes $V_1 \cdot 0.8 = 195.4$ m/s. The corresponding outlet angle is then:

$$\cos \beta_2 = \frac{C_a}{V_2} = \frac{180}{195.4} \quad (11.28)$$

Which yields $\beta_2 = 22.9^\circ$. Plugging these values into Equation 11.24 yields, with $\lambda = 1$ for the first estimate:

$$\Delta T_{0,S} = \frac{1}{1005} \cdot 231 \cdot 180 \cdot (\tan 52.1 - \tan 22.9) = 35.6K \quad (11.29)$$

With this temperature rise per stage, $364.6/35.6 = 10.2$ stages, or 11 stages are needed. This number of stages would yield a λ of roughly 0.86, which would in turn change the temperature rise per stage to $0.86 \cdot 35.6 = 30.6$, which would then yield 12 stages required to achieve the desired compression ratio.

11.4. Final Design

Contributors: Moritz

The final engine has the following dimensions and performance figures, and a schematic of what this engine could look like can be seen in Figure 11.14:

Table 11.3: Engine Characteristics of a single engine

Sea-level thrust	238.6 kN
Cruise thrust	16.2 kN
Cruise TSFC	28.6 g/kNs
Cruise Specific Thrust	810.7 N/kg
Mass	3780 kg
Inlet diameter	1.24 m
Number of compressor stages	12

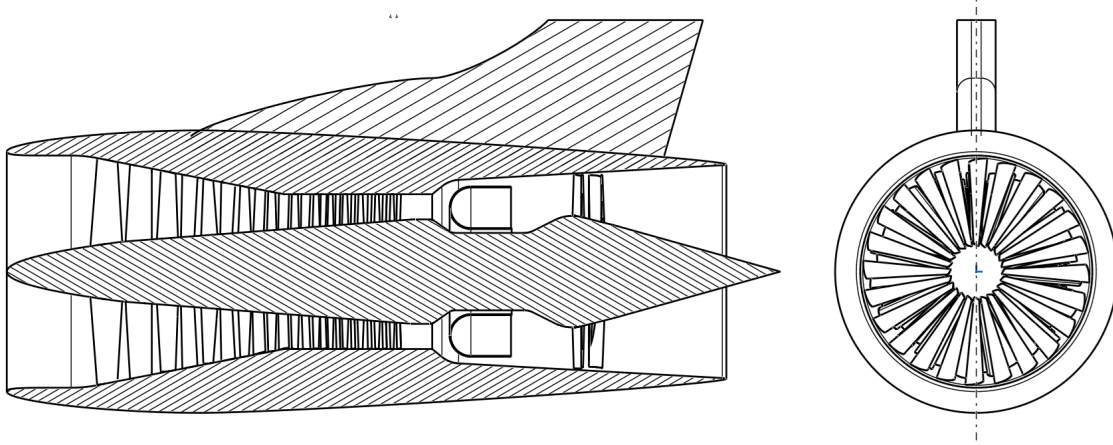


Figure 11.14: A schematic of the SCAI engine

11.5. Propulsion Sensitivity Analysis

Contributors: Moritz

The effects on aircraft performance of a varying TSFC will be discussed in Chapter 17. In this section, the effects of varying some of the normally fixed input parameters, specifically the effect of the efficiencies on the TSFC and the effect of flight time on the bypass ratio design point will be analysed and discussed.

11.5.1. Efficiency Sensitivity

The values used for the efficiencies in calculations are from Table 11.2. The analysis was performed by varying the efficiencies by $\pm 1\%$ and $\pm 3\%$. The results can be seen in Figure 11.15. It becomes clear which efficiencies have the biggest impact of the fuel performance. The burner efficiency η_b has an almost linear effect, as a 1% change in efficiency

²This is an empirical number that relates inlet to outlet flow velocities of a blade row, as long as the ratio is larger than 0.72 (ergo the criterion is higher than 0.72) the flow is stable.

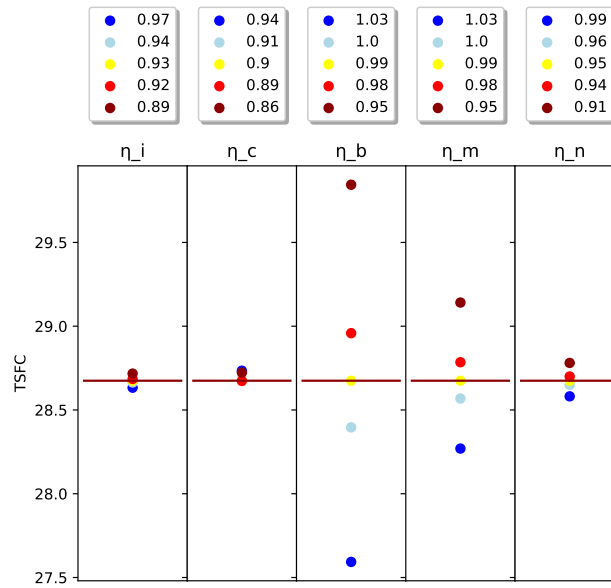


Figure 11.15: Sensitivity Analysis of the TSFC for a varying efficiency input

results in roughly a 1% change in TSFC (do note that both the burner and mechanical efficiency have an efficiency value of more than 100% in the range. This is obviously impossible, but these were left in to keep consistency between the analysis of the 5 values). The second most impactful is the mechanical efficiency, being a little more than 40% as impactful as the burner efficiency. It becomes clear that to maximise engine performance it is very important to have the burners be as efficient as possible and mechanical losses be kept to an absolute minimum.

11.5.2. Design Point Sensitivity to Flight Time

As the bypass ratio is a key design parameter of the engine which can not easily be changed once an engine is built, it is key to select the correct bypass ratio from the start. As one of the big unknowns in the SCAI project is the aerosol injection rate, it is wise to analyse the effect of flight time (which is directly proportional to the injection rate) on the design point. As bypass ratio has been directly linked to the total mass by determining that to maximise payload-to-fuel it is paramount to minimise the total engine and fuel mass, it is possible to find a bypass ratio for which this total is minimal. For the relatively short flight time of 3.14 hours, a bypass ratio of 0 would offer up the lightest solution, but then the question remains whether this is the case for all flight durations. Figure 11.16 shows a plot of the total engine plus fuel weight as a function of the bypass ratio, for a variety of flight duration factors. Here, the factor 1 is equal to a flight time of 3.14 hours, the determined flight time of the SCAI mission.

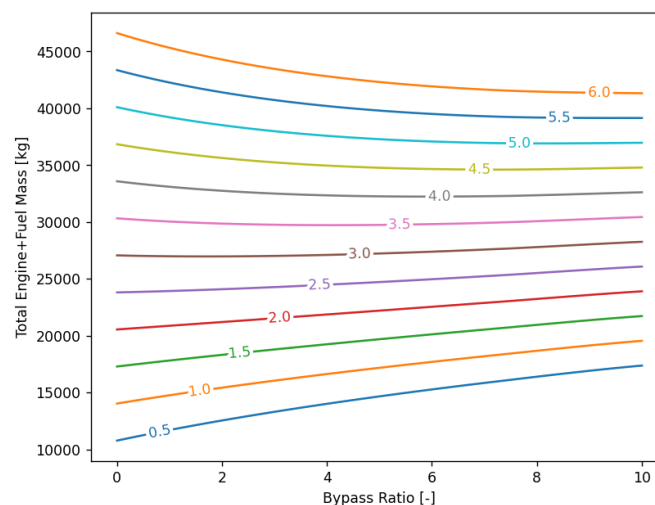


Figure 11.16: Engine plus Fuel mass as a function of bypass ratio, for a variety of flight time factors, where 1 equals a flight time of 3.14 hours.

As can be seen, as the flight time increases, it does at some point become better to select a higher-bypass engine. This makes sense as the fuel weight will become a bigger and bigger fraction of that total weight as flight time increases. If one takes the sustainability and cost aspect into account, a flight time factor of roughly 3-3.5 (equally a total flight time of

roughly 10 hours), a high-bypass turbofan becomes the clearly preferred option.

The flight time of 3.14 hours assumes an aerosol injection rate of 2.33 kg/s. This is the optimistic, high flow rate scenario. If this was an unachievable rate and instead the lower boundary was the realistic scenario, the flight time would be roughly 2.5 times as long for the same payload (if this was determined during the design this would impact the design in more ways, but this assumes nothing else on the aircraft changes, see Figure 17.4). This is still less than that 3-3.5 flight time factor threshold determined in Figure 11.16 and as such, the turbojet design point will remain relevant for the entirety of the expected flight durations.

11.6. Results Validation

Contributors: Moritz

To ensure that the obtained values are accurate, or to quantify the difference the real world and the 1-D flow model, the actual engine performance of previously analysed engines was compared to the performance characteristics computed by the 1-D flow model. In Figure 11.17, this comparison can be seen. There are a couple things to note about this plot. Firstly, it is clear that the engine models limited detail prevents it from being super accurate, though for the more modern engines it does compute performance characteristics that are quite accurate, being within 10% of real world characteristics. The poorly computed engines are generally older/bigger than the accurately modelled engines. It makes sense that as engines get newer, they become more efficient. As the efficiencies used in the engine model have been kept constant for all engines, it makes sense that some of the discrepancy comes from here. It does not fully explain the difference, however. Secondly, it also becomes clear that the model does not consistently over- or underestimate the engine performance. It is important to point out that all of these engines are low-bypass turbofans or turbojets. One thing that can help is comparing the input parameters of the SCAI engine to an existing engine. The bypass ratio, turbine inlet temperature and overall pressure ratio of the PW1120 is very close to those of the SCAI engine, being 0 (as it is a turbojet), 1550 K and 26.8 respectively. It can also be seen that this engine is among the most accurately predicted, which gives good hope that the flow model correctly predicts the engine performance for these inputs. The main difference between the SCAI engine and the PW1120 is the size, with the SCAI taking in roughly 3 times the amount of air per second compared to the PW1120. This puts it comparatively close to the computed performance of the GE4, for which the performance has been overestimated by some 20% for thrust and underestimated by some 10% for the TSFC. Based on where the computed values of the PW1120 and GE4 lie w.r.t. their real-life performance figures, it is not unreasonable to assume that the thrust of the SCAI engine is somewhat overestimated in the 1-D flow model. The difference in TSFC is likely a bit smaller, but will probably still be present.

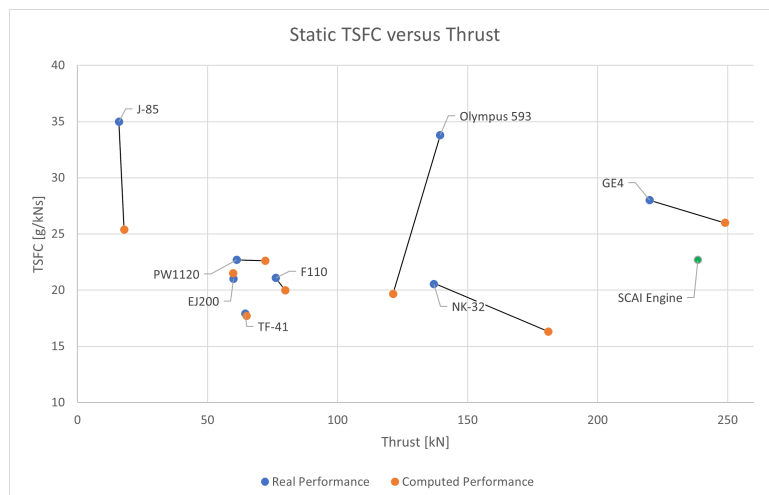


Figure 11.17: Computed versus real static engine performance of a variety of engines.

The engine size is the other point of uncertainty. While the engine is not particularly large compared to modern high-bypass turbofans, one has to remember that the SCAI engine is a turbojet, with all of the air taken in flowing through the combustor instead of bypassing 90% of the ingested air. The result is a rather large engine core, bigger than what one would see on those modern high-bypass turbofans. The result is a lower mean blade speed as the turbines are still limited by the blade tip speed going faster than Mach 1.1. There are some other effects that also affect compressor performance, such as compressor stall or surging. This is the reason the pressure ratio has not been set to be close to modern turbofan limits. It could turn out that the desire for 2 engines is a killer requirement by virtue of the required engine size being infeasible to the aforementioned reasons and as such it could turn out that the engines would have to be downscaled to a size such that 4 or more engines would be used instead. At that point, using a modified existing engine such as the EJ200 or M88 would be a very realistic option.

Stability and Control

In this chapter, the stability and control of the aircraft is analysed. In Section 12.1, the forward and aft cg positions are determined. The horizontal and vertical stabilisers are designed in Section 12.2 and Section 12.3 respectively. The control surfaces, that is, the elevator, ailerons and rudder, are sized in Section 12.4. The landing gear design is explained in Section 12.5. Finally, a dynamic stability analysis is performed in Section 12.6. The verification and validation for this chapter is explained in Section 12.7, and a sensitivity study is performed in Section 12.8.

12.1. Aircraft Balance

Contributors: Carmen, Blanca

Firstly, the longitudinal position of the aircraft centre of gravity at operational weight, including the injection system, was estimated. The c.g. for each component was found, and the total c.g. position, measured from the nose, was calculated with Equation 12.1.

$$x_{cg} = \frac{\sum_{i=1}^n x_i \cdot m_i}{\sum_{i=1}^n m_i} \quad (12.1)$$

This c.g. position is heavily affected by the position of the wing along the fuselage, and the fuselage length, which varies with the chosen tail length. After several iterations, the tail length was chosen such that there is no tail strike during take-off, as will be explained in Section 12.5, and to ensure the smallest possible required tail area, as shown in Section 12.8. A final operational empty weight c.g. of 7.235 m longitudinally was obtained. Furthermore, in order to obtain the forward and aft c.g. positions, a loading diagram for the payload and the fuel was then plotted and is shown in Figure 12.1. This shows the variations of the c.g. as the $CaCO_3$ and the fuel are loaded. It should be noted that the c.g. values are normalised with the MAC.

The curved line represents the aerosol being loaded in the tank, from the front to the back. The tank is placed in the cylindrical section of the fuselage. It is assumed that during flight, the aerosol will be transported from the tank to the trailing edge of the wing, starting from the back. Hence, it is expected that unloading during flight will not alter the obtained c.g. limits. The straight line represents the loading of the fuel in the wing. For simplification, given the large number of fuel tanks, it is assumed that all the fuel is loaded at the same longitudinal position as the fuel centre of gravity. As a result, a straight line is obtained. As can be seen in the diagram, the c.g. limits are determined by the aerosol loading and the fuel loading is not found limiting in this case. A margin of 2% of the MAC, was added to the c.g. limits to obtain aft and forward c.g. of 0.088 and 0.3455, respectively. These correspond to 6.393 and 7.307 meters as measured from the nose.

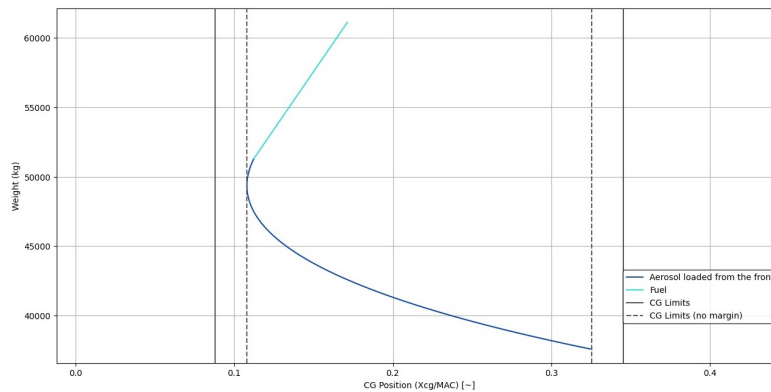


Figure 12.1: Payload and Fuel Loading Diagram

12.2. Horizontal Stabiliser

Contributors: Carmen, Blanca

In this section, the horizontal tail is designed, starting with the configuration and airfoil selection. The sizing procedure is then explained.

Horizontal Tail Configuration

With a twin-body configuration, there was an opportunity to join the two inbound horizontal stabilisers from both fuselages. This configuration was chosen because it helps reduce the overall structural weight by creating an additional connection

between the two fuselages, increasing stiffness without adding significant weight. Additionally, the horizontal stabiliser can be made longer than in a separated design, as both ends are supported.

Since the engines are mounted on the wings, the vertical position of the horizontal stabiliser can be freely chosen along the span of the vertical tail, as there is no concern about interference with the engine wake. To avoid reducing the effective aspect ratio of the vertical stabiliser, placing the horizontal stabiliser at mid-height was ruled out [36]. As a result, the two configurations considered were the conventional tail and the T-tail. Although the T-tail is generally advantageous for placing the horizontal stabiliser outside the wing wake and reducing downwash effects, a major concern with this configuration is the risk of deep stall [31].

This is prone to happen at high angles of attack where the turbulent wake from the wing is directed to the control surface, drastically reducing their effectiveness and thus possibly making stall recovery impossible [37]. Additionally, since the aerosol is to be released from the horizontal tail, a T-tail configuration would require all related systems to pass through the vertical tail, resulting in unnecessary complexity and added weight. For these reasons, a conventional tail was chosen, where the horizontal stabiliser is mounted on the fuselage.

The only possible way to satisfy the different longitudinal trim requirements at different flight conditions is to change the horizontal tail lift through a change in its angle of attack. For this, a fixed tail with an elevator was chosen since it is lighter, cheaper and structurally easier to design than an all-moving or adjustable tail. The design of the elevator will be explained later in subsection 12.4.1.

As the aircraft centre of gravity moves during cruising flight, the airfoil section must be able to create both positive and negative lift; therefore, the tailplane must behave similarly in both positive and negative angles of attack [31]. This is achieved by employing either a symmetrical airfoil section or an inverted non-symmetric one. However, due to the negative camber of the latter, undesirable pitching moments are created, and thus a symmetrical airfoil was chosen. Similar to the wing, since the aircraft flies limited within the coffin corner, a supercritical airfoil was chosen to delay shock-induced separation and reduce wave drag. Furthermore, a thick airfoil is needed to accommodate the injection systems that the horizontal tailplane contains to disperse the aerosol, as mentioned in Section 9.2. From the available NASA supercritical airfoils, the NACA SC(2)-0012 was found to have the largest thickness-to-chord ratio and thus was chosen to be employed.

Horizontal Tail Sizing

For the sizing of the tailplane, a scissor plot was generated, as shown in Figure 12.2. This plot includes both a stability line and a controllability line, which intersect to define the design space. Using the most forward and aft centre of gravity positions identified in Section 12.1, the optimal horizontal tailplane area relative to the wing area (S_h/S) can be determined to ensure stability and controllability across the full centre of gravity range. This is indicated by the black line in the plot, resulting in a value of $S_h/S = 0.143$, corresponding to a horizontal tail surface area (S_h) of 39.0 m². The stability and controllability boundaries used in the plot are given by Equation 12.2 and 12.3, respectively. The procedure described in [38] and [39] was followed to compute the necessary derivatives and parameters for the plot.

$$\frac{S_h}{S} = \frac{1}{\frac{C_{L\alpha_h}}{C_{L\alpha_{A-h}}} \left(1 - \frac{d\epsilon}{d\alpha}\right) \frac{l_h}{\bar{c}} \left(\frac{V_h}{V}\right)^2} \cdot \bar{x}_{cg} - \frac{\bar{x}_{ac} - 0.05}{\frac{C_{L\alpha_h}}{C_{L\alpha_{A-h}}} \left(1 - \frac{d\epsilon}{d\alpha}\right) \frac{l_h}{\bar{c}} \left(\frac{V_h}{V}\right)^2} \quad (12.2)$$

$$\frac{S_h}{S} = \frac{1}{\frac{C_{L_h}}{C_{L_{A-h}}} \frac{l_h}{\bar{c}} \left(\frac{V_h}{V}\right)^2} \cdot \bar{x}_{cg} + \frac{\frac{C_{m_{ac}}}{C_{L_{A-h}}} - \bar{x}_{ac}}{\frac{C_{L_h}}{C_{L_{A-h}}} \frac{l_h}{\bar{c}} \left(\frac{V_h}{V}\right)^2} \quad (12.3)$$

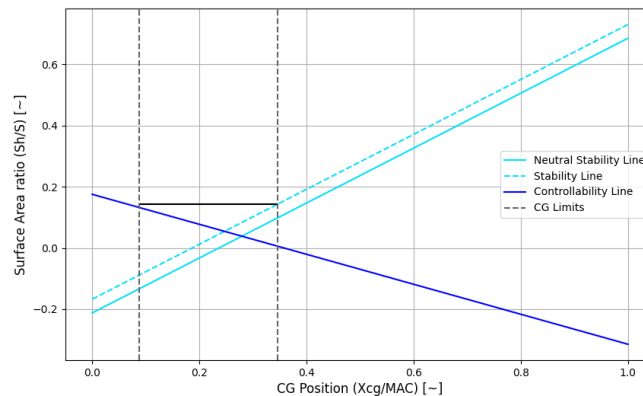


Figure 12.2: Scissor Plot used to determine the horizontal tail-to-wing surface area ratio.

To achieve the given S_h/S value, many iterations were performed by changing the positions of all aircraft components, as well as the tail length. This led to a different $x_{cg_{OEM}}$, which in turn moved the forward and aft c.g. limits after loading. Additionally, due to the change in tail length, stability and controllability lines in the scissor plots changed too, where an increase in tail length decreased the required S_h/S value as expected. These iterations were stopped once the smallest required tail surface was achieved, and the chosen tail arm length (l_t) of 13.5 m, ensured that the tip-back angle was not exceeded. The tip-back angle requirement is explained in Section 12.5

Knowing that the horizontal tail spans across the 2 fuselages, the span (b_h) is fixed to a value of 16m. With this and the obtained surface area, the aspect ratio (A_h) of 6.56 was calculated.

Although sweep is typically beneficial for increasing the critical Mach number [37] and taper helps reduce tail weight [31], for this design, where the tail connects two fuselages, the horizontal stabiliser was designed without either. This choice avoids additional structural complexity. As a result, it will have a constant chord of 2.44 meters along its entire span.

Dihedral angles are usually necessary to position the empennage outside the engine slipstream [37]. However, this is not necessary for this aircraft since the engines are positioned on the outer wings and the horizontal tail between the fuselages, and thus are already outside of the engine wake. Therefore, adding a dihedral would just add complexity to the structure, and thus it was decided not to have any.

Since the tail is fixed, the required tail incidence angle to counteract the pitching moment about the centre of gravity during cruise flight was determined [31]. This fixed setting was designed to satisfy the trim condition in cruise without the need for elevator deflection. However, small elevator inputs can still be used to trim the aircraft in other flight conditions, as discussed in subsection 12.4.1. Using the equation in Equation 12.4, a tail incidence angle of -1.73 degrees was found to be necessary.

$$i_h = \alpha_h - \alpha_f + \epsilon \quad (12.4)$$

Finally, to verify the suitability of the design, the aircraft's longitudinal trim condition was evaluated, along with a dynamic analysis, which will be discussed later in Section 12.6. For this, the sign of the longitudinal stability derivative, C_{m_α} , was examined using Equation 12.5. A negative value of this derivative is required to ensure static longitudinal stability. The analysis yielded a value of -1.02, indicating that the aircraft is statically stable and satisfies the longitudinal trim requirement.

$$C_{m_\alpha} = C_{L_{\alpha_{wf}}} (h - h_0) - C_{L_{\alpha_h}} \eta_h \frac{S_h}{S} \left(\frac{l}{\bar{C}} - h \right) \left(1 - \frac{d\epsilon}{d\alpha} \right) \quad (12.5)$$

12.3. Vertical Stabiliser

Contributors: Carmen, Blanca

The vertical tail is a major contributor in maintaining directional control. A basic aircraft design requirement is the symmetric about the x-z plane. This is desired because then the vertical tail is not required to produce any lift to maintain directional trim in a normal flight condition. To ensure this, the vertical airfoil section must be symmetric, as a nonsymmetrical one creates an aerodynamic pitching moment. A commonly applied airfoil is the NACA0012 and this was chosen for the design.

For this same reason of achieving symmetry about the x-z plane, the vertical tail incidence angle (i_v), defined as the angle between the vertical tail chord line and the aircraft x-z plane, and the dihedral angle (Γ_v), must be zero.

To start sizing the vertical stabiliser, it was first necessary to determine the volume coefficient (\bar{V}_V), which is defined as in Equation 12.6. A typical range for aircraft was found in literature to be from 0.02 to 0.12 [31], and the smallest of this was used since the wing surface and span are so large compared to the vertical tail arm (which is assumed to be equal to the horizontal tail arm). Knowing this, the total vertical tail surface area was found to be 31.9 m². This was a first estimate and was later validated during rudder sizing in subsection 12.4.3. If adjustment due to rudder size had been needed, the tail size would have been revisited.

$$\bar{V}_V = \frac{l_V S_V}{bS} \quad (12.6)$$

For the vertical tail, a low aspect ratio is desired to decrease bending moment and stress at the vertical tail root and thus decrease aircraft weight, as well as decrease induced drag, fatigue and flutter that a high aspect ratio would more likely cause. Therefore, typical values range from 1 to 2 [31], and so a value of 1.5 was chosen for this aircraft. With this and the above mentioned surface area, a span (b_v) of 4.89 m was obtained for each tail and a mean aerodynamic chord (\bar{C}_v) of 3.26 m.

Adding a taper ratio is beneficial to reduce the bending stress on the vertical tail root. However, it adds complexity to the tail manufacturing process, increases the empennage weight and reduces directional control due to a smaller yawing moment arm [31]. Therefore, a compromise between these positive and negative features was needed, and a value of 0.6 was decided, and was found to be a reasonable value based on literature [37]. With this, the chord at the root and tip was found to be 4.00 m and 2.40 m, respectively.

Increasing the sweep angle of the vertical tail increases the yawing moment arm, which improves the directional control, as well as decreases the wave drag in the high subsonic flight regime [31]. For this reason, aircraft with high airspeeds, and thus experience compressibility effects, have typical values of sweep between 35° and 50° [37]. Therefore, a value of 42° was decided.

As will be explained in subsection 12.4.3, the sizing of the rudder led to a significant reduction in the required vertical tail surface area to achieve lateral stability in engine failure conditions. By keeping the same aspect ratio, taper and sweep, and using the obtained volume coefficient of 0.0128 resulted in a new surface area of 20.4 m^2 , a span of 3.92 m, MAC of 2.61 m, chord root of 3.20 m, and a tip chord of 1.92 m.

The tail geometry parameters are summarised below, in table Table 12.1

Table 12.1: Tail Geometry Parameters

	$S \text{ [m}^2\text{]}$	$A \text{ [-]}$	$b \text{ [m]}$	$\lambda \text{ [-]}$	$\Lambda_{25} \text{ [}^\circ\text{]}$	$l_t \text{ [m]}$	$\bar{V} \text{ [-]}$	$\bar{C} \text{ [m]}$	$c_r \text{ [m]}$	$c_t \text{ [m]}$
Horizontal Tail	39.0	6.56	16	0	0	13.5	0.530	2.44	2.44	2.44
Vertical Tail	20.4	1.5	3.92	0.6	42	13.5	0.0128	2.61	3.20	1.92

12.4. Control Surfaces

Contributors: Carmen, Blanca

Control surfaces are key to control the aircraft. In this section, the elevator is sized for pitch control, the ailerons are designed for adequate roll control, and the rudder is analysed to ensure appropriate lateral stability. The obtained dimensions are summarised in Table 12.2. In the horizontal tail dimensions, as well as the sizing and integration of the ailerons and the elevator are shown in Figure 12.3.

Table 12.2: Control Surface Parameters

Elevator		Ailerons		Rudder	
$c_e/c_h \text{ [-]}$	0.38	$c_a/c \text{ [-]}$	0.25	$c_r/c_v \text{ [-]}$	0.45
$b_e/b_h \text{ [-]}$	0.9	$\delta_a \text{ [deg]}$	20	$b_r/b_v \text{ [-]}$	1
$\delta_e \text{ [deg]}$	15	$y_{ail_{in}} \text{ [-]}$	0.65	$\delta_r \text{ [deg]}$	30
		$y_{ail_{out}} \text{ [-]}$	0.95		

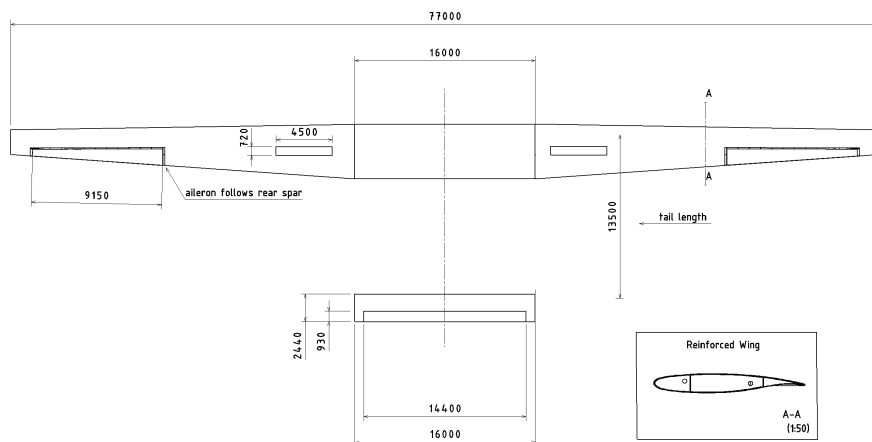


Figure 12.3: Wing and Tail dimensions

12.4.1. Elevator

The primary function of the elevator is to achieve longitudinal control. An increment in tail lift can be achieved by a deflection of the elevator, which can be approximated by Equation 12.7 [31].

$$C_{L_h} = C_{L_{\alpha_h}} (\alpha_h + \tau_e \delta_E) \quad (12.7)$$

The elevator span typically ranges from 80% to 100% of the horizontal tail span [31]. For this design, it was set to cover 90% of the horizontal tail span.

The required elevator-to-tail chord ratio was calculated for take-off conditions, since control surface effectiveness is reduced at low speeds. It must be capable of rotating the aircraft about the main landing gear with a specified angular pitch acceleration. For large transport aircraft, this requirement typically falls within 4 to 6 degrees per second squared [31]. A value of 4deg/s² was chosen to represent a more critical case.

This condition must be met with the centre of gravity at its most forward allowable position, as this demands the greatest nose-up (negative) elevator deflection. For added safety, the elevator is designed to achieve the required pitch acceleration at stall speed instead of take-off speed. Stall speed is typically 1.1 to 1.3 times lower than take-off speed, making this a more conservative design criterion [31].

During take-off rotation, the elevator must generate sufficient negative lift on the horizontal tail to produce the required nose-up pitching moment. This was calculated using the pitching moment equation shown in Equation 12.8.

$$L_h = \frac{L_{wf}(x_{mg} - x_{ac,wf}) + M_{ac,wf} + ma(z_{cg} - z_{mg}) - MTOM \cdot g(x_{mg} - x_{cg}) + D(z_D - z_{mg}) - T(z_T - z_{mg}) - I_{yy,mg}\ddot{\theta}}{x_{ac,h} - x_{mg}} \quad (12.8)$$

Here, the subscript mg refers to the main gear. Note that with the centre of gravity at its forward limit, both the aircraft weight and engine thrust generate nose-down (negative) pitching moments. The term $I_{yy,mg}$ represents the mass moment of inertia about the y-axis, taken at the main gear location, and $\ddot{\theta}$ is the specified angular pitch acceleration in radians.

The required tail lift coefficient to satisfy the requirement was found to be -0.22.

Initially, the maximum negative elevator deflection was set to be 20 degrees. With the use of Equation 12.7, and this maximum negative elevator deflection, the required effectiveness was found to be 0.44 which corresponds to an elevator to tail chord ratio of 0.21 [9]. This value is still small, given that typical values range from 0.1-0.5 [31], hence the deflection angle can be lowered.

If the elevator deflection angle exceeds 20 degrees, flow separation over the tail surface is likely to occur [31]. Near the stall of the horizontal tail, even small deflections can lead to a significant loss of pitch control effectiveness. To avoid this, the maximum elevator deflection was further lowered to 15 degrees. This adjustment resulted in a required control effectiveness of 0.59, corresponding to an elevator-to-tail chord ratio of 0.38, as summarised in Table 12.2. This value dictates the minimum required elevator area to achieve the required lift for take-off rotation at the maximum negative elevator deflection. Further reducing the deflection would require a larger chord ratio, which could also increase the risk of flow separation on the tail.

It must be checked that this 15-degree deflection does not cause the elevator to stall. The tail stall angle of attack during take-off rotation is given by Equation 12.9

$$\alpha_{h_s} = \pm \left(\alpha_{h_s, \delta_e=0} - 1.15 \cdot \frac{c_e}{c_h} \delta_e \right) \quad (12.9)$$

The tail stall angle of attack with the elevator deflection was found to decrease from 24 to 9.75 degrees, which is well over the take-off rotation angle of 5.4 degrees, calculated from Equation 12.21 in Section 12.5. Hence, there is no risk of the tail stalling during lift-off.

Furthermore, with the given elevator geometry, the longitudinal trim requirement during cruise was checked with the c.g. at its most aft position. The downwards elevator deflection required to maintain the aircraft's longitudinal trim during cruise was calculated using Equation 12.10.

$$\delta_e = - \frac{\left(\frac{T \cdot z_T}{qS\bar{c}} + C_{m0} \right) C_{L_{\delta_e}} + (C_L - C_{L0}) C_{m_{\alpha}}}{C_{L_{\alpha}} C_{m_{\delta_e}} - C_{m_{\alpha}} C_{L_{\delta_e}}} \quad (12.10)$$

z_T is the vertical distance from the c.g. to the thrust line. C_{L1} is the lift coefficient at cruise and C_{L0} is the zero-lift-coefficient. The lift coefficient due to an elevator deflection ($C_{L\delta_e}$) was calculated using Equation 12.11 and the pitching moment coefficient due to an elevator deflection ($C_{m\delta_e}$) and was approximated with Equation 12.12 where η_h is the horizontal tail efficiency parameter. The derivative $C_{m\alpha}$ was obtained from Equation 12.5.

$$C_{L\delta_e} = C_{L\alpha h} \eta_h \frac{S_h}{S} \frac{b_e}{b_h} \tau_e \quad (12.11)$$

$$C_{m\delta_e} = -C_{L\alpha h} \eta_h \bar{V}_h \frac{b_e}{b_h} \tau_e \quad (12.12)$$

Additionally, the performance of the elevator during cruise was also checked, since the low air density at the high operational altitude reduces its effectiveness. However, the required deflection angle for trim during cruise was found to be less than 1 degree. Hence, this phase was not found limiting, and the elevator will mostly be used for take-off and landing pitch control.

12.4.2. Ailerons

To ensure controllability, roll control surfaces are required. As high manoeuvrability is not necessary for this aircraft's intended application, a conventional configuration using ailerons was selected. One aileron is placed on each wing. These are sized based on the specified roll rate requirement for the most critical flight phase. This was found to be during landing, since the effectiveness of control surfaces is lowest at lower speeds. For category III aircraft, that is, aircraft with a MTOM larger than 30000kg, at the landing phase and for a level of acceptability 1, the time to achieve a bank angle of 30 degrees shall be less than 2.5 seconds [31].

The aileron-to-wing chord ratio was determined to be 0.25, since it is placed at the rear spar of the wing. This corresponds to an effectiveness of 0.46 [40]. Ailerons are located outboard of the wing, since the wing root stalls before the wing tip. Therefore, they can remain active after stall to allow for spin recovery, along with the rudder. As an initial estimation to run the iterations, the inner and outer edges of the aileron were placed at 75% and 95% along the outer part of each wing. The absence of high lift devices allowed for freedom to vary the spanwise location of the ailerons.

When ailerons are deflected more than around 25 degrees, flow separation tends to occur, which can lead to a loss of roll control effectiveness [31]. Hence, the maximum deflection was set to 20 degrees (both up and down).

The non-dimensional control derivative $C_{l\delta_a}$ is the change in rolling moment per unit change of aileron deflection, and is given by Equation 12.9 [31].

$$C_{l\delta_a} = \frac{2C_{l\alpha}\tau}{Sb} \int_{b_i}^{b_o} c(y) y dy \quad (12.9)$$

Where $C_{l\alpha}$ is wing lift curve slope, τ is the aileron effectiveness parameter and the $c(y)$ is the variation of the chord length along the span of the outer wing, which is integrated from the inner to outer positions of the ailerons.

The change of rolling moment for a given roll rate is given by Equation 12.8 [31].

$$C_{l_p} = -\frac{4(c_{l\alpha} + c_{d0})}{Sb^2} \int_0^{\frac{b}{2}} y^2 c(y) dy \quad (12.8)$$

Due to the fact that the aircraft's drag due to roll rate is not increased with an increase in roll rate, the rolling motion is initially not linear. However, when the resisting moment against the rolling motion is equal to the aileron-generated aerodynamic moment, the aircraft will continue to roll with a constant roll rate, P . This is given by Equation 12.13 [31].

$$P_{ss} = -\frac{C_{l\delta_a}}{C_{l_p}} \delta a_{\max} \left(\frac{2V_{app}}{b} \right) \quad (12.13)$$

Where V_{app} is the approach speed, which is 1.3 times the stall speed at sea-level [31]. $C_{l\delta_a}$ and C_{l_p} are the control derivatives given above, and δa_{\max} is the maximum aileron deflection.

The time to achieve the required bank angle can be calculated as shown in Equation 12.14 [31].

$$t = \sqrt{\frac{2 \cdot \phi_{req}}{P_{ss}}} \quad (12.14)$$

For landing, and at maximum aileron deflection, this time was found to be larger than the required 2.5 seconds for the initial aileron span. Several iterations were performed until the requirement was met, leading to the aileron spanning from

65% to 95% of the outer wings, as summarised in Table 12.2. Additionally, the calculations were performed for cruise conditions, where it was found that a 12-degree deflection would be sufficient to achieve the required roll rate.

12.4.3. Rudder

Two fundamental roles of the rudder are directional control and directional trim. Therefore, the rudder's design parameters are determined by directional trim and control requirements. Depending on the phase of flight and aircraft type, the rudder serves multiple functions, including crosswind landings, maintaining directional control during asymmetric thrust on multi-engine aircraft, turn coordination, and spin recovery. However, the most critical flight condition changes depending on the aircraft configuration. For wing-installed multi-engine aircraft, the critical conditions are asymmetric thrust and cross-wind landing [31], and thus only these two were considered for the design of the rudder.

Since one engine may suddenly fail during flight, the thrust of the other engine may impose a yawing moment about the aircraft's centre of gravity, disturbing the aircraft's directional trim and deviating the direction of flight. In this condition, known as the asymmetric power condition, the rudder must produce a side force that generates a moment to counteract the yawing moment caused by the operating engine. The critical asymmetric power condition occurs for a multi-engine aircraft when all the engines at one side fail at low flight speeds [31]. This speed may not exceed 1.13 stall speed at the most unfavourable c.g. location and the most critical take-off configuration. Low speeds are considered to be critical because it causes the effectiveness of the control surface to decrease. To prevent flow separation, the maximum rudder deflection allowed, both to the left and to the right, is 30°[31].

The following Equation 12.15 was used to determine the required rudder deflection to directionally trim the aircraft under asymmetric thrust conditions.

$$\delta_R = \frac{T_L \cdot y_T}{-\bar{q} \cdot S \cdot b \cdot C_{n_{\delta_R}}} \quad (12.15)$$

$$C_{n_{\delta_R}} = -C_{L_{\alpha_V}} \cdot \bar{V}_V \cdot \eta_V \cdot \tau_r \cdot \frac{b_R}{b_V} \quad (12.16)$$

Here, T_L is the thrust required to take-off with one engine inoperative, as explained in Section 10.5, while y_T is the lateral distance of the engines from the fuselage centreline. This engine placement was chosen to minimise structural loads on the wing. The term \bar{q} refers to the dynamic pressure, where the velocity is set to be 1.13 times the stall speed, as defined by the previously stated requirement [31]. The parameter $C_{n_{\delta_R}}$, given by Equation 12.16, denotes the aircraft yawing moment coefficient due to rudder deflection derivative. This derivative is influenced by two geometric ratios: the rudder-to-vertical tail span ratio (b_R/b_V) and the rudder-to-vertical tail chord ratio (C_R/C_V) (as it affects the rudder angle of attack effectiveness parameter τ_r). These ratios were treated as free variables and adjusted to ensure that the required rudder deflection remained below the maximum allowable limit of 30°.

Another important function of the rudder is to ensure a safe landing in the presence of crosswinds. During such conditions, the aircraft may deviate off the runway if not properly controlled. To prevent this, the rudder is used to align the aircraft with the runway heading and must therefore be sufficiently effective to counteract the yawing moment induced by the specified cross-wind conditions. According to airworthiness standards, aircraft must be able to carry out landings for 90° cross-winds of up to a wind velocity of 25 knots [31]. The critical aircraft speed at cross-wind landing is the minimum speed ($1.1 V_{stall}$). Solving Equation 12.17 and 12.18 simultaneously, the required rudder deflection (δ_R) for this requirement can be found. Similar to designing for asymmetric thrust, varying the geometric ratios varies the required rudder deflection.

$$\frac{1}{2} \rho V_T^2 S b \left(C_{n_0} + C_{n_\beta} (\beta - \sigma) + C_{n_{\delta_R}} \delta_R \right) + F_w \cdot d_c \cos \sigma = 0 \quad (12.17)$$

$$\frac{1}{2} \rho V_W^2 S S C_{Dy} - \frac{1}{2} \rho V_T^2 S \left(C_{y_0} + C_{y_\beta} (\beta - \sigma) + C_{y_{\delta_R}} \delta_R \right) = 0 \quad (12.18)$$

After analysing both critical scenarios simultaneously, it was found that asymmetric thrust was more critical for this aircraft as a larger rudder deflection was needed to counteract it. Through this process, the rudder was sized to its maximum allowable dimensions: $b_R/b_V = 1$ and $C_R/C_V = 0.45$, following the constraint that the rudder-to-tail chord ratio must remain below 0.5 [31], as summarised in Table 12.2.

With this rudder configuration, the required deflection was only 20.8°, well below the maximum limit of 30°, indicating that either the rudder or the tail size could be reduced. Reducing the vertical tail area was preferred to decrease the structural weight and lower bending stresses at the tail root. Through iterative adjustments, the vertical tail volume coefficient was decreased from the initial estimate of 0.02 to 0.0128. At this value, the rudder deflection required increased to 29.2°, which still complied with the 30° maximum. However, any further reduction in tail volume coefficient, would result in exceeding the allowable deflection. Therefore, 0.0128 was selected as the minimum viable value that satisfies the engine-out condition. These changes in vertical tail sizing have been reported previously in Section 12.3.

This rudder size was then checked for engine failure at cruise conditions, where at low densities present in stratospheric altitudes the rudder effectiveness also decreases. Using again Equation 12.15, but with T_L being the maximum thrust that can be delivered by one engine at cruise altitude and using the cruise velocity to obtain the dynamic pressure \bar{q} . This resulted in a necessary deflection of 10.5 degrees, and thus can be achieved by the current rudder size.

12.5. Landing Gear Design

Contributors: Carmen, Blanca

Given the aircraft's twin-body design, each fuselage is equipped with its own nose strut and main landing gear strut. The wheel dimensions were determined using a graph from Torenbeek [15], which considers the load on each wheel and the maximum allowable tyre pressure, as given by Equation 12.19 [9].

$$p = 430 \cdot \ln(LCN) - 680 \quad (12.19)$$

The Load Classification Number (LCN) represents the strength rating of major runways. Landing gear must be designed based on the lowest LCN among all runways the aircraft is expected to use. For this reason, the specifications of the airports selected for the mission, as presented in Chapter 19, were examined. The lowest LCN found was 37, at Perth Airport (PER) in Australia. The maximum allowable tyre pressure was thus determined to be 872.7 kPa.

The load on each wheel depends on the position of the centre of gravity. For this reason, the nose and main landing gears were sized based on their most critical loading conditions. The main landing gear carries the highest load when the centre of gravity is at its most aft position, while the nose gear experiences the greatest load when it is at the most forward position.

The nose gear load must carry at least 8% of the MTOM for adequate steering capabilities [15]. Hence, the main gear will support a maximum of 92% of the MTOM.

The nose wheel was placed at a fixed position in the middle of the nose cone, 0.77m from the nose. The required position of the main landing gear was then determined using moment equilibrium about the aft centre of gravity, using Equation 12.20. This ensures that the main gear is located behind the aft c.g., to account for the tip-over requirement, as will be explained below.

$$d_{mw} \cdot P_{mw} \cdot N_{mw} = P_{nw} \cdot N_{nw} \cdot d_{nw} \quad (12.20)$$

In Equation 12.20, d_{nw} and d_{mw} are the distances from the aft cg of the nose and main wheels, respectively. The main gear was found to be 8.198 m from the nose.

Using these fixed positions, the maximum load on the nose wheel was calculated with the same equation, this time using distances measured from the forward centre of gravity.

With the maximum loads on the main and nose gears known, the number of wheels was selected to ensure the loads could be supported while keeping the wheel size small enough to fit within the fuselage. Two wheels were placed on each main gear strut and two on the nose gear. Their dimensions are given in Table 12.3

Table 12.3: Gear dimensions

	Wheel radius [m]	Tire radius [m]	Tire thickness [m]
Nose landing gear	0.279	0.4318	0.089
Main landing gear	0.4826	1.092	0.343

Main Landing Gear Position Constraints

There are two constraints for the main landing gear position that must be checked. These are the tip-over angle and the tip-back angle, or minimum required scrape angle.

The tip-over angle is defined as the angle between the vertical line at the main gear location and the line connecting it to the most aft centre of gravity. According to Torenbeek [15], this angle should be greater than 15 degrees. In this design, it was measured to be 16.54 degrees, as shown in Figure 12.4, satisfying the requirement.

The minimum scrape angle is defined as the angle between the ground and the aircraft fuselage when the nose is at its maximum pitch-up position during take-off, with the tail just touching the ground and the landing gear fully extended. To avoid tip-back during rotation, this angle must be at least 5 degrees greater than the take-off rotation angle [31]. The take-off rotation angle, expressed in radians, was calculated using Equation 12.21 and based on the method described by Torenbeek [15].

$$\alpha_{TO} = \frac{1}{C_{L\alpha}} \left(C_{L_{\max, \delta_f=0}} - C_{L_0} - 0.2 \cdot C_{L_{\max, TO}} \right) \quad (12.21)$$

This was found to be 5.53 degrees. Hence, the scrape back angle must be larger than 10.53 degrees. The measured scrape angle was measured to be 12 degrees, as shown in Figure 12.4, satisfying the requirement.

The track width between the main landing gears is set to 16m, the span of the middle wing section. As a result, the lateral position of the main gears is fixed. This removes the need to account for the turnover requirement, which is typically a concern in landing gear design for conventional aircraft [15] [31].

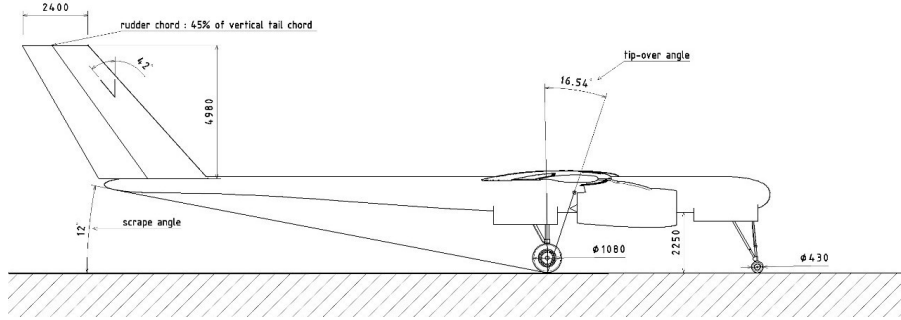


Figure 12.4: Landing Gear Position Constraints

12.6. Dynamic Stability

Contributors: Inés, Maxine

To perform a dynamic analysis of the aircraft's stability, a simplification of the equations of motion for both the symmetric and asymmetric eigenmotions of the aircraft is used, based on a number of assumptions explained below. Results from [22] indicate that cruise conditions represent the most critical phase for achieving dynamic stability, primarily due to the significant density differences at stratospheric altitudes compared to standard flight levels. Therefore, the following calculations focus on cruise conditions. Additionally, landing and take-off eigenvalues are included in the end to demonstrate that cruise is indeed the most critical case, while also enabling comparison of the resulting stability derivatives with those of conventional aircraft during low altitude operations.

Starting with the symmetric equations of motion, the following matrix is considered for the short-period oscillation, where the airspeed can be assumed to be constant, given the short oscillation period this motion shows.

$$\begin{bmatrix} C_{Z\alpha} + (C_{Z\delta} - 2\mu_c) D_c & C_{Zq} + 2\mu_c \\ C_{m\alpha} + C_{m\delta} D_c & C_{mq} - 2\mu_c K_Y^2 D_c \end{bmatrix} \begin{bmatrix} \alpha \\ \frac{qc}{V} \end{bmatrix} = \underline{0} \quad (12.22)$$

On the other hand, the following simplification is used for phugoid motion, assuming all accelerations are negligible due to the high period it presents.

$$\begin{bmatrix} C_{Xu} - 2\mu_c D_c & C_{Z0} \\ C_{Zu} & 2D_c \mu_c \end{bmatrix} \begin{bmatrix} \hat{u} \\ \theta \end{bmatrix} = \underline{0} \quad (12.23)$$

For asymmetric equations of motion, the aperiodic rolling motion is described by the following equation, assuming that the aircraft can only roll about the longitudinal axis.

$$(C_{\ell_p} - 4\mu_b K_X^2 D_b) \frac{pb}{2V} = 0 \quad (12.24)$$

The Dutch roll is described by the set of equations shown below, under the assumption that the rolling component is discarded.

$$\begin{bmatrix} C_{Y\beta} - 2\mu_b D_b & -4\mu_b \\ C_{n\beta} & C_{nr} - 4\mu_b K_Z^2 D_b \end{bmatrix} \begin{bmatrix} \beta \\ \frac{rb}{2V} \end{bmatrix} = \underline{0} \quad (12.25)$$

Finally, spiral motion is calculated as per equation Equation 12.26, approximating the motion by assuming all linear and angular accelerations to be negligible.

$$\begin{bmatrix} C_{Y\beta} & C_L & 0 & -4\mu_b \\ 0 & -\frac{1}{2} D_b & 1 & 0 \\ C_{\ell\beta} & 0 & C_{\ell_p} & C_{\ell_r} \\ C_{n\beta} & 0 & C_{n_p} & C_{n_r} \end{bmatrix} \begin{bmatrix} \beta \\ \varphi \\ \frac{pb}{2V} \\ \frac{rb}{2V} \end{bmatrix} = \underline{0} \quad (12.26)$$

In order to solve these equations of motion and obtain the eigenvalues that characterise the stability of the aircraft, a number of derivatives are calculated. From previous calculations for control surface sizing and analytical expressions found in [41],

all aerodynamic derivatives are calculated, as shown in Table 12.4. It is important to note that these equations are based on steady flight conditions, which is appropriate given that cruise is being evaluated in this case.

Table 12.4: Stability Derivatives

V	$= 206.5 \text{ m/s}$	μ_b	$= 31.54$	μ_c	$= 684.5$
		K_X^2	$= 0.0165$	K_Z^2	$= 0.0170$
C_{Y_β}	$= -0.392$	C_{ℓ_β}	$= -0.0254$	C_{n_β}	$= 0.037$
		C_{ℓ_p}	$= -1.0991$	C_{n_p}	$= -0.10382$
		C_{ℓ_r}	$= 0.0775$	C_{n_r}	$= -0.0403$
C_{X_u}	$= -0.0452$	C_{Z_u}	$= -1.7523$	C_{Z_0}	$= -0.8761$
C_{Z_α}	$= -5.3566$	$C_{Z_{\dot{\alpha}}}$	$= -0.2142$	C_{Z_q}	$= -2.524$
C_{m_α}	$= -0.9154$	$C_{m_{\dot{\alpha}}}$	$= -1.017$	C_{m_q}	$= -5.148306$

Once all these derivatives are determined, the following eigenvalues are found for the dynamic response of the aircraft.

Table 12.5: Eigenvalues for simplified equations of motion for cruise condition

Parameter	Short Period	Phugoid	Aperiodic Roll	Dutch Roll	Spiral
$\lambda_{\text{simplified}}$	$-0.3495 \pm 2.158j$	$-0.0009611 \pm 0.03724j$	-1.419	$-0.03359 \pm 0.5001j$	0.001587

Through the eigenvalues obtained, it can be observed that the aircraft presents stability in all eigenmotions except for spiral motion, which is considered acceptable based on REQ-SYS-ARD-6. However, there is a discrepancy in some of the eigenvalues of the aircraft compared to the normal aircraft dynamic response, specifically short-period and aperiodic roll. These last eigenmotions are characterised by big damping, and therefore, a relatively big real part is present in the eigenvalues of these motions. However, since the aircraft is flying in the stratosphere, the density of air is significantly smaller than the density at normal flight altitudes, affecting the non-dimensional mass and moment coefficient magnitudes, leading to different eigenvalue magnitudes from conventional aircraft at normal flight regimes. For comparison with usual flight conditions, takeoff and landing are analysed and can be seen in Table 12.6. As expected, the real part for both short-period and aperiodic roll in these conditions is considerably larger and within the expected order of magnitude.

Table 12.6: Eigenvalues for simplified equations of motion for take-off and landing

Condition	Parameter	Short Period	Phugoid	Aperiodic Roll	Dutch Roll	Spiral
Take-off	$\lambda_{\text{simplified}}$	$-1.603 \pm 2.516j$	$-0.003036 \pm 0.1489j$	-6.529	$-0.248 \pm 0.718j$	0.003133
Landing	$\lambda_{\text{simplified}}$	$-1.816 \pm 2.852j$	$-0.003440 \pm 0.2046j$	-7.399	$-0.2809 \pm 0.8140j$	0.004231

12.7. Verification and Validation

Contributors: Maxine, Carmen, Blanca

To verify the control surface designs, all code scripts were carefully checked to ensure that the equations were implemented correctly. Detailed calculations for a theoretical aircraft with known parameters were taken from the book *Aircraft Design: A Systems Engineering Approach* [31]. These parameters were used as inputs for a series of unit tests, and the resulting outputs matched those presented in the book. For the tail sizing, all values obtained in the code were verified with the values from the 2016 DSE project *Stratospheric Aerosol Geoengineering Aircraft (SAGA)* [22] and the 2023 DSE project *European Stratospheric Research Aircraft (ESRA)* [23], due to the high-altitude mission similarities.

The dynamic stability calculations used a series of approximations to determine the stability derivatives. In order to verify that all formulas were correctly implemented, a series of unit tests was performed. These tests focused on hand calculations with simple values, checking all calculations performed and their implementation in the eigenmotion calculations.

Validation of the dynamic stability was performed through comparison of validated values [22]. This acts as a sanity check, indicating if the results are within the expected range for all flight stages. As can be seen in Table 12.7, values are comparable for phugoid and aperiodic roll time to half period. However, values vary significantly for short-period motion, Dutch roll, and spiral. As discrepancies remain at sea-level conditions, these changes may be due to a vastly different aircraft geometry or assumptions made during the analysis. Therefore, further analysis using CFD tools is necessary to address these discrepancies and reduce the assumptions made during the future detailed design phase.

Table 12.7: Eigenmotion Parameters and Model Comparisons

Eigenmotion	Parameter	Cruise	Take-off	Landing	Validation sea-level	Validation 20km
Short period	ω_n [s ⁻¹]	2.19	2.516	2.852	0.743	0.726
	ζ [-]	0.16	0.537	0.537	1.171	0.641
Phugoid	ω_n [s ⁻¹]	0.037	0.149	0.205	0.045	0.015
	ζ [-]	0.026	0.020	0.016	0.028	0.028
Aperiodic roll	$T_{1/2}$ [s]	0.488	0.106	0.0936	0.158	0.839
Dutch roll	ω_n [s ⁻¹]	0.501	0.718	0.814	0.043	0.036
	$T_{1/2}$ [s]	20.64	2.80	2.46	35.1	190
Spiral	T_2 [s]	1186.01	221.24	163.83	11.061	45.21

12.8. Sensitivity Study

Contributors: Carmen, Blanca

A sensitivity study was performed to investigate how the required horizontal stabiliser area changes with the chosen tail arm, assuming a fixed wing position. The tail arm, l_t is defined as the distance between the aerodynamic centres of the wing and horizontal tail.

Moving the tail further away from the wing results in a longer fuselage, which changes the operational empty weight C.G. This in turn results in different forward and aft cg limits, as explained in Section 12.1. Additionally, the tail arm affects the stability and controllability lines in the scissor plot, as shown in Figure 12.2, leading to a different allowable design space. For each tail length, the selected surface area is the minimum required to remain within this region. These values are shown in Figure 12.5. As the tail arm increases, the required tail surface area is expected to decrease, since a longer moment arm allows the tail to generate the necessary pitching moment with less lift. However, as shown in Figure 12.5, beyond a certain length, further increasing the tail arm shifts the C.G. limits too far aft, causing an increase in tail area. For visualisation, the generated scissor plots for 10.5m and 15.5m tail arms are shown in Figure 12.6 and Figure 12.7 respectively.

An optimal length of 13.5 metres results in the minimum required stabiliser area. Hence, the results of this sensitivity study prove that the chosen tail arm is the optimal for this design.

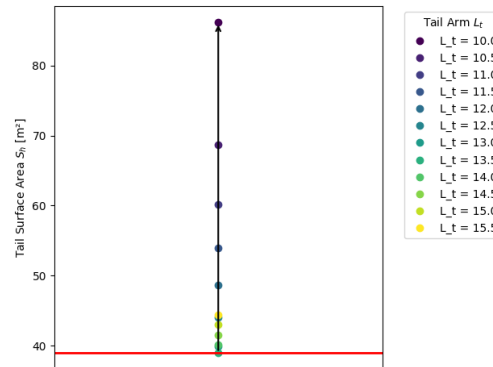


Figure 12.5: Horizontal tail surface area sensitivity to change in tail arm

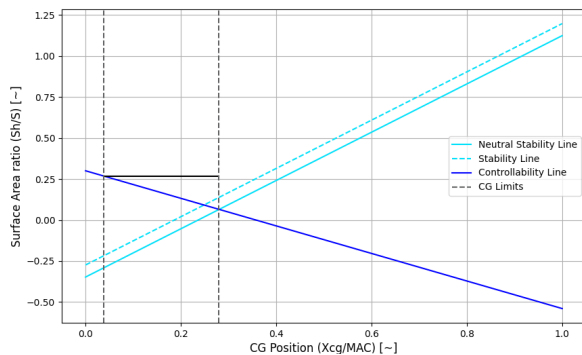


Figure 12.6: Scissor Plot for a 10m Tail Arm

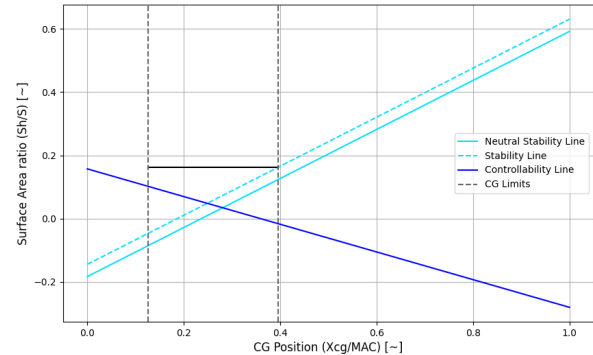


Figure 12.7: Scissor Plot for a 15.5m Tail Arm

Structural Analysis

The design of the wingbox is a multi-faceted process, and for each step, detail is incredibly important. First, the implemented design methodology is explained. Section 13.2 explains the loading the wingbox has to withstand. Afterward, in Section 13.3, a design selection is performed in which materials and string types are chosen. Then the design of the wingbox is analysed in to see if the design is feasible. Finally, a dynamic analysis is performed in Section 13.5 to determine the aeroelastic characteristics.

13.1. Design Methodology

Contributors: Pavel

The first step in the design process was choosing the model used for analysis. In this case, the wingbox was idealised as a boom-skin structure, where stringers and spar caps were treated as discrete boom areas. From Chapter 8 the wingspan, airfoil coordinates, and chord length are used to initialise the wing geometry. Based on this geometry, the placement wingbox with its spars and stringers is determined.

Once the geometry and parameters of the wing were defined, a Python-based tool was used to assess the structural performance. This script calculated the loading of the wingbox and evaluated internal shear forces and bending moments. Moreover, the cross-sectional properties along the span were reviewed for key failure modes. Furthermore, the total mass and internal volume of the wingbox were calculated.

If the structure passed all failure criteria, the next step involved evaluating its stiffness characteristics. Spanwise deflection and twist distributions were calculated and compared against design constraints to verify structural feasibility.

13.2. Loading

Contributors: Pavel, Barnabas

Understanding the various loads acting on the aircraft is essential for the structural design and verification of the wingbox. The forces that the wingbox must withstand are calculated in this section, and key loading scenarios are identified based on regulatory requirements.

13.2.1. Loads on the Structure

To ensure sufficient structural strength, limiting loading cases had to be identified. For the first step of the analysis, given the high aspect ratio and the modest fuselage, loads of the weight groups presented in Chapter 7 were determined along the wingspan. For the internal loading, two loading cases were considered to ensure that the structure is suitable for ground operations as well as in-flight conditions.

The wing structure weight was simplified as a uniform load along the span. This approach is conservative, as with the presence of taper, the structural weight is lower closer to the tip, lowering the resultant bending moment. In the wing, fuel is stored in tanks that were similarly simplified, using a uniformly distributed weight spanning from 0.1 to 0.9 spanwise location.

The lift was idealised to be elliptical, which is desired for maximum aerodynamic efficiency and results from the taper. In reality, the lift is usually reduced close to the wing tips; hence, this assumption was also considered conservative.

The engines were considered as point masses at 33% and 66% spanwise locations. The positioning of the engines resulted from calculations to reduce the maximum bending moment at the wing roots by finding the location where the positive moment in flight conditions equals the negative moment on the ground. This way, the weight of the wing is minimised, assuming that the wingbox has symmetric bending stiffness.

Lastly, the fuselages were placed at -8 m and +8 m locations from the midpoint of the span, which complies with ICAO code F regulations[16]. The fuselages, given the small relative diameter to the wingspan, were also taken as point masses. In addition to the value listed for the fuselage, weights of smaller components were added to the fuselage location, as these were assumed to be placed in the fuselage. The mass of the fuselage group was obtained by subtracting wing mass (M_w), engine mass (M_e), and fuel mass (M_f) from MTOM to guarantee that all the components adding to the weight are covered.

13.2.2. Load factor

According to the Code of Federal Regulations (CFR) for transport-category aircraft¹, aircraft structures must be capable of withstanding specific limit load factors resulting from both manoeuvres and gust loads. These requirements resulted in the following limiting load factors: $n_{ult_{pos}} = 3.8$ and $n_{ult_{neg}} = -1$. The associated manoeuvre–gust envelope is shown in Figure 13.1.

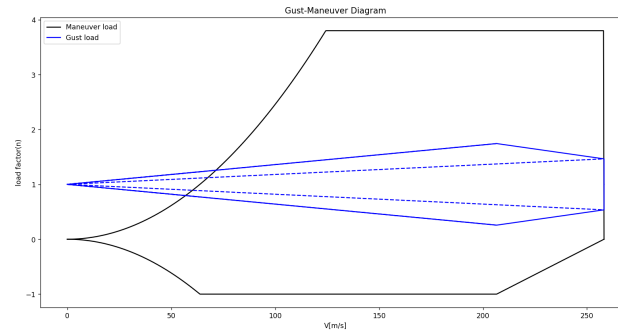


Figure 13.1: Manoeuvre-gust Diagram

From the figure, two load cases could be determined. The first case is a load factor of 3.8 with a speed of 258 m/s, and the second case is a load factor of -1 with a speed of 206 m/s. These values were used to determine the loads on the structure. An additional safety factor of 1.5 was applied to the limiting load factors to determine the ultimate load factor.

13.3. Design Selection

Contributors: Pavel

This section outlines the design choices made for the wingbox regarding the geometry, materials and structural components. These choices were based on standard aerospace practices and performance.

13.3.1. Cross-Section Geometry

The wingbox cross-section consists of two spars connected by the upper and lower wing skins, which were modelled as I-beams and placed at 25% and 75% of the chord length². Between the spars, the skin is reinforced by stringers, which were spaced uniformly along both the upper and lower skin. This uniform spacing ensures effective load distribution and minimises the risk of local buckling. Figure 13.2 is an engineering drawing illustrating the placement of spars and stringers within the wing box cross-section.

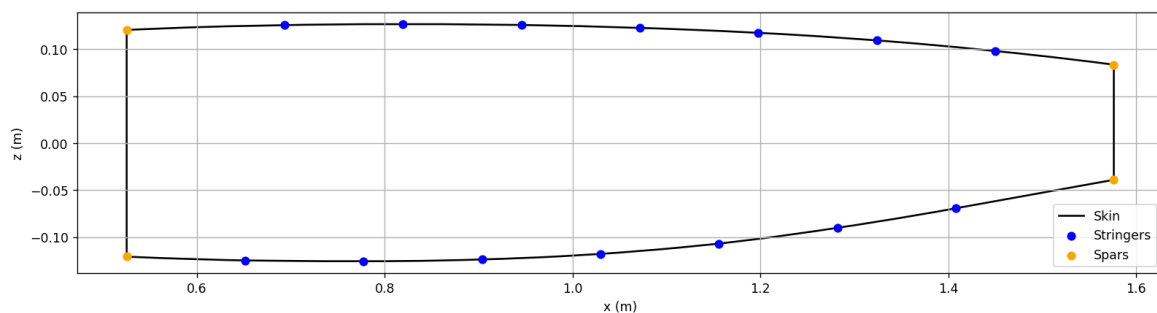


Figure 13.2: Cross-sectional View of the Wingbox at the Tip

13.3.2. 3-D Geometry

The wingbox extends spanwise between the main structural ribs and follows the aerodynamic planform of the wing. Using the Burgess rule [42], a total of 42 ribs were placed in each outer wing, while there are 30 ribs in the inner wing between the two fuselages. The most common rib spacing is 0.2 m - 1.0 m³. Accordingly, ribs were spaced at 0.2 m near the wing root, increasing gradually to 1.0 m toward the tip.

Furthermore, the wing was split into three distinct parts. The outer wing was split into two regions: the root configuration spans the first two-thirds of the outer wing, while the tip configuration covers the remaining third. The wing between the

¹URL: <https://www.ecfr.gov/current/title-14/chapter-I/subchapter-C/part-25/subpart-C/subject-group-ECFR3e855ea22ea15d0>cited 18 June 2025

²URL: https://www.fzt.haw-hamburg.de/pers/Scholz/H00U/AircraftDesign_7_WingDesign.pdf?cited 18 June 2025

³URL: https://delftxdownloads.tudelft.nl/AEASMix_Introduction_to_Aerospace_Structures_and_Materials/Module_3/AEASMix_2018_305_Ribs-slides.pdfcited 18 June 2025

fuselages was the last part; here a constant configuration is assumed.

13.3.3. Material Selection

In the aerospace industry, multiple materials are often considered, such as aluminium, steel, titanium, and composites [43]. In the end, aluminium alloys were considered most suitable for the design, as they have an excellent strength-to-weight ratio while simultaneously being recyclable. A trade-off study between several aluminium alloys was conducted, with their key properties summarised in Table 13.1.

Alloy	ρ [g/cm ³]	UTS [MPa]	σ_y [MPa]	E [GPa]	G [GPa]	α [$\mu\text{m}/\text{m}^\circ\text{C}$]
2014-T3 ⁴	2.8	405	245	72.4	28	22.7
2024-T86 ⁵	2.78	515	440	72.4	28	23.2
2324-T39 ⁶	2.77	475	370	72.4	27	23.2
7050-T7651 ⁷	2.83	552	490	71.7	26.9	25.4
7075-T6 ⁸	2.81	572	503	71.7	26.9	23.4

Table 13.1: Aluminium Alloy Material Properties

Ultimately, the 7075-T6 and 2024-T86 aluminium alloys were chosen. The 7075-T6 will be used for the stringers and spars in the wingbox as it has a high stiffness-to-weight ratio and is widely used in aerospace applications. Moreover, its high yield strength makes it well-suited for withstanding bending and shear loads encountered in the wing structure, particularly in the spar caps and stringers, where mechanical strength is critical.

However, the 2024-T86 alloy will be used for the skin of the wingbox. The 2024-T86 alloy has a lower density than the 7075-T6 alloy, which allows for a lightweight structure. Furthermore, the skin is mostly used to carry the shear present in the structure, and this alloy has a higher shear modulus.

13.3.4. Stringer Selection

Multiple stringers can be used for the wingbox as shown in Figure 13.3, each of these stringers has its strengths and weaknesses, but for the wingbox Z-stringer was chosen.

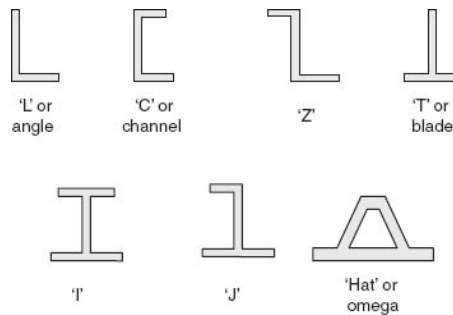


Figure 13.3: Stringer-Types

Z-stringers were selected due to their favourable structural characteristics. The Z-shaped profile provides good resistance against local buckling and torsion while keeping the manufacturing, assembly, and maintenance relatively easy. The dimensions of the Z-stringer are presented in Figure 13.4, but for the sake of simplifying the analysis, both flanges are assumed to have the same width.

⁴URL: <https://www.matweb.com/search/DataSheet.aspx?MatGUID=99d7172865024225a08cb274cd499648&ckck=1> cited 18 June 2025

⁵URL: <https://www.matweb.com/search/DataSheet.aspx?MatGUID=604ac627c0d04393be03554f9e39915bc> cited 18 June 2025

⁶URL: <https://www.matweb.com/search/DataSheet.aspx?MatGUID=4f69ae41e6a74640b2bbe4d010e8faa0> cited 18 June 2025

⁷URL: <https://www.matweb.com/search/DataSheet.aspx?MatGUID=a8298bba8d02486c97c06990a3c215d9> cited 18 June 2025

⁸URL: <https://www.matweb.com/search/DataSheet.aspx?MatGUID=4f19a42be94546b686bbf43f79c51b7d> cited 18 June 2025

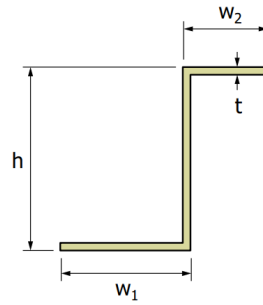


Figure 13.4: Z-stringer Dimensions

13.4. Wingbox Analysis

Contributors: Pavel

The wingbox analysis began by calculating the section properties of the aircraft; these properties were evaluated along one centimetre intervals.

13.4.1. Section Properties

As mentioned, the cross-section was idealised using boom area theory, which allowed for the calculation of stiffness properties and internal stresses under various loading conditions. Firstly, the centre of gravity of each cross-section was calculated with the equations below, after which the coordinates were shifted for further calculations.

$$\bar{x} = \frac{\sum_{i=1}^n B_i \tilde{x}}{\sum_{i=1}^n B_i} \quad \bar{z} = \frac{\sum_{i=1}^n B_i \tilde{z}}{\sum_{i=1}^n B_i}$$

The moments of inertia of each cross-section were then calculated using the following equations.

$$I_{xx} = \sum_{i=1}^n z_i^2 B_i \quad I_{zz} = \sum_{i=1}^n x_i^2 B_i \quad I_{xz} = \sum_{i=1}^n x_i z_i B_i$$

These values measure the cross-sectional stiffness and were subsequently used to calculate the stresses in the boom. A preliminary estimate of the polar moment of inertia of the wingbox was made by using Equation 13.1 to verify whether the wingbox complies with the aeroelasticity requirements.

$$J = I_{xx} + I_{zz} \quad (13.1)$$

13.4.2. Forces

In Section 13.2, the loading on the wing was calculated. The internal shear force results in a shear flow around the wingbox. As the wingbox is a closed section, the shear flow was broken down into its basic shear flow(q_b) and its complementary shear(q_{s0}). These shear flows were calculated with Equation 13.2 and Equation 13.3 respectively.

$$q_b = -\frac{V_z I_{zz}}{I_{xx} I_{zz} - I_{xz}^2} \left[\sum_{i=1}^n B_i z_i \right] + \frac{V_z I_{xz}}{I_{xx} I_{zz} - I_{xz}^2} \left[\sum_{i=1}^n B_i x_i \right] \quad (13.2)$$

$$q_{s0} = -\frac{\oint (q_b) ds}{\oint ds} \quad (13.3)$$

These shear flows can then be summed up to get the resulting shear flow from the shear force, see Equation 13.4.

$$q_s = q_b + q_{s0} \quad (13.4)$$

Since the shear force does not act on the shear centre, a resulting torque will be produced. The centre of pressure on the wing was assumed to be at 25% of the chord length, which was used to calculate the shear centre. The torque produced by the shear force is then simply the shear centre multiplied by the shear force; this resulted in a shear flow from the torque, calculated with the equation below.

$$q_T = \frac{T}{2A_m} \quad (13.5)$$

In addition to shear and torsion, the structure must also withstand bending. The bending experienced by each boom follows from Equation 13.6

$$\sigma_y = \frac{M_x I_{zz} z - M_x I_{xz} x}{I_{xx} I_{zz} - I_{xz}^2} \quad (13.6)$$

Moreover, due to temperature changes and different thermal expansion coefficients, the structure experiences thermal stress. It is assumed that the spar caps and the stringer are perfectly bonded to the skin which results in Equation 13.7 and Equation 13.8 for the thermal stresses of the structure.

$$\sigma_1 = \frac{E_1 E_2}{E_1 + E_2} \cdot (\alpha_2 - \alpha_1) \cdot \Delta T \quad (13.7) \quad \sigma_2 = -\sigma_1 \cdot \frac{E_1}{E_2} \quad (13.8)$$

The resulting thermal stresses are approximately 0.5 MPa, which is significantly lower than the bending stresses of the wing; therefore, these stresses are ignored.

The skin of the wingbox contributes to the boom area of each element, so Equation 13.9 and Equation 13.10 were used to take this into account.

$$B_1 = \frac{t_{\text{skin}} b}{6} \left(2 + \frac{\sigma_2}{\sigma_1} \right) \quad (13.9) \quad B_2 = \frac{t_{\text{skin}} b}{6} \left(2 + \frac{\sigma_1}{\sigma_2} \right) \quad (13.10)$$

Given that the skin contribution is known, the moments of inertia and stresses were recalculated.

13.4.3. Failure Analysis

Multiple failure modes of the wingbox were considered such as crippling, shear buckling, Euler buckling, and yielding. The failure did not consider the coupling of different forces for simplification.

Crippling

The first failure mode that was checked is crippling, as the wingbox is a stiffened panel. The first step in calculating the crippling of the wingbox was to calculate the crippling of the supporting structure, including spar caps and stringers. This was done by calculating the crippling stress of each section using Equation 13.11 and then calculating the crippling stress of the whole part by using Equation 13.12.

$$\frac{\sigma_{cc}^{(i)}}{\sigma_y} = \alpha_{al} \left[\frac{C}{\sigma_y} \frac{\pi^2 E}{12(1-\nu^2)} \left(\frac{t}{b} \right)^2 \right]^{1-n_{al}} \quad (13.11)$$

$$\sigma_{cc} = \frac{\sum \sigma_{cc}^{(i)} A_i}{\sum A_i} \quad (13.12)$$

As aluminium alloys were used, the values for α_{al} and n_{al} were 0.8 and 0.6, respectively. The value of C depends on how the section is supported. Here, Figure 13.5 shows the coefficient value C for different boundary conditions and aspect ratios (a/b).

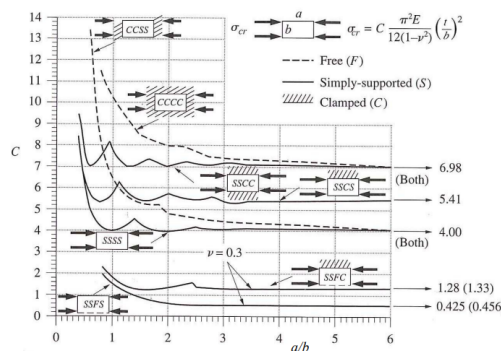


Figure 13.5: Buckling Coefficient[44]

First, $a/b > 6$ was assumed so that the asymptotic value was used to produce a conservative estimate. The flanges of the stringer are simply supported with a free end, while the web is simply supported all around, which led to C values of 0.425 and 4.0, respectively. For the spars, both the flanges and web are simply supported, which led to a C value of 4.0 for both. Lastly, the skin is assumed to be simply supported as well to provide a conservative measure.

Applying a stiffener to the skin improves its structural rigidity, thus providing better support for this portion of the skin. Hence, the likelihood of buckling is significantly reduced. Now, the effective width ($2w_e$), which is the part of the skin that will be able to carry the same stress as the stiffener, could be calculated using Equation 13.13.

$$2w_e = t \sqrt{\frac{C\pi^2}{12(1-\nu^2)}} \sqrt{\frac{E}{(\sigma_{cc})_{stiffener}}} \quad (13.13)$$

Here, the constant for C is different from the buckling coefficient and was based on the stiffener pitch and thickness of the skin, as displayed in Figure 13.6.

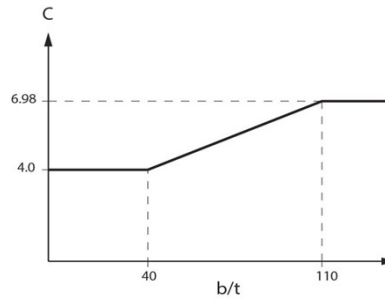


Figure 13.6: Effective Width Coefficient[44]

The crippling stress of the skin was then determined by Equation 13.14, taking into account the effective width.

$$\sigma_{cr} = C \frac{\pi^2 E}{12(1-\nu^2)} \left(\frac{t}{b} \right)^2 \quad (13.14)$$

As such, the crippling stress of every component of the wingbox was calculated. Thus, Equation 13.11 could be used again for the entire wingbox.

Shear buckling

Another possible buckling mode is shear buckling, specifically shear buckling of the skin and spar webs, since these carry the shear flow. The critical shear stress could be calculated by using Equation 13.15, which is identical to Equation 13.14 but with a different coefficient.

$$\tau_{cr} = \frac{\pi^2 k_s E}{12(1-\nu^2)} \left(\frac{t}{b} \right)^2 \quad (13.15)$$

Similarly to the crippling coefficient discussed above, k_s depends on the support of the structure and the aspect ratio. As such Figure 13.7 shows the values for this coefficient for different cases.

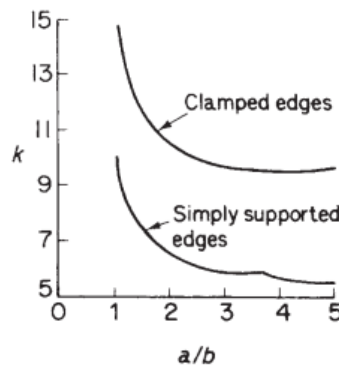


Figure 13.7: Shear Buckling Coefficient[45]

As before, a large aspect ratio is assumed. Hence, the asymptotic value could be used. Here, the skin was again assumed to be simply supported, similarly to crippling.

Euler Buckling

The equation used to describe Euler buckling is Equation 13.16

$$P_{cr} = C \frac{\pi^2 EI_{xx}}{L^2} \quad (13.16)$$

Since the stringers and spar caps can be modelled as columns, this failure mode is evaluated for them. The column length L corresponds to the rib spacing. The constant C depends on the boundary conditions of the structure. As the ribs clamp the stiffeners on both sides, a value of 4 is taken for C .

Yielding

The final failure mode taken into account was the yield of the wingbox. Although yielding was most likely not the primary failure mode, it was used as a sanity check for the wingbox. Yielding simply occurs when the stress of the boom exceeds the yielding stress of the material.

13.4.4. Loading diagrams

The resulting moments and torque of the wingbox led to a deflection and twist of the wingbox. The positive load factor discussed in Section 13.2, was taken as the loading case. For the deflection, another load case was considered, as this was limiting for the sizing of the landing gear.

Deflection

The deformation of the wingbox consists of both shear deformation and moment deformation. As the beam is long, the deformation from shear was neglected. Equation 13.17 was used to calculate the deflection by integrating twice along the span of the wing.

$$M_x(y) = -EI_{xx}(y) \frac{d^2 v}{dy^2} \quad (13.17)$$

To solve this differential equation, the following initial conditions were applied at the root:

$$v(0) = 0$$

$$\theta(0) = 0$$

Here, $\theta(y) = \frac{dv}{dy}$ represents the slope of the deflection. These conditions assumed a rigid attachment of the wingbox to the fuselage, resulting in zero initial displacement and rotation. The resulting internal moment and deflection diagrams are shown in Figure 13.8 and Figure 13.9 respectively for the $n_{ult_{pos}}$ loading case.

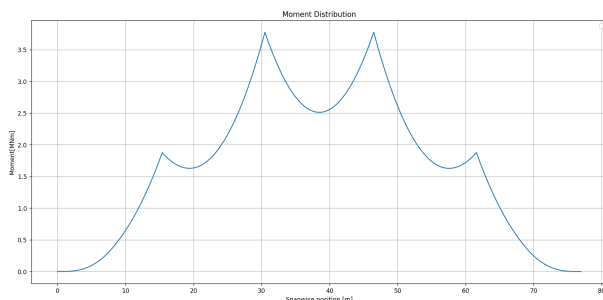


Figure 13.8: Moment Distribution

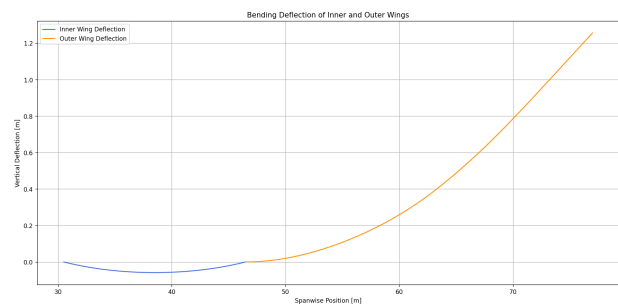


Figure 13.9: Bending Deflection

As a general rule of thumb, wing deflection should remain below 10–15% of the span.⁹ Both the inner and outer wings comply with this requirement.

This was not the only requirement for the deflection of the wing; for the landing gear sizing, it was important to know how much the wing and engine deflect to ensure they do not touch the ground. The limiting case for the downward deflection was determined to be take-off. To determine this the deflection of the wing is calculated as if it is parked and then a load factor of 1.5 is applied to account for dynamic loads. The resulting moment distribution and deflection are shown in Figure 13.10 and Figure 13.11 respectively.

⁹URL: https://elib.dlr.de/140326/1/2020_dlrmagazin-166-bending-instead-of-snapping.pdf?cited 18 June 2025

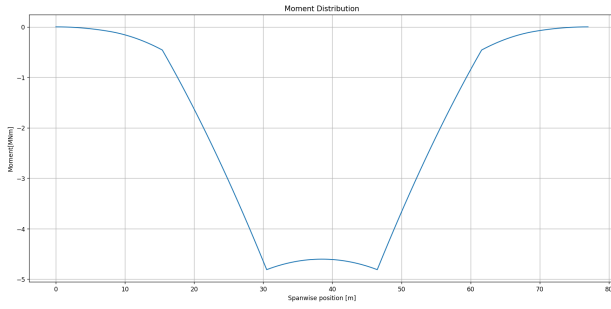


Figure 13.10: Moment Distribution

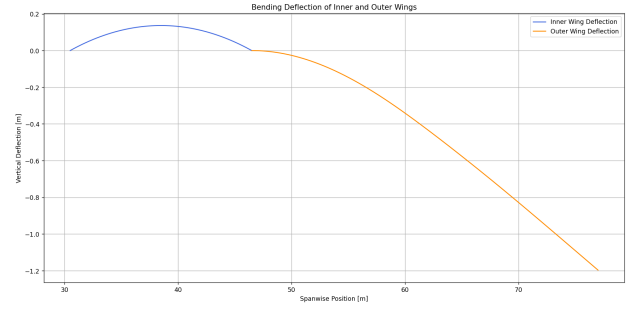


Figure 13.11: Bending Deflection

Twist

The resulting torque on the structure from the shear force twists the wingbox along the span. By integrating Equation 13.18 the twist along the span of the wing was obtained

$$\frac{d\theta}{dy} = \frac{T(y)}{4A_m^2(y)G} \oint_{L_m} \frac{1}{t} ds \quad (13.18)$$

Again, the differential equation for twist needed an appropriate initial condition to be solved. It was again assumed that the wingbox is rigidly attached to the fuselage, resulting in $C = 0$ as the initial condition. The corresponding torque and twist diagrams Figure 13.12 and Figure 13.13 are from the $n_{ult_{pos}}$ loading case.

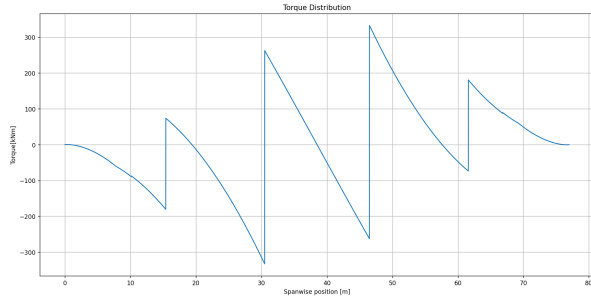


Figure 13.12: Torque Distribution

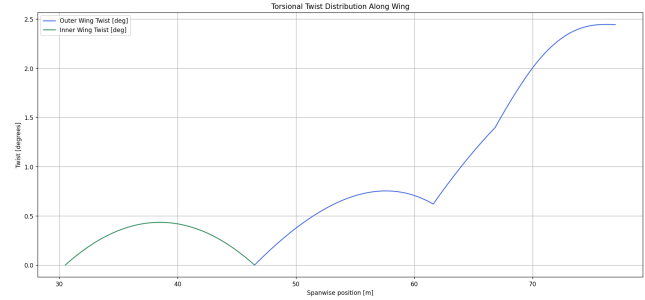


Figure 13.13: Torsional Twist

13.4.5. Fatigue

A preliminary fatigue analysis was performed on the wingbox to determine whether the lifetime is sufficient for the mission. The fatigue of the structure is heavily dependant on the S-N curve of the material used in the structure. No sufficient information on the S-N curve of the materials used in the wingbox could be found so instead the S-N curve of aluminium 2017-T4 was used as a reference [46]. The method used to determine the life-time of the aircraft was based on Megson [45]. The life of the aircraft, in terms of flights, is shown in Equation 13.19

$$N_{flight} = \frac{1}{D_{total}} \quad (13.19)$$

Where D_{total} is the total damage inflicted on the wingbox which is governed by Equation 13.20

$$D_{total} = D_{GAG} + D_G R_{av} + D_{extra} \quad (13.20)$$

The damage caused by the ground–air–ground cycle is D_{GAG} which is calculated from the take-off and cruise loading. A life factor of 3 and a safety factor of 1.5 was applied to allow for the variability of loading. D_G is the damaged sustained by the aircraft per km by gusts which is multiplied by the range, R_{av} , to gain the total damage from gusts. R_{av} follows from the flight profile while D_G was approximated by Equation 13.21

$$D_g = \frac{46.55}{2l_{10}} \left(\frac{K_n}{C} \right)^2 \left(\frac{k_1 V_e}{S_\infty} \right)^{5.26} \quad (13.21)$$

The constant K_n is taken as 1.43 to ensure a high lifetime while C and S_∞ follow from the S-N curve. S_∞ is the stress at which the S-N curve is approximately flat. C is defined by Equation 13.22

$$C = \left(\frac{S_a}{S_\infty} - 1 \right) \sqrt{N_a} \quad (13.22)$$

Here S_a and N_a are reference values on the S-N curve. The amount of gusts per $km(l_{10})$ is determined by ESDU data¹⁰. V_e is the equivalent airspeed which is taken from the flight profile and k_1 , the gust correction factor, is set to one as the aircraft flies at a high altitude where gusts are weaker. Lastly, the D_{extra} value is taken as 25% of the total damage to account for other fatigue inducing events. This leads to 12364 flights which amounts to 24.7 years of service. However, the calculations performed are a preliminary estimate and aluminium 2017-T4 is less durable than the actual materials chosen for the wingbox. Furthermore, with proper maintenance and replacement of parts the life-time can be extended.

13.5. Dynamic analysis - Aeroelasticity

Contributors: Barnabás

In addition to the static loads described in Section 13.2, the dynamic behaviour of the structure also needed to be assessed. The interactions of inertia-, aerodynamic- and elastic forces required special attention when setting the structural requirements to ensure integrity in various operating conditions. Based on their oscillatory nature, aeroelastic effects are commonly split into static- (see subsection 13.5.2) and dynamic (see subsection 13.5.3) phenomena [47]. Given the dynamic occurrence, periodic aeroelastic phenomena are defined by their frequencies in the time domain, while static modes occur due to dynamic pressure; both are proportional to the free-stream velocity. On the other hand, due to the nature of the mission, the range of operating speeds is tightly determined. The objective of the analysis was to ensure that the structure has sufficient elastic properties to limit and withstand the considered static and dynamic loads in the required cruise conditions. The most relevant effects of each will be treated separately.

13.5.1. Model setup and assumptions

Given the exceptional complexity of fluid dynamics, in this preliminary stage of the design, a simplified model was used for the first analysis. As a common practice in engineering, to account for uncertainties, a conservative approach needed to be ensured, while having the accuracy to enable an efficient design. The assumptions and models used for different calculations are described in the following paragraphs.

In subsection 13.5.2 and subsection 13.5.3, quasi-steady, subsonic flow was assumed for the analysis. This implies that the flow characteristics are independent of time; thus, the wing does not experience excitation from the airflow. Furthermore, due to the entirely subsonic flow, the effects of shockwaves are neglected. The response of the system was determined using linear equations of motion, and due to the non-oscillatory nature of the phenomena, deviations were assumed to be instantaneous. As a result, static motions were determined in terms of dynamic pressure and the dynamic system response was given by damping characteristics.

The steady static and dynamic analyses were performed on a simplified wing geometry that featured the most defining properties while neglecting those assumed not to be limiting. For the sake of simplicity, the main wing was modelled as a rectangular plate with the determined span and uniform chord set to the MAC. The elastic properties of the wing were determined in Section 13.4, and are constant for the entire span. As the highest load is always present at the root of the wing (see Section 13.2), this assumption was taken as conservative.

13.5.2. Static analysis

Static behaviour describes non-oscillatory interactions between the structure and the surrounding airflow. As a result of a non-rigid wing, its aerodynamic properties, such as lift distribution, are altered [47], which influences design properties. According to Wright and Cooper[47], the two most critical static phenomena are divergence and control reversal, both potentially fatal, and hence need to be prevented.

Divergence

Due to aerodynamic loads, the wing is subject to torsional load that deforms its structure. As a result of the twist along the spanwise axis, the local angle of attack (α) is also affected, which changes the lift distribution. Exceeding a certain limit load, this twist enters a positive feedback loop that eventually causes structural failure [47]. The critical load was defined in terms of dynamic pressure and was obtained using the following equation:

$$q_w = \frac{3GJ}{ec^2s^2C_{l_\alpha}} \quad (13.23)$$

where q_w is the limit dynamic pressure, GJ is the torsional rigidity, e is the fraction of the distance of elastic and aerodynamic axes to the chord, c is the constant chord, s is the span of the wing section and C_{l_α} is the lift-curve slope. The corresponding flight velocity is then given by the relation:

¹⁰URL: https://www.esdu.com/cgi-bin/ps.pl?t=doc&p=esdu_69023dcited 23 June 2025

$$q = \frac{1}{2} \rho V^2$$

Thus, for the given atmospheric conditions, limit velocity equals [47]:

$$V_{\text{div}}(h) = \sqrt{\frac{6GJ}{ec^2 s^2 C_{l_\alpha} \rho(h)}}$$

Control reversal

Unlike with a rigid wing, the effectiveness of flight controls decreases at high speeds. As a result of airfoil deformation, the deflection of control surfaces reverses in extreme cases and the corresponding high velocity is called the control reversal speed. Flying above this limit is unsafe due to loss of controllability and hence not allowed. Similarly to divergence, control reversal is defined through dynamic pressure with the following expression [47]:

$$q_{\text{rev}} = \frac{3GJ}{ec^2 s^2 C_{l_\alpha}} \cdot \frac{ea_c}{ea_c - b_c} = q_w \cdot \frac{ea_c}{ea_c - b_c}$$

$$V_w = V_{\text{div}} \cdot \sqrt{\frac{ea_c}{ea_c - b_c}}$$

where V_w is divergence speed as defined in Equation 13.23, a_c is aileron lift curve slope and b_c is aileron moment curve slope.

In Figure 13.14, both limit speeds are plotted for altitudes up to 22 km. In conclusion, the considered torsional rigidity was found sufficient for static failure modes. For the calculation, the following parameters were used:

Torsional rigidity	GJ:	$3.64 \cdot 10^7 \text{ N} \cdot \text{m}^2$ (see subsection 13.5.3)
Relative distance of aerodynamic and elastic axes	e:	0.2 [-]
Mean aerodynamic chord	\bar{c}:	3.5480 m
Semi-span	s:	30.5000 m
Lift curve slope	C_{L_α}:	5.7296 1/rad
Aileron lift-curve slope	a_c:	3.4893 [-]
Aileron moment-curve slope	b_c:	-0.5923 [-]

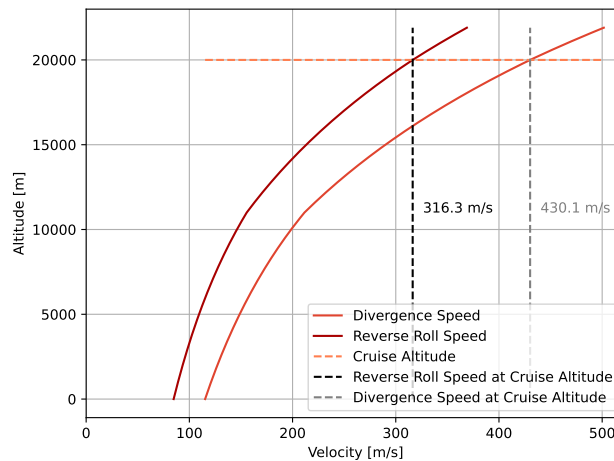


Figure 13.14: Limit Velocities vs Altitude

13.5.3. Dynamic analysis

Dynamic behaviour of the idealised structure (see subsection 13.5.1) was analysed for multiple potential failure modes, with flutter being assumed to be the most prominent and thus limiting in terms of required structural rigidity[47]. Unlike static phenomena, flutter is difficult to predict as it is an interaction of multiple modes that all determine flutter characteristics.

Flutter

Flutter is a phenomenon resulting from the coupled deformational modes of the main wing. These two modes are bending and torsion, as shown in Figure 13.15, and are described in terms of torsional- and flexural rigidity GJ and EI , respectively.

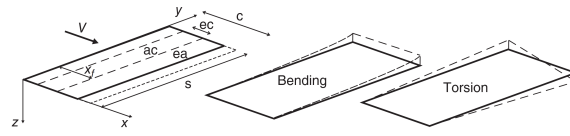


Figure 13.15: Deformation modes of the main wing [47]

To formulate equations of motion, the binary approach suggested by Wright and Cooper [47] was adopted. The oscillatory motion of the wing is expressed by the equations of motion in the matrix form:

$$m \begin{bmatrix} \frac{sc}{5} & \frac{s}{4} \left(\frac{c^2}{2} - cx_f \right) \\ \frac{s}{4} \left(\frac{c^2}{2} - cx_f \right) & \frac{s}{3} \left(\frac{c^3}{3} - c^2 x_f + cx_f^2 \right) \end{bmatrix} \begin{Bmatrix} \ddot{q}_b \\ \ddot{q}_t \end{Bmatrix} + \rho V \begin{bmatrix} -\frac{cs}{10} C_{l_\alpha} & 0 \\ -\frac{c^2 s}{8} e C_{l_\alpha} & -\frac{c^3 s}{24} M_{\dot{\theta}} \end{bmatrix} \begin{Bmatrix} \dot{q}_b \\ \dot{q}_t \end{Bmatrix} + \left\{ \rho V^2 \begin{bmatrix} 0 & \frac{cs}{8} C_{l_\alpha} \\ 0 & -\frac{c^2 s}{6} e C_{l_\alpha} \end{bmatrix} + \begin{bmatrix} \frac{4EI}{s^3} & 0 \\ 0 & \frac{GJ}{s} \end{bmatrix} \right\} \begin{Bmatrix} q_b \\ q_t \end{Bmatrix} = \begin{Bmatrix} 0 \\ 0 \end{Bmatrix}$$

$$m \mathbf{A} \ddot{\mathbf{q}} + \rho V \mathbf{B} \dot{\mathbf{q}} + (\rho V^2 \mathbf{C} + \mathbf{D}) \mathbf{q} = \mathbf{0}$$

where \mathbf{A} is the mass matrix, \mathbf{B} and \mathbf{C} are aerodynamic matrices and \mathbf{D} is the stiffness matrix. Note that structural damping was not considered, as was suggested by Wright and Cooper [47], and the non-symmetrical aerodynamic matrices introduce coupling between the modes.

The system response is then expressed in terms of damping ratios for each mode using an eigenvalue solution. The eigenvalues of the system were obtained using Equation 13.24:

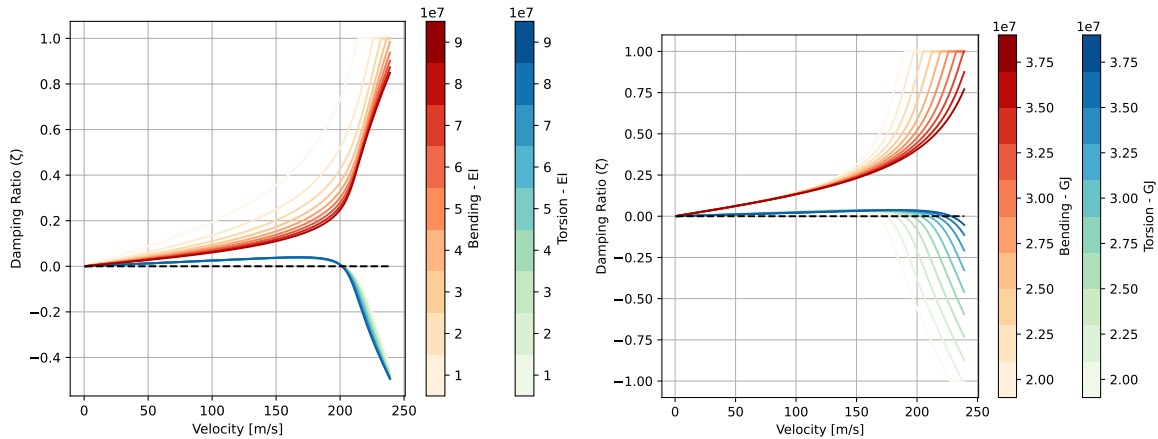
$$\left(\begin{bmatrix} 0 & \mathbf{I} \\ -\mathbf{A}^{-1}(\rho V^2 \mathbf{C} + \mathbf{D}) & -\mathbf{A}^{-1}(\rho V \mathbf{B}) \end{bmatrix} - \mathbf{I} \lambda \right) \mathbf{q}_0 = \mathbf{0} \quad (13.24)$$

Solving Equation 13.24 for λ yielded two distinct complex eigenvalues for the given set of inputs. The corresponding damping ratios were calculated using the following relation:

$$\zeta = -\frac{\text{real}(\lambda)}{|\lambda|} \quad (13.25)$$

Having obtained damping ratios as a function of altitude and free-stream velocity, damping coefficients were calculated for multiple sets of input parameters. Based on the results, the required values of EI and GJ could be determined. Damping was plotted against velocity for the following inputs:

Mass per unit area	m:	81.9809 kg/m ²
Semi-span	s:	30.5000 m (outer wing)
Mean aerodynamic chord	\bar{c}:	3.5480 m
Lift curve slope	C_{L_α}:	5.7296 1/rad
ISA altitude	h:	20000 m
Maximum allowable speed	V	223 m/s



(a) Effect of flexural rigidity on damping ratios for torsional and flexural modes for $GJ = 3 \cdot 10^7 \text{ Nm}^2$ **(b)** Effect of torsional rigidity on damping ratios for torsional and flexural modes for $EI = 2 \cdot 10^7 \text{ Nm}^2$

Figure 13.16: Effect of varying rigidity on flutter

As can be seen in Figure 13.16, flutter speed is mainly driven by torsional rigidity GJ , while EI has a marginal effect on the limit velocity. For this reason, the flutter analysis was mostly conclusive in terms of GJ , that was determined to be no smaller than $3.64 \cdot 10^7 \text{ Nm}^2$ for $M_{\text{crit}} = 0.735$ in cruise conditions. The flutter was plotted for $GJ = 3.64 \cdot 10^7$ and $EI = 2 \cdot 10^7$ in Figure 13.17:

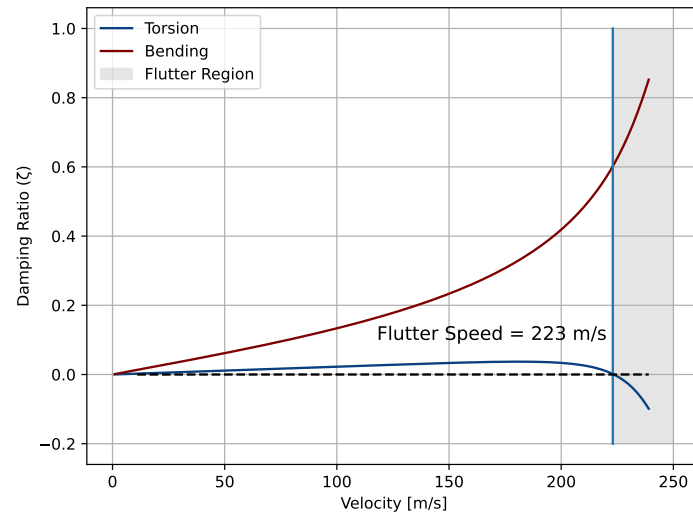


Figure 13.17: Damping ratios of torsional and flexural modes, with $EI = 2 \cdot 10^7$ and $GJ = 3.64 \cdot 10^7$ and no aerodynamic damping ($M_{\dot{\theta}} = 0$)

Aerodynamic Damping Sensitivity

In subsection 13.5.3, the effects of aerodynamic damping were not considered, as accurately predicting the pitch damping coefficient $M_{\dot{\theta}}$ requires more detailed analysis. To ensure that the structure is dynamically stable regardless of the value of $M_{\dot{\theta}}$, its effects were neglected for a conservative approach. To investigate the sensitivity of the model to theta, the damping coefficients corresponding to the mentioned modes are plotted in Figure 13.18 for a range -2 to 0 of values for $M_{\dot{\theta}}$; in literature, -1.2 is commonly used as an estimate.

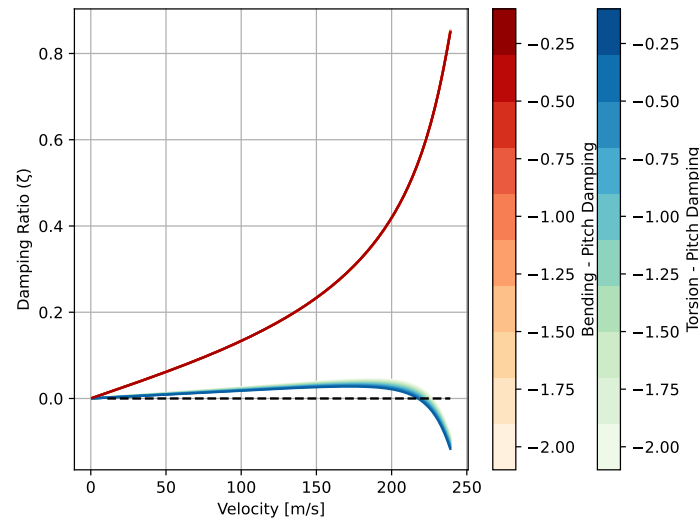


Figure 13.18: Effect of pitch damping on flutter modes

As shown in Figure 13.18, introducing aerodynamic damping has a marginal effect on flutter speed and, the flutter speed increases with increasing magnitude of $M_{\dot{\theta}}$ that aligns with previous expectations.

13.6. Wingbox Design

Contributors: Pavel, Barnabás

The results of the static- (see Section 13.4) and dynamic analyses (Section 13.5) are then used to determine values for required structural rigidity. The results are shown in Table 13.2, the higher structural requirement is limiting for each deformation mode. The required flexural rigidity was determined to be $9.13 \cdot 10^7 \text{ Nm}^2$, while torsional rigidity shall be no smaller than $3.93 \cdot 10^7$.

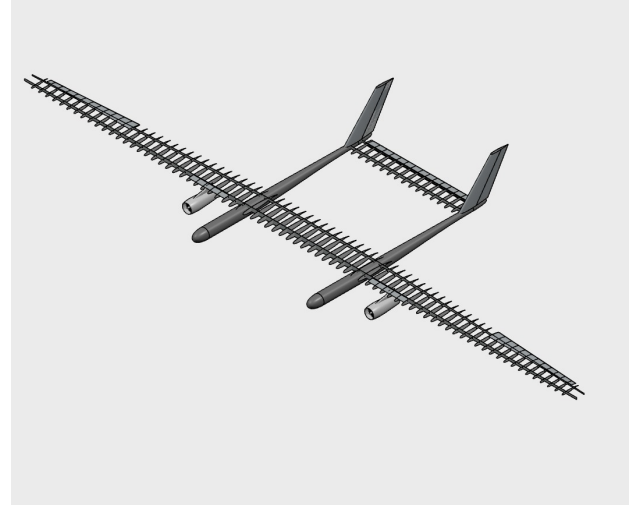
Table 13.2: Structural Requirements

Mode	Static Requirement	Dynamic Requirement
Flexural Rigidity (EI) [Nm^2]	$9.13 \cdot 10^7$	$2.00 \cdot 10^7$
Torsional Rigidity (GJ) [Nm^2]	$3.93 \cdot 10^7$	$3.64 \cdot 10^7$

Note that, as described in subsection 13.5.3, the aeroelasticity analysis is not conclusive for EI , the value $2.00 \cdot 10^7$ is demonstrated to be sufficient (Figure 13.17) and is non-limiting.

With the mentioned structural requirements and the geometry shown in Figure 13.2, the section properties of the wingbox are listed in Figure 13.19. The internal structure of the aircraft is visualised in Figure 13.20

Parameter[mm]	Tip	Root	Middle
skin thickness	4	7	7
Stringer			
thickness	3	6	6
flange width	15	25	25
web height	40	50	50
Forward spar			
thickness web	5	7	7
thickness flange	20	20	20
flange width	60	70	70
Aft Spar			
thickness web	5	7	7
thickness flange	5	10	10
flange width	20	40	40

Figure 13.19: Wingbox Parameters**Figure 13.20:** CAD Model showing wing structure

This led to a final mass of 9526 kg, which is almost a ton below the wing mass estimation from Class II; however, the mass of the ribs was not accounted for in the wingbox mass.

13.7. Verification and Validation

Contributors: Pavel, Barnabas

To verify whether the wingbox design is correct, all code scripts were checked to ensure everything was properly implemented. This was achieved through a series of unit tests. Furthermore, individual functions such as bending stress were verified using by using hand calculations for simplified cases.

The outcome of the design is validated using values of reference aircraft. Due to the lack of publicly available data, the SAGA concept [22] was chosen for comparison. The corresponding values are listed in Table 13.3.

Parameter	SCAI	SAGA [22]
Skin Thickness Tip [mm]	4	3
Skin Thickness Root [mm]	7	5
Front Spar Thickness Tip [mm]	5	1
Aft Spar Thickness Tip [mm]	5	1
Front Spar Thickness Root [mm]	7	4
Aft Spar Thickness Root [mm]	7	2

Table 13.3: Table showing data of SAGA concept

As visible in Table 13.3, the dimensions are slightly higher when compared to SAGA. This difference is most likely resulting from the significantly larger wing area. Even though the relative difference is notable, the magnitude of values falls in the expected range.

Internal Layout and Aircraft Systems

The design consists of a number of different complex and mostly autonomous systems working together. These include the injection, fuel, hydraulic and electrical systems. Next to these physical systems, the design uses digital systems to complete its mission. These digital systems work closely together with the hardware present in the aircraft, and the functioning and layout will also be explained. Diagrams will therefore also be shown for the communication flow, the data handling, and the connection between the hardware and software.

14.1. Injection system layout

Contributors: Inés

In order to prevent agglomeration, the generators will be placed in the wings and horizontal stabiliser for immediate dispersal through the nozzles after fluidisation as can be seen in Figure 14.1. This will, at the same time, provide bending relief for the wings. The nozzles will be positioned as close as possible to the trailing edge of the airfoil, aligned in a row. In this arrangement, the flow from each nozzle will interact with that of its neighbours, causing additional collisions at high velocities that help further break down agglomerates. The necessary air and aerosol for fluidisation will be continuously

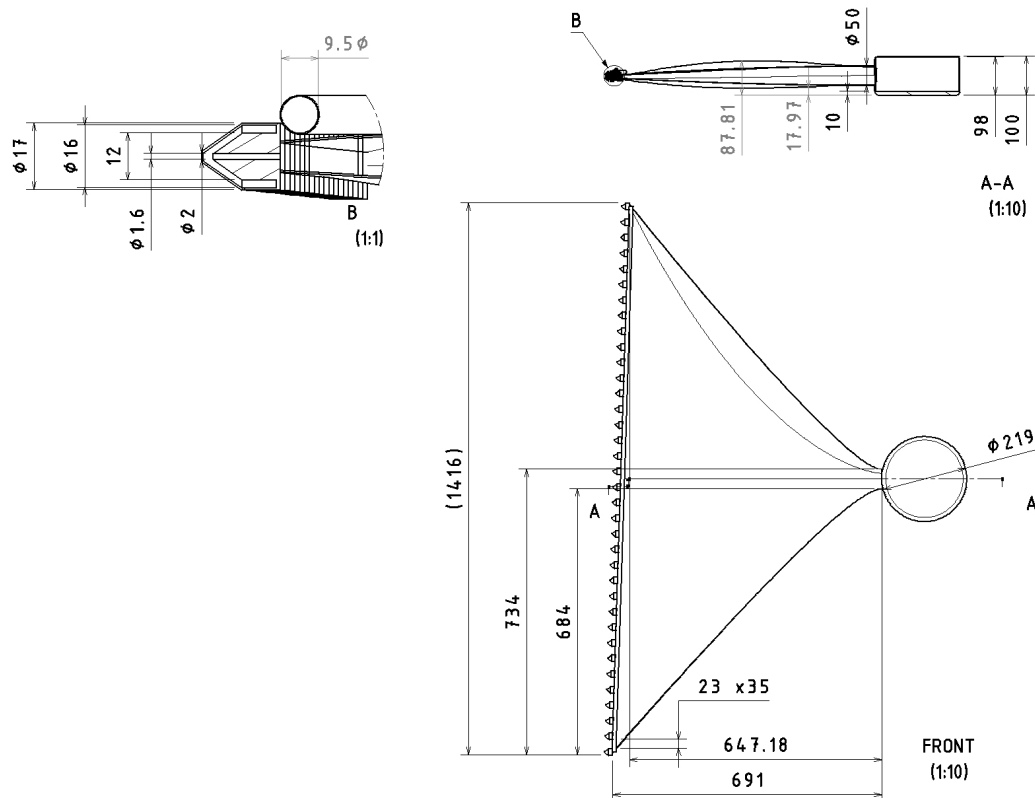


Figure 14.1: Injection System Drawing

replenished inside the generators through feeding lines of both air and aerosol. The air will come from the outside of the aircraft through inlets, while the required aerosol will come from aerosol tanks located in the fuselage, which will be continuously fed into the generators, again through fluidisation.

The tank's location is decided to ensure easy loading of the aerosol into the aircraft. Since the aerosol is a powder rather than a liquid like fuel, its handling is more complex. Storing the aerosol in the wing would therefore introduce several loading problems. To ensure even distribution within the tank, the fuselage can be opened, allowing for easy loading without the need for any feeding lines. This makes the fuselage the most practical and efficient location for the aerosol tanks.

The storage tanks' dimensions are restricted by the fuselage diameter. As explained in Section 8.5, the fuselage diameter is designed to be β times bigger than the aerosol tank diameter. Given this value, the dimensions are calculated assuming a cylindrical shape to store the necessary volume. The volume of the tank (V_{tank}) is designed to account for both the required mass of aerosol and the additional air volume needed to fluidise it to transport it to the generators, as previously explained. Therefore, the final dimensions of the aerosol tanks to store 13749.8 kg of payload are:

Table 14.1: Dimensions of the storage tanks for a payload of 13749.8 kg

Radius (X) [m]	0.605
Height (Y) [m]	4.383

On the other hand, the dimensions of the generator is restricted by the thickness of the airfoil. The configuration proposed by the McNeill group takes into account a subwoofer with approximately 0.5x0.5x0.5 meters, which significantly exceeds the width of the airfoil. Therefore, an alternative acoustic and mechanical agitator must be considered to fit these dimensions. Considering a cylindrical shape for simplification, and a 15 L volume, the dimensions of a generator are:

Table 14.2: Dimensions of the generators

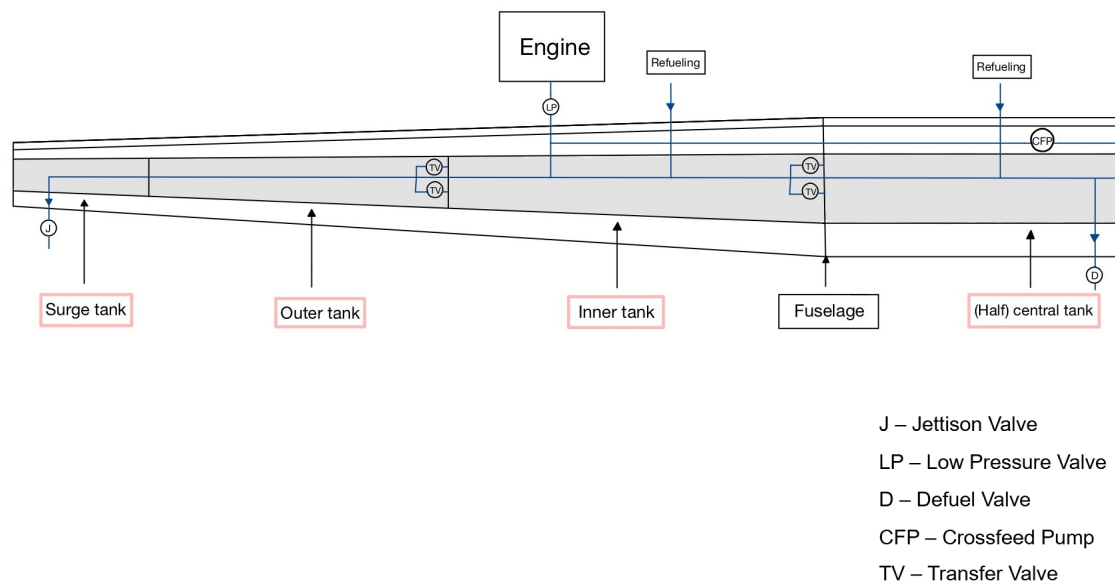
Radius (X) [m]	0.145
Height (Y) [m]	0.2269

Where the height is restricted to be the thickness to chord ratio times the smallest chord of the wing.

14.2. Fuel System Layout

Contributors: Inés

Given that the volume of the wing is 51.43 m³, all the fuel can easily be stored in the wings. The fuel system will then be composed of 7 fuel tanks in total: 1 main tank, 2 inner tanks, 2 outer tanks and 2 surge tanks, placed symmetrically along the wing, as seen in Figure 14.2. The figure shows the right wing of the aircraft, where the grey area corresponds to the fuel tanks. In the trailing edge space necessary for the generators is delimited.

**Figure 14.2:** Fuel System Layout

The main fuel tank will be positioned in the centre section of the wing, between the two fuselages, where the largest available chord length and the 16-meter span allow for the installation of a larger tank. The inner and outer tanks are then located across the remaining span of the wing, and finally, the surge tanks will be located at the tip of the aircraft to allow air in as fuel is consumed, to prevent vacuum, as well as catch fuel expansion or overflow due to heat. All the tanks will be connected through valves in order to allow for the fuel to be delivered to any of the 2 engines at any time.

14.3. Hydraulic System Layout

Contributors: Maxine

The aircraft hydraulic systems consist of two independent, symmetrical systems located in both fuselages, supplying hydraulic power to their respective sides of the aircraft. These systems are connected by a cross-feed valve, allowing for the control of one system through the other system in emergency scenarios, ensuring reliability and redundancy. Each system includes a hydraulic fluid reservoir, connected to three types of pumps powering the system. Here, the primary source of hydraulic power is the engine-driven pump [48]. For situations where the engines are inoperative, such as during ground operations or engine failure, an electric motor-driven pump (EMDP) is included, allowing for hydraulic functionality.

Lastly, a ram air turbine can be deployed as an emergency source, such that in case both the engines and the electrical power fail, the control surfaces, brakes, and steering mechanisms remain operable. Additionally, each system is equipped with an accumulator, which can supply short-duration hydraulic pressure which can be used for lowering the landing gear in case of pump failure. Additionally, both systems are connected by a cross-feed valve, allowing one system to power the systems connected to the other system in case of system failure. The main systems serviced by the hydraulic systems include wheel brakes, landing gear deployment, steering, and control surfaces such as elevators, rudders, ailerons, and spoilers [48]. Here, brakes and landing gear steering systems are supplied with an additional local hydraulic generation system (LEHGS), to be used in case of hydraulic system failure [49]. Additionally, all control surfaces are equipped with Electro-Hydrostatic Actuators (EHAs), which work as a self-contained, electrically powered hydraulic system, allowing for full use of the control surfaces, even in the case of full hydraulic system failure, as well as catastrophic engine failure leading to a distribution to the tubing system. These backup systems will be powered by the emergency flight controller power, supplied by the Auxiliary Power Unit, to ensure power in case of engine failure [50]. In case of full system failure, including the accumulators, the landing gears may be deployed by use of gravity once released.

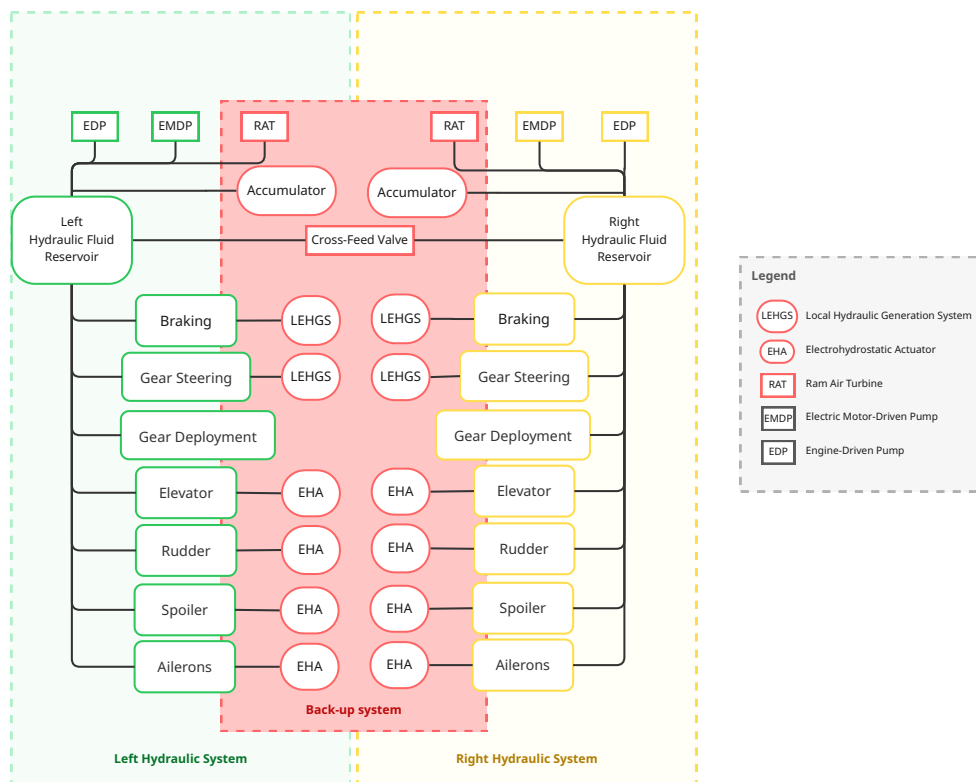


Figure 14.3: Hydraulic System Layout

14.4. Electrical System Layout

Contributors: Bas

An overview of the electrical system layout is shown in Figure 14.4. The diagram includes all aircraft components connected to the electrical system. It also shows the voltages of the electrical components and AC power generated by the power generators. The power production and consumption of each of the aircraft components in Figure 14.4 is broken down in Section 15.3.

The electrical system of the design is symmetric between the left and right fuselages, and the two main electricity buses are connected through the middle wing section. The Auxiliary Power Unit (APU) generates the power needed while the aircraft is grounded and acts as fallback in case of power issues while in the air. The APU also starts both engines, and itself is started from the power stored in the main batteries. The left and right engines produce the electricity while in the air, each powering their respective AC buses for all injection system components and fuel systems.

The high voltage AC current is transformed to a lower voltage DC current by a Transformer Rectifier Unit (TRU), which then powers the left and right DC electricity buses. DC power is used by certain aircraft components such as communications, avionics, flight controllers and (external) lighting. This DC power has a lower voltage of 28V and also powers the main batteries of the aircraft. The DC power from the batteries is used to power on the APU and to power the emergency battery if necessary. The power in the main batteries can flow back through an inverter (INV) to be converted back to high-voltage

AC current to power the main AC bus.

The generators also power a shared aircraft essentials bus, which powers the essential components such as the landing gear, control surfaces and wing anti-icing. The APU can also power this aircraft essentials bus. To introduce more redundancy, the APU ensures a full emergency battery, which powers a backup flight controller, sensors and communication system in case of complete failure of one or more of these critical systems.

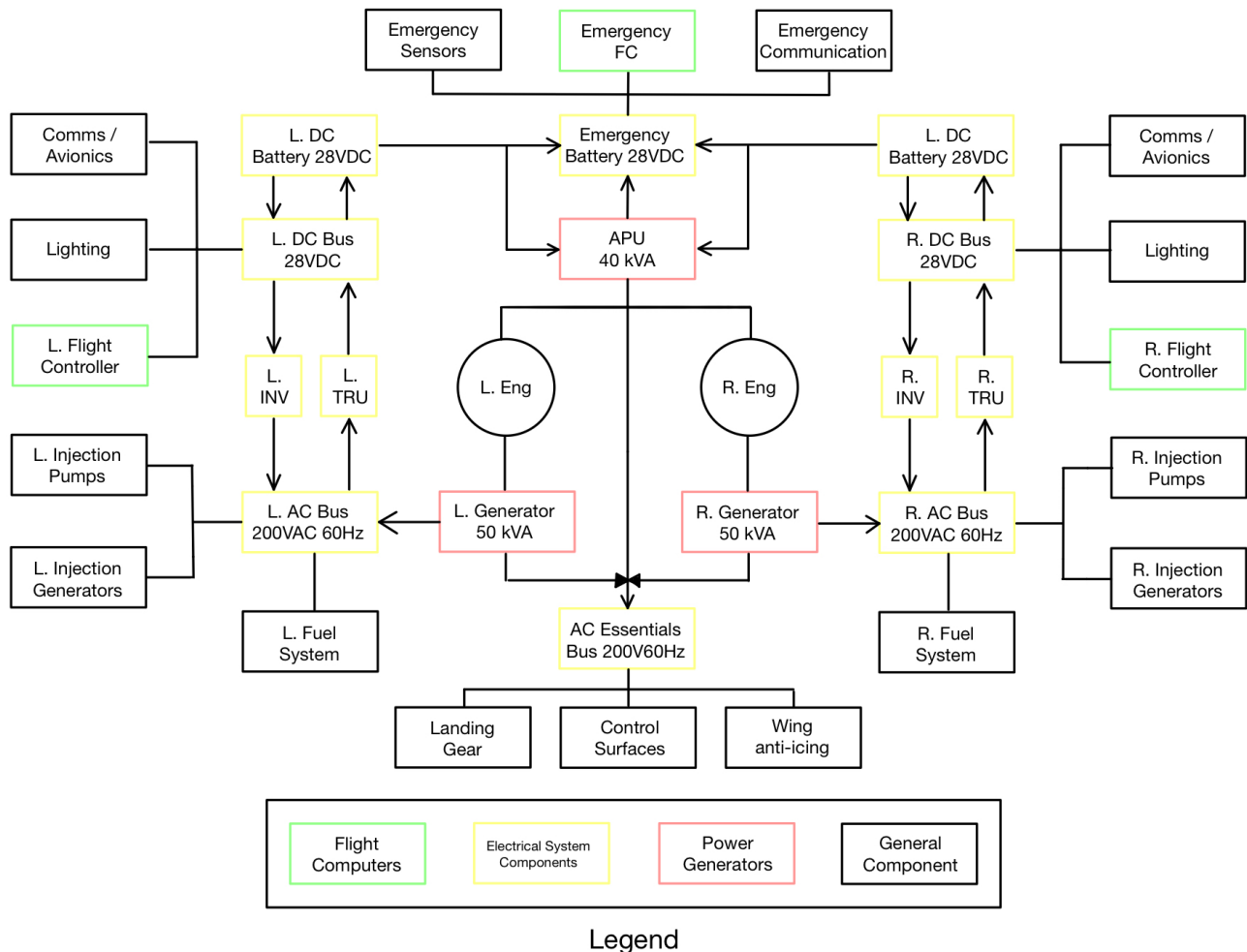


Figure 14.4: Electrical system layout

14.5. Communication Flow Diagram

Contributors: Bas

Communication happens between a number of different subsystems, both inside the aircraft itself as well as external systems. The main hubs of data are the three (including emergency back-up) flight controllers. As the designed aircraft operates unmanned, these flight controllers need all the available data from the aircraft in order to make decisions and fly on autopilot. The communication flow diagram based on this structure is shown in Figure 14.5.

The flight controllers consist of a number of different, separately operating software systems, shown inside the light green box in Figure 14.5. All data is gathered by the monitoring system, which collects data from the different sensors inside and outside of the aircraft. The control system is responsible for operating the engines, control surfaces and payload injection system. The navigation system is responsible for navigating the aircraft using the control system and data from the communication system.

The communication system is responsible for communicating with external systems. The aircraft communicates with both the nearest ground base and airbase. The airbase is responsible for handling the aircraft traffic landing and taking off from the airbase. Therefore, the aircraft communicates with the air traffic controller of the airbase for navigation instructions.

The ground base is responsible for the mission aspect of the operation. For this, it uses live weather and fleet data to determine the mission profile for each aircraft, and gives the aircraft instructions during the entire mission. The ground base also logs all the received data. This data can be used for a number of different post-mission tasks, such as optimising future mission profiles, keeping track of the injected aerosol and planning necessary maintenance.

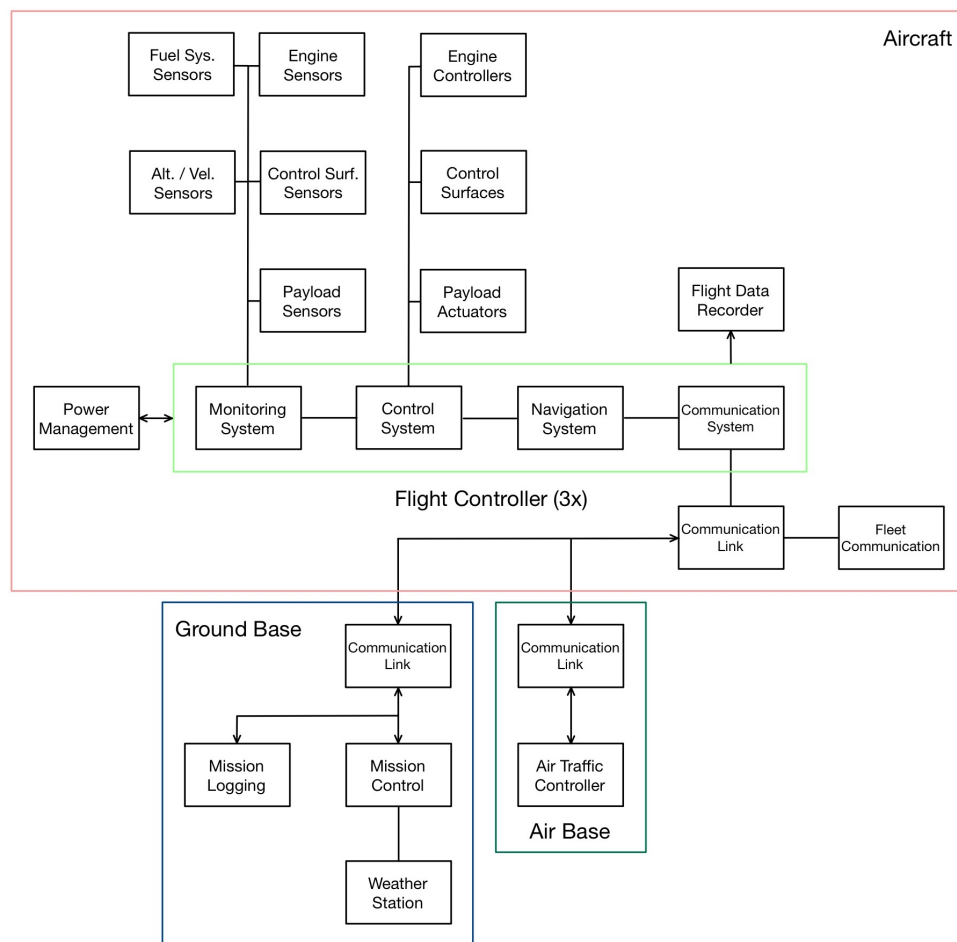


Figure 14.5: Communication flow diagram

14.6. Hardware / Software Diagram

Contributors: Bas

In the design, a large number of hardware components such as sensors are present, as has already been shown in Section 14.4 and Section 14.5. Since the aircraft will be flying autonomously, the entire mission will be flown by the flight computer software. The hardware-software integration is therefore highly important.

The complete hardware-software structure is shown in Figure 14.6. The aircraft will be flown by an autopilot in the flight computer, which will need to make decisions based on the data from a large number of sensors. The data of these sensors will be gathered and analysed by a number of code systems which monitor, control and navigate the aircraft. The systems use each other's outputs as inputs, and their outputs are combined into the autopilot software module, which will then make the final decisions based on the received data from each of the software systems and is responsible for sending signals to the different control hardware components inside the aircraft. These controllers mechanically operate the engines, control surfaces, injection system and APU/generators. The electricity generated by the APU and engine generators powers all hardware components, including the flight computer. As SCAI operates autonomously, it is completely dependent on its sensors and flight computers. Therefore, for redundancy in case of failure, next to the two normal flight computers, a third emergency flight computer is located in the central wing section. Each of the internal and external sensors will be in the aircraft twice, one in each fuselage.

As the software of the autonomous aircraft consists of many different systems performing separate functions, as shown in Figure 14.6, the aircraft will require a large codebase. Modern aircraft such as the Boeing 787 runs on 6.5 million lines of code¹. However, a rapid increase in lines of code necessary for modern vehicles is seen, with the F-35 fighter containing more than 8 million lines of code². The codebase of the design will need to handle monitoring, control, navigation and communication of the aircraft, thereby performing more functions than the afore mentioned aircraft to enable fully autonomous flying. The software is therefore expected to reach more than 30 million lines of code, which at an estimated cost of 100 USD per line[51], would cost a total of 3.0 billion USD.

¹URL: <https://www.flightglobal.com/boeing-readies-first-787s-systems/73963.article>

²URL: <https://www.388fw.acc.af.mil/News/Article-Display/Article/1280043/hill-robins-to-provide-f-35-software-su>

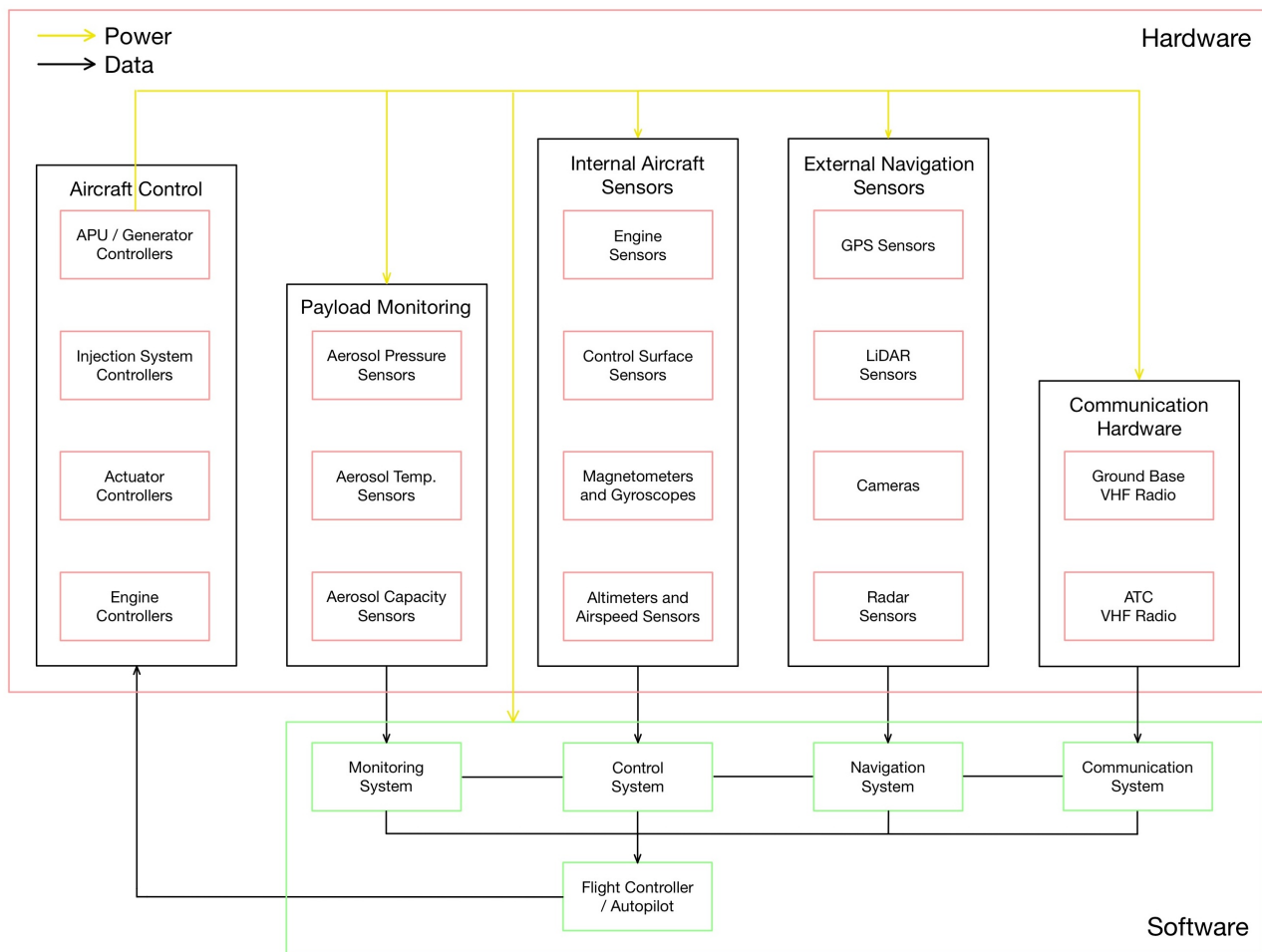


Figure 14.6: Hardware/Software integration diagram

14.7. Data Handling Diagram

Contributors: Bas

Given the large volume of data flowing through the hardware and software components shown in Figure 14.6, a data handling diagram was made to show the direction and amount of data flowing through the system. The diagram can be found in Figure 14.7. The diagram shows the one or two-way flow of data between hardware components, including the processing of data inside the three flight computers. The direction of the flow of data is given by arrows. A dual-headed arrow thus means two components both share to and take data from each other. Each arrow is labelled with one or more numbers, their meaning is explained in Table 14.3. Each number corresponds to a certain data package, with its own estimated frequency in pps (packages per second) and volume of each data packet in bytes (8 bits). These two numbers multiplied by each other gives the data rate of the flow.

A large volume of data is produced by all the sensors and electronic systems present in the aircraft, as well as received through VHF communication with ATC and ground bases. This data is collected on the main data bus and is temporarily stored in the flight computer memory. The data is checked for anomalies and used by the flight computer CPUs to make decisions and instructions for the aircraft subsystems. The most important parameters are stored in the flight computer storage for future use during the mission or potential post-flight analysis if necessary. A small amount of data is also stored inside the crashworthy flight data recorder, also known as the black box. Only 88 parameters are required to be stored in this drive³, which will be stored using 256 12-bit entries per second, the data rate capacity of a typical modern flight data recorder³.

The frequency of the data packets being send depends on the importance of the specific data flow. Some sensor data such as those of the engines or payload are only used for monitoring the correctly functioning of the subsystems, while other data flows such as navigation sensor data or control surface instruction data is actively used for controlling the aircraft in a safe manner, thus requiring a significantly lower latency between data packets.

³URL: https://aerospace.honeywell.com/content/dam/aerobt/en/documents/learn/products/recorders-and-transmitters/datasheet/N61-2073-000-000_HFR5-DFlight_Data_Recorder-datasheet.pdf

The communication data send and received by the aircraft will be transmitted while being encrypted. All communication data therefore passes through an encryptor/decryptor module to code or decode the signals. This ensures protection from cyberattacks, as unwanted parties sending false instructions to the autonomous aircraft could end in a catastrophe.

Table 14.3: Data flow explanations for Figure 14.7

ID	Data	Frequency [pps]	Package Size
1	Stored Flight Data	5 (Increases when data changes rapidly)	10 MB
2-3	Aircraft Data	60	50 MB
4	Electrical System Data	5	10 MB
5	Electrical System Instructions	5	500 B
6	Aircraft Instruction Data	5	0.1 MB
7	Aircraft Position Data	5	200 B
8	Navigation Sensor Data (LiDAR, cameras, radars)	1 to 20 (Depends on flight phase)	20 MB
9	Payload Sensor Data (Pressure, temperature, volume)	5	1,000 B
10	Injection System Instructions (Generators, nozzles)	1	200 B
11	Engines Sensor Data	1	5,500 MB
12	Propulsion System Instructions	10	500 B
13	Control Surfaces Status Data	60	500 B
14	Control Surfaces Instructions	60	500 B
15	Flight Recorder Data	1 (Increases when data changes rapidly)	384 B

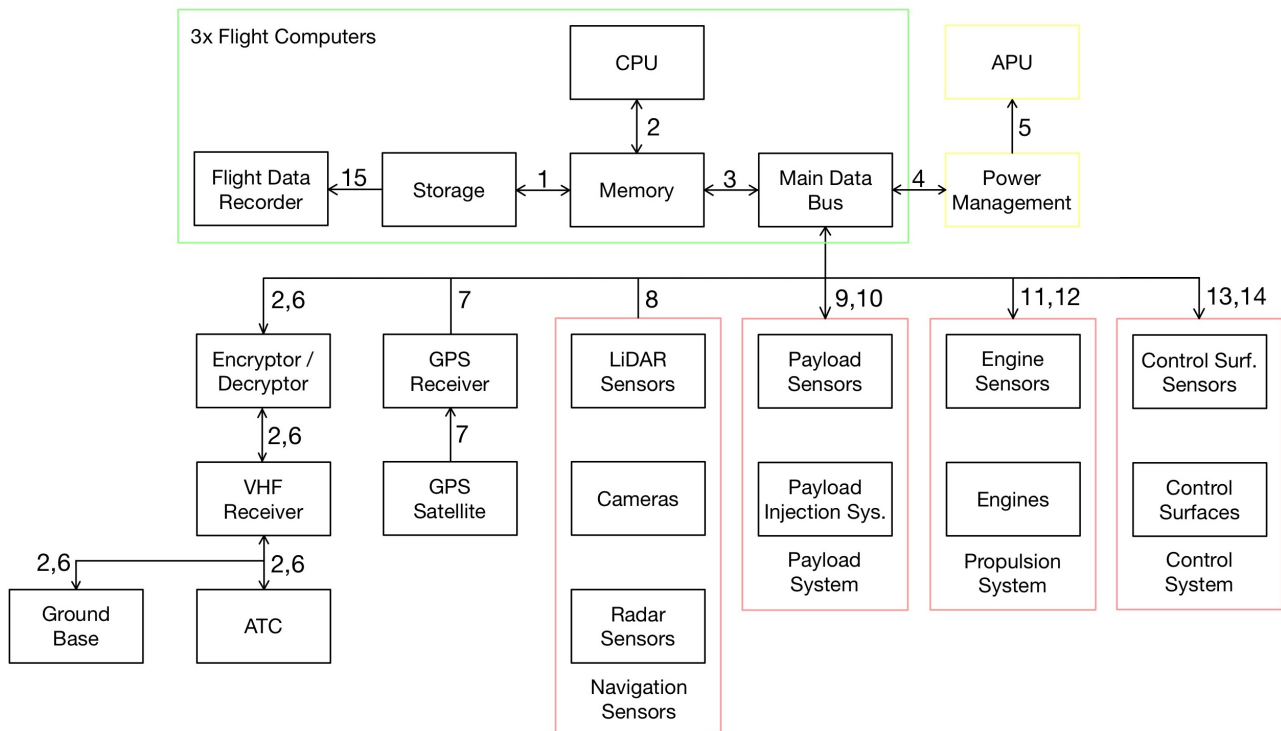


Figure 14.7: Data handling diagram

Resource Allocation

Resource allocation allows for the optimisation of available resources and minimises inefficiencies by planning. Effective resource management is thus fundamental to achieving the viability and operational success of the project. This chapter describes the resource allocation for the project in terms of cost, mass and power.

15.1. Cost Breakdown

Contributors: Pavel, Konstantinos

In this section a Cost Breakdown Structure (CBS) is plotted, in an effort to identify all the costs involved in the development, production and operation of the system. These are later quantified in Figure 15.1. There are 3 top-level categories included [9, p.579–597]. These are RDT&E (Research, Development, Testing, and Evaluation), Production and Operational Costs, which are further split into 2 sub-levels as shown in Figure 15.1. Additionally, the legend distinguishes between Labour, Material, Equipment, and Overhead Costs (ongoing expenses not directly associated to one of the aforementioned categories). This classification supports a more detailed cost analysis during the system operation, including the identification, management, and mitigation of the cost drivers.

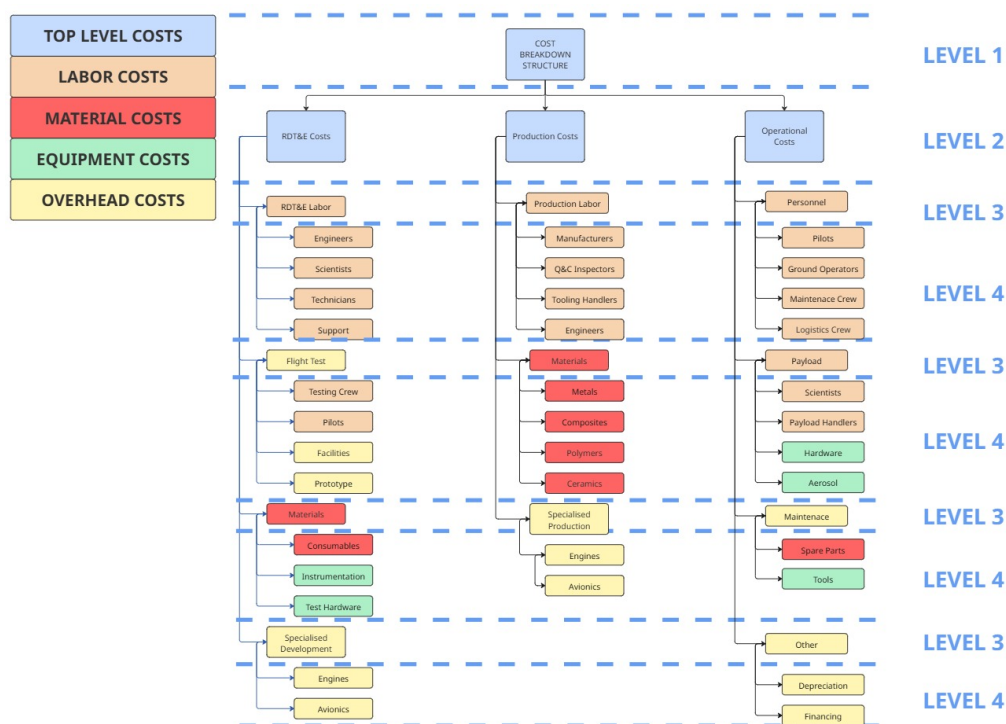


Figure 15.1: Cost Breakdown Structure

It is important to note that the quantitative cost analysis presented in Figure 15.1, the methodology developed by Justin McClellan et al. [53] is extensively used. In this approach, the engines and avionics are treated as distinct cost elements. To maintain consistency with this methodology, they are also represented as separate categories in the CBS, as shown in Figure 15.1.

Moving on, the financial viability of the system is evaluated, by calculating the net positive balance between its earnings and costs. It does so by quantifying the cost elements identified in Figure 15.1 and estimating the system's cash inflow based on market share projections derived from the literature review in Chapter 2. The Return on Investment (ROI) is then quantified as the difference between the two.

Costs

The cost of the aircraft is divided into two main components: recurring and non-recurring costs. Recurring costs include ongoing operational expenses, while non-recurring costs cover one-time investments such as production and RDT&E (Research, Development, Testing, and Evaluation). All figures are adjusted to April 10, 2025, euro values, and the analysis that follows is based on the methodology of Justin McClellan et al. [53].

Recurring Cost

The recurring cost of the aircraft fleet is the summation of multiple smaller costs. These include fuel, crew, maintenance, depreciation, financing, and the payload. The fuel cost is based on the fuel used in the class II weight estimation multiplied by the fuel cost. The fuel cost used is the peak fuel cost for 2009 which is \$0.68/kg. The maintenance cost is approximated by the spare parts used and the maintenance labour. The maintenance cost from spare parts are calculated with the equations below.

$$\text{Spare Parts/Supplies / block hour} = 3.3 \cdot \left[\frac{C_a - C_e}{10^6} \right] + 10.2 + \left[58 \cdot \left(\frac{C_e}{10^6} \right) - 19 \right] \cdot N_e$$

$$\text{'Spare Parts/Supplies / sortie} = 4 \cdot \left[\frac{C_a - C_e}{10^6} \right] + 6.7 + \left[7.5 \cdot \left(\frac{C_e}{10^6} \right) + 4.1 \right] \cdot N_e$$

The labor hours for maintenance are calculated with the following equation:

$$\text{Maintenance, Supportcost/blockhour} = 139.2 \frac{MMH}{FH}$$

The maintenance man hours per flight hour is assumed to be 10. The other variables used in the equations are the cost of the aircraft (C_a), cost of engines per aircraft (C_e), and number of engines per aircraft (N_e). The crew rates in FY1999 dollars are in Table 15.1 which are then multiplied by 2.080 labour hours in a standard year.

Table 15.1: Personnel Cost Rates Used

Title	Rate Used[\$]
Logistics Personnel	100
Site Lead	300
Flight Crew 1	153
Flight Crew 2	280
Mission Specialist	228
UAV Operator Labour	106
Mission Director	49
Maintenance Technician	65
Engineer	133
Tooling Personnel	81
Manufacturing Personnel	81

The payload weight cost is simply the payload mass multiplied by the cost of the payload. The depreciation of the aircraft is calculated by using the capitalised production costs (Materials, Engine, and Avionics) of the aircraft. A residual value percentage of 10% is used over 15 years of service¹. Interest costs are calculated under the assumption that the fleet is financed through bonds, as the fleet is likely funded by a coalition of governments. The annual financing cost is estimated using the yield of a 15-year AAA-rated ECB bond as of April 10, 2025, which is 2.933%². Assuming an interest-only bond structure, the annual interest cost is determined by multiplying this yield by the costs incurred by the fleet.

Non-recurring Cost

The RDT&E cost and production cost are estimated by empirical relations which require parameters from other subsystems. The turbine entrance temperature (T_i) in Rankine is from Chapter 11 and the number of prototypes is assumed to be five, as multiple existing aircraft also use this amount. The production rate (R) in aircraft per month is based on the fleet size so the last variable that is needed is the difficulty factor (D_f). Although McClellan[53] provides a difficulty factor of one for the given cruise altitude, a value of 1.5 is assumed as the twin-fuselage aircraft is an unconventional aircraft.

RDT&E Cost

The RDT&E Cost has multiple components to it. Firstly, all the labour hours are calculated which consists of engineering, manufacturing, and tooling. The equations for the RDT&E engineering, manufacturing, and tooling hours are described in Equation 15.1.

¹URL: <https://www.iata.org/contentassets/4a4b100c43794398baf73dcea6b5ad42/airline-disclosure-guide-aircraft-acquisition.pdf> cited 21 May 2025

²URL: https://www.ecb.europa.eu/stats/financial_markets_and_interest_rates/euro_area_yield_curves/html/index.en.html cited 21 May 2025

$$h_{RD_{eng}} = 0.0317W_e^{0.791} \cdot V_{max}^{1.526} \cdot N_p^{0.183} \cdot D_f \quad (15.1a)$$

$$h_{RD_{man}} = 28.984W_e^{0.74} \cdot V_{max}^{0.543} \cdot N_p^{0.524} \cdot D_f \quad (15.1b)$$

$$h_{RD_{tool}} = 4.013W_e^{0.764} \cdot V_{max}^{0.899} \cdot N_p^{0.178} \cdot R^{0.066} \cdot D_f \quad (15.1c)$$

These hours are given for FY 1999 dollars so they are scaled and then multiplied by the labour rates in Table 15.1 to obtain the final labour costs, provided later in the report. The other variables used are empty weight (W_e) in lbs and the maximum cruise speed (V_{max}) in kts. Additional RDT&E components include development support, flight testing, materials procurement, and engine development. The avionics development cost is treated separately and is dependent on sophistication but it is assumed to be 10% of the total development cost for an unmanned aircraft. Furthermore, there are costs associated with development support, flight test, materials, and engine development whose empirical relations are given in Equation 15.2

$$\text{RDT\&E Development Support Costs} = 66 \cdot W_e^{0.63} \cdot V_{MAX}^{1.3} \quad (15.2a)$$

$$\text{RDT\&E Flight Test Costs} = 1807.1 \cdot W_e^{0.325} \cdot V_{MAX}^{0.822} \cdot N_p^{1.21} \quad (15.2b)$$

$$\text{RDT\&E Materials Costs} = 16 \cdot W_e^{0.921} \cdot N_p^{0.799} \quad (15.2c)$$

$$\begin{aligned} \text{RDT\&E Engine Development Costs} = 1,000,000,000 + [2 \cdot (2251 \cdot (0.043T + \\ 243.25M_{max} + 0.969T_i - 2228)) \cdot (N_p \cdot N_e)] \end{aligned} \quad (15.2d)$$

In addition to the parameters previously mentioned the thrust per engine(T) in lbf is used.

Production Cost

The production labour costs have the same breakdown as the RDT&E costs (engineering, manufacturing, and tooling). The remaining costs are then materials, engine production, and avionics production. The avionics production cost is assumed to be 10% of the total production cost for an unmanned vehicle. The equations for the production engineering, manufacturing, and tooling hours are described in Equation 15.3.

$$h_{PD_{eng}} = 7.07 \cdot W_e^{0.777} \cdot V_{max}^{0.894} \cdot N_p^{0.163} \cdot D_f \quad (15.3a)$$

$$h_{PD_{man}} = 10.72 \cdot W_e^{0.82} \cdot V_{max}^{0.4846} \cdot N_p^{0.641} \cdot D_f \quad (15.3b)$$

$$h_{PD_{tool}} = 8.71 \cdot W_e^{0.777} \cdot V_{max}^{0.696} \cdot N_p^{0.263} \cdot R^{0.066} \cdot D_f \quad (15.3c)$$

Table 15.2 breaks down all the costs of the system, converted to euros, for the different design phases. The final computed costs can be found in the rightmost column of the preliminary costs. The production cost in the table is the production cost of the final fleet, while the operations fleet measures the annual operational cost of the final fleet.

Table 15.2: Complete Cost Breakdown of the Aircraft throughout the different design phases

Type of Cost	Initial Cost [bil €]	Final Cost [bil €]
RDTE Labor	2.66	3.09
Development Support	0.24	0.34
Flight Test	0.098	0.12
Materials	0.077	0.13
Engine Development	0.13	0.10
Avionics Development	0.36	0.42
Total RDTE Cost	3.56	4.21
Production Labour	23.27	24.09
Materials	3.14	4.21
Engine	6.74	3.89
Avionics Production	3.68	3.58
Total Production Cost	36.84	35.78
Fuel	4.20	3.83
Personnel	10.6	7.41
Payload	2.31	2.31
Maintenance	4.69	2.94
Depreciation	0.81	0.70
Financing	1.19	1.17
Total Operational Cost	23.52	18.08

Income

Having determined the costs, the total earnings shall be evaluated. In subsection 2.5.1 it was determined that if effective, the system will dominate approximately the entire Solar Radiation Management (SRM) market share, which corresponds to 55% of the geoengineering market. This corresponds to the blue segment shown in the pie chart in Figure 2.1, splitting the geoengineering market into its constituents. Additionally, based on Section 2.3, the market is expected to grow to USD 73.9 billion by 2030, resulting in an estimated market value for the system of at least USD 40.65 billion. This is the market value of the system.

The budget to make the system, as provided by the coalition of governments, is restricted by stakeholder requirements REQ-STK-15, REQ-STK-16, and REQ-STK-17. For the development of the design, a budget of 9 billion euros is available, since a new engine is being designed. For the manufacturing of the entire fleet, 150 million per aircraft are provided, resulting in a total manufacturing budget of 57.75 billion euros. Finally, a budget for the annual operating costs of 23.10 billion euros is available, given that 60 million per aircraft are to be used. Adding up the constituent values, a total of 89.85 billion euros is acquired.

Return on Investment

Having determined both the yearly costs and the income of the system, a financial balance can be determined by using Equation 15.4. This determines the profit of the aerosol injection system by subtracting the expenditure from the income:

$$\text{Profit} = \text{Income} - \text{Expenditure}, \quad \% \text{Profit} = \frac{\text{Profit}}{\text{Expenditure}} \times 100 \quad (15.4)$$

This results in a profit of 31.91 billion euros or a ROI (% Profit) of 54.96%.

15.2. Mass Breakdown

Contributors: Bas

The mass of the aircraft's subsystems, payload and fuel changed significantly throughout the design process. The empty operative mass (OEM) and maximum take-off mass (MTOM) of the design were calculated using class I and class II weight estimation methods. The changes OEM throughout the different design phases, as well as the composition of the OEM, are shown in Table 15.3. The payload mass and computed fuel mass are added to the OEM to get the MTOM. The changes in MTOM and its composition are shown in Table 15.4.

The concept masses were derived in the baseline report [54] and were based on a class I weight estimation only, in combination with subsystem weight estimations based on percentages from Raymer's method[29]. The initial masses were determined in the midterm report [10] using a single class II weight estimation based on a large number of assumptions and guesses in parameters. The preliminary masses result from a large iterative process between class I and class II weight estimations with most initial guesses replaced by calculations for the different subsystems.

The weight estimation methods are explained in more detail in Section 7.4. The actual OEM in Table 15.3 refers to the sum of all the computed subsystem weights. A contingency value, which was defined in the baseline report [54], is added to the actual OEM yielding the current OEM. The specification OEM originates from the requirements. The target value is determined by subtracting the same contingency value as before from the specification OEM. The same process also applies to the different values for the MTOM in Table 15.4.

Table 15.3: Operative empty mass breakdown

Subsystem	Concept mass (Class I) [t]	Initial mass (Class II) [t]	Preliminary mass [t]
Wing	7.19	5.31	10.5
Horizontal Stabilizer	0.09	0.12	0.23
Vertical Stabilizer	0.33	0.21	0.32
Fuselage	4.09	3.22	4.07
Fuel System	4.89	0.15	0.13
Engine Nacelles		1.13	1.95
Engines	22.7	6.0	15.0
Main Landing Gear	2.74	0.67	0.84
Nose Landing Gear	0.73	0.09	0.17
Actual OEM	42.8	16.9	34.4
Current OEM	85.6	21.97	39.6
Specification OEM	85.6	44.2	39.1
Target OEM	42.8	34.0	34.0
Contingency	100%	30%	15%

Table 15.4: Maximum take-off mass breakdown

Subsystem	Concept mass (Class I) [t]	Initial mass (Class II) [t]	Preliminary mass [t]
Payload	17.0	17.0	17.0
Fuel	18.7	13.3	9.87
OEM	42.8	16.9	33.3
Actual MTOM	78.5	47.2	61.1
Current MTOM	157.0	61.4	70.3
Specification MTOM	157.0	84.5	74.8
Target MTOM	78.5	65.0	65.0
Contingency	100%	30%	15%

15.3. Power Breakdown

Contributors: Bas

Due to the many different electrical systems present in SCAI as described in Section 14.4, as well as the aircraft being unmanned, a power budget should be made to ensure enough power is available throughout the entire flight. This was done by estimating the maximum power consumption of each of the subsystems based on the calculations in the respective chapters, as well as data from Roskam [48] and Voth et al. [55]. The breakdown of the power is given in Table 15.5. As shown in the table, the avionics and hydraulic systems consume the most power. The high power consumption estimated for the avionics subsystem is mostly caused by the large number of sensors, radars and constant communication with both ground bases and airbases required for autonomous flying. This is also the reason for the relatively large power consumption of the flight controllers, as the three of them constantly need to make a very large number of calculations, predictions and decisions to operate SCAI autonomously.

The power consumed will be provided by one of the turbines inside the engines. Both engines will be designed to produce a 200V 60Hz AC power of 50 kVA, such that the two engines combined produce a total power of 100 kVA, to ensure a margin of about 20% on top of the current value of the power budget. The APU will provide the start-up power as well as emergency power in case of failure of one or both of the engines. For the APU, the APS2300³ is chosen, which is capable of providing an emergency 200V AC power of 40 kVA⁴.

Summing up the power consumption of all the subsystems results in the actual value of the power budget. A contingency value of 15% is added to this to determine the current value of the power budget. This contingency value was determined for the preliminary design phase in the midterm report[10]. The specification consumption follows from the system requirements, and the target value is found by subtracting the contingency from the specification consumption. Additionally, power is stored in two 28VDC batteries to power emergency systems in case of failure of the power system or production. The energy stored in the batteries will also be used for APU start-up. The batteries will both have a capacity of 28 Ah, of which a flight-proven model exists which is being used on the A320⁵. The total battery capacity therefore equals 56 Ah, thus complying with system requirement REQ-MIS-PWR-6. These batteries will be able to provide emergency power to the aircraft for half an hour.

Table 15.5: Power consumption per subsystem

Source	Power Produced [kVA]
2 x Engine	100
APU	40
Subsystem	Power Consumed [kVA]
Injection system	13.3
Hydraulic system	20.0
Fuel system	6.5
Flight controllers	10.0
Avionics	15.0
(External) Lighting	4.0
Wing anti-icing	10.0
Current consumption	78.8
Actual consumption	90.62
Specification consumption	100
Target consumption	87.0
Contingency	15%

³URL: <https://www.prattwhitney.com/en/products/auxiliary-power-units#:~:text=The%20APU%20comprises%20a%20single,with%2090kVA%20of%20electrical%20power.>

⁴URL: https://www.aircraft-commerce.com/wp-content/uploads/aircraft-commerce-docs/General%20Articles/2021/139_MTCE_A.pdf

⁵URL: <https://saft.com/en/media-resources/press-releases/saft-new-skyzen-batteries-double-maintenance-intervals#:~:text=Since%20summer%202018%2C%20two%2028Ah,emergency%20backup%20for%20critical%20systems.>

3D Model

In this chapter, the engineering drawing and the 3D model developed by CATIA 3D Experience are presented. This includes rendered views from various perspectives and an engineering drawing with key dimensions, found in Section 16.2.

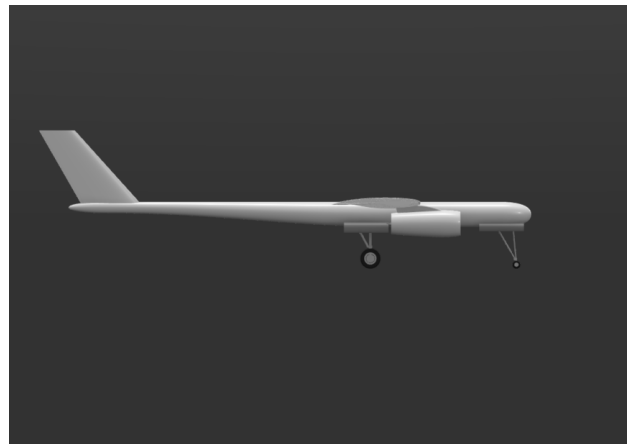
16.1. 3D Model

Contributors: Konstantinos, Moritz

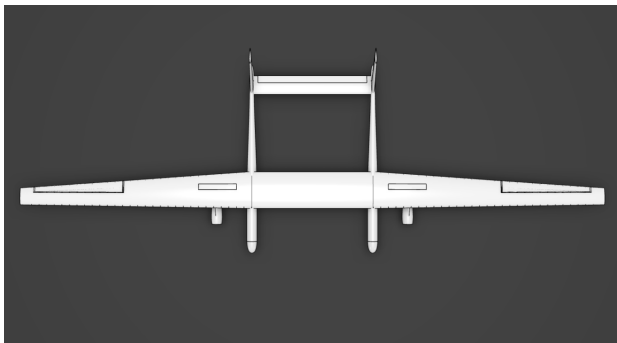
Figure 16.1 offer some renders and views of SCAI. Figure 16.1a is an artistic representation generated using a combination of the 3D-model created in CAD and OpenAI tools . In contrast, , Figure 16.1c and 16.1d were created using just the CAD model and as such are fully true to the design.



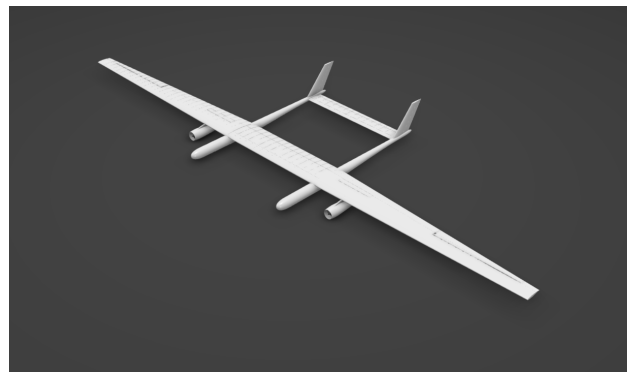
(a) Artistic representation of SCAI at cruise



(b) Side view of SCAI, including landing gear



(c) Top view of the CAD model illustrating the control surfaces



(d) ISO view of the CAD model to scale

Figure 16.1: 3D model views of the SCAI system

16.2. Engineering Drawing

Contributors: Konstantinos, Moritz

The aircraft has a total fuselage length of approximately 23 meters. Similarly, the wings span 77 meters while its height with the gears retracted is merely 1.5 meters. The wing root chord is 4.6 meters, which tapers to 2.1 meters in the tip. The control surfaces are bigger than conventional aircraft to account for the increased MTOM and the low-density environment, as shown in Figure 16.2.

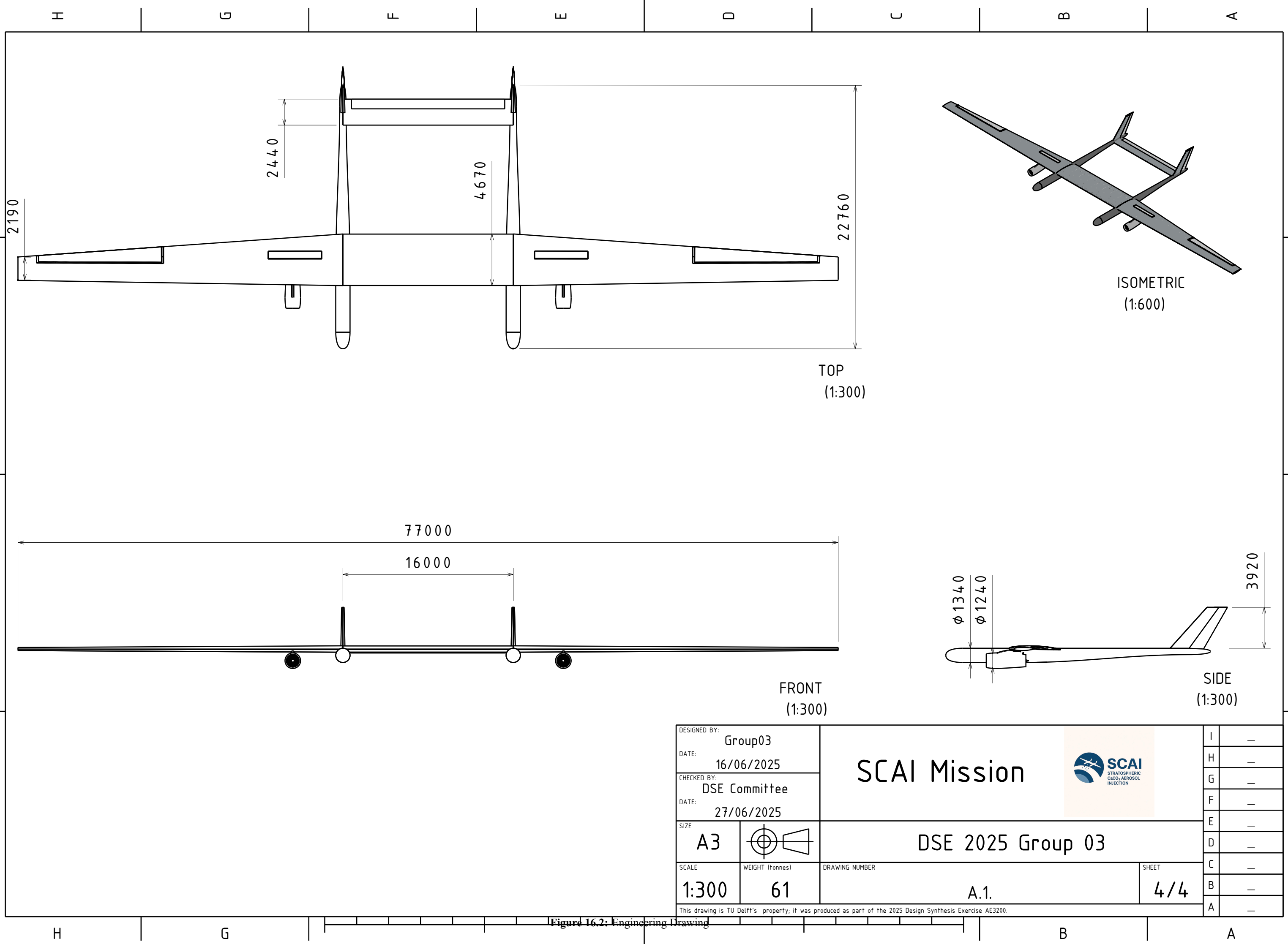


Figure 16.2: Engineering Drawing

Sensitivity Analysis

Sensitivity analyses for the design of the different subsystems have been performed throughout the relevant chapters which have been used to justify design decisions. This chapter will provide an overall sensitivity analysis of the design to assess its robustness and feasibility. It also serves as an extra tool for validation as it gives an insight into the overall trends the model predicts which were checked against expectations based on physics.

During the design process, several variables were identified to be difficult to determine, creating some uncertainty in their value. These were chosen as the inputs for the global sensitivity study. The reasons for the chosen parameters and their search ranges are as follows:

- **Aspect ratio:** Determined based on what is structurally achievable. The aspect ratio is not dictated by any requirement nor does it have a theoretical limit. Therefore, the design was tested for different aspect ratios. A reasonable range was determined by the reference aircraft in the baseline report [54], which generally includes high aspect ratio aircraft.
- **Injection altitude:** Although a value of 20 km is specified in the requirements, it is known that injecting the aerosol at a higher altitude increases the time the aerosol stays in the stratosphere. Therefore, the effect of increasing the ceiling altitude on the design was studied. The range of altitudes useful for SAI was studied.
- **Nozzle mass flow rate:** This is a highly uncertain parameter and active research is still performed on this topic. Yet, it is directly proportional to the required endurance of the aircraft. The sensitivity to this parameter is therefore checked to assess possible changes in the design to increase the injection rate and assess the downsides associated with a lower value than initially expected. The search range was determined by taking the upper and the lower limit of injection rate presented in Chapter 9, setting the lower limit as the low-bound and taking a symmetric range about the chosen higher-bound injection rate.
- **Compressor pressure ratio:** This was chosen as the metric to represent engine efficiency. A sensitivity study is performed to assess how the design would change when a more or less advanced engine is used. A reasonable search range was determined based on past engine data.

The dependent variables were chosen to provide a good overall representation of the aircraft. The aircraft size is represented by the MTOM and the span, the latter having a hard requirement of 80 meters due to airport limitations. The efficiency of the design is represented by looking at the annual operational costs and payload per fuel metric. An overall limitation of the analysis is that the cost estimation is not detailed enough to accurately capture the effects of all varied variables, especially the R&D costs associated with changing the compressor pressure ratio or the aspect ratio. Therefore these values were kept in a range for which technology is already well-demonstrated.

17.1. Aircraft Size Sensitivity

Contributors: Máté, Bas

First of all, the aircraft size sensitivity to variations in the aforementioned parameters was studied. The first metric that was used for this was the maximum take-off mass. The results can be found in Figure 17.1. In this plot, the blue horizontal line shows the final MTOM of the design, and the red horizontal line shows the specification value of the MTOM. As can be seen in the plot, increasing the aspect ratio, aerosol flow rate and fuel efficiency lowers the MTOM of the design. For the ceiling altitude, the opposite is true. The MTOM of the design is most sensitive to changes in the ceiling altitude, while the fuel efficiency has only a minor impact. The sensitivity study confirms expected behaviour. As density decreases exponentially with ceiling altitude, the wing area required to reach the ceiling altitude increases exponentially. With this, the operative empty mass and fuel mass also increase, increasing the overall MTOM. A higher fuel efficiency slightly reduces the fuel mass that needs to be brought on board, which causes a minor reduction in MTOM, as also proven by the sensitivity study.

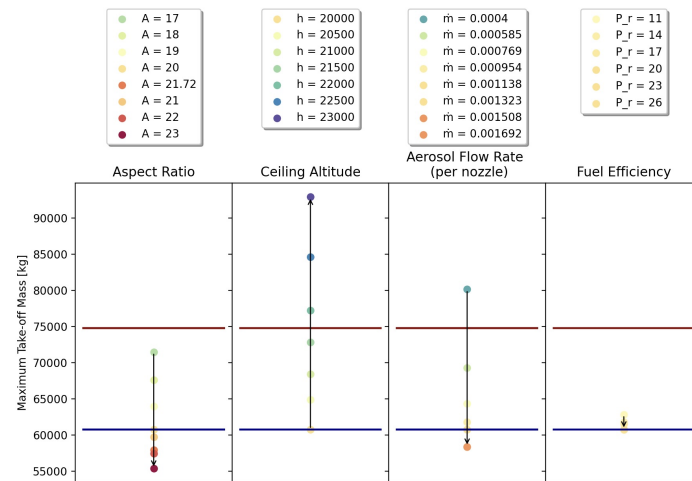


Figure 17.1: MTOM sensitivity to various parameters

The next sensitivity analysis that was done was used to determine if the span chosen was sensitive to the previously explained parameters. The results can be found in Figure 17.2. Again, the blue horizontal line shows the current span of the final design. As can be seen in the plots, increasing the aspect ratio and ceiling altitude increases the span above the regulatory limit of 80 meters. The results make sense, as increasing the aspect ratio is done by increasing the span, and a higher ceiling altitude means the required wing grows exponentially, causing a large growth in wingspan. The results, therefore, show that a higher aspect ratio or ceiling altitude cannot be used. Increasing the aerosol flow rate or fuel efficiency beyond the current values decreases the span, due to a reduction in flight time and fuel mass. This reduction in span is however to an almost insignificant extent. This proves that the span is not highly sensitive to these chosen parameters.

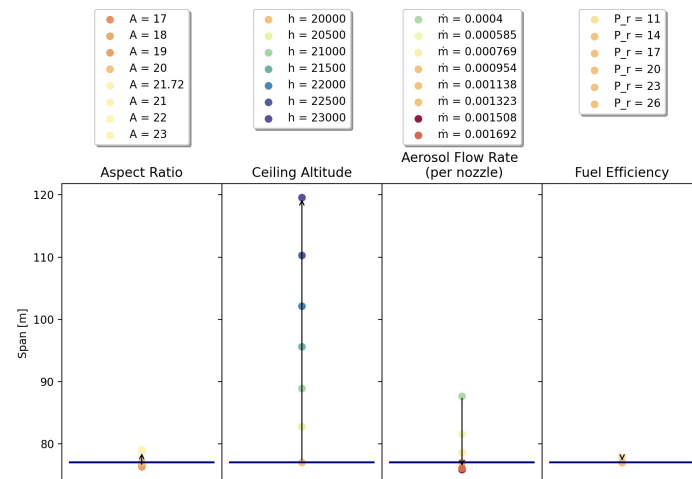


Figure 17.2: Span sensitivity to various parameters

17.2. Efficiency Sensitivity

Contributors: Máté, Bas

Next, the effects of the four parameters on the efficiency of the design were studied. To do this, first a sensitivity study was performed on the effect of the parameters on the operational, production and RDT&E costs. The results for the operational costs are shown in Figure 17.3. In the figure, the dark blue horizontal lines show the final value for the operational costs. The arrows connecting the data points show that the operational costs decrease for increasing aspect ratio, aerosol flow rate and fuel efficiency. This is expected behaviour, as an increase in these three parameters increases the efficiency of the design, and thus the amount of fuel used. An increase in aerosol flow rate also significantly reduces the flight time, reducing the operational costs even more. An increase in ceiling altitude has however the opposite effect. Flying at a higher altitude increases the size of the aircraft, significantly increasing the fuel, maintenance and thus operational costs. The operational costs are mainly dominated by the aerosol flow rate, where a potential decrease in flow rate significantly increases the operational costs due to the longer flight times required. A lower aerosol flow rate than expected thus poses a significant risk to the operating costs of the mission.

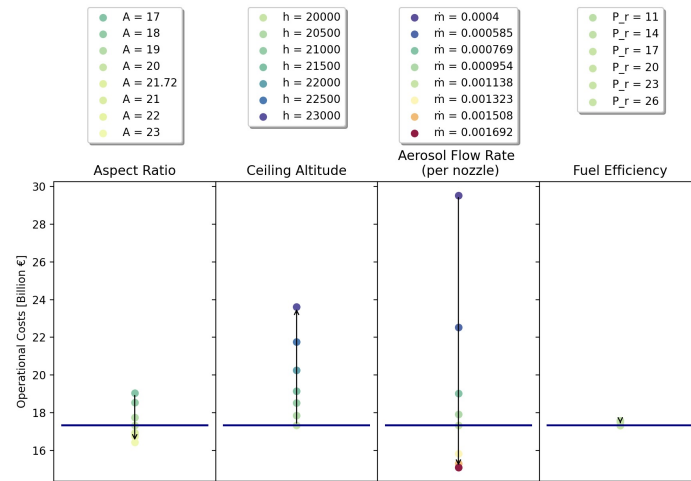


Figure 17.3: Sensitivity of the operational costs to various parameters

Finally, a sensitivity analysis of the payload per fuel carried was performed. The results are shown in Figure 17.4. As seen from the plot, the payload per fuel metric depends on all four of the altered parameters. The aspect ratio, aerosol flow rate and fuel efficiency all have a clear positive effect, as all three of them increase the efficiency of the design, and thus decrease the fuel mass required. The payload per fuel therefore increases. An increase in ceiling altitude however decreases the payload that can be brought per unit of fuel. This is because the increased ceiling altitude increases the size of the aircraft and the fuel required, while the payload mass remains the same. The blue line shows that only a further increase in aspect ratio or aerosol flow rate increases the payload per fuel. The aspect ratio can however not be increased further, as the span can not be increased past 80 meters, and the aerosol flow rate is limited by the currently available technology.

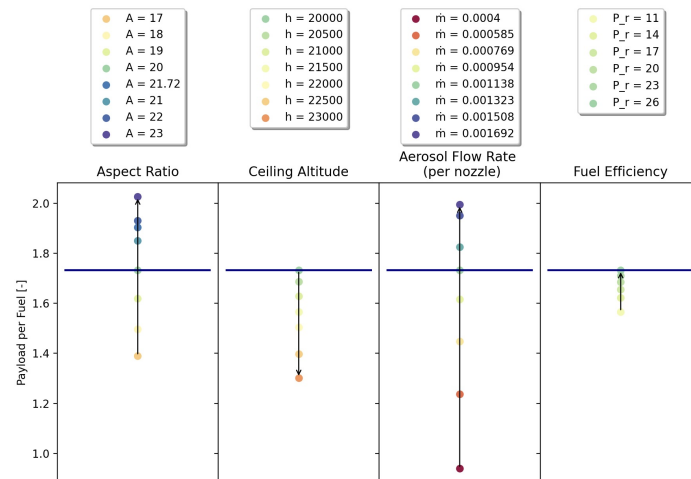


Figure 17.4: Sensitivity of the 'payload per fuel' metric of the design to various parameters

Overall, the sensitivity study shows that the design is robust as iterations converged at all the searched parameters. It also validates the models to some extent, because the trends show expected behaviour from physics. An exception from this is the cost model, which does not consider the extra costs associated with developing a more advanced engine and the cost of achieving a higher aspect ratio.

Verification and Validation

To ensure the design was made correctly, and the right design was made for the stakeholders' needs, thorough verification and validation (V&V) procedures were used, both on a subsystem level as well as on a complete system level. In this chapter, design tool verification will be further explained in addition to the already described V&V methods in the analysis chapters. Next, the requirement validation methods for the final design will be given, followed by a compliance matrix showing the compliance of the design with the system requirements so far.

18.1. Design Tools Verification and Validation

Contributors: Bas

The design tools used for the different analyses performed were verified and validated throughout the report. In Figure 18.1 the individual code coverages for each of the design tools are shown which provides high confidence in the verification process of the design tools. The coverage percentage shows the percentage of code statements that have been reached by the written tests and were therefore included in the tests. A total coverage of 71% was found, with most of the missed statements originating from plotting functions and initial script starting statements, for which tests would not be useful.

The verification process caught errors and discrepancies throughout the written design tools scripts which would otherwise not have been found. This helped make the design tools more accurate in providing reliable results. After updating the codebase numerous times and successfully running all of the tests written, the total coverage of both unit and system tests provided enough confidence for each of the subsystem departments in the correct implementation of the models used. After verification of the implementation, validation of the models themselves was performed to ensure the design tools predict real-world phenomena to the desired accuracy.

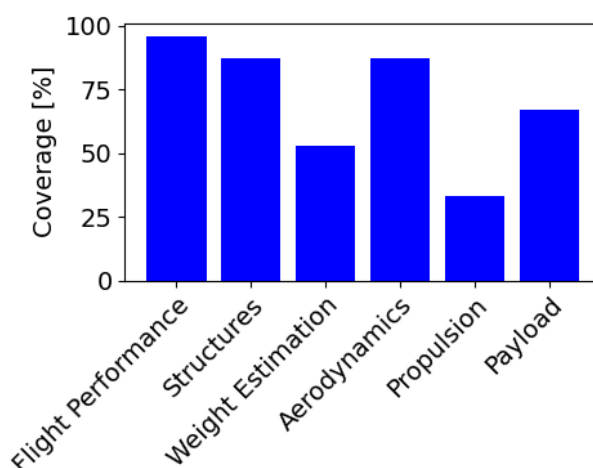


Figure 18.1: Design tools coverage percentage of lines of code reached by unit and system tests

The validation of the design tools was done in their relevant chapters. Design tool validation is often done with real-world data from relevant aircraft, tests, prototypes or simplified cases. Given the novelty of the design, not a lot of reference data was available for this process. Therefore, modern, commercial aircraft were often used, given the large amount of data available on these aircraft. In many scenarios, this data could still be used to validate the design tools made for the design of a high altitude aircraft. For some cases, data from high altitude aircraft such as the Lockheed U-2 or designs from past Design Synthesis Exercise reports were used. After the models used were validated, they could be used for requirement verification. The design tools were used on the design and the results were compared to the stakeholder and system requirements to check if these requirements are met by the design. System requirement compliance is shown in detail in Table 18.2 and Table 18.3. Stakeholder requirement compliance has been checked and shown in each of the technical subsystem verification & validation sections.

18.2. Requirement Validation

Contributors: Konstantinos, Bas

In order to make sure the right design has been made, each of the requirements should be validated. This can be done using

Inspection (I), Analysis (A), Demonstration (D) and/or Testing (T). For each of the system requirements which followed from the stakeholder requirements, a validation method was determined. For each requirement validation method, the necessary facilities and the expected costs were also determined. An overview of all the validation methods is given in Table 18.1.

It was found that even after optimising the necessary validation tests, four separate test flights are necessary, as well as five weeks of wind tunnel testing. Based on the expected costs in Table 18.1, an estimate of \$356.6 million USD was determined for the total testing budget. This is a significant part of the RDT&E budget from Figure 15.1 which is necessary to prove to the stakeholders that the right design has been made for their needs.

Table 18.1: Verification methods and details for all system requirements

Requirement	Method	Test Details and Facilities	Expected Cost
REQ-MIS-PDI-1	D	A test injection flight will be performed, with a trailing second aircraft measuring the injected aerosol concentration.	Two flights cost: 66k \$
REQ-MIS-PDI-2	T	The mass flow behind the injection system is measured on a test bench using a mass flow sensor.	Testing facility costs: 356m \$
REQ-MIS-PDI-3	D	A goniophotometer shall be used to measure the light emitted at different angles for a specific volume of aerosol.	Testing facility costs: 356m \$
REQ-MIS-MPR-2	D	Injection height shall be measured during a test flight.	Flight cost: 33k \$
REQ-MIS-MPR-3	D	A max endurance test flight shall be performed.	Flight cost: 33k \$
REQ-MIS-MPR-4	D	A max range test flight shall be performed.	Flight cost: 33k \$
REQ-MIS-MPR-6	D	A test flight shall perform a maximum range diversion manoeuvre.	Flight cost: 33k \$
REQ-MIS-MPR-7	D	The sensors shall be tested under controlled low visibility conditions on a test bench.	Testing facility costs: 356m \$
REQ-MIS-MPR-8	D, A	A scale model shall be tested in a wind tunnel, and numerical calculations shall be performed to ensure compliance with airworthiness authorities.	Wind tunnel cost: 31k \$
REQ-MIS-REC-1 REQ-MIS-REC-2 REQ-MIS-REC-3 REQ-MIS-REC-4 REQ-MIS-NREC-1 REQ-MIS-NREC-2	D D D D D D	All costs after one full year of operation will be compared to the yearly estimated costs using detailed financial reports.	A financial consultant shall be employed for 49k \$/year.
REQ-MIS-OSC-1	D	Total operating days shall be measured during the first operational year.	- \$
REQ-MIS-OSC-2	D	Total years of production shall be measured during the entire operation	- \$
REQ-MIS-DSC-1	D	The design completion date shall be determined.	- \$
REQ-MIS-MNP-1 REQ-MIS-MNP-2 REQ-MIS-MNP-3 REQ-MIS-MNP-4 REQ-MIS-MNP-5 REQ-MIS-MNP-6 REQ-MIS-MNP-7	I I I I I I I	Number of staff is verified by reviewing HR and payroll records.	A HR manager shall be employed for 49k \$/year.
REQ-MIS-ABS-1	I	The logistics team shall ensure enough payload is available at any given instance and weekly keep detailed supply records.	A logistics team shall be employed for 49k \$/year
REQ-MIS-ABS-2	I	The logistics team shall ensure enough fuel is available at any given instance and weekly keep detailed supply records.	A logistics team shall be employed for 49k \$/year
REQ-MIS-ABS-3	I	The logistics team shall acquire the required maintenance tools.	A logistics team shall be employed for 49k \$/year
REQ-MIS-ABS-4	I	The logistics team shall ensure the selected airports have an ATC available during operation hours.	A logistics team shall be employed for 49k \$/year
REQ-MIS-ABS-5	I	The airport records are inspected to ensure compliance with the design.	A logistics team shall be employed for 49k \$/year
REQ-MIS-ABS-6	I	The airport records are inspected to ensure compliance with the design.	A logistics team shall be employed for 49k \$/year
REQ-MIS-ABS-7	I	The logistics team shall ensure enough spare parts are available at any given instance and weekly keep detailed supply records.	A logistics team shall be employed for 49k \$/year
REQ-MIS-ABS-8	I	The logistics team shall ensure enough spare aircraft are available at any given instance.	A logistics team shall be employed for 49k \$/year
REQ-MIS-GBS-1	D	Each ground base shall demonstrate its ability to connect with the communication subsystem of the aircraft before each flight.	An operations team shall be employed for 49k \$/year

REQ-MIS-GBS-2	D	The weather predictions of each ground base shall be validated with official providers (national weather services). Reports shall be updated frequently.	An operations team shall be employed for 49k \$/year
REQ-MIS-GBS-3	D	Before each operational day, a communications check shall be performed between all ground bases.	An operations team shall be employed for 49k \$/year
REQ-MIS-GBS-4	D	Co-architecture of the design of products and their manufacturing systems shall be used to ensure their compatibility.	These are included in the non-recurring production costs and, thus, are not accounted for here.
REQ-MIS-GBS-5	D	A top-quality testing facility is used to ensure each part of the testing plan can be performed.	Testing facility costs: 356m \$
REQ-MIS-GBS-6 REQ-MIS-GBS-7	A A	The aircraft production and assembling reliability shall be analysed using mathematical models.	A design team shall be employed for 49k \$/year
REQ-MIS-MSS-1	A	The minimum and maximum payload weight of the design shall be analysed using mathematical models.	A design team shall be employed for 49k \$/year
REQ-MIS-MSS-2	A	The maximum take-off weight shall be analysed for the design.	A design team shall be employed for 49k \$/year
REQ-MIS-MSS-3	A	The propulsion subsystem mass and OEM shall be computed and compared.	A design team shall be employed for 49k \$/year
REQ-MIS-MSS-4	A	The structure subsystem mass and OEM shall be computed and compared.	A design team shall be employed for 49k \$/year
REQ-MIS-MSS-5	A	The minimum and maximum fuel weight shall be analysed for the design.	A design team shall be employed for 49k \$/year
REQ-MIS-MSS-6	A	The minimum and maximum centre of gravity location shall be computed and compared to the chord length.	A design team shall be employed for 49k \$/year
REQ-MIS-PWR-1 REQ-MIS-PWR-2 REQ-MIS-PWR-3 REQ-MIS-PWR-4 REQ-MIS-PWR-5 REQ-MIS-PWR-7	T T T T T T	The subsystems shall be tested on a test bench using a Wattmeter.	Testing facility costs: 356m \$
REQ-MIS-PWR-6	T	The total battery capacity shall be tested by discharging it, for a constant known current until the cut-off Voltage. The time it takes shall be recorded.	Testing facility costs: 356m \$
REQ-MIS-PWR-8	T	The main power bus voltage shall be measured on a test bench using a voltmeter.	Testing facility costs: 356m \$
REQ-MIS-ENV-1	T	The propulsion subsystem shall be tested at sea-level operating conditions while measuring the fuel consumption and thrust level.	Turbofan testing facility: 16k \$ ¹
REQ-MIS-ENV-2	A	For each subsystem, a detailed End of Life shall be developed to ensure recyclability of the materials used.	A logistics team shall be employed for 49k \$/year
REQ-MIS-ENV-3	A	For each subsystem, a detailed LCA shall be conducted to minimise the carbon emissions of the production process.	A logistics team shall be employed for 49k \$/year
REQ-MIS-ENV-4	A	The noise emissions shall be modelled during the design phase to ensure compliance with the airworthiness authorities.	A design team shall be employed for 49k \$/year
REQ-MIS-ENV-5	A, D	The End of Life plan shall include a detailed analysis about the decommissioning of the aircraft, which shall be demonstrated after each aircraft is decommissioned.	A logistics team shall be employed for 49k \$/year
REQ-SYS-PLD-1	T	The particle size shall be measured while running the injection system on a test bench at cruise conditions using a cytometer [4].	This falls under the responsibility of the scientific community.
REQ-SYS-PLD-2	A	The total payload capacity of the aircraft shall be analysed for the design.	A design team shall be employed for 49k \$/year
REQ-SYS-PLD-3	T	The payload subsystem configuration shall be tested on a test chamber at cruise temperatures, and the payload temperature shall be measured to ensure proper insulation.	Testing facility costs: 356m \$
REQ-SYS-PLD-4	T	The payload contents shall be measured on a test bench at cruise conditions using a cytometer[4], to determine the percentage of impurities.	This falls under the responsibility of the scientific community.

¹URL: https://aerospace.honeywell.com/content/dam/aerobt/en/documents/learn/services/asset-availability/user-documents/2022_Engine_Rental_Policy_Pricing.pdf

REQ-SYS-PLD-5	D	The payload storage subsystem shall be tested by being exposed to water flow in a test chamber, and the container contents will be analysed for humidity after the test.	Testing facility costs: 356m \$
REQ-SYS-CNT-1	T	The control subsystem's function shall be verified on a test bench, by providing it with a variable-controlled input and testing its response.	Testing facility costs: 356m \$
REQ-SYS-CNT-2	T	The control subsystem's response to programmed gust inputs shall be tested on a test bench.	Testing facility costs: 356m \$
REQ-SYS-CNT-3	T	The control subsystem's response to incorrect, malfunctioning sensor input shall be tested on a test bench and its reaction recorded.	Testing facility costs: 356m \$
REQ-SYS-CNT-4	T	The control subsystem's response to inputs simulating a CAT II approach with low visibility conditions shall be recorded.	Testing facility costs: 356m \$
REQ-SYS-PRP-1	A	The available thrust of the aircraft at delivery altitude shall be simulated and compared to the weight at this point.	A design team shall be employed for 49k \$/year
REQ-SYS-PRP-2	T	The propulsion system shall be tested in an engine test setup to measure the engine emissions at maximum thrust setting.	Turbofan testing facility: 16k \$ ²
REQ-SYS-ARD-1	A	The flight performance of the design will be analysed using analytical and numerical (CFD etc.) methods.	A design team shall be employed for 49k \$/year. Software costs: 5k \$
REQ-SYS-ARD-2	A, T	The flight performance of the design will be analysed using analytical and numerical (CFD etc.) methods. Additionally, a wind tunnel test shall be performed.	A design team shall be employed for 49k \$/year. Software costs: 5k \$. Wind tunnel costs: 31k \$
REQ-SYS-ARD-3	A, D	A reliability analysis shall be performed to assess when the aerodynamic coefficient of a subsystem deteriorates under a predetermined threshold. Frequent maintenance shall take place to ensure that all surfaces meet the expected quality standards.	An operations team shall be employed for 49k \$/year
REQ-SYS-ARD-4 REQ-SYS-ARD-5 REQ-SYS-ARD-6	A, T A, T A, T	The directional stability shall be tested using CFD and stability simulations. Additionally, a wind tunnel test shall be performed to measure the pressure distributions around the aircraft.	A design team shall be employed for 49k \$/year. Software costs: 5k \$. Wind tunnel costs: 31k \$
REQ-SYS-ARD-7	A, T	CFD simulations will be used to make sure the minimum lift coefficient at delivery altitude is at least <TBD> % of the sea-level value. Additionally, an estimation shall be conducted using the wind tunnel at representative Reynolds numbers and equivalent airspeeds to replicate the true airspeed at an altitude of 20 km.	A design team shall be employed for 49k \$/year. Software costs: 5k \$ Wind tunnel costs: 31k \$
REQ-SYS-ARD-8	A, T	Analytical Models and Numerical Simulations, like CFD, will be used to determine the stall speed at delivery altitude. Additionally, an estimation shall be conducted using the wind tunnel at representative Reynolds numbers and equivalent airspeeds to replicate the true airspeed at an altitude of 20 km.	A design team shall be employed for 49k \$/year. Software costs: 5k \$. Wind tunnel costs: 31k \$
REQ-SYS-STR-1	A, T	The stresses will be determined using representative FEM analysis and taking aeroelasticity considerations into account. The structural components will be tested under an Ultimate Load-Wing Test to simulate the aerodynamic loads.	A design team shall be employed for 49k \$/year. Software costs: 5k \$. Testing facility costs: 356m \$
REQ-SYS-STR-2	A	The minimum and maximum payload weight of the design shall be analysed using mathematical models.	A design team shall be employed for 49k \$/year
REQ-SYS-STR-3	A, T	A fatigue and creep analysis will take place to determine a safe threshold between maintenance times. A test structure subsystem will be tested in pressure chambers and bending trees for a large number of times to test the structure's ability to survive all operations in a week without degradation. A creep and fatigue test will be performed.	A design team shall be employed for 49k \$/year. Testing facility costs: 356m \$
REQ-SYS-STR-4	A	A thermal analysis shall take place to determine the expansion and contraction coefficients of the structure.	A design team shall be employed for 49k \$/year. Software costs: 5k \$

²URL: https://aerospace.honeywell.com/content/dam/aerobt/en/documents/learn/services/asset-availability/user-documents/2022_Engine_Rental_Policy_Pricing.pdf

REQ-SYS-STR-5	A,T	Load paths shall be analysed using FEM. Operation capabilities will be determined under partial or holistic part failure.	A design team shall be employed for 49k \$/year. Software costs: 5k \$. Testing facility costs: 356m \$
REQ-SYS-STR-6	I	A test aircraft will be inspected to determine the accessibility of the design.	An operations team shall be employed for 49k \$/year
REQ-SYS-STR-7	A	The End of Life plan shall include a detailed analysis about the recyclability or reusability of the materials used.	A logistics team shall be employed for 49k \$/year
REQ-SYS-AVI-1	T, D	The avionics subsystems communication range shall be tested and compared to the ground station coverage range. Communication tests shall be performed at regular time intervals throughout the mission's duration.	A design team shall be employed for 49k \$/year, an operations team shall be employed for 49k \$/year
REQ-SYS-AVI-2	T,D	The tracker shall be tested by providing a variable-controlled input and its response recorded. It shall be demonstrated to work under all operational conditions.	A design team shall be employed for 49k \$/year
REQ-SYS-AVI-3	T,D	The sensor shall be tested by providing a variable controlled input and its response recorded. It shall be demonstrated to work under all operational conditions during a test flight.	A design team shall be employed for 49k \$/year, Flight cost: 33k \$
REQ-SYS-AVI-4	T, D	The avionics subsystems transmission/receiving range shall be tested and compared to the ground station transmission/receiving range. Tests shall be performed at regular time intervals throughout the mission's duration.	A design team shall be employed for 49k \$/year, an operations team shall be employed for 49k \$/year
REQ-SYS-AVI-5	T	The pointing accuracy of the avionics subsystem shall be tested on a test bench, using tests like the Boresight Accuracy Test ³ and Tracking Accuracy Test ⁴ .	A design team shall be employed for 49k \$/year. Testing facility costs: 356m \$

18.3. Design Requirements Compliance

Contributors: All

The compliance of the design with each of the system requirements is shown in the compliance matrices found in Table 18.2 for the mission requirements and Table 18.3 for the system requirements. In the case that compliance with a requirement was verified a check mark (✓), accompanied by the section of this report in which the compliance has been checked, and a short explanation of how compliance was verified are shown. In case the requirement was not met, a cross (×) as well as the achieved value is given, if calculated. For some requirements no value could be computed yet, and an explanation for this is given, together with a method for checking compliance in the future.

Table 18.2: Design compliance with mission requirements

ID	Description	Stk. Req.	Compliance	Section
REQ-MIS-PDI-1	The system shall disperse the aerosol with a 0.0025 g/cm ³ concentration.	REQ-STK-2	✓ The generated aerosol has a concentration of 0.0025 g/cm ³ and upon injection this reduces significantly.	Section 9.2
REQ-MIS-PDI-1.1	The aerosol distribution system shall prevent the agglomeration of particles during dispersion.	REQ-STK-2	✓ The aerosol generators and nozzles break up agglomerates before and during injection.	Section 9.2
REQ-MIS-PDI-2	The aerosol injection rate shall be no lower than 0.1 g/s.	REQ-STK-2	✓ An injection rate of 0.774 kg/s per aircraft was determined.	Section 9.2
REQ-MIS-PDI-2.1	The aerosol shall be injected at a constant rate throughout the year.	REQ-STK-2	✓ The required flights are spread constantly throughout the 250 operating days.	Section 19.2

Table 18.2 continued on next page

³URL: https://www.inframet.com/boresight_systems.htm

⁴URL: <https://www.antesky.com/what-are-methods-for-antenna-tracking-system/>

Table 18.2 continued from previous page

ID	Description	Stk. Req.	Compliance	Section
REQ-MIS-PDI-3	The aerosol injection shall provide radiative forcing of 1 W/m^2 after 15 years.	REQ-STK-3	× Demonstration is necessary, as unexpected stratospheric effects may occur.	-
REQ-MIS-MPR-2	The system shall deliver the payload at mission altitude with a maximum variance of 2 km of the target altitude.	REQ-STK-4	✓ The payload is injected at the altitudes 20km and 21.5km.	Section 10.4
REQ-MIS-MPR-3	The system shall have a minimum endurance of 240 minutes.	REQ-STK-4	✓ The maximum endurance was calculated to be 316 minutes.	Section 10.5
REQ-MIS-MPR-4	The system shall have a minimum range of 1500 km.	REQ-STK-4	✓ Range calculated to be 1730 km at MTOM.	Section 10.3
REQ-MIS-MPR-6	The system shall have diversion capabilities of 45 minutes with reserve fuel.	REQ-STK-9	✓ Loiter time was calculated to be 53.5 minutes with planned reserve fuel.	Section 10.5
REQ-MIS-MPR-7	The system shall take off and land under low visibility conditions, below <TBD>meters of Runway Visual Range (RVR).	REQ-STK-9	Cannot be accurately be verified with computer models, should be verified in the future using a demonstration with a prototype flight computer and sensors in low visibility conditions.	-
REQ-MIS-MPR-8	The system shall take off and land with gusts up to 20 knots.	REQ-STK-20	× Could not be verified with an analysis with the available resources.	-
REQ-MIS-MPR-9	The system shall be able to operate within a temperature range of -70°C to 50°C .	REQ-STK-2	× A temperature response analysis could not yet be performed with the available resources.	-
REQ-MIS-MPR-10	The system shall withstand vibration levels up to <TBD> g RMS	REQ-STK-2	× A vibrations analysis could not yet be performed with the available resources. The vibration levels present could also not yet be estimated and are left TBD.	-
REQ-MIS-REC-1	The maintenance cost shall not exceed 30 % of the total yearly operational costs.	REQ-STK-17	✓ The maintenance costs were estimated to be 20% of the operational costs due to the large personnel and fuel costs.	Figure 15.1
REQ-MIS-REC-2	Personnel training and salaries shall remain within 50 % of the annual operating cost.	REQ-STK-17	✓ The personnel costs were found to be 45% of the annual operating costs.	Figure 15.1
REQ-MIS-REC-3	The yearly fuel cost per aircraft shall not exceed 20 % of the total operating cost per aircraft.	REQ-STK-17	✓ The fuel costs were estimated based on the total fuel mass consumption, resulting in a share of 17% of the operational costs.	Figure 15.1
REQ-MIS-REC-4	The yearly material cost per aircraft shall not exceed 20% of the total manufacturing cost per aircraft.	REQ-STK-16	✓ The materials were found to only account for 8.5% of the production costs using mass and labour cost estimation formulas.	Figure 15.1

Table 18.2 continued on next page

Table 18.2 continued from previous page

ID	Description	Stk. Req.	Compliance	Section
REQ-MIS-NREC-1	Purchases for specialised manufacturing equipment shall not exceed 20 % of the total non-recurring manufacturing costs.	REQ-STK-16	× The required specialised manufacturing equipment are not yet known, and the costs could not yet be estimated.	-
REQ-MIS-NREC-2	Tooling and setup costs shall not exceed 20 % of the total non-recurring manufacturing cost.	REQ-STK-16	× Tooling and setup costs were not yet estimated as no methods were found.	-
REQ-MIS-OSC-1	The fleet shall be operational for at least 250 days in a year.	REQ-STK-3	✓ The operations and logistics have been designed to operate 250 days per year.	Section 19.2
REQ-MIS-OSC-1.1	Each flight duration shall not exceed a maximum of 360 minutes.	REQ-STK-3	✓ The planned flight profile including loiter was found to not exceed the maximum endurance achievable by the design of 316 minutes.	Section 10.4
REQ-MIS-OSC-2	The manufacturing of the entire fleet shall take no more than 15+5 years.	REQ-STK-21	× Can not yet be checked, post-DSE operations	-
REQ-MIS-OSC-2.1	The manufacturing of the first 10% of aircraft in the fleet shall take no more than 5 years.	REQ-STK-21	× Can not yet be checked, post-DSE operations	-
REQ-MIS-OSC-2.2	The manufacturing schedule shall include a buffer of 30 calendar days or more for every used technology with a TRL lower than 7.	REQ-STK-21	✓ Given the novelty of the design, a conservative manufacturing schedule has been chosen similar to that of the most modern aircraft at this moment.	Chapter 22
REQ-MIS-DSC-1	The conceptual design of the fleet shall be completed by 27/06/2025.	REQ-STK-23	✓ As of this report, the conceptual design of the fleet has been completed.	All
REQ-MIS-MNP-1	The production line shall have a full team of <TBD> trained employees.	REQ-STK-21	× Can not yet be checked, post-DSE operations	-
REQ-MIS-MNP-2	<TBD> technicians shall be trained to service the fleet.	REQ-STK-3	× Can not yet be checked, post-DSE operations	-
REQ-MIS-MNP-3	<TBD> trained technicians shall be available during aircraft downtime for pre-flight inspections.	REQ-STK-3	× Can not yet be checked, post-DSE operations	-
REQ-MIS-MNP-4	<TBD> safety operators shall be trained to operate the fleet.	REQ-STK-3	× Can not yet be checked, post-DSE operations	-
REQ-MIS-MNP-5	A trained safety team of <TBD> employees shall be available during all fleet operating hours.	REQ-STK-3	× Can not yet be checked, post-DSE operations	-
REQ-MIS-MNP-6	<TBD> ground operators shall be trained to operate the fleet.	REQ-STK-3	× Can not yet be checked, post-DSE operations	-
REQ-MIS-MNP-7	A team of <TBD> ground operators shall be available during fleet operating hours for flight preparation and control.	REQ-STK-3	× Can not yet be checked, post-DSE operations	-
REQ-MIS-ABS-1	Each available airport shall be able to supply the Calcite payload to the fleet aircraft operated there.	REQ-STK-2	✓ This was one of the criteria used during the selection process, all airports comply.	Section 19.3

Table 18.2 continued on next page

Table 18.2 continued from previous page

ID	Description	Stk. Req.	Compliance	Section
REQ-MIS-ABS-2	Each available airport shall be able to supply the Jet-A fuel to the fleet aircraft operated there.	REQ-STK-4	✓ This was one of the criteria used during the selection process, all airports comply.	Section 19.3
REQ-MIS-ABS-3	Each available airport shall have the required equipment available needed for maintenance of the fleet aircraft.	REQ-STK-3	× While the chosen airports can perform maintenance on commercial aircraft, the availability of the necessary equipment could not yet be verified.	-
REQ-MIS-ABS-4	Each available airport shall have an available ATC during fleet operating hours.	REQ-STK-20	✓ This was one of the criteria used during the selection process, all airports comply.	Section 19.3
REQ-MIS-ABS-5	Each available airport shall be able to support the fleet aircraft of size 20 by 80 meters.	REQ-STK-2	× Could not yet be verified if each airport can and is willing to handle an aircraft with a span of 80 meters. The required length is smaller than most aircraft operated at these airports.	-
REQ-MIS-ABS-6	Each available airport shall be able to support the fleet aircraft of mass 50,000 kg.	REQ-STK-2	✓ All chosen airports handle commercial aircraft significantly heavier than 50,000 kg.	Section 19.3
REQ-MIS-ABS-7	Each air base shall have <TBD> spare parts in storage for needed aircraft part replacements.	REQ-STK-3	× Can not yet be verified as spare parts required are still TBD, and the design has not been manufactured yet.	-
REQ-MIS-ABS-8	Each air base shall have <TBD> spare aircraft available for replacement during fleet aircraft maintenance downtime.	REQ-STK-3	× The possibility to store spare aircraft at the air bases can not yet be verified.	-
REQ-MIS-GBS-1	Each ground base shall be equipped with the communication technology required to communicate with the fleet aircraft.	REQ-STK-20	× Can not yet be checked, post-DSE operations once ground bases are set up.	-
REQ-MIS-GBS-2	Each ground base shall be equipped with a weather station.	REQ-STK-2	× Can not yet be checked, post-DSE operations once ground bases are set up.	-
REQ-MIS-GBS-3	Each ground base shall be able to communicate with all other mission ground bases.	REQ-STK-3	× Can not yet be checked, post-DSE operations once ground bases are set up.	-
REQ-MIS-GBS-4	A production facility able to follow the production plan for the designed aircraft shall be established.	REQ-STK-21	× Can not yet be checked, post-DSE operations	-
REQ-MIS-GBS-5	The testing equipment installed shall allow for testing each manufactured system.	REQ-STK-20	× Can not yet be checked, post-DSE operations	-
REQ-MIS-GBS-6	The production facility shall be able to follow the production plan with a minimum reliability of 95%.	REQ-STK-16	× Can not yet be checked, post-DSE operations	-
REQ-MIS-GBS-7	The production facility shall be able to follow the assembly plan with a minimum reliability of 95%.	REQ-STK-16	× Can not yet be checked, post-DSE operations	-

Table 18.2 continued on next page

Table 18.2 continued from previous page

ID	Description	Stk. Req.	Compliance	Section
REQ-MIS-MSS-1	The payload mass range on each vehicle shall be within 0 and 17,000 kg.	REQ-STK-17	✓ The aircraft has been designed around a maximum payload mass of 17,000 kg.	Section 9.2
REQ-MIS-MSS-2	The vehicle shall have a maximum MTOM of maximally 80,000 kg.	REQ-STK-6	✓ The design was calculated to have an MTOM of 60,771 kg.	Section 15.2
REQ-MIS-MSS-3	The propulsion subsystem shall have a mass fraction less than 0.4.	REQ-STK-18	✗ Propulsion mass fraction was found to be 0.5.	Section 15.2
REQ-MIS-MSS-4	The structure subsystem shall have a mass fraction less than 0.4.	REQ-STK-18	✓ Structure mass fraction was found to be 0.35.	Section 15.2
REQ-MIS-MSS-5	The vehicle shall be able to carry within 3,000 and 10,000 kg fuel.	REQ-STK-18	✓ The maximum fuel mass was set to the required fuel mass for the mission, which was found to be 9,870 kg.	Section 15.2
REQ-MIS-MSS-6	The total centre of gravity range in operation shall be less than the chord length.	REQ-STK-20	✓ A mass balance showed cg limits of 0.17 and 0.455 times the MAC, showing a total range of 0.285 times the chord.	Section 12.1
REQ-MIS-PWR-1	The payload ejection system shall not use more than 35 kVA of power.	REQ-STK-2	✓ The injection system was found to only use 13.12 kVA in total.	Section 9.2
REQ-MIS-PWR-2	The payload temperature control shall not use more than 2 kVA of power.	REQ-STK-2	✓ The entire payload system was found to consume 13.12 kVA, including environmental control.	Section 15.3
REQ-MIS-PWR-3	The vehicle shall produce at least 200VAC 70 kVA of AC power.	REQ-STK-20	✓ The engines produce 100 kVA, with an additional emergency 40 kVA being produced by the APU.	Section 15.3
REQ-MIS-PWR-4	The vehicle shall have a power margin of at least 30%.	REQ-STK-20	✓ The vehicle was found to have a power margin of 40 % at maximum consumption with both engines operational.	Section 15.3
REQ-MIS-PWR-5	The avionics of the vehicle shall not use more than 20 kVA of power.	REQ-STK-20	✓ The avionics subsystem was estimated to use 15 kVA of power.	Section 15.3
REQ-MIS-PWR-6	50 Ah of energy shall be stored in the batteries of the vehicles.	REQ-STK-20	✓ Two 28Ah batteries were chosen to supply the emergency power and start up the APU.	Section 15.3
REQ-MIS-PWR-7	The propulsion subsystem shall not use more than 20 kVA of power.	REQ-STK-20	✓ The propulsion subsystem was determined to be the source of power production.	Section 15.3
REQ-MIS-PWR-8	The main power bus shall be at 200 volts.	REQ-STK-20	✓ The main power bus was chosen to operate at 200 VAC.	Section 14.4
REQ-MIS-ENV-1	The vehicle shall have a maximum specific fuel consumption of 29 g/kNs.	REQ-STK-18	✓ At cruise conditions, the engines have an SFC of 28.6 g/kNs	Section 11.4

Table 18.2 continued on next page

Table 18.2 continued from previous page

ID	Description	Stk. Req.	Compliance	Section
REQ-MIS-ENV-2	50% of the aircraft shall be made of recyclable materials.	REQ-STK-12	✓ The stringers, spars and skin of the wing-box and fuselage are all made out of recyclable aluminium, which accounts for most of the aircraft.	subsection 13.3.3
REQ-MIS-ENV-3	The manufacturing of the complete fleet shall have a total carbon dioxide emission of maximally 1 Mt.	REQ-STK-18	✓ Using an LCA, the total emission was found to be 0.53 Mt of CO ₂ for manufacturing the entire fleet.	subsection 21.2.2
REQ-MIS-ENV-4	The maximum noise created by the system as measured on the ground shall not exceed 90 dB.	REQ-STK-20	× Noise could not yet be analysed with the available resources.	-
REQ-MIS-ENV-5	The non-recyclable materials in the vehicle after decommissioning of the aircraft shall be brought to a disposal facility.	REQ-STK-14	✓ The end of life plan states that non-recyclable materials are brought to a disposal facility.	Section 21.3
REQ-MIS-ENV-6	Each vehicle shall be able to operate for at least <TBD> years.	REQ-STK-14	× Could not be determined with an analysis.	-

Table 18.3: Design compliance with system requirement

ID	Description	Stk. Req.	Compliance	Section
REQ-SYS-PLD-1	The aerosol particles shall be between 200 and 250 nm.	REQ-STK-2	× Can not yet be checked, post-DSE operations include generator and nozzle system testing.	-
REQ-SYS-PLD-2	Each flight shall transport at least 10 tonnes of solid aerosol.	REQ-STK-2	✓ The aircraft has been designed for carrying a solid aerosol payload of almost 15 tonnes.	Section 9.2
REQ-SYS-PLD-2.1	The total payload weight shall not exceed 50% of the MTOM.	REQ-STK-2	✓ The MTOM for a payload of 17t was found to be 60.8t, ratio therefore is 28%.	Section 15.2
REQ-SYS-PLD-3	The payload shall be contained at a temperature of 293.15 K.	REQ-STK-2	✓ The system will operate at temperatures below 293.15 K and storage will be climate controlled.	Section 9.2
REQ-SYS-PLD-4	The payload shall contain less than 1% impurities by mass.	REQ-STK-2	× Can not yet be checked, post-DSE operations	-
REQ-SYS-PLD-5	The payload shall be humidity sealed.	REQ-STK-2	✓ The aerosol system is fully sealed from the outside environment up until injection.	Section 9.2
REQ-SYS-CNT-1	The control subsystem shall maintain stable flight conditions throughout the flight mission.	REQ-STK-20	✓ The aircraft was found to be dynamically stable during flight.	Section 12.6
REQ-SYS-CNT-1.1	The subsystem shall include onboard software to ensure stability when static stability is not fulfilled.	REQ-STK-20	✓ The flight computer's software runs a control system using navigation sensors and has the authority to control the aircraft control surfaces to ensure stability.	Section 14.6

Table 18.3 continued on next page

Table 18.3 continued from previous page

ID	Description	Stk. Req.	Compliance	Section
REQ-SYS-CNT-2	The control subsystem shall provide aircraft stability for crosswinds up to 20 knots.	REQ-STK-8	× While dynamically stable, crosswinds could not yet be simulated with the available resources.	-
REQ-SYS-CNT-3	The control system shall remain operable in case of a single component failure or damage.	REQ-STK-20	✓ For redundancy, three flight computers and two power buses are used.	Section 14.6
REQ-SYS-CNT-3.1	The control subsystem shall include redundant sensors, actuators, and processors.	REQ-STK-20	✓ Three flight computers are used, as well as a normal set of sensors and actuators as well as an emergency set.	Section 14.6
REQ-SYS-CNT-4	The control subsystem shall support the CAT II Landing capabilities.	REQ-STK-9	× Could not be verified through analyses, should be verified using simulations which support Cat II circumstances.	-
REQ-SYS-CNT-4.1	The control subsystem shall at least support an ILS, MLS or GLS approach.	REQ-STK-9	× Could not yet be verified, requires expensive simulations or a prototype test.	-
REQ-SYS-PRP-1	The propulsion system shall provide a thrust-to-weight ratio of at least 6 at delivery altitude.	REQ-STK-4	✓ The engines have a thrust-to-weight ratio of 6.1	Section 11.4
REQ-SYS-PRP-1.1	The maximum thrust shall be at least 30.5 kN at cruise	REQ-STK-4	✓ 2 Engines can provide ≈32kN of thrust at cruise conditions.	Section 11.4
REQ-SYS-PRP-2	The propulsion system shall have a maximum of <TBD> emissions of greenhouse gases.	REQ-STK-18	× The total greenhouse gas emissions could not yet be analysed with the available resources and are left TBD.	-
REQ-SYS-PRP-2.1	The propulsion system shall have a specific fuel consumption (SFC) of maximally 29 g/kNs.	REQ-STK-18	✓ The engines have an SFC of 28.6 g/kNs	Section 11.4
REQ-SYS-ARD-1	The aerodynamic configuration shall provide steady flight at the delivery altitude.	REQ-STK-4	✓ The wing was found to generate enough lift at delivery altitude for every mission phase. Section 10.4	
REQ-SYS-ARD-1.1	The aerodynamic configuration shall provide at least 550 kilo Newtons of Lift at delivery altitude.	REQ-STK-4	✓ The wing was found to be able to support the MTOM of 596.2 kN at delivery altitude	Section 10.4
REQ-SYS-ARD-2	The parasitic drag coefficient shall not exceed 0.02.	REQ-STK-18	✓ Using component drag build-up method, a C_{D_0} of 0.0042 was found.	subsection 8.4.2
REQ-SYS-ARD-3	The aerodynamic coefficients over any surface shall not degrade below 95% of the initial values at any point during the operations.	REQ-STK-20	Could not be determined through analyses with the available resources.	-
REQ-SYS-ARD-4	The aerodynamic control surfaces shall provide directional stability to maintain controlled approach and departure.	REQ-STK-8	✓ The aircraft was found to be directionally stable using a dynamic stability analysis.	Section 12.6
REQ-SYS-ARD-4.1	The weathervane stability coefficient $C_{n\beta}$ shall be at least 0.1.	REQ-STK-8	× The weathervane stability coefficient $C_{n\beta}$ could not yet be determined using the simplifications made.	Section 12.6

Table 18.3 continued on next page

Table 18.3 continued from previous page

ID	Description	Stk. Req.	Compliance	Section
REQ-SYS-ARD-5	The aerodynamic control surfaces shall provide directional stability during cross winds of at least 20 knots.	REQ-STK-8	× A directional stability analysis, including cross winds, could not yet be performed with the available resources.	-
REQ-SYS-ARD-6	The system shall be stable in the Dutch roll eigenmode.	REQ-STK-20	✓ The system eigenvalue was found to have a negative real part, and the system is thus damped and stable, in the Dutch roll stability mode.	Section 12.6
REQ-SYS-ARD-6.1	The lateral and directional stability should be balanced.	REQ-STK-20	✓ The stability coefficient found showed stability in the Dutch roll eigenmode and an almost stable spiral eigenmode by being in the centre of the lateral stability ($C_{n\beta}$ - $C_{l\beta}$) diagram.	Section 12.6
REQ-SYS-ARD-7	The minimum lift coefficient at delivery altitude shall be at least 0.6 as indicated on the airfoil selected.	REQ-STK-4	✓ This requirement is met as $C_{L_{des}}$ is determined to be 0.87.	subsection 8.4.3
REQ-SYS-ARD-8	The minimum stall speed at delivery altitude shall not be higher than 200 m/s.	REQ-STK-4	✓ V_{stall} at an altitude of 20km was found to be 190.5 m/s.	Section 10.4
REQ-SYS-STR-1	The structural subsystem shall withstand aerodynamic loads across the full flight envelope.	REQ-STK-20	✓ The largest found value for lift and drag were used as limiting case, analyses showed the structure withstands these loads.	Section 13.7
REQ-SYS-STR-1.1	The load factor shall remain within the range of -1.5 and 4.	REQ-STK-20	✓ The maximum load factors on the design were determined to be -1 and 3.8, being within the limits.	Section 13.2
REQ-SYS-STR-2	The structure shall support a payload mass of up to 17 tons per flight.	REQ-STK-2	✓ The wingbox and fuselage were found to support the 17 tons of payload using V&V.	Section 13.7
REQ-SYS-STR-3	The structure shall withstand 21 operations per week without degradation.	REQ-STK-3	✓ A fatigue analysis was performed and the structure can withstand 12364 operations	subsection 13.4.5
REQ-SYS-STR-3.1	The material structural properties shall not degrade below 95% of the initial values at any point during the operations.	REQ-STK-3	× Could not be determined through analyses with the available resources.	-
REQ-SYS-STR-4	The structure shall withstand all thermal expansion and contraction cycles experienced during its lifetime.	REQ-STK-20	✓ The forces on the aircraft due to temperature changes are incredibly small compared to other forces	subsection 13.4.2
REQ-SYS-STR-4.1	The expansion coefficient α shall be limited to no more than $10^{-4}/K$.	REQ-STK-20	✓ The chosen materials for the structure have lower expansion coefficients	Section 13.3
REQ-SYS-STR-5	The structure shall be designed to be fail-safe, maintaining load paths under partial failure or damage.	REQ-STK-20	✓ Load paths were analysed to remain intact in case of partial failure for the wing box.	Section 13.4

Table 18.3 continued on next page

Table 18.3 continued from previous page

ID	Description	Stk. Req.	Compliance	Section
REQ-SYS-STR-6	The critical load-bearing elements shall allow for access to inspect, repair and maintain.	REQ-STK-3	✓ The wing box and fuselage have been designed for accessibility.	Section 13.4
REQ-SYS-STR-7	The materials used in the system shall be recyclable or reusable.	REQ-STK-12	✓ Recyclable aluminium alloys were chosen.	subsection 13.3.3
REQ-SYS-AVI-1	The avionics subsystem shall be able to communicate with at least one ground station at all times during operation.	REQ-STK-20	× Communication range could not yet be determined, ground stations are not yet set up.	-
REQ-SYS-AVI-2	The avionics subsystem shall make the aircraft visible in CAT II circumstances.	REQ-STK-9	× Could not yet be proved, the external lighting should be demonstrated to be visible in CAT II circumstances.	-
REQ-SYS-AVI-3	The avionics subsystem shall collect aircraft altitude data.	REQ-STK-20	✓ The avionics subsystem contains the necessary sensors to collect altitude data.	Section 14.6
REQ-SYS-AVI-3.1	The altitude data shall have a minimum bit rate of 200 bit/s.	REQ-STK-20	✓ The aircraft positioning data has a bit rate of 1 kB/s	Section 14.7
REQ-SYS-AVI-4	The avionics subsystem shall transmit the collected data to the nearest ground station.	REQ-STK-20	✓ The data is sent to the ground station.	Section 14.5
REQ-SYS-AVI-5	The avionics subsystem shall have a minimal pointing accuracy of <TBD> rad.	REQ-STK-20	× Pointing accuracy required could not yet be determined, avionics subsystem pointing accuracy should be verified using a test setup.	-

Operations and Logistics

In this chapter, a concept of operations and logistics for the chosen design concept was developed. The fleet will consist of unmanned twin-body aircraft, each carrying 17 000 kg of payload, 13750kg of which is aerosol, and is expected to operate for 250 days per year. To minimise the number of aircraft required, each unit is intended to perform multiple flights per day.

To visualise the operations of one aircraft, a CONOPS diagram is presented in Section 19.1. The fleet size is then estimated in Section 19.2 and the airports are selected in Section 19.3. An alternative mission in case the injection of CaCO_3 is not ready is explained in Section 19.4

19.1. Concepts of Operations and Logistics Diagram

Contributors: Blanca, Carmen

A Concept of Operations diagram for one aircraft was developed for visualisation and shown in Figure 19.1. The operations can be divided into three sections: payload handling, airport ground operations, and flight operations.

Payload Handling

A dedicated facility will be located near every airport, where aerosols will be generated and stored. This supporting infrastructure will likely need to be constructed, contributing to costs.

A convoy of trucks will transport the payload from the storage facility to the aircraft for loading before each flight. Since 6 Mt of aerosol needs to be delivered to the aircraft at 8 airport locations in 250 days, around 3000 t of aerosol has to be delivered daily to each airport. Using common 12-tyre trucks with 30 t load capacity¹, 100 truck deliveries are needed per day. For this, 10 trucks per airport will be needed where each will do 10 deliveries each day. Once the trucks reach the aircraft, trained personnel will load the aerosol into the aircraft using specialised machinery. Because of this, operating costs will rise due to additional labour requirements. Each truck will need a driver, and trained personnel will be required to handle and inspect the payload.

Airport Ground Operations

On the airport grounds, pre-flight operations, aircraft maintenance, and post-flight operations will be carried out. These include collecting and processing data, subsystem inspections, fast aircraft maintenance, and refuelling and reloading of the payload.

It is assumed that both departures and arrivals will take place at the same airport to minimise reliance on multiple locations, ensuring the mission can still be carried out if another airport becomes unavailable. In addition, this simplifies scheduling and coordination, as well as reduces communication between multiple air traffic control systems, allowing for faster turnaround times and a more reliable flight schedule.

The aircraft are scheduled to depart at different times throughout the day to improve operational efficiency. This staggered timing allows some aircraft to be in flight while others undergo ground operations.

As the aircraft are unmanned, the flights will be continuously monitored on ground for smooth flight. As calculated in Section 19.2, there will be 43 to 44 aircraft operating from each airport, each flying five times per day. Given the intensity and frequency of operations, amounting to approximately 200 flights daily, careful flight monitoring will be essential. To ensure a high level of situational awareness and responsiveness, each operator will be assigned to only two aircraft, with two additional operations managers overseeing the airport's fleet as a whole and coordinating the team. These operators will be responsible for flight monitoring, mission execution, and handling in-flight contingencies, all managed through a central mission control system. This setup will require approximately 80 operators at each airport, organized into three rotating shift to ensure continuous coverage throughout the day. This way, each operator will work 8 hours a day, with breaks included, for five days a week, to comply with the 250 operational days a year.

The choice of an autonomous aircraft proved beneficial not for the design itself, as it allowed for a lighter and more efficient configuration, but also for its suitability in the high-frequency mission operations. The centralized mission control centre, which allows operators to manage two aircraft simultaneously, reduces the number of personnel needed compared to the number of trained pilots that would otherwise be required. It should be noted that training and certification for drone operators is typically shorter and less costly than for licensed pilots, further supporting large-scale deployment.

¹URL: <https://trucksup.com/types-of-trucks-and-their-load-capacities/>

Ground-based control also allows for quick intervention or reassignment in response to unexpected events. In conclusion, automation of the mission improves operational efficiency.

Flight operations

After climbing to an altitude of 20 km, payload injection will begin. The aircraft will follow a meridian track while releasing half of the payload. The aircraft will follow a meridional path while releasing half of its payload. At mid-flight, it will turn around and climb to an altitude of 21.7 km, made possible by the reduced weight due to payload release and fuel burn, as shown in the flight profile in Figure 10.2 of Chapter 10. It will then return along the reciprocal track while injecting the other half of the payload. The higher return altitude is intended to prevent plume interactions between the outbound and inbound flights [56].

Flying along a meridian, or constant longitude, is chosen to minimise plume interactions between successive aircraft operating at the same altitude. Since stratospheric winds are generally perpendicular to these tracks, the plumes are expected to disperse quickly enough to prevent overlap [56].

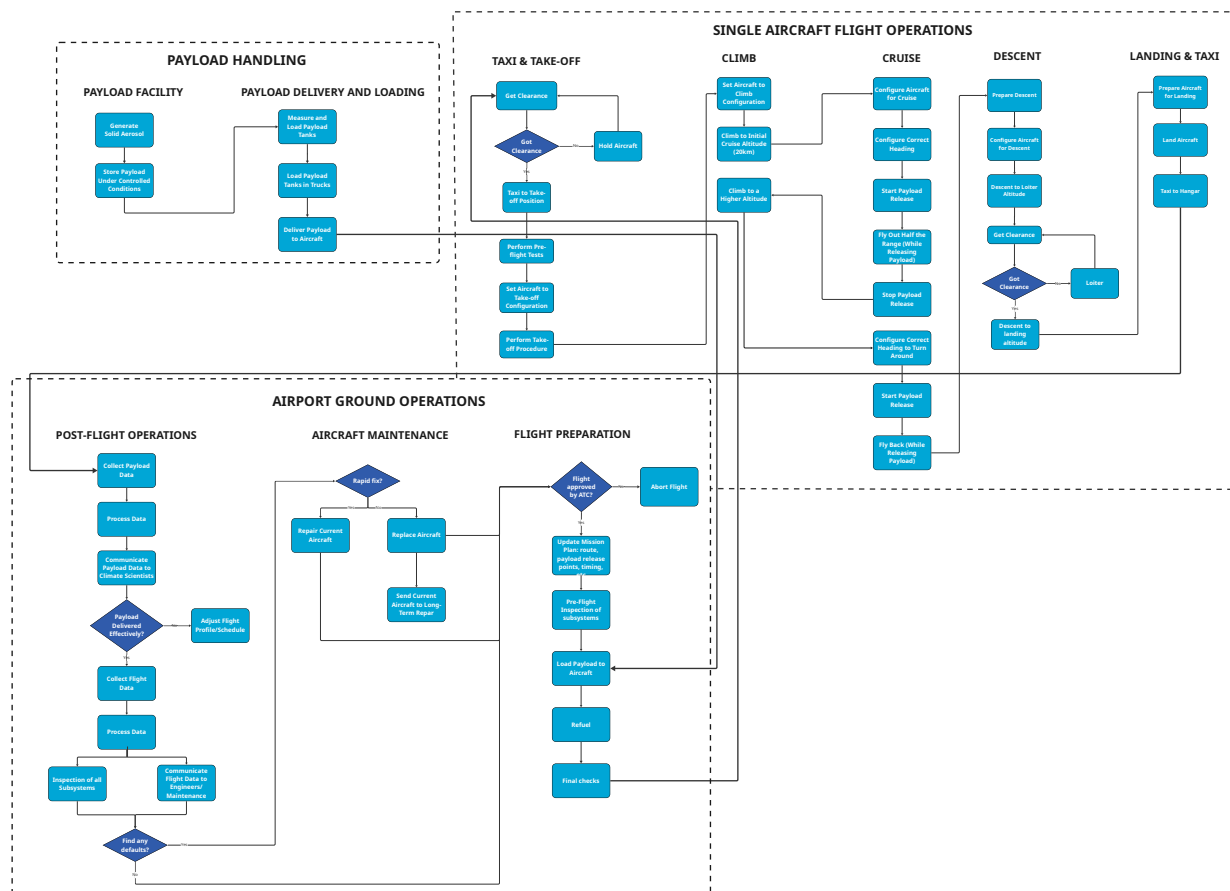


Figure 19.1: CONOPS diagram

19.2. Fleet size

Contributors: Blanca, Carmen, Pavel

In order to estimate the number of sorties per day of each aircraft, the total block time was estimated. The total time from the start of climb to the end of descent is shown as 188.9 minutes in Figure 10.2, representing a worst-case scenario that includes 45 minutes of loitering. In reality, it is unlikely that all aircraft in the fleet will loiter on every sortie. Since loitering is expected in only 5–10% of flights, and the 45-minute duration is a conservative upper bound, the average loiter time is much lower. To account for this, only 10% of the loiter duration (4.5 minutes) was added to the base flight time, resulting in a more representative adjusted time of 148.4 minutes. To account for pre-flight time, warm up, taxiing and shut down, an extra 25 minutes were added [53]. The total block time is thus 173.4 minutes, or 2.89 hours

In between flights, each aircraft undergoes a series of ground operations, as shown in the CONOPS diagram, shown in Figure 19.1. Commercial airliners typically achieve turnaround times of 60-120 minutes [53]. Hence, an average of 90 minutes was taken for this specific mission, attaining a total time for the operation of a single aircraft of 4.39 hours. To account for any delays and errors in time estimates, it is assumed each aircraft will perform 5 flights per day.

It is decided that the fleet size will have a buffer of 10% to leave spare aircraft in case an operating aircraft is grounded for maintenance and needs to be replaced, or if additional aircraft are needed due to delays.

For the initial delivery of 0.5 Mt of CaCO_3 per year, with 250 operational days, and for 13750 kg of aerosol per aircraft, 146 flights per day would be needed. With 5 flights per aircraft a day, a fleet of 30 aircraft would be required. Adding the 10% buffer, 33 aircraft would be needed.

Later on, for the delivery of 6 Mt of CaCO_3 per year, a fleet of 385 aircraft would be required. These final fleet size values are shown in Table 19.1

Table 19.1: Fleet and Payload Distribution Overview

Mission Phase	Payload Delivered per Year [Mt]	Fleet Size	Number of Airports
Initial Phase	0.5	33	4
Final Phase	6.0	385	8

It should be noted that this fleet size is calculated based on the assumed 2.33 kg/s payload drop rate, which is still theoretical. If this were to change, the payload carried per aircraft would scale accordingly, as depicted in Figure 9.3 in Chapter 9. This would directly change the required number of aircraft needed to carry all the necessary aerosol. A smaller injection rate would also lead to a longer cruise flight, which could again lead to an increase in fleet size.

19.3. Selected Airports

Contributors: Blanca, Carmen

The fleet is required to operate from airports located near latitudes 30°N, 15°N, 15°S, and 30°S, to disperse the aerosols around the tropics, where there is a favourable atmospheric circulation for full globe coverage. Additionally, the runway length of these airports must be more than 2500 m to comply with REQ-STK-7. A list of possible airports that meet these requirements was given in the Baseline Report, which also took into account the political stability and available infrastructure of the country.

The 16 m centre wing section will require airports that are capable of accommodating aircraft with ICAO category F. All chosen airports are civil airports, as they are already equipped to handle large-scale operations and high volumes of commercial flights. However, some modifications will still be required to adapt to the mission's operations. Before further narrowing down the list of potential airports, the mission range was used to ensure that selected airports are sufficiently spaced to minimise the risk of plume interactions, and achieve appropriate aerosol dispersion. This was found to be 1721.8km without loiter.

The airport selection was then narrowed down to four for the initial delivery, and will be expanded to eight for the final delivery as listed in Table 19.2. For visual reference, these selected airports are shown in Figure 19.2 with a circle of radius 861km (half of the range) around them to show the possible coverage achieved. Here, the airports for the initial mission phase are shown in green, and the additional ones for the final mission phase in grey.

Table 19.2: Selected Airports

	Airport Code	Country	Latitude [°]	Runway Length [m]
Initial	DUR	South Africa	-29.970	3701
	BSB	Brazil	-15.871	3301
	BKK	Thailand	13.681	3701
	LAX	USA	33.943	3686
Additional	PER	Australia	-31.940	3445
	CNS	Australia	-16.883	3197
	PUJ	Dominican Republic	18.568	3101
	CAI	Egypt	30.122	4001

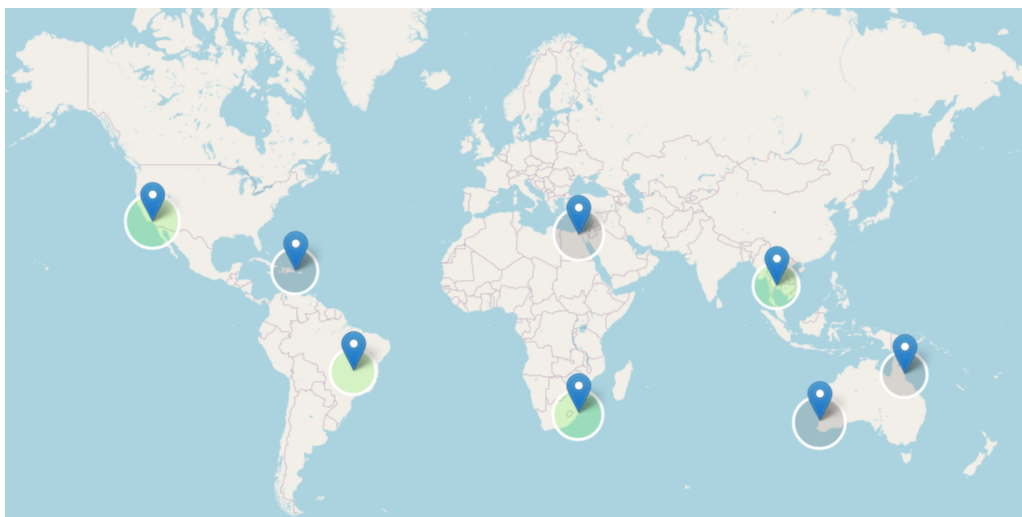


Figure 19.2: Selected airports showing the possible range covered.

19.4. Fallback Mission: Calcite Injection Technology not Ready

Contributors: Inés

Calcite was selected as the payload for this mission. Consequently, a fallback plan should be established to address the scenario in which the fluidisation technology to avoid agglomeration of these particles, mentioned in Section 9.2, is not developed on time or ultimately proven unfeasible. It was decided that in case the ideal particle size for calcites cannot be achieved, alumina would be the substitute payload. This would entail some changes in the operations that should be taken into account.

According to a study by Vattioni et al. [3], if 5.7 Mt of CaCO_3 per year is to be injected, an equivalent 7.5 Mt of Al_2O_3 would be needed. The initial 0.5 Mt of CaCO_3 per year translates to around 0.66 Mt of Al_2O_3 , while the 6 Mt of CaCO_3 per year corresponds to about 7.9 Mt of Al_2O_3 . This would, in turn, increase the fleet size.

Assuming each aircraft would be carrying 13750 kg of aerosol, the fleet size would consist of 43 instead of 33 aircraft at initial deployment, and 506 instead of 385 aircraft at final deployment. This translates to a 31.5% increase in the total operational and manufacturing costs, and an increase in payload cost as well. Additionally, the operations and logistics should be adjusted, likely requiring the use of more airports. This would not pose a significant issue, as there is a wide range of airports available within the required latitudes. Furthermore, the environmental effects of aluminium should also be considered, especially the uncertainty in the ozone depletion.

This is a risk that needs to be taken into account, and make sure the customer is ready to accept the higher costs and efforts that this change in payload would entail. Alternatively, to counteract the loss of efficiency in the use of alumina as payload, concept ideas such as adding aluminium-powered rocket boosters or carrying missiles powered by aluminium rockets to inject alumina aerosol at higher altitudes should not be discarded. This would increase the suspension time of the alumina in the stratosphere and potentially decrease the environmental effects as suggested by Lee et al.[57].

Reliability, Availability, Maintainability and Safety

In this chapter, the Reliability, Availability, Maintainability and Safety (RAMS) of the design are described. These terms, even though distinguishable, depend upon each other. High Reliability and Maintainability naturally lead to high Availability. Likewise, Safety often requires a reliable and well-maintained system to minimise risks and failures that can cause issues to the people and the system alike. This chapter describes each of these aspects in detail, while outlining and exploring their interrelations and demonstrates how they collectively influence and elevate the performance of the system. At this preliminary design phase, a RAMS determination strategy was developed, which will be performed at a later stage when more parameters are known, as described in Section 23.1.

20.1. Reliability

Contributors: Konstantinos, Bas

To start off, the reliability of the system was considered. The reliability of the design directly affects the downtime and additional operating costs due to unscheduled maintenance. A high reliability is therefore desired to keep the operational costs per aircraft within the margin indicated by 'REQ-STK-17'. The reliability per component can be determined using Equation 20.1 [58], where $f(t)$ is the item failure density function:

$$R(t) = 1 - \int_0^t f(t)dt \quad (20.1)$$

Given that, due to the early stage of the design, no failure density functions were available yet, and thus a real estimate of the reliability of the design could not yet be made. However, based on reliability data [59], the failure rate per million flight hours were found for each of the components present in the aerosol payload system, to provide a first-order estimate of this specific subsystem, given that this subsystem is one of the main characteristics of the design. These failure rates are listed in Table 20.1, together with recommended additional maintenance procedures during the different A, C and D maintenance checks described later in Section 20.3. A similar analysis could be done in the future for the other subsystems.

Table 20.1: Payload system component failure rates and additional maintenance

Component	Failure rate / 10^6 hours [59]	Advised additional maintenance
Generators	1.082	During A checks, should be visually inspected and lubricated if necessary. During a D check, should be completely disassembled and individual parts should be inspected and replaced if necessary.
Nozzles	3.664	During A checks, should be visually inspected for wear and fatigue. Should be detached during C checks to be cleaned and tested using a test setup.
Motor	8.882	During A checks, should be visually inspected and lubricated if necessary. Should be disassembled completely during a D check, and each part should be inspected and replaced if necessary.
Regulator	2.188	During A checks, the regulators should be checked for visible outside damage. The regulators should be tested using a test setup and calibrated or replaced if necessary during C checks.
Relay	0.144	During C checks, the relays should be tested using a test setup.
Tank	0.991	During A checks, the outside of the tanks should be checked for damage or corrosion. During C checks, the tanks should be removed from the aircraft for thorough internal inspection, cleaning, and replacement if necessary.

Continued on next page

Table 20.1 continued from previous page

Component	Failure rate / 10^6 hours	Advised additional maintenance
Valve	8.452	During A checks, the valves should perform a test run. During D checks, the valves should be dismantled completely, inspected, and replaced if necessary.
Filter	1.763	During A checks, the filters should be visually inspected and replaced if necessary.
Pipes	0.452	During A checks, the outside of the pipes should be visually inspected for damage or signs of corrosion. During C checks, the pipes should be thoroughly cleaned and tested for signs of fatigue.
Temperature sensor	96.203	During A checks, the sensors should be cleaned and inspected for visual damage. During C checks, the sensors should be removed from the payload bay and tested and calibrated using a test setup.
Humidity sensor	96.203	During A checks, the sensors should be cleaned and inspected for visual damage. During C checks, the sensors should be removed from the payload bay and tested and calibrated using a test setup.
Pressure sensor	96.203	During A checks, the sensors should be cleaned and inspected for visual damage. During C checks, the sensors should be removed from the payload bay and tested and calibrated using a test setup.
Compressor	4.793	During C checks, should be removed from the aircraft and dismantled to check and test for damage or fatigue.
Circuit	1.305	During A checks, should be checked running test processes on the circuits. During C checks, should be thoroughly inspected for circuit wear or damage.
Battery	14.138	During A checks, the outside of the batteries should be checked for damage and corrosion. During a C check, the battery power output should be checked with a multimeter.
Pump	0.361	Should perform a test run during A checks, should be dismantled during C checks for complete inspection.

As can be seen from the table, certain components of the injection system such as the batteries and sensors have a significantly higher failure rate. Additional maintenance procedures focused on these components are performed weekly and yearly during A and C checks to reduce the failure rate, improving the overall reliability of the payload system and total the design.

20.2. Availability

Contributors: Konstantinos

Availability is defined as the ability of the system to perform the mission within the preallocated time frame [58]. According to the same book, unlike reliability, which measures the ability of the system to function properly, availability provides a metric on how often the system is available for use. The simple representation of availability is the ratio between the Mean Time Between Failure (MTBF) over the summation of MTBF with the Mean Time To Repair (MTTR), as shown in Equation 20.2 [58]:

$$A = \frac{MTBF}{MTBF + MTTR} \quad (20.2)$$

The Mean Time Between Failures (MTBF) is an important reliability metric [60] used to determine the average time between the repairable failures of a system, and can be described as the integral of the reliability function on the time domain or the limit to zero of the same function on the Laplace domain [60], as shown in Equation 20.3 and 20.4:

$$MTBF = \int_0^{\infty} R(t)dt \quad (20.3)$$

$$MTBF = \lim_{s \rightarrow 0} R(s) \quad (20.4)$$

MTTR represents the average time required to repair a failed component and is described as the ratio between the total time to maintain and the number of repairs needed [60], as shown in Equation 20.5:

$$MTTR = \frac{t_{repair}}{n_{repair}} \quad (20.5)$$

The fleet availability differs with respect to each individual aircraft, using $A_{fleet} = 1 - (1 - A_{aircraft})^n$ with n being the number of aircraft in the fleet. Using a fleet exponentially increases the availability of the overall system ensuring that "REQ-STK-3", concerning the minimum amount of operational days, is met.

20.3. Maintainability

Contributors: Bas

Maintenance of the aircraft fleet is an important aspect of RAMS for maximising both aircraft operation time and sustainability as required by 'REQ-STK-3' and 'REQ-STK-18', by keeping the aircraft in good condition and repairing any damage before more drastic reparations or decommissioning of the entire aircraft becomes inevitable.

The maintenance of the designed fleet will follow a process similar to commercial aviation. Scheduled maintenance should take place in three categories, varying in frequency and thoroughness. The fastest procedure is the A-check, which should happen about once every week, and consists of visual checks of important parts such as the control surfaces and landing gear, as well as filter and oil servicing.[61] This takes about one full day.[62]

Next to this mostly visual check, heavier maintenance procedures will also be required. The first one of which is a C check, which might take up to two weeks, and involves the inspection and testing of most parts of the aircraft.¹ This check will be performed every year.[62]

Finally, the last common maintenance check that should be performed is the D check, which should happen about every six years. This is the most thorough and labour-intensive maintenance procedure, as it requires stripping of the aircraft, testing of operational and structural elements, and detailed visual inspections.[62] Due to the large number of man-hours required, this procedure might take up to two months.[63]

Even though the aircraft will fly unmanned, thorough maintenance will prevent accidents which could still pose a threat to human safety, and additionally will also have economic benefits. According to the explained maintenance scheme, a single aircraft will be grounded on average about 66 days per year. While this is significant, it ensures the aircraft will have a high chance of reaching its expected operational lifetime of 30 years without being replaced early by a new aircraft, which saves costs. The downtime of the aircraft will have to be filled in by spare aircraft.

The maintainability of the aircraft during operation can be characterised using Equation 20.6 [64]. This formula links the Mean Time Between Maintenance (MTBM) to the Mean Time Between Failure (MTBF) and Mean Time Between Preventive Maintenance (MTBPM). The MTBF is calculated as shown in Section 20.2, see Equation 20.3 and Equation 20.4.

$$MTBM = \frac{1}{1/MTBF + 1/MTBPM} \quad (20.6)$$

Given that early stage of the design, actual estimations or calculations of the maintainability of the fleet could not yet be determined and is thus something that should be done during the final design phase and start of operations.

20.4. Safety

Contributors: Bas

The safety of the design should ensure that no human's health is at risk during operation or handling of the system. This includes the protection of the system itself, as a failure of the aircraft during operation could lead to the loss of an aircraft and potential casualties. To ensure this, different health and operational hazards and corresponding mitigation strategies have been identified.

¹URL: <https://www.aviationpros.com/aircraft-maintenance-technology/aircraft-technology/article/10388655/whats-this-a-check-c-check-stuff> Accessed: June 12th 2025

Fuel Failure

During ground operation, while handling the fuel system, the fuel is at risk of ignition. Given the high flammability of the aircraft fuel used, care should be taken while refuelling the aircraft or when performing maintenance or inspections on the fuel system. One of the safety measures that should be taken is the availability of Halon fire extinguishers nearby, which should be used to extinguish aircraft fuel fires².

Heating of Calcite

Calcite itself is a safe substance and has not been proven to pose a threat to human health³. It is also not burnable or flammable. However, after heating, it decomposes into calcium oxide and carbon dioxide at temperatures of 700 ° C.[65] This could happen in case of a fire during handling of the aerosol, loading of the aerosol into the aircraft, handling of a loaded aircraft, or a fire in a hangar, maintenance, production or storage facility where the solid aerosol is present. The released calcium oxide can cause irritation in the lungs, eyes and skin, and more significant exposures can cause fluid build-up in the lungs, a severe medical emergency³. To decrease this safety risk as much as possible, all facilities where the calcite is stored should provide proper ventilation and access to showers for staff to immediately wash off any calcium oxide. During direct handling of the solid aerosol, such as during the loading of the solid aerosol into the aircraft, ground staff should wear respiratory masks and eye protection.

Loss of Communication

Given that the designed aircraft is unmanned, a ground station is responsible for providing the aircraft with directions and instructions. In case of failure to communicate with the aircraft, it should be prevented that the aircraft stops flying and crashes at all times. Therefore, the automatic pilot inside the aircraft should keep the aircraft flying, and potentially bring it back down to earth safely in case the lack of communication continues for a longer period of time to prevent an aircraft crash.

Loss of Propulsion

As the aircraft is designed to fly at high altitude, the thrust-to-weight ratio of the design is relatively high compared to commercial aircraft. Even so, the design only uses two engines, and while it can remain flying with one engine inoperative, the loss of the second engine could end catastrophically. To decrease the chance of this happening, the automatic pilot running on the aircraft should constantly monitor its own engines, and in case of any anomalies in one or both of the engines, it should immediately warn the ground staff and navigate to a safe landing area such that thorough inspection and maintenance can take place.

Turbine burst

Next to a general loss of propulsion, turbojet engines have the known risk of a turbine burst occurring. Failure of a turbine blade, which due to its extremely high rotational speeds carries a lot of kinetic energy, can result in an uncontained engine failure. In this case, the turbine blade perforates the engine nacelle and potentially the wing and/or the fuselage. This critical situation could pose a serious safety risk if enough damage to the aircraft is caused to bring it down, or if one of the fuel tanks is hit while still partly full. As the failure of a turbine or compressor blade, as well as the resulting damage, is very difficult to reliably predict, these engine components are instead labelled as safety critical parts⁴. This means that extra care should be taken in the rotor debris zone, which can be done by for example installing tear straps⁵ to try to keep the failure contained and protect critical aircraft parts.

²URL: <https://skybrary.aero/sites/default/files/bookshelf/1177.pdf>

³URL: <https://nj.gov/health/eoh/rtkweb/documents/fs/0325.pdf> Accessed: 12th of June

⁴URL: <https://www.easa.europa.eu/en/faq/19013> Accessed: 12th of June

⁵URL: <https://www.easa.europa.eu/en/document-library/easy-access-rules/online-publications/easy-access-rules-acceptable-means?page=23> Accessed: 12th of June

Sustainable Development Strategy

This chapter covers the Sustainable Development Strategy for the mission. It commences with Section 21.1 where the preliminary conceptual choices concerning sustainability are presented. It then proceeds with Section 21.2, presenting methods used to assess the environmental impact of the design. It concludes with an End of Life plan, at Section 21.3, where a sustainable strategy for managing the system when no longer in operation is presented.

21.1. Sustainable Conceptual Design Choices

Contributors: Konstantinos, Bas

During the conceptual design phase of the aircraft, different aircraft concepts were created, on which a trade-off was performed. Each of the design concepts that were under consideration met the sustainability requirements set. However, to further reduce the environmental impact of the fleet of aircraft, the concepts required to be assessed and compared in further detail. During the trade-off, criteria related to the sustainability of the concepts received a higher weight. For example, criteria such as mass, propulsion efficiency and aerodynamic efficiency directly or indirectly affect the environmental impact of the aircraft through reduction of emissions and noise pollution and were, therefore, weighed higher than other criteria. This ensured that the final concept was selected partly based on being the most sustainable design.

After selecting the design concept, certain design choices were made. Various methods were utilised to implement and assess sustainability in this design process. An example is the method of Design for Environment (DfE), which was implemented in the process for designing both the conceptual and final design. DfE is the process of designing a product in such a way that its effect on the environment is minimised. DfE was, and will be, applied in multiple different areas, the first one being the definition of the system requirements. After selecting a design concept, sustainability considerations were incorporated when redefining the requirements, such that fulfilling these requirements inherently contributes to achieving the minimum set sustainability targets.

DfE was implemented at the subsystem level. To begin with, for aerodynamics, a design that minimises drag was of high importance. This was achieved with a high aspect ratio wing and two fuselages of small diameter, that contribute in a very small portion of the C_D . Similarly, the fuselages were shaped in such a way as to minimise wave drag, a prominent form of drag in the transonic-sonic boundary. Lastly, sustainable materials were implemented, as shown in Table 21.2, where 70% of the wing is retrieved. For payload, similar considerations were taken. First, a high-tech aerosol container was selected which can be pressurised for an increased amount of cycles. Additionally, it was ensured that the release of the payload has no prominent negative externalities in the planet or humanity. This is described in detail in Section 21.4. In fact, if successful, the injection of the aerosol shall mitigate the effects of the climate crisis, one of the biggest problems society faces in the 21st century [2], proving the sustainable nature of the design.

Next, DfE was used during the design of the propulsion subsystem. The propulsion subsystem should provide enough thrust for the design to sustain flight, while minimising the fuel consumed to do so. The Thrust Specific Fuel Consumption (TSFC) is a metric that therefore had to be minimised. DfE was implemented by using the TSFC as one of the trade-off criteria for choosing the engine type. After choosing the most efficient option, a final engine design was made based on an existing turbojet engine, which was improved to increase efficiency even further. Finally, as explained in Section 21.3, the engines are considered high-valued parts that shall be thoroughly inspected and repaired after decommissioning of an aircraft to be reused. In case the engine itself has to be decommissioned, 60% of the engine will be recycled due to the recyclable materials used, such as steel and titanium.

DfE was, lastly, integrated into the design of the aircraft structure by optimising the structural performance. This was done, in Chapter 13, by analysing several loading cases and optimising for the least amount of structure to be able to withstand these loads. Less structure subsequently decreased the structural mass and MTOM improving propulsive efficiency, requiring less fuel on board and reducing its consumption. Also, a material trade-off was performed for the wing box and fuselage structures. Two highly recyclable aluminium alloys were chosen

instead of composites to ensure reuse of materials. As seen in Section 21.3, this resulted in a recycling percentage of 70 to 85% of the materials.

21.2. Methods of Assessment of Sustainable Design

Contributors: Konstantinos, Bas

This section describes the methods used to assess the sustainability of the design. The methods were applied at two stages; to begin with, as a means to trade off between the environmental impact of the conceptual designs. In order to determine the most sustainable option, a meaningful quantity indicating a design's environmental impact was necessary. These same methods were used to assess the environmental impact of the final design.

21.2.1. Average Temperature Response

The Average Temperature Response (ATR) is a metric representing the global mean temperature change caused by the operation of an aircraft over its lifetime. It estimates the temperature change associated with the greenhouse gas (GHG) emissions over a defined time period [66] and is the best fitting metric for usage in aeronautics. Consequently, it provided an excellent way to verify "REQ-STK-18", by proving that the temperature change caused by the operation of the aircraft is significantly smaller than the one caused by the injection of the payload. The process was the following: the ATR was calculated using the integral in Equation 21.1, as suggested by E.S.Dallara et.al [66].

$$ATR = \frac{1}{H} \int_0^{\infty} \Delta T(t) \cdot w(t) dt \quad (21.1)$$

where the H is the years of sustained operation of a particular aircraft (taken as 25, as specified in subsection 13.4.5), $\Delta T(t)$ the time-varying global mean temperature over H years and $w(t)$ a weighting function, which reduced to 1 as Equation 21.1 was applied for a time before the aircraft has ceased operation ($t < H$). The time-varying global mean temperature, given by Equation 21.2, is a convolution integral of the radiative forcing $RF_i(t)$ and a climate response function $G_T(t)$, given in Equation 21.2.

$$\Delta T(t) = \int_0^t G_T(t - \tau) \cdot \sum_i RF_i(\tau) d\tau \quad (21.2)$$

Here, \sum_i denotes the summation over all greenhouse gases (GHGs) considered in the analysis, which are limited to CO_2 , H_2O , and SO_4 , based on the availability of sufficient parameters in the literature [66]. The climate response function $G_T(t)$, adopted from the same source, is presented in Equation 21.3.

$$G_T(t) = S \cdot \left(\frac{\alpha_t}{\tau_{t1}} \cdot e\left(-\frac{t}{\tau_{t1}}\right) + \frac{1 - \alpha_t}{\tau_{t2}} \cdot e\left(-\frac{t}{\tau_{t2}}\right) \right) \quad (21.3)$$

with S , τ_{t1} , τ_{t2} and α_t are gas sensitivity parameters found in literature [66]. The radiative forcing $RF_i(t)$ for each gas is another relation shown in Equation 21.4.

$$RF_i(t) = s_i(h) \cdot \int_0^t G_i(t - \tau) \cdot E_i(\tau) d\tau \quad (21.4)$$

Notice that $RF_i(t)$ is case sensitive meaning that all $s_i(h)$, $G_i(t)$ and $E_i(\tau)$ depend on the GHG analysed at each point. $s_i(h)$ is an altitude-dependent scaling factor taking into account the different atmosphere layers the flight occurs at, $G_i(t)$ the gas-specific response function and $E_i(t)$ the utilisation rate (number of missions at time t) calculated using:

$$e_i = EI_i \cdot \text{Fuel Mass}, \quad \text{and} \quad E_i(t) = e_i \cdot U(t)$$

with $U(t)$ is a utilization constant factor, and EI_i the emissions index. Detailed relations for $i = \text{CO}_2$, H_2O , SO_4 can be found in the Appendices of the paper from E.S.Dallara et.al [66].

Having performed the aforementioned procedure, Equation 21.2 was varied over time for a single aircraft's operation to obtain Figure 21.1. This consists two main parts; for the first half of the graph up to H years, the aircraft emits GHGs due to its sustained operations. This is visualised by the gradual increase in the global mean temperature. This increase is, however, very small accounting for a ΔT in the order of mK . Although the

sustained operations over the years are expected to cause a significant cumulative increase in ΔT across the fleet, this increase is not anticipated to reach dangerously high levels, staying at the same order of magnitude. The second half, after the aircraft has ceased operations ($H > t$), shows the gradual dissipation of the GHGs in the atmosphere, resulting in a temperature decrease. This shows an asymptotic trend with the x-axis, meaning that even after ceasing operations, the effects of the mission are sustained in the atmosphere for an indefinite number of years, longer than the 100-year span shown here. This effect, even though small, might cause an issue in the long run when the cumulative effect of all aircraft over the years is considered. Last but not least, Equation 21.2 depends on Equation 21.4, which is in turn dependent on $s_i(h)$ the altitude-dependent scaling factor. A $s_i(h)$ for 20 km high is used, the cruise altitude:

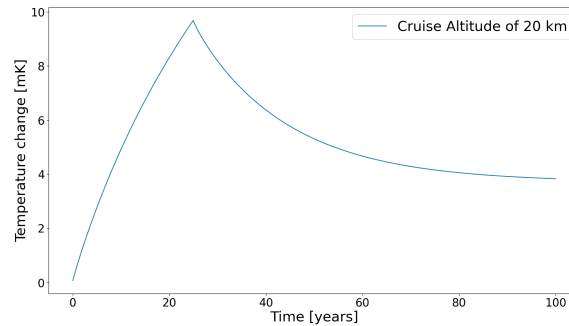


Figure 21.1: Global Mean Temperature Variation due to the operation of a single aircraft at cruise altitude.

Overall, these results, in combination with the engine plume characteristics discussed in subsection 8.6.2, formulate the environmental assessment of the system. Both findings indicate minimal negative externalities, with the temperature increase from the aircraft's operation being on the order of 10^{-3} K, and the propulsion gases decaying rapidly after ejection.

It must be acknowledged that the environmental assessment method presented in subsection 21.2.1 is a simplification and is subject to uncertainties. While the results account for altitude effects through the $s_i(h)$ factor and include a range of GHGs in the emissions profile, they do not capture variations in local atmospheric conditions or seasonal changes. Furthermore, mission specific aspects, such as the increased angle of attack (AOA) required to maintain steady cruise altitude and the decrease in engine efficiency with altitude, are not directly included. Instead, they are indirectly accounted for using the fuel mass consumed at each altitude. Last but not least, it should be noted that, according to the Schmidt–Appleman criterion [67, Fig.3], contrails generally do not form in the stratosphere, as their formation requires the colder and more humid conditions typically found in the upper troposphere (approximately 10.5 to 15.5 km altitude). As a result, the total positive radiative forcing is decreased by the absence of the artificially created "clouds" that warm the planet, and as a result, the analysis is conservative on that aspect on the cruise altitudes.

21.2.2. LCA

A Life Cycle Assessment (LCA) was used to determine the environmental impacts of the chosen design by focusing on the specific material production and manufacturing stages of the aircraft's lifecycle. The LCA method offers an extensive overview of the environmental impact as well as the economic viability of the mission, and thus the sustainability of the design [68]. This portion of the total environmental impact of the design has proved to not be insignificant and should therefore not be ignored. While LCA offers detailed insights, the application is constrained by time and resource limitations, especially due to the reliance of a first-order LCA on the limited amount of freely available LCA databases. A simplified LCA was thus considered, specifically focused on the manufacturing stage of the design, based on general transport aircraft LCA datasets, to accommodate project constraints.

The process followed is the following [68]: The goal and the scope of the LCA are defined. For this case, a preliminary goal is: *"The LCA study of the aircraft-based system is undertaken to acquire data for improving the environmental aspects of the system's design and manufacturing. The analysis data will be used to identify environmentally weak points where system improvement can be made by the designing and manufacturing team, and to compare possible disposal scenarios for the end-of-life plan."*

The scope, which encompasses the product, function, functional unit, reference flow and system boundaries, is the following. The function of the system is *"To deliver the payload"* and the functional unit *"To deliver 17 tonnes of the payload at the desired altitude (about 20km)"*. The reference flow, indicating the amount of product that is necessary to fulfil the function, is estimated at 518 aircraft per day (Chapter 19).

Moving to the system boundaries, the analysis used was the *"Cradle to Gate: From raw material to finished product"* approach [68]. Thus, it included the designing and manufacturing phases and the development of the end-of-life plan only, limiting its boundaries. The *"aircraft-based system"* mentioned at the goal definition refers to a single unit of the design made, and the analysis was limited to the aircraft engines, parts and assembly, as datasets are available for these processes. Last but not least, the analysis was focused on the GHG of CO₂, CH₄, and H₂O, as they are the main emissions of the production of conventional aircraft, and data can be readily found in LCA databases.

Moving on to the Life Cycle Inventory, the LCA was based on publicly available data from Life Cycle Inventory (LCI) databases, a Life Cycle Inventory database (LCI DB). Data on the GHG was collected for the manufacturing of the engines and separate aircraft parts, as well as the total aircraft assembly[68] and were scaled for the system based on the production costs. These were then used for Life Cycle Impact Assessment, where the significance of potential environmental impacts, based on life cycle inventory results, were evaluated.

The Life Cycle Assessment was performed on a single unit of the design. The impact of the design after its operational life was analysed separately in the end-of-life plan. An overview of the emissions found after performing the LCI is given in Table 21.1. For this, the Federal US LCA Commons database¹ was used. The data in this database is normalised with total production costs in USD2012, the final emissions were therefore computed using the calculated production costs in Figure 15.1. The emission estimations available in the database are the total emissions related to the entire processes listed in Table 21.1, and therefore include, among others, materials processing, parts manufacturing, assembly processes, and testing and validation procedures.

Table 21.1: LCI of the different production aspects of one aircraft

Process	CO ₂	CH ₄	H ₂ O
Aircraft assembly	386t	6.62 kg	43.17t
Engine manufacturing	93.5t	1.62 kg	7.6t
Aircraft parts production	887.8t	13.86 kg	63.6t
Total per aircraft	1,367t	22.1 kg	114.4t

As can be seen from the table, especially the CO₂ emissions are significant, with the production of one aircraft producing as much carbon dioxide as 23 flight missions. Also, the H₂O emissions, which are described as fresh drinking water and thus wasteful, are significant. While the total greenhouse gas emissions of the entire aviation industry are highly difficult to quantify, in one paper, Pierrat E. [69] tries to estimate the equivalent CO₂ emissions of 88 relevant aviation systems manufacturing companies. The paper found an equivalent total emission of 11.4 MtCO₂ for the manufacturing and materials stages, out of which 2213 aircraft have been produced. This yields an average environmental impact of 5,150 tCO₂, significantly higher than the value of 1,367t found in Table 21.1. The environmental impact of the design therefore, falls far below the industry average for commercial aircraft. Manufacturing of the entire fleet of 385 aircraft produces an estimated 0.53 Mt of CO₂, which is lower than the 1 Mt limit set by system requirement REQ-MIS-ENV-3, which followed from stakeholder requirement REQ-STK-18. This system requirement is therefore complied with.

The LCA can be improved in the future through the use of multiple different LCI datasets from industrial-grade paid databases, or by creating an LCI specific to the design when it reaches its production stage.

By combining ATR, LCA and a detailed End of Life plan, a broad coverage of the environmental impact of the system was achieved. The ATR focuses on the temperature change caused by the operation of the aircraft, whereas the LCA supplements this by quantifying and evaluating the environmental impact during the design and manufacturing phases, with End of Life, discussed in Section 21.3, covering the deposition stage.

21.3. End of Life

Contributors: Konstantinos, Bas

¹URL: <https://www.lcacommons.gov/lca-collaboration/search/query=aircraft>

Finally, another important part of the environmental impact of the design is the way the aircraft is handled after being decommissioned. For this, its End of Life (EoL) was properly planned out and measures such as sustainable material choices were taken during the design process to facilitate the decommissioning of the aircraft in a sustainable way. Aiming to follow the principle of a Circular Economy, maintenance, reuse and recycling of parts and materials was prioritised over end-of-life disposal. When the aircraft is dismantled after its operating years, the materials used are either recycled or wasted. The amount of material reused or wasted was calculated, and the results can be found in Table 21.2. The materials used for each section were determined in subsection 13.3.3 and the weight per section were determined using a Class II estimation and the total mass breakdown can be found in Section 15.2. Lastly, the disposal scenario for an A330-200 [70] was used to distinguish between valuable(recycled) and wasted mass.

Table 21.2: End of Life per subsystem based on the Disposal Scenario of an A330-200 aircraft [70]

Aircraft Section	Material Used	Disposal Scenario [70]	Total Weight [t]	Valuable [t]	Wasted [t]
Fuselage	Al7075-T6, Al2024-T86	85% Recycle; 15% Landfill	4.07	3.46	0.61
Wing	Al7075-T6, Al2024-T86	70% Recycle; 30% Landfill	10.5	7.35	3.15
Empennage	Al7075-T6, Al2024-T86	64% Recycle; 36% Landfill	0.55	0.35	0.20
Landing Gears	Aluminium, rubber	80% Recycle; 20% Landfill	1.01	0.81	0.20
Engines	Steel, Titanium	60% Recycle; 40% Landfill	16.95	10.17	6.78
Total weight [t]			33.08	22.14	10.94
Total weight [%]			100	67	33

At the end of an aircraft's life (EoL), reusable parts like propulsion, hydraulics, avionics, and electronic units shall be removed, inspected, repaired, and reused in new or existing aircraft (an approach already practised in commercial aviation [70]). In the scenario that reuse isn't possible due to wear, fatigue or other factors, parts made from recyclable materials will be recycled, reducing environmental impact. This is shown in Table 21.2, where 67% of the non-reusable mass of the aircraft is considered as valuable after ceasing operations. As can also be seen in Table 21.2, the design prioritises recyclable materials over non-recyclable materials such as composites; metal alloys are preferred, even with the slight weight penalty induced by their usage, to enable higher recycling yield and minimise ecological footprint. The material selection is described in more detail in subsection 13.3.3.

21.4. Social Sustainability

Contributors: Maxine

Social sustainability is achieved in multiple aspects of the project's design, manufacturing, and operation processes. Firstly, to achieve true social sustainability, it is essential to ensure that resources used in the project are responsibly sourced by using ethically mined materials and promoting fair production practices. Additionally, all workers involved in the design, production, and operation of this project should be treated with respect, ensuring their rights are protected and paying them a fair wage.

Due to the novel nature of the project, a positive impact may be achieved on local communities through the creation of job opportunities and investments in local economies. Active engagement with local stakeholders is pursued to understand their needs and to maximise social benefit. Transparent public communication shall be prioritised, clearly showing the project objectives and benefits, as well as possible risks and the suggested mitigation strategies. Concerns shall be addressed early to promote public acceptability of the project.

If successful, aerosol injection could help mitigate climate change by reducing global temperatures, which could lead to a decrease in weather-related health crises, benefiting global populations. Additionally, possible adverse effects of aerosol injection on human health shall be investigated thoroughly. To promote equity of access, it is essential that the benefits of the project are shared fairly across all regions and that no community is disproportionately exposed to any potential risks.

Lastly, aircraft noise was minimised through the selection of newer and quieter engine models and the selection of operating bases in remote areas to affect the minimum number of people and wildlife.

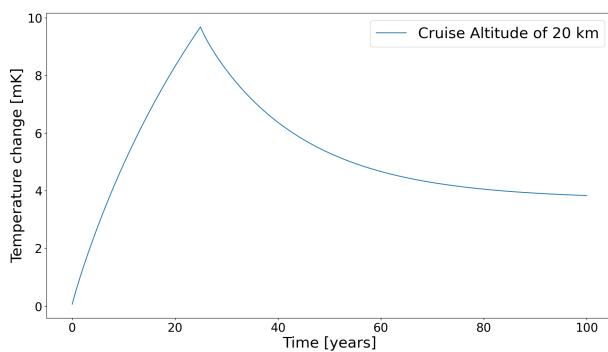
Finally, the mission shall incorporate continuous social impact assessments, ensuring that any issues are addressed promptly and that social sustainability goals, including public acceptability and equitable outcomes, are met.

21.5. Verification and Validation

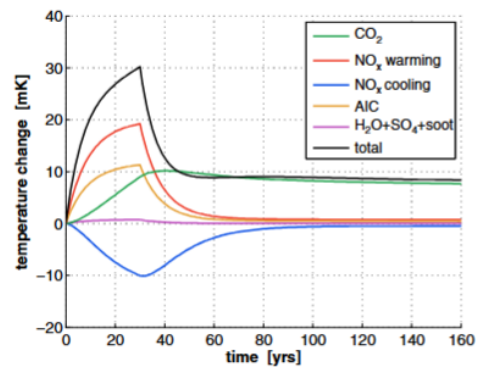
Contributors: Konstantinos, Bas

As conducted throughout the report verification for the design tool developed to obtain the ATR data and Figure 21.1 was performed, achieving a perfect coverage. Additionally, the methodology followed for all environmental impact assessment methods (Section 21.2) was verified via literature and, in particular, the papers by E.S.Dallara et al. [66] for ATR and K.M.Lee et al.[68] for LCA.

A similar procedure was followed for validation, where the output throughout Chapter 21 was compared to the two aforementioned studies. To begin with, the Average Temperature Response values come in agreement with the values obtained by both E.S.Dallara et al. [66] and the "ESRA" 2023 DSE project [23]. The temperature increase induced by the system's operation are in the same order of magnitude (mK) and the trends followed are identical, as shown in Figure 21.2, where the plots of the two studies are compared:



(a) The baseline ATR results obtained in subsection 21.2.1.



(b) ATR plots obtained by E.S.Dallara et al. [66]

Figure 21.2: Validation of the ATR data obtained in subsection 21.2.1 against the paper by E.S.Dallara et al. [66]

Validation of the life cycle assessment was performed by comparing the results to the estimations made in the paper of Pierrat E. [69]. This paper estimated the total CO₂ emissions of the aviation manufacturing sector. From this, a value for the CO₂ emissions per aircraft could then be found. This value was significantly higher than the result of the LCA, more than three times as much. A possible explanation for this could be the fact that the paper includes the manufacturing of military aircraft and wide-body commercial aircraft, of which the production emissions are logically more significant. This comparison does, however, provide more confidence in the correct order of magnitude of the LCA results.

Production Plan

Contributors: Inés

In this chapter, the production plan of the aircraft is detailed, which is the process that will take place once the final detailed design of the aircraft is finalised until the launch of the mission. This will be mainly focused on the manufacturing, assembly and integration plan of the aircraft, followed by a manufacturing flow diagram to show the production timeline, as shown in Figure 22.1.

The first step is to obtain the necessary manufacturing tooling, personnel and supplier contracts for the different parts of the aircraft. Following the normal subassembly manufacturing of an aircraft, its production will be offshored to different countries, ideally following the expertise already established in the aviation industry ¹. Given the complexity and low production volume of the different parts of the aircraft, this will be done in a batch process, reducing costs per part while still allowing for quality testing and customisation.

Once the global part manufacturing is finalised, the aircraft will be assembled in a final assembly line (FAL). The locations of the subassembly production processes, as well as the FAL, will likely be determined by the international governmental coalition funding and controlling the process. This will, at the same time, constrain the production process by the decisions driven by the industrial and economic interests of the countries involved.

As a final step, the integration of the aircraft systems must be performed. This will be a complex and critical process for the success of the mission. As specified in Section 14.4, the aircraft fully depends on the correct functioning of all the systems in the aircraft, given that it is unmanned.

On the other hand, the aerosol production will follow a completely different production process. Calcium carbonate powders are prepared by two different methods: attrition and precipitation. The precipitated form is available in several crystal habits and sizes and has a much finer particle size distribution, for which reason it is of most interest in this case [4]. Given the large amounts of aerosol needed, large-scale production in industrial installations at ground level and subsequent transport to the aircraft fleet locations will be necessary regularly. For this reason, a logistics plan to deliver the aerosol is developed for the airports as specified in Section 19.1

A sustainable approach for the production plan is followed, aligned with the objectives expressed in Chapter 21. The use of renewable energy for the different manufacturing processes is maximised, imposing a minimum of 30 % of all industrial installations to be run by green energy.

Based on the Stratolaunch production timeline, the prototype production is assumed to be 5 years, and final testing another 2 years ². Following this, the actual production rate of the fleet is approximated to be 3 aircraft per month, based on Table 22.1, choosing an approximate rate by selecting the biggest and newest aircraft models chosen.

Airbus	A220	A320neo*	A330neo	A350
Aircraft Produced	8	39	3	1
Boeing	737 MAX	767	777	787
Aircraft Produced	38	2	4	5

Table 22.1: Aircraft Production in May 2025

Given this production rate, 1 year of production will be needed to obtain the initial fleet size, and 10 years for the final fleet size.

¹<https://simpleflying.com/airbus-opens-a320-fal-in-old-a380-hangar/> Cited 13 June 2025

²URL: <https://planehistoria.com/scaled-composites-stratolaunch/> Cited 13 June 2025

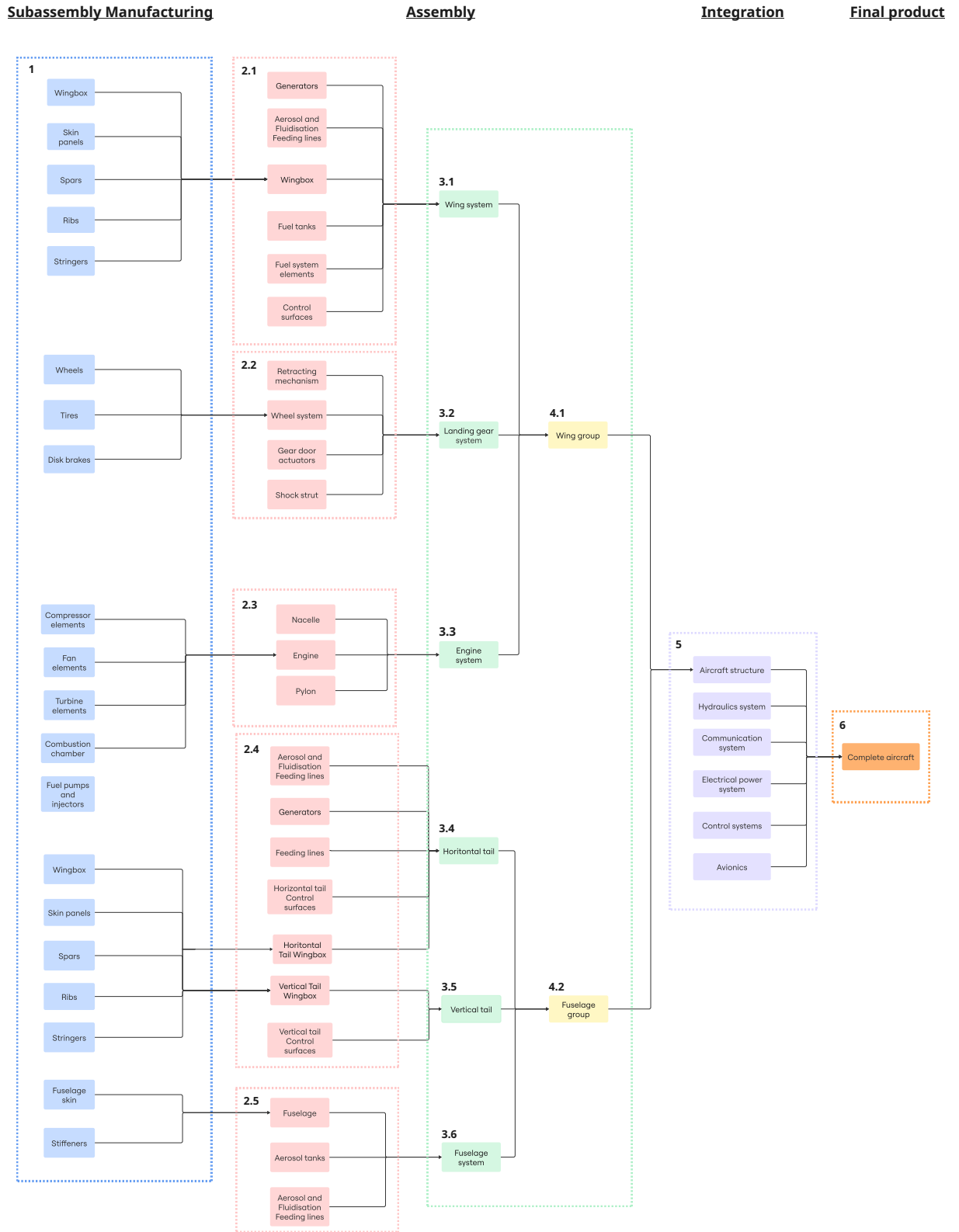


Figure 22.1: Manufacturing Flow Diagram

Future Planning

With the preliminary design completed, the next phases of the mission are analysed and the planning can commence. This chapter describes the future planning of the following stages of the mission, such as detailed design, testing and certification, operation, and end-of-life. The structure of this plan is visualised in both a project design and development logic and a Gantt chart.

23.1. Project Design and Development Logic

Contributors: Maxine

A project design and development logic is a structured visualisation of the activities to be performed in the mission's lifetime, starting at the design phase. Figure 23.1 shows the activities following the preliminary design phase.

Preliminary Design

The preliminary design phase is completed during the design synthesis exercise, which focuses on selecting and designing the outlines of a concept.

Detailed Design

The subsystems are designed during the detailed design phase, and detailed analysis is performed, including extensive CFD, FEM, and weight iterations. In this stage, special attention will be given to the RAMS plan as described in Chapter 20. A certification plan is initiated early in this phase. After performing iterations, a final design is presented and reviewed, and manufacturing documentation is released to prepare for prototype production.

Testing and Certification

This phase includes performing all necessary tests to validate and certify the aircraft, including system, integration, static, and full mission tests. Data is collected throughout. Following testing, compliance with requirements is assessed. If compliance is rejected, the process iterates back to the detailed design phase for revisions. If compliance is confirmed, the final design is presented to stakeholders in a final review, and the process for receiving the certification is commenced.

Production

Once certification has been received, aircraft production is started, and airworthiness is demonstrated for all produced aircraft.

Operation

The operational phase includes the planning of detailed operational procedures and personnel training, which will start in the latter stages of the testing and certification phase, as well as the commencement of operations. The mission operations start with a reduced fleet and are scaled up to the full fleet in 15 years. Throughout the entire operational phase, continuous maintenance activities are performed.

End-of-Life

This phase starts once the first aircraft reaches its end-of-life and continues parallel to the operational phase. The end-of-life activities include the recycling and reusing of aircraft materials and the production of replacement aircraft.

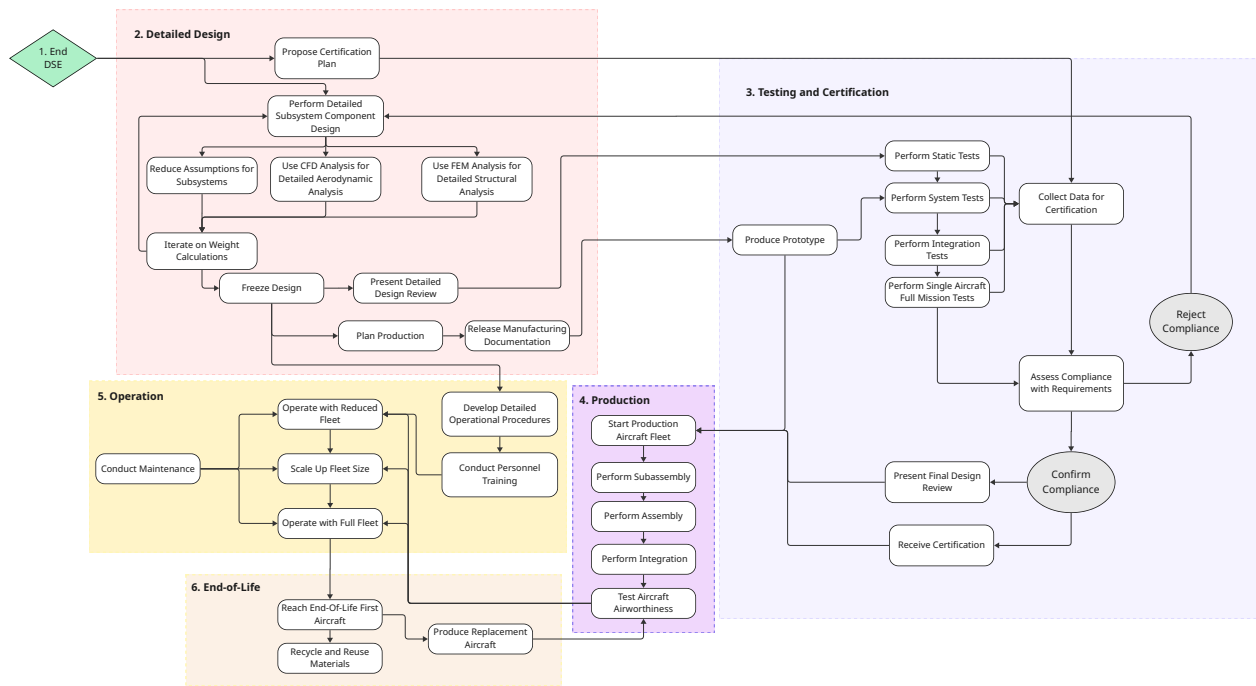


Figure 23.1: Project Design and Development Logic

23.2. Project Gantt Chart

Contributors: Maxine

Figure 23.2 shows the Gantt Chart for the future phases of the project as described in Section 23.1. This shows all major activities and their dependencies, as well as the estimated duration in months. Additionally, the main milestones are shown above. Due to the novel nature of the mission, longer than normal detailed design and testing phases were assumed¹. Additionally, due to the large fleet size, production is estimated to have an extended duration; however, initial fleet operations can commence as soon as this amount of aircraft has been demonstrated to be airworthy.

¹<https://www.easa.europa.eu/en/domains/aircraft-products/aircraft-certification> cited: 13 June 2025

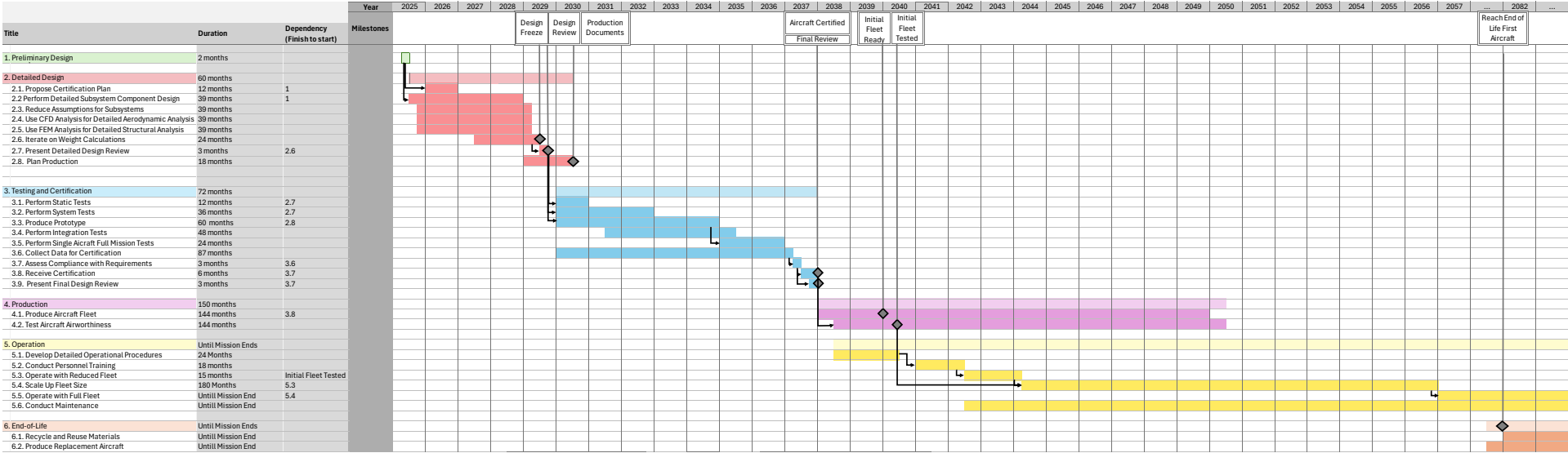


Figure 23.2: Project Gantt Chart

Conclusion

Contributors: Maxine

Actions against climate change have become increasingly urgent, with climate effects becoming more prominent every year. Stratospheric Aerosol Injection has been proposed as a possible mitigation technique, reducing the global temperature while long-term solutions, such as carbon capture and carbon neutrality, are implemented. Specifically, solid aerosols have been a new focus of research, due to the indicated reduction in harmful environmental effects, such as stratospheric heating, compared to liquid aerosols.

The preliminary design of a stratospheric aircraft optimised for solid aerosol injection presented in this report demonstrates practical insights into the feasibility and potential of Solid Stratospheric Aerosol Injection, a targeted, less harmful approach to climate mitigation. These insights may act as a supplement to current research, allowing for a better view of the large-scale implementation of this proposed geoengineering technology.

The proposed aircraft was chosen to be a twin fuselage of diameter 1.344 m with a large aspect ratio of 20 and a wing surface area of 272.96 m². This configuration achieved a good lift-to-drag ratio, and aeroelasticity was determined to be within an acceptable range based on the analysis performed.

As calcium carbonate has a very high agglomeration tendency, special care had to be taken in the design of the injection system. The chosen system consists of 62 generators utilising steel balls and acoustic vibrations to break off agglomerated particles and feed the aerosolised material into a series of 36 nozzles. The nozzles utilise high-velocity air to break up particles further.

An initial fleet of 33 and a final fleet of 385 aircraft carrying 17000kg payload will inject solid CaCO₃ aerosol from near the airfoil trailing edge during cruise at altitudes of 20km and 21.7km. These aircraft will operate from the aircraft located near latitudes 30°N, 15°N, 15°S, and 30°S.

The total cost was determined to be USD 58.07 billion. By 2030, the market value of the system was estimated to be USD 40.65 billion, and the total profit was estimated to be 31.91 billion euros.

While challenges remain, the preliminary design outlined in this report offers a practical demonstration of stratospheric aerosol injection technology, applied in real life and the related benefits and costs.

24.1. Recommendations

Contributors: Máté

The final design presented in this report corresponds to a preliminary design by global standards. It has been determined that the mission is feasible, has potential for immense benefits and a sizing is suggested for the optimal delivery of the payload within the operational constraints. For the future design, it is suggested to keep iterating the detailed properties of all the subsystems into the overall designs to update weight and drag estimates. The autonomous system should also be designed.

Moreover, it is suggested to invest in increasing the injection rate of calcite aerosolisation technology as the sensitivity studies show that an improvement in this field would make the overall mission much easier. It is also suggested to quantify the effect of injection altitude on aerosol residence time, because delivering less payload to higher altitudes, although inefficient, is also feasible.

Furthermore, more detailed analysis of the aerodynamic design must be performed using CFD and wind tunnel data to verify the aerodynamic design and characterise the wake effects on aerosol agglomeration. Finally, the structure must be validated using FEM simulations and structural tests to verify integrity and safety.

Bibliography

- [1] Vattioni, S., Luo, B., Feinberg, A., Stenke, A., Vockenhuber, C., Weber, R., Dykema, J. A., Krieger, U. K., Ammann, M., Keutsch, F., Peter, T., and Chiodo, G., “Chemical Impact of Stratospheric Alumina Particle Injection for Solar Radiation Modification and Related Uncertainties,” *Geophysical Research Letters*, Vol. 50, No. 24, 12 2023.
- [2] Stefanetti, F., Vattioni, S., Dykema, J. A., Chiodo, G., Sedlacek, J., Keutsch, F. N., and Sukhodolov, T., “Stratospheric injection of solid particles reduces side effects on circulation and climate compared to SO₂ injections,” *Environmental Research: Climate*, Vol. 3, No. 4, 2024.
- [3] Vattioni, S., Peter, T., Weber, R., Dykema, J. A., Luo, B., Stenke, A., Feinberg, A., Sukhodolov, T., Keutsch, F. N., Ammann, M., Vockenhuber, C., Döbeli, M., Kelesidis, G. A., and Chiodo, G., “Injecting solid particles into the stratosphere could mitigate global warming but currently entails great uncertainties,” *Communications Earth and Environment*, Vol. 6, No. 1, 12 2025.
- [4] Neukermans, A., Cooper, G., Foster, J., Galbraith, L., and Jain, S., “Methods for Dispersal of Precipitated Calcium Carbonate for Stratospheric Aerosol Injection,” *Journal of Atmospheric and Oceanic Technology*, 7 2021.
- [5] Ward, R. X., Hack, M., and McNeill, V. F., “A low-cost solid aerosol generator of high stability,” Tech. rep., 2025.
- [6] Saravanamuttoo, H., Rogers, G., and Cohen, H., *Gas Turbine Theory*, Prentice Hall, 5th ed., 2001.
- [7] Statistics Market Research Consulting, “Geoengineering Market Forecasts to 2030 - Global Analysis By Type (Carbon Dioxide Removal, Solar Radiation Management, Weather Modification and Other Types), Technology, Planetary Ecosystem, Application, End User and By Geography,” 11 2024.
- [8] Tec-shs, *Technology Readiness Levels Handbook For Space Applications*, 1st ed., 9 2008.
- [9] Raymer, D. P., *Aircraft Design: A Conceptual Approach*, American Institute of Aeronautics and Astronautics, Sylmar, California, 3rd ed., 1999.
- [10] DSE Group 3, “Midterm Report Stratospheric Aerosol Injection Mission,” Tech. rep., Delft University of Technology, Delft, 5 2025.
- [11] Sharpe, P. D., *AeroSandbox: A Differentiable Framework for Aircraft Design Optimization*, Ph.D. thesis, 2021.
- [12] Roskam, J., *Airplane Design: Preliminary sizing of airplanes*, DARcorporation, 2005.
- [13] EASA, “Certification Specifications and Acceptable Means of Compliance for Large Aeroplanes (CS-25),” Tech. rep., 2023.
- [14] Anderson, J., “Fundamentals of Aerodynamics,” .
- [15] Torenbeek, E., *Synthesis of Subsonic Airplane Design*, Delft University Press, Delft, The Netherlands, 1982.
- [16] International Civil Aviation Organization, “Aerodrome Design Manual Part 2 — Taxiways, Aprons and Holding Bays,” Tech. rep., International Civil Aviation Organization, 2020.
- [17] Ničā, M., Scholz, D., and Hamburg, W., “Estimating The Oswald Factor From Basic Aircraft Geometrical Parameters,” Tech. rep., 2012.
- [18] Vos FPP MFM Hoogreef FPP BTC Zandbergen SSE, R., “Aerospace Design and Systems Engineering Elements I The Design of the Fuselage,” Tech. rep.
- [19] Steenwijk, B. . and Druetta, P., “Numerical Study of Turbulent Flows over a NACA 0012 Airfoil: Insights into Its Performance and the Addition of a Slotted Flap,” 2023.
- [20] Slaboch, P. E. and Volpe, J. A., “An Operational Model for the Prediction of Jet Blast,” Tech. rep.
- [21] Kleinstein, G., “An approximate solution for the axisymmetric jet of a laminar compressible fluid,” *Quarterly of Applied Mathematics*, Vol. 20, No. 1, 4 1962, pp. 49–54.
- [22] DSE Group 2, “Final Design Report Stratospheric Aerosol Geoengineering Aircraft,” Tech. rep., Delft University of Technology, Delft, 2016.
- [23] DSE Group 14, “Final Report European Stratospheric Research Aircraft,” Tech. rep., Delft University of Technology, Delft, 6 2023.
- [24] Smith, W., “The cost of stratospheric aerosol injection through 2100,” *Environmental Research Letters*, Vol. 15, No. 11, 10 2020, pp. 114004.
- [25] U.S. Department of the Interior U.S. Geological Survey, “Mineral commodity summaries 2025,” Tech. rep., Reston, VA, 2025.
- [26] Israelachvili, J. N., *Intermolecular and Surface Forces*, Elsevier, Santa Barbara, 3rd ed., 2011.
- [27] Bergström, L., “Hamaker constants of inorganic materials,” *Advances in Colloid and Interface Science*, Vol. 70, 1997, pp. 125–169.
- [28] Francis, L. F. and Roberts, C. C., “Dispersion and Solution Processes,” *Materials Processing: a Unified Approach to Processing of Metals, Ceramics, and Polymers*, 1 2024, pp. 431–548.
- [29] Raymer, D. P., *Aircraft Design: A Conceptual Approach*, American Institute of Aeronautics and Astronautics Inc., 6th ed., 2018.
- [30] Duncan, J. S., “United States Standard for Terminal Instrument Procedures (TERPS),” 2018.
- [31] Sadraey, M. H., “Aircraft design: a systems engineering approach,” Tech. rep., 2013.
- [32] Scholz Dieter, “Aircraft Design,” Tech. rep., Hamburg University of Applied Sciences, 2015.

- [33] Varriale, C., "AE2230-I Flight Mechanics Lecture 6 - Cruise performance: operations," 2024.
- [34] Roskam, J. and Edward Lan, C.-T., *Airplane Aerodynamics and Performance*, DARcorporation, 1997.
- [35] Ruijgrok, G. J. J., *Elements of airplane performance*, VSSG, 2009.
- [36] Fabrizio, O., "AE3211-I Systems Engineering and Aerospace Design: Design for Lateral-Directional Aspects, Design for Ground Operations, Use of SE for Aircraft Design," Tech. rep., Delft University of Technology.
- [37] "9 Empennage General Design," Tech. rep., Hamburg University of Applied Sciences (HAW Hamburg).
- [38] Fabrizio, O., "AE3211-I Systems Engineering and Aerospace: Design Requirement Analysis and Design principles for A/C stability & control (Part 1)," Tech. rep., Delft University of Technology.
- [39] Fabrizio, O., "AE3211-I-Systems Engineering and Aerospace Design: Requirement Analysis and Design principles for A/C stability & control (Part 2)," Tech. rep., Delft University of Technology.
- [40] Torenbeek, E., "Advanced Aircraft Design," Tech. rep., 2013.
- [41] Caughey, D. A., "Introduction to Aircraft Stability and Control Course Notes for M&AE 5070," .
- [42] F Zabm Washington, b. A., "RELATION OF RIB SPACING TO STRSS § IN WING," Tech. rep., 1920.
- [43] NASA, "Aerospace Materials Characteristics," .
- [44] Howard D. Curtis, *Fundamentals of Aircraft Structural Analysis*, 1996.
- [45] T. H. G. Megson, *Aircraft Structures for Engineering Students*, 4th ed., 2007.
- [46] Strzelecki, P., Correia, J. A., and Sempruch, J., "Estimation of fatigue S-N curves for aluminium based on tensile strength – proposed method," *MATEC Web of Conferences*, Vol. 338, 2021, pp. 01026.
- [47] R. Wright, J. and E. Cooper, J., "INTRODUCTION TO AIRCRAFT AEROELASTICITY AND LOADS," Tech. rep., 2015.
- [48] Roskam, J., "Airplane Design Part IV: Layout Design of Landing Gear and Systems Design * Analysis * Research," Tech. rep.
- [49] Fu, Y., Gou, Z., Wang, M., Zhu, D., and Lin, Z., "Design and Experimental Verification on Characteristics of Local Electro-Hydraulic Generation System," *2020 IEEE International Conference on Mechatronics and Automation, ICMA 2020*, 10 2020, pp. 389–394.
- [50] Van Den Bossche, D., "THE A380 FLIGHT CONTROL ELECTROHYDROSTATIC ACTUATORS, ACHIEVEMENTS AND LESSONS LEARNT," *ICAS*, 2006.
- [51] Wertz, J., Everett, D., and Puschell, J., *Space Mission Engineering - The New SMAD*, 2011.
- [52] EUROCAE, "ED-112A | MOPS for Crash Protected Airborne Recorder Systems," Tech. rep., EUROCAE, 9 2013.
- [53] Pierce, J. R., Weisenstein, D. K., Heckendorn, P., Peter, T., and Keith, D. W., "Efficient formation of stratospheric aerosol for climate engineering by emission of condensable vapor from aircraft," *Geophysical Research Letters*, Vol. 37, No. 18, 9 2010.
- [54] DSE Group 3, "Baseline Report Stratospheric Aerosol Injection Mission," Tech. rep., Delft University of Technology, Delft, 5 2025.
- [55] Voth, V., Lübke, S. M., and Bertram, O., "Estimating Aircraft Power Requirements: A Study of Electrical Power Demand Across Various Aircraft Models and Flight Phases," *Aerospace*, Vol. 11, No. 12, 11 2024, pp. 958.
- [56] Janssens, M., de Vries, I. E., and Hulshoff, S. J., "A specialised delivery system for stratospheric sulphate aerosols: design and operation," *Climatic Change*, Vol. 162, No. 1, 8 2020, pp. 67–85.
- [57] Lee, W. R., Vioni, D., Bednarz, E. M., MacMartin, D. G., Kravitz, B., and Tilmes, S., "Quantifying the Efficiency of Stratospheric Aerosol Geoengineering at Different Altitudes," *Geophysical Research Letters*, Vol. 50, No. 14, 7 2023, pp. e2023GL104417.
- [58] Elsayed, E., *RELIABILITY ENGINEERING*, 1996.
- [59] Robert G.Arno, *NONELECTRONIC PARTS RELIABILITY DATA*, Reliability Analysis Center, 12 1981.
- [60] Dhillon, B. S., *Reliability, quality, and safety for engineers*, CRC Press, 2005.
- [61] Shannon, M. and Ackert, P., "Basics of Aircraft Maintenance Programs for Financiers Evaluation & Insights of Commercial Aircraft Maintenance Programs," Tech. rep., 2010.
- [62] Van Den Bergh, J., De Bruecker, P., Beliën, J., and Peeters, J., "Aircraft maintenance operations: state of the art," Tech. rep., 2013.
- [63] Kulkarni, A., Yadav, D. K., and Nikraz, H., "Aircraft maintenance checks using critical chain project path," *Aircraft Engineering and Aerospace Technology*, Vol. 89, No. 6, 2017, pp. 879–892.
- [64] Manary, J., "Patent: Method, system and computer-readable medium for predicting the operational availability of a weapon system," 12 2004.
- [65] Karunadasa, K. S., Manoratne, C., Pitawala, H., and Rajapakse, R., "Thermal decomposition of calcium carbonate (calcite polymorph) as examined by in-situ high-temperature X-ray powder diffraction," *Journal of Physics and Chemistry of Solids*, Vol. 134, 11 2019, pp. 21–28.
- [66] Dallara, E. S., Kroo, I. M., and Waitz, I. A., "Metric for Comparing Lifetime Average Climate Impact of Aircraft," *AIAA Journal*, Vol. 49, No. 8, 2011.
- [67] Rosenow, J., Schultz, M., and Fricke, H., "Impact of ocean currents on contrail formation on global scale," Tech. rep., 2014.
- [68] Lee, K.M. and Inaba, A., "Life Cycle Assessment Best Practices of ISO 14040 Series Ministry of Commerce, Industry and Energy Republic of Korea Asia-Pacific Economic Cooperation Committee on Trade and Investment," 2004.

-
- [69] Pierrat, E., Rupcic, L., Hauschild, M. Z., and Laurent, A., “Global environmental mapping of the aeronautics manufacturing sector,” *Journal of Cleaner Production*, Vol. 297, 5 2021, pp. 126603.
- [70] Vasco de Oliveira Fernandes Lopes, J., Aeroespacial Júri Presidente, E., João Manuel Lage de Miranda Lemos Orientador, D., Agostinho Rui Alves da Fonseca Co-Orientador, D., and Paulo Jorge Trigo Ribeiro, D., “Life Cycle Assessment of the Airbus A330-200 Aircraft Dissertação para obtenção do Grau de Mestre em Novembro 2010,” Tech. rep.